

Martin Schlerf

**Vom Fachbereich VI
Geographie / Geowissenschaften
der Universität Trier**

zur Verleihung des akademischen Grades

**Doktor der Naturwissenschaften
(Dr. rer. nat.)**

genehmigte Dissertation

**Determination of structural and chemical forest
attributes using hyperspectral remote sensing data
– Case studies in Norway spruce forests**

**Betreuer:
Univ.-Prof. Dr. Joachim Hill**

**Berichterstattende:
Univ.-Prof. Dr. Joachim Hill
Apl.-Prof. Dr. Willy Werner**

Datum der wissenschaftlichen Aussprache: 14.12.2005

Trier 2006

Table of contents

ABBREVIATIONS	V
LIST OF FIGURES	VII
LIST OF TABLES	X
CHAPTER 1 INTRODUCTION	1
1.1 Remote sensing of forest environments	1
1.2 Hyperspectral remote sensing	4
1.3 Forest characteristics for ecosystem modeling and inventory	6
1.4 Objectives and structure of thesis	8
CHAPTER 2 FUNDAMENTALS	9
2.1 Remote sensing	9
2.1.1 Physical principles	9
2.1.2 Atmospheric effects	12
2.1.3 Topographic effects	15
2.1.4 Geometric effects	16
2.2 Spectral reflectance properties of forests	16
2.2.1 The molecular level	17
2.2.2 The leaf level	19
2.2.3 Soil optical properties	23
2.2.4 The canopy level	24
2.2.5 Spectral reflectance properties of Norway spruce	30
2.2.6 Age dependence of forest reflectance	31
2.3 Remote sensing of forest attributes	32
2.3.1 Classes of forest attributes	32
2.3.2 Attributes related to forest type	33
2.3.3 Structural attributes	34
2.3.4 Chemical attributes	40
CHAPTER 3 MATERIAL	46
3.1 Study sites	46
3.1.1 Idarwald	46
3.1.2 Gerolstein	50
3.2 Field and laboratory data	50
3.2.1 Field data	50
3.2.2 Chemical laboratory analysis	55
3.2.3 Spectral reflectance measurements	56
3.3 HyMap image data	57
3.3.1 The HyMap sensor	57
3.3.2 The HyMap data sets	59
3.3.3 Radiometric correction	59

3.3.4 Geometric correction	64
3.3.5 Extraction of reflectance spectra from HyMap imagery	65
3.4 Forest Geographic Information System	66
CHAPTER 4 STATISTICAL AND PHYSICAL METHODS	67
4.1 Overview	67
4.2 Image classification	68
4.2.1 Introduction	68
4.2.2 Spectral Angle Mapper	69
4.3 Statistical methods	70
4.3.1 Correlation analysis	70
4.3.2 Regression analysis	71
4.3.3 Artificial neural networks	73
4.3.4 Ratio-based and orthogonal vegetation indices	74
4.3.5 The red edge inflection point	75
4.3.6 Derivative spectra	77
4.3.7 Continuum-removal and band-depth normalisation	78
4.3.8 Non-linear least-squares spectral matching	79
4.4 Physically-based reflectance modeling	80
4.4.1 Canopy reflectance models	80
4.4.2 The Invertible Forest Reflectance Model	81
4.4.3 Inversion of reflectance models	83
4.5 Validation	84
CHAPTER 5 MAPPING FOREST COVER TYPE THROUGH IMAGE CLASSIFICATION	86
5.1 Introduction	86
5.2 Implementation of additional information	87
5.3 Image classification	89
5.3.1 Data preprocessing	89
5.3.2 Training	90
5.3.3 Classification	91
5.3.4 Validation	92
5.4 Results and discussion	92
CHAPTER 6 DETERMINATION OF FOREST STRUCTURAL ATTRIBUTES	97
6.1 Introduction	97
6.2 Developing predictive models	98
6.2.1 Introduction	98
6.2.2 Computation of vegetation indices	99
6.2.3 Analysis of forest stand variables	99
6.2.4 Relationships between vegetation indices and forest variables	106
6.2.5 Absorption features related to leaf area index and crown volume	112
6.2.6 Maps of forest attributes	112
6.2.7 Conclusions	113
6.3 Inversion of a forest reflectance model	118
6.3.1 Introduction	118
6.3.2 Parameterisation of the forest reflectance model	118
6.3.3 Overview of the inversion procedure	123
6.3.4 Forward reflectance modeling	123
6.3.5 Spectral sampling	124

6.3.6 Network architecture and training	124
6.3.7 Validation of inversion results and modification of network architecture	127
6.3.8 Maps of forest attributes	130
6.3.9 Conclusions	130
CHAPTER 7 ESTIMATION OF FOREST CHEMICAL ATTRIBUTES	131
7.1 Introduction	131
7.2 Developing predictive models	134
7.2.1 Selection of absorption features	134
7.2.2 Developing regression equations	134
7.3 Removing water from absorption features in the mid infrared	136
7.3.1 Testing the modified least squares spectral matching approach	136
7.3.2 Coupling least squares spectral matching with stepwise multiple regression	138
7.4 Estimating leaf chemicals from laboratory reflectance data	140
7.4.1 Effects of sensor bandwidth and sensor noise	140
7.4.2 Selected wavebands by stepwise multiple regression	141
7.4.3 Comparing different sets of spectral data	144
7.4.4 Application of regression models to an independent data set	144
7.5 Estimating chemical forest attributes from HyMap reflectance data	145
7.5.1 Scaling-up from leaf level to canopy level	145
7.5.2 Comparing different sets of spectral data	146
7.5.3 Maps of leaf chlorophyll concentration and leaf nitrogen concentration	149
7.5.4 Relations of foliar chemicals with other parameters	150
7.5.5 Accuracy requirements for ecological applications	153
CHAPTER 8 CONCLUSIONS AND FUTURE PERSPECTIVES	156
REFERENCES	165
SUMMARY	183
ZUSAMMENFASSUNG	186
APPENDIX A : FIELD DATA	189
A1: Plots at Idarwald test site	189
A2: Plots at Gerolstein test site	191
APPENDIX B : CHEMICAL ANALYSIS DATA	192
B1: Needle samples	192
APPENDIX C : MATLAB CODE	195
C1: INFORM model	195
C2: Inversion routine	201
ACKNOWLEDGEMENTS	204

Abbreviations

5S	5S Simulation of the Satellite Signal in the Solar Spectrum
ANN	Artificial neural network
AVIRIS	Airborne Visible/Infrared Imaging Spectrometer
BDN	Band-depth normalisation, Band depth-normalised spectra
BLR	Bivariate linear regression
C_{AB}	Chlorophyll a+b concentration
CASI	Compact Airborne Spectrographic Imager
CD	Crown diameter
CET	Central European Time
CF	Common factor
C_N	Nitrogen concentration
CO	Canopy cover, fraction of canopy closure
CR	Continuum-removal, Continuum-removed spectra
CR model	Canopy reflectance model
C_w	Water concentration
DAIS	Digital Airborne Imaging Spectrometer
DEM	Digital elevation model
dm	dry matter
DN	Digital number
DRFL	First difference of reflectance spectra
DWRS	First difference of water removed spectra
ENVI	Environment for Visualisation of Images
F-data	Field-Spec-II data
FH-data	Field-Spec-II data resampled to HyMap wavebands
FHN-data	Field-Spec-II data resampled to HyMap wavebands plus noise
FoGIS	Forest Geographic Information System
GCP	Ground Control Points
GIS	Geographic Information System
GPS	Global Positioning System
GVI	Greenness vegetation index
H	Canopy height
HyMap	Hyperspectral Mapper
IGM	Inverted Gauss model
INFORM	Invertible forest reflectance model
LAI	Leaf area index, effective leaf area index
LAI_c	Canopy leaf area index
LAI_s	Single tree leaf area index
LGI	Lagrange interpolation
LNC	Leaf nitrogen content or concentration
LSM	Least squares spectral matching

LWC	Leaf water content or concentration
mid-IR	Middle infrared
MLR	Multivariate linear regression
MNF	Minimum Noise Fraction
MVI	Mid-infrared vegetation index
NDVI	Normalised difference vegetation index
near-IR	Near infrared
OAA	Overall Accuracy
PBH	Perimeter-at-breast-height
PC	Principal component
PCA	Principal Component Analysis
PLSR	Partial least squares regression
PVI	Perpendicular vegetation index
R	Reflectance
r	Correlation coefficient
R ²	Coefficient of determination
REIP	Red edge inflection point
RFL	Reflectance spectra
RGB	Red-Green-Blue
rmse	Root mean squared error
ROI	Region of interest
RVI	Ratio vegetation index
SAM	Spectral Angle Mapper
SBM	Stem biomass
SD	Stem density
SMR	Stepwise multiple linear regression
SNR	Signal-to-noise ratio
SWIR	Short wave infrared
thermal-IR	Thermal infrared
TM	Thematic Mapper
TSAVI	Transformed soil-adjusted vegetation index
VI, VIs	Vegetation index, Vegetation indices
VOL	Crown volume
WRS	Water removed spectra

List of figures

Figure 1.1:	Vegetation parameters in forests with relevance to ecosystem simulation models	2
Figure 1.2:	Strategies to extract forest attributes from remote sensing data	3
Figure 1.3:	The concept of imaging spectrometry	5
Figure 2.1:	Interactions of incoming solar radiation with the atmosphere and the contamination of the satellite-measured radiance	13
Figure 2.2:	Absorption features of organic materials and water	17
Figure 2.3:	Typical spectra of leaf reflectance, transmittance and absorptance.....	20
Figure 2.4:	Internal structure of a dicotyledonous leaf (from Govaerts et al., 1996) and interaction of leaf tissues with incoming radiation	21
Figure 2.5:	Spectrum of specific absorption coefficients of <i>in vivo</i> chlorophyll a+b and <i>in vivo</i> carotenoids.....	22
Figure 2.6:	Classification of soil spectral curves into five general types.....	23
Figure 2.7:	Schematic representation of the changes in canopy reflectance during growth and senescence	24
Figure 2.8:	Schematic variation of canopy reflectance as a function of leaf area index for the red and near-IR domain.....	25
Figure 2.9:	Oblique (left) and nadir (right) view of black spruce (<i>Picea mariana</i>) demonstrating the gap effect.....	26
Figure 2.10:	Black spruce (<i>Picea mariana</i>) observed in backward scattering (left) and forward scattering (right) direction	26
Figure 2.11:	Causes for directional reflectance anisotropy of vegetation canopies and the associated typical shapes of the BRDF on the principal solar plane.....	27
Figure 2.12:	Variation of simulated forest canopy reflectance	29
Figure 2.13:	Measured reflectance spectra of Norway spruce at the needle, branch, and canopy level.....	30
Figure 2.14:	Measured reflectance spectra of Norway spruce for changing numbers of branches and corresponding values of cumulative LAI	31
Figure 2.15:	Canopy reflectance of Norway spruce as a function of stand age	32
Figure 3.1:	Location of study sites	47
Figure 3.2:	General map of Idarwald test site.....	51
Figure 3.3:	General map of Gerolstein test site with stand boundaries, locations of field plots and locations of targets used for radiometric calibration.....	53
Figure 3.4:	Woodman climbing a tree at Idarwald test site.....	54
Figure 3.5:	Signal-to-noise ratio measured while viewing a 50% reflectance target	56
Figure 3.6:	Raw (left) and cross-track illumination corrected (right) HyMap image profiles (upper part) and corresponding portions of the HyMap scene (lower part) at Idarwald.....	58
Figure 3.7:	Schematic representation of the sensor recalibration	59
Figure 3.8:	Atmospherically corrected HyMap reflectance spectra from various forested and non-forested areas at Idarwald study site.....	60

Figure 3.9:	Modelled against measured radiance in six wavebands based on ten reference targets at Gerolstein test site.....	63
Figure 3.10:	Extraction of spectra for various radii	64
Figure 3.11:	(A) Change of reflectance with increasing circle radius across the visible region (HyMap-bands 4-12) and (B) the near-infrared region (HyMap-bands 20-32). (C) Change of the coefficient of variation with increasing circle radius across the visible region (HyMap-bands 4-12) and (D) the near-infrared region (HyMap-bands 20-32).....	65
Figure 4.1:	Continuum-removal for chlorophyll absorption in vegetation.....	78
Figure 4.2:	Schematic view of the link between LIBERTY, SAIL, and FLIM models showing the input variables used for the simulation	80
Figure 5.1:	Four datasets of varying spectral and spatial resolution	87
Figure 5.2:	Estimated against field-measured stem density (cross-validated) at Idarwald test site	88
Figure 5.3:	Stem density (unit: ha ⁻¹) at the Idarwald obtained from black/white orthophotos.....	88
Figure 5.4:	Reflectance spectra of forest types considered in the classification process.	90
Figure 5.5:	Map of forest type at Idarwald.	96
Figure 6.1:	LAI as a function of stand age for Norway spruce stands at Idarwald test site	100
Figure 6.2:	Correlograms for six stand attributes and both reflectances (left) and first derivative reflectance spectra (right)	102
Figure 6.3:	Crown volume (VOL) as a function of stand age for Norway spruce stands at Idarwald test site.....	104
Figure 6.4:	Stem biomass (SBM) as a function of stand age for Norway spruce stands at Idarwald test site.....	104
Figure 6.5:	2D-correlation plot that shows the correlation (R ²) between LAI and narrow band RVI values	106
Figure 6.6:	Linear regression between best narrow band PVI and LAI	110
Figure 6.7:	Linear regression between best narrow band PVI and crown volume	111
Figure 6.8:	Wavelength position of selected optimal narrowband VIs for LAI (left) and VOL (right)	112
Figure 6.9:	Map of effective leaf area index at Idarwald obtained from an empirically derived predictive equation.....	115
Figure 6.10:	Map of crown volume at Idarwald obtained from an empirically derived predictive equation	116
Figure 6.11:	Map of stand mean leaf area index at Idarwald.....	117
Figure 6.12:	Measured (red) and modelled (blue) forest canopy reflectance for certain values of canopy LAI	121
Figure 6.13:	Measured (red) and modelled (blue) forest canopy reflectance against canopy LAI	121
Figure 6.14:	Modelled versus measured forest canopy reflectance for certain values of canopy LAI in different wavebands.....	122
Figure 6.15:	General procedure for estimating canopy attributes from remote sensing data through inversion of a forest reflectance model.....	123
Figure 6.16:	Structure of the Artificial Neural Network used to invert the INFORM model	125
Figure 6.17:	Modelled against measured forest canopy variables	126

Figure 6.18:	Map of effective leaf area index at Idarwald obtained through inversion of a forest reflectance model	128
Figure 6.19:	Map of stem density at Idarwald obtained through inversion of a forest reflectance model	129
Figure 7.1:	Location of absorption features related to total chlorophyll (a), water (b), and protein (c, d, e) used in the regression analysis	133
Figure 7.2:	Cross-validated rmse against number of wavebands selected by stepwise multiple regression for the Field-Spec-II data resampled to HyMap spectral bands (DWRS data set).....	134
Figure 7.3:	A) Matching of fresh needle (stack layer) spectrum in the 1500-1780 nm region with the water spectrum and with a combination of the water and the protein spectrum, B) residual spectra between the measured and the modeled spectra.....	136
Figure 7.4:	Positions of wavebands that have been selected by SMR between DWRS spectral data (resampled to HyMap wavebands) and three leaf chemicals .	139
Figure 7.5:	Estimated against measured leaf total chlorophyll concentration (C_{AB}) (left) and estimated against measured leaf nitrogen concentration (C_N) (right)	150
Figure 7.6:	Map of leaf chlorophyll concentration at Gerolstein test site	151
Figure 7.7:	Map of leaf nitrogen concentration at Gerolstein test site	152
Figure 7.8:	Statistical measures for three main phases and five main geological epochs that occur in the study area	153

List of tables

Table 2.1:	Absorption features in vegetation reflectance spectra related to leaf nitrogen concentration	19
Table 2.2:	Selected literature results on the estimation of forest structural attributes.	37
Table 2.3:	Selected literature results on the estimation of foliar chemicals from spectral variables using different methodologies	41
Table 3.1:	Soil substrates occurring at the Gerolstein test site	48
Table 3.2:	Soil chemical indicators for three typical soil profiles occurring at the Gerolstein test site.....	49
Table 3.3:	Spectral configuration of the HyMap sensor.....	57
Table 4.1:	Broadband vegetation indices investigated in this study	75
Table 5.1:	Training data used in the forest classification.....	89
Table 5.2:	Summary of accuracies	91
Table 5.3:	Confusion matrices for 5 different datasets: A: hyperspectral, 5 m; B: multispectral, 5 m; C: hyperspectral, 30 m; D: multispectral 30 m, E: hyperspectral 5 m and orthophoto derived stem density	93
Table 6.1:	Resulting subsets after stratification according to forest stand age	97
Table 6.2:	Summary statistics for forest stand attributes.....	98
Table 6.3:	Linear correlation between forest stand variables	98
Table 6.4:	Linear correlation between forest stand attributes and HyMap reflectance resampled to TM spectral bands	100
Table 6.5:	Statistics of the first component factor of the varimax rotation (CF1) compared to the Eigenvector of the first principal component PC1.....	103
Table 6.6:	Linear correlation between principal components and HyMap reflectance resampled to TM spectral bands	103
Table 6.7:	Best narrow band RVI and PVI derived from 2D-correlation plots for different subsets	107
Table 6.8:	Cross-validated R^2 (first line) and cross-validated rmse (second line) for linear regression between broadband and hyperspectral (narrowband VIs and REIP) indices and forest stand variables LAI and VOL.....	109
Table 6.9:	Summary statistics for leaf area index in five age classes	113
Table 6.10:	Relationships between canopy leaf area index and the attributes canopy cover, stem density and canopy height	119
Table 6.11:	Inputs to the INFORM model used to compare modelled with measured reflectance spectra derived from field data and modelled values of CO and LAI_c	119
Table 6.12:	Important parameters that were kept constant during all model simulations.....	120
Table 6.13:	Statistics of canopy variables used to simulate forest reflectance	124
Table 7.1:	Summary of data for three chemicals at two sites. C_{AB} = Chlorophyll a+b concentration, C_N = Nitrogen concentration, C_W = Water concentration	132
Table 7.2:	Five absorption features used in the regression analysis.....	133

Table 7.3:	The cross-validated coefficient of determination (R^2) and the cross-validated rmse between two sets of spectral data (features at 1800 nm, 2100 nm, and 2300 nm) and nitrogen and water for 1 st year needle reflectance spectra resampled to HyMap spectral bands	137
Table 7.4:	The cross-validated coefficient of determination (R^2) and the cross-validated rmse between spectral data (DWRS) and concentrations of chlorophyll, nitrogen and water.....	138
Table 7.5:	Wavebands that have been selected by SMR between DWRS spectral data (resampled to HyMap wavebands) and three leaf chemicals.....	140
Table 7.6:	Wavelengths correlated with nitrogen (Nit), protein (Pro), total chlorophyll (Chl) and water (Wat) by multivariate statistical measures	142
Table 7.7:	The cross-validated coefficient of determination (R^2) and the cross-validated rmse between three types of spectral data (resampled to HyMap wavebands) and three leaf chemicals.....	143
Table 7.8:	Wavebands selected by SMR using three sets of spectral data (resampled to HyMap wavebands) and three leaf chemicals.....	143
Table 7.9:	The performance of regression equations developed from the calibration dataset (Gerolstein) that were afterwards applied to the validation data set (Idarwald) for estimation of chemicals	145
Table 7.10:	The cross-validated coefficient of determination (R^2) and the cross-validated rmse between five types of spectral data (HyMap imagery) and three leaf chemicals.....	147
Table 7.11:	Wavebands selected by SMR using five sets of spectral data (HyMap imagery) and three leaf chemicals.....	148
Table 7.12:	Wavebands that have been selected by SMR between CR spectral data (HyMap imagery) and three leaf chemicals	149
Table 8.1:	Determination of leaf area index (n = 39) using different methods and data.....	159
Table 8.2:	Determination of chemical forest attributes using laboratory and HyMap data and three types of spectral derivatives	160

Chapter 1 Introduction

1.1 Remote sensing of forest environments

A significant progress has been realised in the remote sensing of forests in recent years linked to technological advances in sensor design, growth in information extraction techniques and increasing requirement to quantitatively describe and understand our environment (Wulder & Franklin, 2003). Remote sensing instruments measure the radiation that is emitted or reflected from the earth's surface. The diversity of instruments available at present and in the future provide data with broad to fine spectral resolution, with large to small spatial resolution and other characteristics (e.g., multi-directionality) suitable for the quantitative and qualitative analysis of forests (Peterson & Running, 1989). A relatively new optical sensor type, the imaging spectrometer, represents a technological advance in remote sensing, as it measures the reflected signal with a very fine spectral resolution (Curran, 1994). These hyperspectral measurements need to be transformed into vegetation attributes in order to use such data for certain applications.

As a result of the technological and methodological advances the need of information derived from forest remote sensing has risen considerably in applications such as forest inventory and management, monitoring of forest fire and disease and environmental change assessment. While traditionally forest information for inventory purposes was gathered in situ or through air photography, remote sensing is becoming central, as an increasing spatial and temporal resolution of observations is desired (Cihlar et al., 2003). The increasing demand for information on the productivity of the world's forests has led to new approaches beyond traditional ground-based forest inventory techniques. The development of physiologically-based process models together with digital remote sensing methodologies allow for a better prediction of forest growth patterns across landscapes (Coops & White, 2003). Remotely sensed forest attributes may be used to initialise, update, and validate ecosystem simulation models. As a key variable, leaf area index is often used to couple remote sensing with process models. The determination of forest attributes by means of remote sensing requires the usage of appropriate sensors and methodologies. Current concepts to remotely sense ecosystem-relevant forest attributes are schematically illustrated in Figure 1.1.

While previously pre-processing of remote sensing images, such as geometric and radiometric adjustments, occupied a large portion of the information extraction process, image analysis has become increasingly able to process the available data into the actual information desired (Wulder & Franklin, 2003). Information extraction from remote sensing data can be described in terms of models of the sensor, atmosphere, and the scene (Strahler et al., 1986; Franklin et al., 2003): In remote sensing of forests, the scene comprises a forested portion of the earth surface viewed at a specific scale. An appropriate image processing strategy is applied depending on whether the attribute to be mapped occurs over spatial extents that are larger or smaller than the spatial resolution of the sensor (Figure 1.2). Mapping of the attribute ‘forest type’ (e.g. tree species, age class) assumes that the image pixel is completely covered by one forest type and thus, many pixels form a forest stand. In this case, image classification would be a suitable processing algorithm. Multispectral classification techniques are used to map

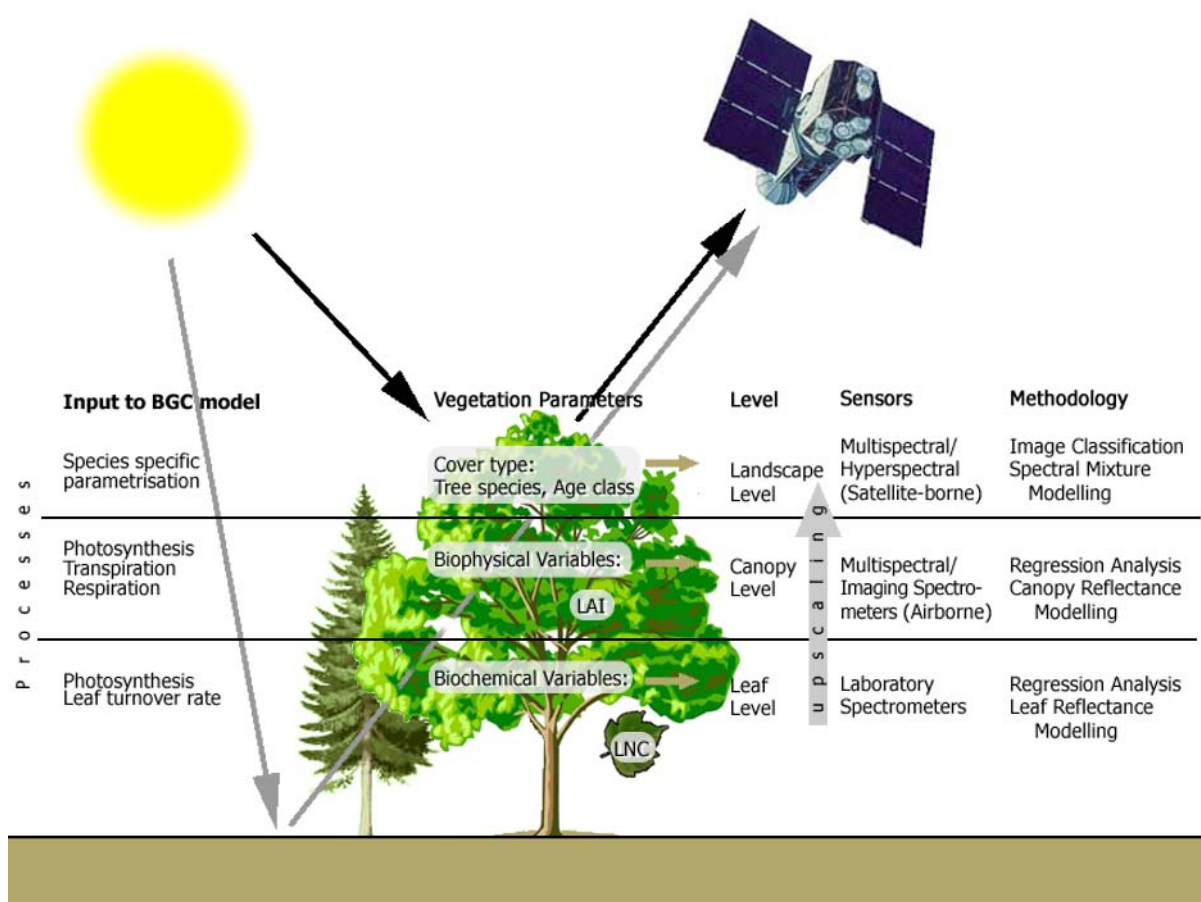


Figure 1.1: Vegetation parameters in forests with relevance to ecosystem simulation models, i.e. biogeochemical (BGC) models, that are open to remote sensing include cover type, leaf area index (LAI), and leaf nitrogen content (LNC). Cover type is usually mapped at the landscape or canopy level using image classification techniques of multispectral satellite imagery. LAI and other structural attributes can be estimated through statistical or physical modeling approaches where both multi- and hyperspectral data may be implemented. Efforts to determine leaf chemical attributes, such as LNC or chlorophyll content commonly start at the leaf level and try to progress towards the canopy and landscape levels.

qualitative attributes into distinct classes. When the focus of the analysis is on attributes that vary within a stand on a sub-pixel level (e.g. leaf area index, canopy cover, biomass or chlorophyll concentration), quantitative processing algorithms have to be chosen. Quantitative attributes can generally be derived through statistical (empirical) or physical approaches. The empirical approach relates measurements of reflectance or vegetation indices to the desired forest variable through a statistically-derived equation. The physical approach calculates reflectance from leaf, canopy and stand characteristics using mathematical equations based on physical principles. These reflectance models can be either used in the “forward mode” to simulate reflectance characteristics from given object properties or in the “inverse mode” to estimate the object property from given reflectance data (Goel, 1989; Asner et al., 2003). Opposed to empirical regression, physically-based approaches have the advantage that they can take into account effects of varying canopy structure, canopy shadow, understorey and soil that all influence the radiation measurements. Spectral mixture analysis uses simple reflectance models to estimate the fractional cover of major types of materials within image pixels.

Forests are generally challenging targets as a consequence of tree dimensions, architectural heterogeneity and spatial-temporal foliage dynamics. Remote sensing of forest structural and

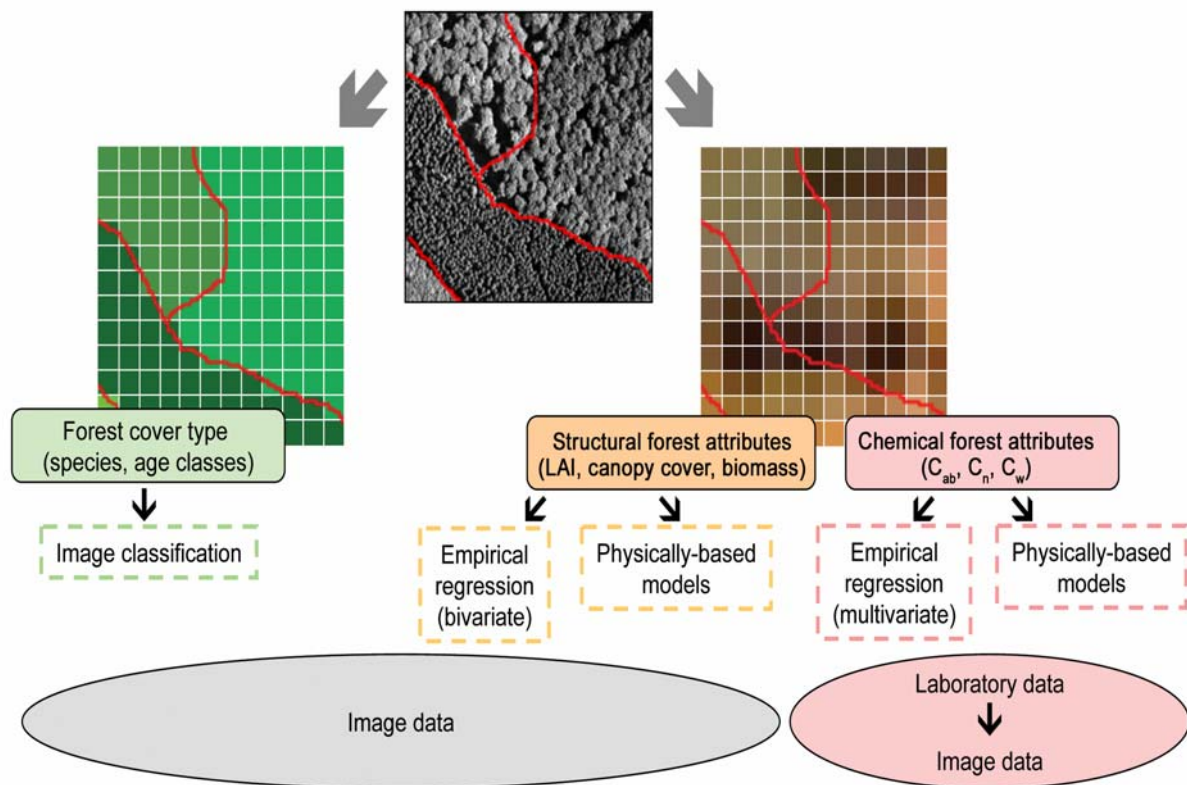


Figure 1.2: Strategies to extract forest attributes from remote sensing data as implemented within the framework of this research. See text and section 1.4 for further details.

chemical attributes is further complicated by the contribution of understory vegetation, litter, soil, bark as well as plant and relief shadow, all of which influence the whole radiometric signal (Spanner et al., 1990; Chen et al., 1999; Soudani et al., 2002). Mapping of forest cover becomes a particularly difficult task when trees of different species and age form mixed stands. Managed forests, in particularly coniferous stands exhibit a number of advantages to remote sensing. The forest stands have a relatively homogenous structure as trees within a single stand are of the same species and age. Coniferous trees, such as Norway spruce (*Picea abies* L. Karst.), with its relatively large number of foliage age classes, do not show very pronounced seasonal changes in stand structure (Vose et al., 1994) and are well suited to combine remotely sensed imagery with field-measured data.

There is a substantial interest in forest monitoring at continental, regional, and local scales. However, the present availability of hyperspectral remote sensing imagery of highest data quality (e.g., the HyMap sensor) is limited to airborne systems which collect data of limited spatial extent. Therefore, the focus of this research is on areas that can be covered by single HyMap scenes and thus, on local studies.

1.2 Hyperspectral remote sensing

Hyperspectral remote sensing or imaging spectrometry refers to the recording of remote sensing data using imaging spectrometers. These instruments collect radiance values in many narrow bands forming continuous spectra. As imaging spectrometer data is characterised by a high spectral resolution compared to multispectral data it is also called hyperspectral. The concept of imaging spectrometry is shown in Figure 1.3. Reflected solar radiation from the earth's surface is dispersed in a spectrometer and recorded in 100-200 spectral images of the scene. For each pixel of the scene a continuous reflectance spectrum is obtained (Vane & Goetz, 1988).

Imaging spectrometry originated from the merging of spectroscopy and imaging. Reflectance spectroscopy, the study of reflected light as a function of wavelength, has been used as a quantitative tool in the laboratory for many years. Optical imaging sensors have been developed since the 1970s (e.g. Landsat MSS, Landsat TM). The first images from an airborne imaging spectrometer (AIS) were acquired in the early 1980s and up to now a wide range of systems have been developed. Several airborne hyperspectral sensors, such as AVIRIS or HyMap, have operated successfully. Spaceborne hyperspectral sensor face certain limitations compared to airborne systems: the lower signal-to-noise ratio (SNR), significantly more atmosphere effects, and detector calibration issues. Nonetheless, first space-borne sensors of more or less hyperspectral type designed for land imaging were launched during the last years. On board of the TERRA platform (launch: 1999) are the Advanced Spaceborne Thermal Emission and Reflectance Radiometer (ASTER) and the Moderate resolution

imaging spectroradiometer (MODIS). EO-1 (launch 2000) hosts the Hyperion hyperspectral imager and the Advanced Land Imager (ALI). In 2002, Envisat which carries the MERIS (Medium Resolution Imaging Spectrometer) instrument was launched by the European Space Agency. Multi-angular systems, that collect spectral data observed under different directions, help to determine structural vegetation characteristics. Examples of such systems are the hyperspectral sensor CHRIS on PROBA (launched in October 2001) and POLDER on ADEOS-2 (launch scheduled for late 2002). Despite an emerging fleet of satellites providing frequent, high spectral resolution data to users, airborne systems will continue to play an important role in forest remote sensing due to their high data quality and their flexible use.

Imaging spectrometry was used initially in geological, then in aquatic and later in ecological and atmospheric research (Curran, 1994). The motivation for the development of imaging spectrometry was mineral identification through diagnostic absorption features (Van der Meer, 1994). These narrow spectral features can not be resolved by multispectral sensors such as Landsat TM because its spectral bandwidth is too wide and the bands are not contiguous (Vane & Goetz, 1988). Plants, in contrast, are composed of the same few chemical compounds and therefore have similar spectral signatures. The spectral variability of vegetation is mainly located within three to five wavelengths regions and the same number of well-placed wavebands could account for most of it. The usage of hyperspectral data to determine forest attributes is based on the assumption that improved identification of particular spectral features will lead to improved discrimination of forest attributes (Lefsky & Cohen, 2003). Curran (2001) states an idealised point of view of the advantage of a hyperspectral over a multispectral sensor in vegetation studies: Whereas a multispectral

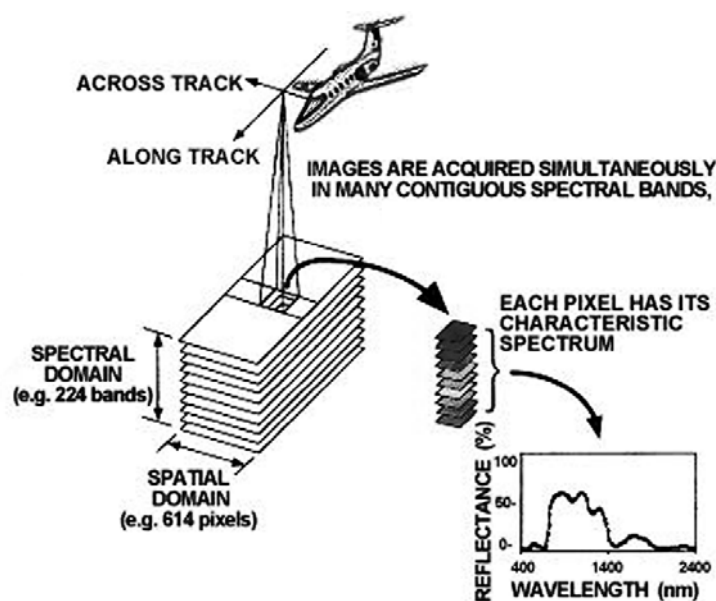


Figure 1.3: The concept of imaging spectrometry (after Vane & Goetz, 1988).

sensor is suitable to identify the type of vegetation observed, the information about the condition of that vegetation resides within narrow spectral features which can be identified solely by sensors with many narrow wavebands.

Useful reviews of the application of imaging spectrometry are provided by Vane & Goetz (1993), Curran (1994), Hill & Megier (1994), Treitz & Howarth (1999) and Van der Meer & De Jong (2001). Past and current research in the field of ecology is mainly concentrating on estimating foliar chemical concentrations of plant leaves (Card et al., 1988; Elvidge, 1990; Curran et al. 1992; Jacquemoud et al., 1996; Fourty & Baret, 1998; Curran et al. 2001) and of canopies (Peterson et al., 1988; Wessman et al., 1988; Serrano et al., 2002; Zarco-Tejada et al., 2004), the estimation of structural canopy attributes (Gong et al., 2003; Lee et al., 2004), and cover type (Franklin, 1994; Martin et al., 1998). Despite intensive research and increasing literature available in the field of hyperspectral remote sensing, it is not yet clear, to what extent hyperspectral remote sensing a) can improve derivation of structural forest attributes compared to traditional sensor types and b) allows determination of chemical forest attributes.

1.3 Forest characteristics for ecosystem modeling and inventory

Terrestrial ecosystems play an important role in the exchange of matter and energy between soil, vegetation and the atmosphere (Mooney et al., 1987; Schimel et al., 2001). In this context, the Earth's forests and woodlands are of particular importance, as they cover approximately 40 percent of the global land surface and provide around 70 percent of the annual net accumulation of terrestrial carbon (Peterson & Running, 1989). Most of the forests located in the mid-latitudes of the Northern Hemisphere act as a carbon sink, however, with considerable spatial and temporal variations and uncertainties (Valentini et al., 2000; Schimel et al., 2000; Canadell et al., 2000). In recent times, these forest ecosystems have been exposed to increasing pressure from environmental changes such as global warming and human population growth. With an increasing need to understand the role of forests in the global carbon budget (e.g. Kyoto protocol) and to assess the impact of environmental changes, these ecosystems have to be quantitatively analysed in order to better understand the prevailing processes. The most important processes occurring in forests include carbon exchange processes (photosynthesis and respiration), evapotranspiration, and nutrient cycling (Waring & Running, 1998). Already at the local level, these processes are difficult to measure (Baldocchi et al. 1996). At regional to global scales, processes are no longer measurable at all (Tenhunen et al., 1998). Consequently, models have been developed which simulate the fluxes of matter and energy. These simulation models require as inputs or for validation purposes accurate estimates of forest structural and chemical properties. Collecting this information by traditional field sampling methods is impracticable to do over regional to global scales (Wessman, 1994; Schimel, 1995). Using remotely sensed information about the

structural and chemical state of the canopy, it is possible to apply ecosystem simulation models to landscapes and regions (Ustin et al., 1991; Wicks & Curran, 2003). Canopy attributes relevant to ecosystem simulation modeling that can be derived from remote sensing are land cover, leaf area index (LAI), and standing biomass (Curran, 1994a). More recently, leaf nitrogen concentration (LNC) has been identified as another major state variable potentially open to remote sensing (Lucas & Curran, 1999). The accurate mapping of the forest into distinct classes of forest types is essential to parameterise an ecosystem model with a suitable set of parameters corresponding to each class (Hall et al., 1995).

One example of process-level ecosystem simulation model is Forest-BGC (Running & Coughlan, 1988). Forest-BGC (Forest-biogeochemical cycles) simulates the cycling of carbon, water, and nitrogen through forest ecosystems. Its generalised clone Biome-BGC (Kimball et al., 1997) is applicable for a range of ecosystems. To run the model requires the input of driving variables, state variables, and parameters. Climatic variables, such as temperature and precipitation are used to drive the model. State variables, such as LAI or transpiration, are controlled by the driving variables. LAI is used within the model to control the absorption of photosynthetically active radiation (PAR), estimate the canopy conductance and regulate the interception of precipitation (Waring & Running, 1999). LNC or leaf chlorophyll concentration controls the photosynthetic capacity of the foliage and, together with absorbed PAR, determines the upper limit for gross photosynthesis. The annual turnover of leaves is also correlated with LAI, LNC, and specific leaf area (Waring & Running, 1999). Finally the model uses parameters, such as specific leaf area or stomatal conductance that are species-specific and assumed to remain constant over time (Running & Gower, 1991).

Forest inventories provide relevant information about the composition, structure and productivity of forest stands (Fournier et al., 2003). Forest inventory data typically exist as quantitative attributes collected from ground surveys or as forest cover maps interpreted directly from aerial photographs. Ground survey attributes include tree heights, stem densities, volumes, species, age classes, among others. Traditionally, forest inventories have been repeated every 10 years or longer while forest ecosystem processes respond on shorter time scales (minutes, days, and years). To monitor the effects of these processes, observation strategies providing appropriate temporal resolutions are required (Cihlar et al., 2003).

In Germany, forest inventories typically exist for forest owned by the state or municipalities, but not for privately owned forest. For instance, in the state of Rhineland-Palatinate about a quarter of the total forest is private (Bundesministerium für Verbraucherschutz, Ernährung und Landwirtschaft, 2004). As private forests may be of great economical and ecological importance, there is a considerable interest of the local and state forest authorities in such inventory data. Consequently, a remote sensing approach capable of mapping important forest attributes such as species type, age class, crown volume and biomass would be of great value.

1.4 Objectives and structure of thesis

The main objective of the research was to determine how forest attributes relevant to forest ecosystem simulation modeling and forest inventory purposes can be estimated from hyperspectral reflectance data. The study was restricted to forest plantations where stands are composed of trees of single species and age type to avoid problems related to mixed stands, stand heterogeneity and temporal dynamics. The investigated species, Norway spruce (*Picea abies* L. Kars.), is widespread throughout Europe and covers more than 50 percent of the Idarwald test site and is also the predominant tree species at Gerolstein test site.

The investigated attributes belong to three categories: Cover type, structural attributes and chemical attributes. The specific research objectives were:

- To investigate whether the forest cover type can be reliably derived from HyMap data using image classification. In this context data with broad to fine spectral resolution and large to small spatial resolution is compared (Chapter 5).
- To investigate the relationship between HyMap reflectance and structural canopy attributes with two different approaches (Chapter 6): 1) predictive models based on vegetation indices, 2) inversion of a forest reflectance model.
- To investigate the relationship between reflectance and chemical attributes using multivariate statistical analysis and to assess the reliability of scaling-up from leaf to canopy level (Chapter 7).

The outline of the study is as follows: Chapter 2 briefly describes the basic principles of optical remote sensing and the spectral properties of vegetation components followed by a review of the literature relevant to the remote sensing of forest attributes. Chapter 3 introduces the Idarwald and Gerolstein study sites and provides a description of the used material including field and laboratory measurements along with the acquisition and pre-processing of the image data. Chapter 4 outlines the methodologies used to derive the forest attributes from the reflectance data. Details are given on the employed image processing techniques, the empirical-statistical methods and the reflectance models. Chapters 5, 6, and 7 present and discuss the results obtained for cover type, structural attributes and chemical attributes. The different results are compared with respect to the applied methods and the characteristics of the input data. Chapter 8 provides conclusions derived from the research and closes with recommendations for future investigations. Summaries in English and German are given at the end of the work.

Chapter 2 Fundamentals

The aim of this chapter is to describe the fundamentals and review the literature relevant to the research. In the first section the basic principles of optical remote sensing are presented in brief. Atmospheric effects and their correction are discussed as it is required for a quantitative interpretation of airborne or satellite image data. Geometric effects are also considered. The next section describes the spectral properties of vegetation components with particular emphasis given to conifers at the needle, branch, and canopy level. In the last section the literature relevant to the remote sensing of forest attributes is reviewed.

2.1 Remote sensing

2.1.1 Physical principles

Remote sensing is defined as the extraction of information about an object without coming into physical contact with it (Schott, 1997). In the environmental sciences, remote sensing usually refers to the use of sensors to record images of the environment which can be interpreted to get useful information (Curran, 1985). This information is transferred from the object to the sensor through electromagnetic radiation. In the domain of passive optical remote sensing the Sun is the source of radiation. Radiation from the Sun reaches objects on the Earth's surface and is reflected. The amount of reflected radiation depends on the properties of those objects. The reflected energy passing through the atmosphere is modified by scattering and absorption processes before it is recorded by a sensor. To understand how reflectance can be measured in remote sensing, basic physical and radiometric principles have to be considered. These are extracted from the textbooks of Curran (1985), Kraus & Schneider (1988), Schott (1997), and Lillesand & Kiefer (2000).

Wave theory describes electromagnetic energy as waves of wavelength λ [μm] and frequency ν [s^{-1}] travelling at the speed of light c [ms^{-1}].

$$c = \lambda \nu \quad 2.1$$

where wavelength is the distance between one peak and the next, frequency is the number of cycles that pass a fixed point in 1 s, and the speed of light in vacuum has a constant value of $2.998 \cdot 10^8 \text{ ms}^{-1}$. It follows that waves with a short wavelength have a high frequency.

Quantum theory describes electromagnetic energy as being transferred in terms of energy packets or quanta. The energy Q [J] of a quantum is given as

$$Q = h\nu = \frac{hc}{\lambda} \quad 2.2$$

where, again, ν [s^{-1}] is the frequency and h [Js] is the Planck's constant with a value of $6.626 \cdot 10^{-34}$ Js. It can be concluded that waves with a short wavelengths have a high energy. To compare measurements of energy over different periods of time, the radiant flux Φ [W] defines the rate at which the energy is propagating as the first derivative of the radiant energy Q [J] with respect to time t [s]:

$$\Phi = \frac{dQ}{dt} \quad 2.3$$

The total energy flux radiated onto a unit area, e.g. of the Earth's surface, from all directions is expressed as the irradiance E [Wm^{-2}] and in the same way the total energy flux radiated away from a unit area in all directions is defined as the radiant exitance M [Wm^{-2}]:

$$E = \frac{d\Phi}{dA} \quad 2.4$$

$$M = \frac{d\Phi}{dA} \quad 2.5$$

Both irradiance and exitance do not provide any angular or directional information of the radiant flux. To quantify what is measured by a sensor, the radiant flux Φ [W] is related to the unit projected area $dA \cos\theta$ [m^2] and the unit solid angle $d\Omega$ [sr^{-1}]. The radiance L [$Wm^{-2}sr^{-1}$] is defined as

$$L = \frac{d^2\Phi}{dA \cos\theta \cdot d\Omega} \quad 2.6$$

As the flux is spectrally variable, each of the radiometric terms will vary with wavelength. Therefore, $L(\lambda)$ [$Wm^{-2}sr^{-1}\mu m^{-1}$] is the spectral radiance, $E(\lambda)$ [$Wm^{-2}\mu m^{-1}$] is the spectral irradiance, and $M(\lambda)$ [$Wm^{-2}\mu m^{-1}$] is the spectral exitance within a wavelength band.

To characterise an object in remote sensing, the spectral radiant exitance leaving the surface of the object $M_{\rho}(\lambda)$ has to be described as proportion of the incoming spectral irradiance $E(\lambda)$. This ratio, the spectral reflectance $\rho(\lambda)$, is the ability of the material to turn an incident flux back into the hemisphere above the material.

$$\rho(\lambda) = \frac{M_{\rho}(\lambda)}{E(\lambda)} \quad 2.7$$

A plot of the spectral reflectance of an object as a function of wavelength is called a spectral reflectance curve. From the spectral characteristics described by the spectral reflectance curve conclusions can be drawn towards various qualitative and quantitative object properties. The wavelengths of reflected electromagnetic radiation particularly valuable in environmental remote sensing are in the visible, near infrared and mid infrared wavebands.

Similarly to reflectance, transmittance τ is the ratio of the transmitted exitance M_τ at the back of a sample to the incoming irradiance, and absorbance α is the ratio of the absorbed flux per unit area incident on a surface M_α to the irradiance onto the surface. Since the conservation of energy requires all the incident flux to be either reflected, transmitted, or absorbed, we have

$$\rho(\lambda) + \tau(\lambda) + \alpha(\lambda) = 1 \quad 2.8$$

Reflectance specifies the proportion of the incident energy which is reflected, but not the direction of the reflected radiation. Reflection can be either of the specular or diffuse type, or a mixture of both. In specular reflection, produced by smooth mirrorlike surfaces, all of the incident radiation is reflected towards the direction opposite to the incident angle. In that case, no interaction of the radiation with the surface takes place and little information is delivered to the sensor. The radiance reflected from diffuse reflectors, also called Lambertian surfaces, is the same in all directions. Most of the natural surfaces appear rough at visible and near infrared wavelengths and have a reflectance behaviour somewhat between the two extremes. Consequently, the reflected radiation reaching a sensor depends on the illumination and viewing geometry (section 2.2.4). However, Lambertian assumptions are often used as an approximation of reality. In that case, the relationship between the exitance M from a surface and the radiance L from that surface can be simplified, so that L becomes independent of the observation angle θ .

$$M = \int dM = \int L \cos \theta d\Omega = \pi L \quad 2.9$$

Substitution of equation 2.9 into Equation 2.7 gives the spectral reflectance of Lambertian surfaces:

$$\rho(\lambda) = \frac{L(\lambda)}{E(\lambda)} \pi \quad 2.10$$

There are basically two types of reflectance measurements, hemispherical and directional. In bi-hemispherical measurements the incident radiation is arriving from all directions and the reflected radiation is collected over all directions (laboratory measurement using an integrating sphere). In bi-directional measurements the angles of incidence and collection refer to one direction only (field or satellite measurement). As reflectance varies for non-Lambertian surfaces with illumination and viewing angle, a complete description of an object's reflectance properties requires measuring the bi-directional reflectance at all possible

combinations of angles. This is achieved by the bi-directional reflectance distribution function (BRDF). To approximate a measurement of bi-directional reflectance in the laboratory or field, the ratio between the spectral radiance $L(\lambda)$ at a certain angle to the object of interest and a diffuse reflector (with known reflectance properties) at the same angle is used instead.

Remote sensors, such as imaging spectrometers, record radiance values spatially registered and in a digital form. To extract spectral reflectance from remotely sensed images, corrections for the effects of the atmosphere and the image geometry have to be made.

2.1.2 Atmospheric effects

When radiation is passing through the atmosphere, it is partly absorbed or scattered. The element of fractional flux attenuated by extinction (absorption and scattering) at a certain location can be expressed as (Schott, 1997):

$$\frac{d\Phi}{\Phi} = -\beta_{ext}(z, \lambda) dz \quad 2.11$$

where $\beta_{ext}(z, \lambda)$ [m^{-1}] is the spectral extinction coefficient and dz [m] is an element of path length. For propagation along a finite path starting at distance zero where we have initial flux Φ_0 to distance z where we have flux Φ_z , we have

$$\int_{\Phi_0}^{\Phi_z} \frac{d\Phi}{\Phi} = \int_0^z -\beta_{ext}(z, \lambda) dz \quad 2.12$$

This can be solved for the simplified case of a homogenous medium to

$$\tau = \frac{\Phi_z}{\Phi_0} = e^{-\beta_{ext}(\lambda)z} \quad 2.13$$

which is known as Lambert-Beer law. The term Φ_z/Φ_0 is a definition of transmittance τ . The product of the spectral extinction coefficient and path length $\beta_{ext}(\lambda) z$ is generally referred to as the spectral optical depth or thickness $\delta(\lambda)$ of a gas layer (Schott, 1997). It stands for the total extinction of a light beam passing through an air mass of thickness z . Spectral extinction coefficient and spectral optical depth both depend on the density and size distribution of molecules and aerosols in the atmosphere. The spectral extinction coefficient $\beta_{ext}(\lambda)$ is the sum of the absorption coefficient $\beta_\alpha(\lambda)$ and the scattering coefficients for Rayleigh scattering $\beta_r(\lambda)$, Mie scattering $\beta_a(\lambda)$ and non-selective scattering $\beta_{ns}(\lambda)$:

$$\beta_{ext}(\lambda) = \beta_\alpha(\lambda) + \beta_r(\lambda) + \beta_a(\lambda) + \beta_{ns}(\lambda) \quad 2.14$$

Atmospheric absorption results in the loss of energy to atmospheric constituents. The most efficient absorbers of solar radiation are water vapour (H_2O), carbon dioxide (CO_2), and ozone (O_3). As these gases absorb radiation in specific wavelength bands, optical remote

sensing is limited to wavelength ranges in which the atmosphere is transmissive, the so called atmospheric windows. Atmospheric scattering merely alters the direction of the radiation. Three types of scattering mechanisms can be distinguished: Rayleigh scatter occurs when radiation interacts with atmospheric molecules (N_2 , O_2 , Ar) that are much smaller in diameter than the wavelength of the interacting radiation. The Rayleigh scattering coefficient β_r is inversely proportional to the fourth power of wavelength λ (Kraus & Schneider, 1988):

$$\beta_r(\theta, \lambda) = k \left(\frac{1}{\lambda^4} (1 + \cos^2 \theta) \right) \quad 2.15$$

where k is a constant factor and θ is the scattering angle (deflection angle from beam direction). As short blue wavelength of about 400 nm are much stronger scattered than longer red wavelengths, the sky, which would appear black in the absence of scattering, appears blue. Mie scatter takes place when the atmospheric particle diameters are approximately equal to the wavelength of the radiation. This scattering effect, caused by aerosols such as water vapour and dust, depends on wavelength according to (Kraus & Schneider, 1988):

$$\beta_a(\theta, \lambda) = k\lambda^{-b} \quad 2.16$$

where k is a constant factor and b varies between 0 and 4. As this function decreases slower

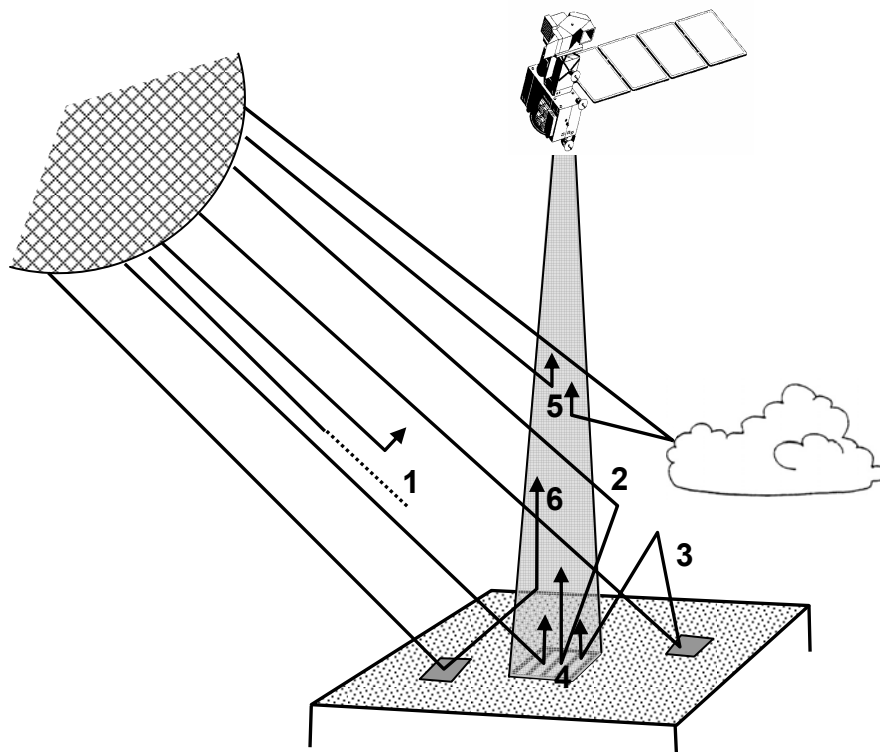


Figure 2.1: Interactions of incoming solar radiation with the atmosphere and the contamination of the satellite-measured radiance (from Tanré et al., 1985; modified after Hill, 1993). Refer to text for further explanations.

with increasing wavelength than the Rayleigh scatter function, Mie scatter tends to influence longer wavelengths. Non-selective scatter occurs when the atmospheric particles are much larger than the radiation wavelengths. It is caused by water droplets in clouds and fog which scatter all visible and near to mid infrared wavelengths about equally ($\beta_{ns}(\theta, \lambda) = \text{constant}$), resulting in a white appearance of clouds.

As the incoming solar irradiance interacts with the atmosphere due to the mentioned absorption and scattering processes, the signal measured at the satellite is contaminated. In order to correct a remotely sensed image, several atmospheric effects have to be considered. There are basically three relevant irradiance and three radiance terms (Figure 2.1): The direct irradiance term (1) is the part of the solar irradiance not affected by absorption or scattering arriving at the Earth's surface. The scattered solar irradiance, the skylight (2), additionally illuminates the target. To a smaller extent, a fraction of already ground-reflected radiation that is again reflected from the atmosphere, arrive at the surface and is named environmental illumination (3). Together, these terms comprise the total irradiance onto the target. The satellite measured radiance L^* is mainly composed of the radiance reflected by the target L_{tar} (4) which is the part of the signal carrying the target information (target radiance). Additionally, a part of the incoming solar irradiance is backscattered towards the sensor without being in contact with the target before (atmospheric radiance, L_{atm}) (5). Finally, reflected irradiance from the environment surrounding the target L_{env} (background radiance) (6) is also directed into the sensor's field of view (Tanré et al., 1985). Setting the at-satellite radiance to $L^* = L_{tar} + L_{atm} + L_{env}$ and the irradiance onto the target to $E = E_0 \cos\theta$, the at-satellite reflectance ρ^* is derived from equation 2.10 (ignoring atmospheric effects) as:

$$\rho^*(\lambda) = \frac{\pi \cdot d_s^2 \cdot (L_{tar}(\lambda) + L_{atm}(\lambda) + L_{env}(\lambda))}{E_0(\lambda) \cos\theta} \quad 2.17$$

where E_0 is the extraterrestrial irradiance, θ is the solar zenith angle and d_s is the earth-sun distance in astronomical units. Various researches have attempted to model the effects of the atmosphere on radiation with the aim of removing those effects from the signal. They developed so called radiative transfer models. For instance, Tanré et al. (1990) developed a model called the 5S code (Simulation of Satellite Signal in the Solar Spectrum). The 5S code computes the solar radiation reflected by the Earth-atmosphere system at satellite altitude in various illumination and observation conditions. The following simplifying assumptions are made (Hill, 1993): The atmosphere is considered to be horizontally homogenous and variations occur only in the vertical direction. The Earth's surface is assumed to have Lambertian reflectance properties; bi-directional effects are neglected. In analogy to the abovementioned terms of radiance (L_{tar} , L_{env} , L_{atm}), the corresponding reflectance terms are used for convenience. The at-satellite reflectance ρ^* is expressed as a function of the target's bi-directional reflectance ρ_{tar} , the mean reflectance of the surrounding area ρ_{env} , and the

atmospheric reflectance ρ_{atm} (Tanré et al., 1990) (the wavelength dependence has been omitted for the sake of clarity.):

$$\rho^* = \left(\frac{\tau_{dir,dif\downarrow} (\rho_{tar} \tau_{dir\uparrow} + \rho_{env} \tau_{dif\uparrow})}{1 - \rho_{env} \rho_{sph}} + \rho_{atm} \right) \tau_{a\uparrow\downarrow} \quad 2.18$$

where $\tau_{a\uparrow\downarrow}$ is the transmittance due to absorption of radiation for the double path from the Sun to the Earth's surface (downward) and from the Earth's surface to the sensor (upward), $\tau_{dir\uparrow}$ is the upward direct transmittance due to scattering, $\tau_{dif\uparrow}$ is the upward diffuse transmittance due to scattering (both depend on the observation zenith angle), and $\tau_{dir,dif\downarrow}$ is the downward direct and diffuse transmittance due to scattering (depends on the sun zenith angle). The factor ρ_{sph} denotes the spherical albedo of the atmosphere; the term $(1 - \rho_{env} \rho_{sph})^{-1}$ increases ρ^* due to radiance reflected by the surrounding area which is then again reflected by the atmosphere towards the target at the Earth's surface, the so called adjacency effect (Kaufman, 1989).

Target reflectance ρ_{tar} is derived from the measured at-satellite reflectance ρ^* by solving equation 2.18 for ρ_{tar} . The transmittance terms $\tau_{dir,dif\downarrow}$, $\tau_{dir\uparrow}$, $\tau_{dif\uparrow}$, and the reflectance terms ρ_{atm} and ρ_{sph} can be calculated from the optical thickness $\delta(\lambda)$ (equation 2.13). While the Rayleigh optical thickness δ_r is spatially and temporally invariant (at constant air pressure), the aerosol optical thickness δ_a strongly varies in space and time and thus, is the main unknown variable in the atmospheric effects on remotely sensed imagery. Its value can be either derived from sun photometer measurements, inversion of the radiative transfer equation or from the image data itself (scene-based). One scene-based approach (Ahern et al., 1977) makes use of the principle that clear water is almost completely black in the near-infrared region of the spectrum. The at-satellite radiance measured in the near-infrared is assumed to be solely caused by scattering effects and consequently, can be used to estimate the aerosol optical thickness at this wavelength. This can be achieved in an iterative process using equation 2.18; the appropriate value of $\delta_a(\lambda)$ is found when the apparent reflectance of the water surface computed by the model equals the measured image reflectance. The approach has been successfully applied on multispectral satellite data (Hill, 1993).

2.1.3 Topographic effects

Measured reflectance of ground objects is, apart of the object's reflectance properties, also influenced by the slope and the aspect of the image terrain. Slopes facing away from the sun appear relatively dark, and sun facing slopes with the same type of cover appear relatively bright. If the surface behaves as a Lambertian reflector, this topographic effect can be corrected using a cosine function which calculates the cosine of the solar zenith angle relative to the local terrain. However, the approach tends to produce overcorrected images especially when the angle between the Sun and the Earth's surface is larger than 55° (Hill et al., 1995).

This can be attributed to the fact that most surfaces are of a non-Lambertian type and that the cosine correction can be applied only to the direct part of the solar irradiance. Therefore, correction of the topographic effect should be directly integrated into atmospheric correction models as they can provide realistic estimates of the direct and diffuse radiation (Hill et al., 1995).

2.1.4 Geometric effects

Raw digital image data usually contain geometric distortions that stem from the image acquisition process. The sources of these distortions are related to variations in the altitude, attitude, and velocity of the sensor platform or are due to factors such as panoramic distortion, earth curvature, atmospheric refraction, relief displacement, or non-linearities in the sweep of the sensor instantaneous field of view (Lillesand & Kiefer, 2000). The aim of geometric correction or image rectification is to make the image conform to a map projection system that represents the surface of the Earth on a plane. Such a procedure is essential to ensure that the position of samples collected in the field can be identified correctly in the image.

Imaging spectrometry data measured by airborne scanning systems particularly suffer from geometric distortions due to variations of the flight path and also of the attitude (roll, pitch, and heading) of the aircraft. These systematic, non-linear distortions can not be compensated for by a traditional polynomial image transformation. Instead, their correction has to be performed on a pixel wise calculation. The parametric geocoding software PARGE (Schläpfer et al., 1998) exactly reconstructs the scanning geometry for each image pixel based on position, attitude, and terrain elevation data and then puts each image pixel to its correct position. The position and attitude of the aircraft has to be recorded during the overflight. A digital elevation model (DEM) of high quality is required. Apart from its geocoding capability, PARGE can also integrate the DEM data into the geometry of the scanner to perform a correction of the terrain induced illumination effects (section 2.1.3).

2.2 Spectral reflectance properties of forests

A successful use of quantitative remote sensing in forestry requires an understanding of the spectral properties of the involved vegetation components. The interaction of electromagnetic radiation with the components of a forest canopy has to be considered on the molecular, cellular, leaf, branch, and canopy level. This summary is based primarily on reviews by Goel (1988), Guyot (1990), Baret (1991), Howard (1991), and Atzberger (1998).

2.2.1 The molecular level

Absorption bands in the spectra of materials are generally caused by electronic and vibrational processes. Isolated atoms and ions have discrete energy states. Electronic processes occur when photons of a specific wavelength are absorbed to shift electrons from a lower to a higher energy state. (Clark, 1999). In plant tissue, *electronic transitions* occur around the magnesium atom of *chlorophyll* resulting in strong absorption bands in the visible part of the spectrum. Chlorophylls are magnesium-containing porphyrins (organic pigments characterized by the possession of a cyclic group of four linked nitrogen-containing rings), chemically related to haemoglobin (Oxford Reference Online, 2004). Chlorophyll a (and similarly, chlorophyll b) has strong absorption bands in the visible domain at 430 nm and 660 nm.

When atoms form molecules, additional energy states are available through *vibrational processes* along the molecular bonds. The frequency of vibration depends on the strength of the bonds and the masses of the atoms bound together. For a molecule with N atoms, there are $3*N-6$ normal modes of vibrations called fundamentals. The energy transitions of fundamentals occur between the ground state and the first level excited vibrational state. Additional vibrations can also take place at approximately multiples of the original fundamental frequency. They are called *overtones* or harmonics when they involve multiples of a single fundamental mode, and *combinations* when different fundamental modes are involved (Clark, 1999).

The energy transitions of overtones are between the ground state and the second or third level excited vibrational state. Because transitions to higher energy states are successively less likely to occur, each overtone is successively weaker in intensity (Weyer, 1985). As the transition to second or third level energy states requires roughly twice or three time more

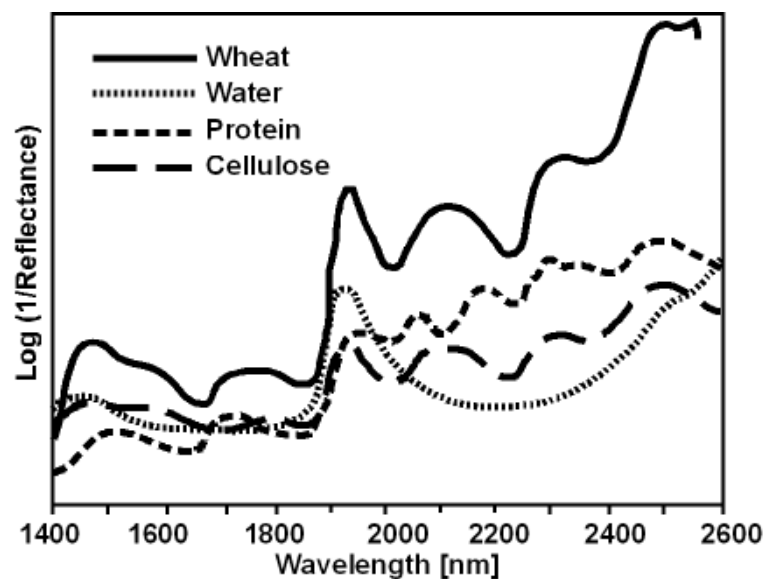


Figure 2.2: Absorption features of organic materials and water (from Weyer, 1985).

energy than it is needed to reach a first level state, the absorption bands occur at twice and three times of the frequency (one-half and one-third of the wavelength) of the fundamental (Weyer, 1985). The most prominent overtone bands observed in the near-IR and mid-IR domains are related to O-H, C-H, and N-H groups (stretch, bend, deformation). Combination bands usually involve stretch combined with one or more bending modes. As many different combinations are possible the near-IR to mid-IR region is very complex (Weyer, 1985).

Absorption bands caused by molecular vibrations are much weaker than those related to electronic processes. In plant tissue, water and organic materials (cellulose, lignin, protein, sugar, starch, tannin, and waxes) show absorption features related to vibrational processes (Figure 2.2). *Cellulose* is a polysaccharide (straight-chain D-glucose polymer) found in the cell walls of plants and forms 30 to 50 percent of the dry weight of most plants. It has near-IR/mid-IR absorptions at 1220, 1480, 1780, 1930, 2100, 2280, 2340, and 2480 nm (Elvidge, 1990). *Lignin* is a complex polymer of phenylpropanoid units and forms 10 to 35 percent of the dry weight in plant materials. It has near-IR/mid-IR absorptions at 1450, 1680, 1930 nm, and around 2100, 2300, and 2500 nm (Elvidge, 1990). *Starch*, a polysaccharide (D-glucose), is the principal food storage molecule in plants and not a major component of most leaf material. It has near-IR/mid-IR absorptions similar to those of cellulose plus absorptions at 990, 1560, and 1700 (Elvidge, 1990). *Proteins* contain many amino acids linked together by peptide bonds. The amide group ($-\text{CONH}_2$), formed by the reaction between adjacent carboxyl ($-\text{COOH}$) and amino ($-\text{NH}_2$) groups, contains C-N, C=O, and N-H bonds that all contribute to the characteristic absorptions related to the peptide linkage (Kokaly, 2001). The protein D-ribulose 1-5-diphosphate carboxylase is the most abundant nitrogen bearing compound in green leaves (30 to 50 percent of leaf nitrogen) and plays the central role in the carbon fixation in photosynthesis. It has minor absorptions in the mid-IR at 1500, 1680, 1740, 1940, 2050, 2170, 2290, and 2470 nm (Elvidge, 1990). Only leaf water has major absorption bands in the mid-IR and largely influences the overall reflectance in that spectral region. Leaf water can obscure absorption features related to protein (and other leaf chemicals) in green leaf materials with considerable consequences for its estimation from reflectance spectra. As protein is difficult to measure directly it is usually derived from total organic *nitrogen* by multiplying with a factor of 6.25 as plant protein roughly contain 16 percent nitrogen (Allen, 1991, cited from Kupiec, 1994). Absorption features related to nitrogen are summarised in Table 2.1.

Table 2.1: Absorption features in vegetation reflectance spectra related to leaf nitrogen concentration (Adapted from Curran, 1989 and Lucas & Curran, 1999)

Wavelength [nm]	Cause of absorption	Chemicals
430	Electron transition	Chlorophyll a
460	Electron transition	Chlorophyll b
640	Electron transition	Chlorophyll b
660	Electron transition	Chlorophyll a
910	C-H stretch, 3 rd overtone	Protein
1020	N-H stretch	Protein
1510	N-H stretch, 1 st overtone	Protein, Nitrogen
1690	C-H stretch, 1 st overtone	Lignin, Starch, Protein, Nitrogen
1940	O-H stretch, O-H deformation	Water, Lignin, Protein, Nitrogen, Starch, Cellulose
1980	N-H asymmetry	Protein
2060	N-H bend, 2 nd overtone / N-H bend / N-H stretch	Protein, Nitrogen
2130	N-H stretch	Protein
2180	N-H bend, 2 nd overtone / C-H stretch / C-O stretch / C-O stretch / C-N stretch	Protein, Nitrogen
2240	C-H stretch	Protein
2300	N-H stretch / C-H stretch / C-H bend, 2 nd overtone	Protein, Nitrogen
2350	CH ₂ bend, 2 nd overtone / C-H deformation, 2 nd overtone	Cellulose, Protein, Nitrogen

2.2.2 The leaf level

Leaves represent the main surfaces of plant canopies where energy and gas are exchanged. Hence, their optical properties are essential to understand the transport of photons within vegetation (Despan & Jacquemoud, 2004). The general shape of reflectance and transmittance curves for green leaves is similar for all species (Figure 2.3). It is controlled by absorption features of specific molecules (section 2.2.1) and the cellular structure of the leaf tissue (Ustin et al, 1999).

The internal tissue of a leaf blade (lamina) is called mesophyll and consists of parenchyma cells. There are two distinct forms. *Palisade mesophyll* lies just beneath the upper epidermis

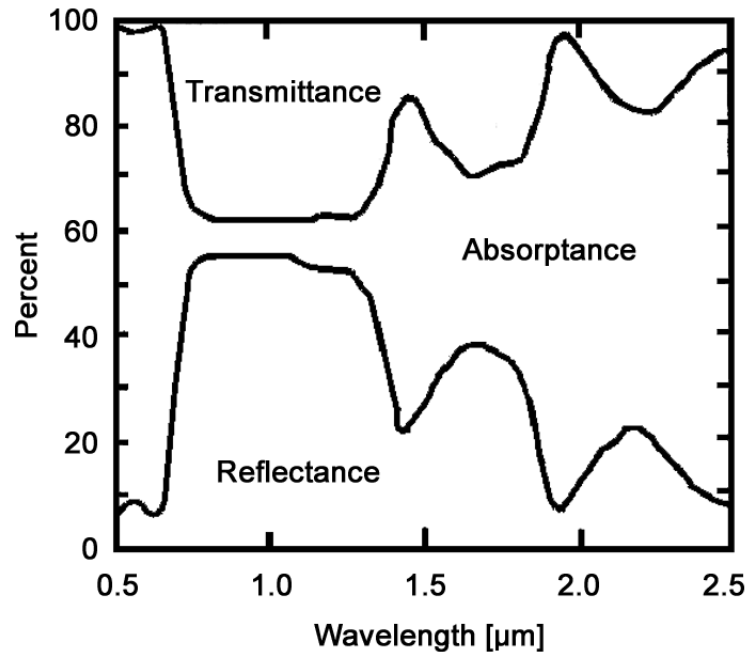


Figure 2.3: Typical spectra of leaf reflectance, transmittance and absorptance (from Atzberger, 1998).

and consists of cells elongated at right angles to the leaf surface. They contain a large number of chloroplasts and their principal function is photosynthesis. *Spongy mesophyll* occupies most of the remainder of the lamina. It consists of spherical loosely arranged cells containing fewer chloroplasts than the palisade mesophyll. Between these cells are air spaces leading to the stomata (Oxford Reference Online, 2005). Due to the random orientation of cells and the large number of air-cell interfaces, the diffusion of light mainly takes place in the spongy mesophyll (Guyot, 1990; Figure 2.4).

Three spectral domains can be distinguished: In the *visible domain* (400-700 nm) absorption by leaf pigments is the most important process leading to low reflectance and transmittance values. The main light absorbing pigments are chlorophyll a and b, carotenoids, xanthophylls, and polyphenols. Chlorophyll a is the major pigment of higher plants and together with chlorophyll b account for 65 percent of the total pigments. Chlorophyll a and b have absorption bands in the blue at around 430/450 nm and in the red domain at around 660/640 nm (Figure 2.5). These strong absorption bands induce a reflectance peak in the green domain at about 550 nm. Carotenoids and xanthophylls absorb mainly in the blue and are responsible for the colour of flowers, fruits, and the yellow colour of leaves in autumn. Polyphenols (brown pigments) absorb with decreasing intensity from the blue to the red and appear when the leaf is dead (Verdebout et al, 1994).

In the *near-infrared domain* (near-IR: 700-1300 nm) leaf pigments and cellulose are almost transparent, so that absorption is very low and reflectance and transmittance reach their maximum values. The level of reflectance on the near-IR plateau increases with increasing

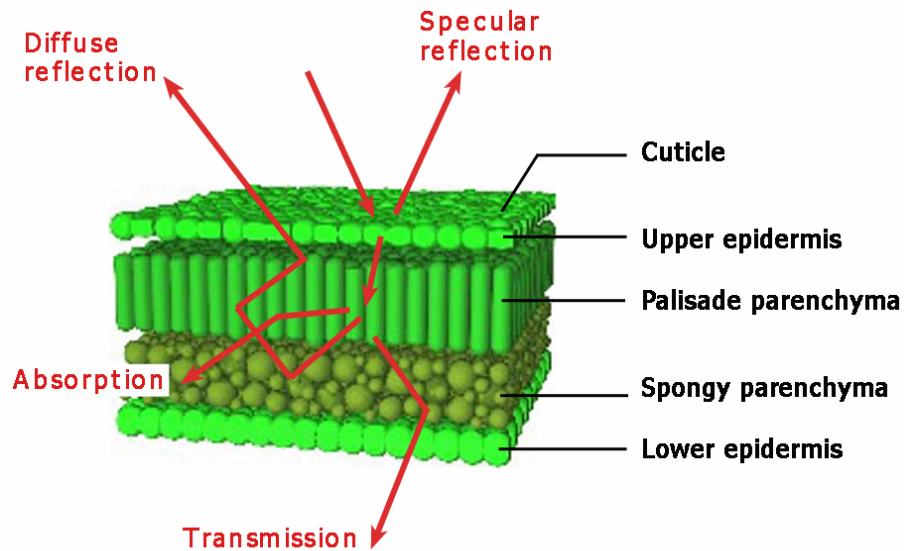


Figure 2.4: Internal structure of a dicotyledonous leaf (from Govaerts et al., 1996) and interaction of leaf tissues with incoming radiation (after Guyot, 1990).

number of intercell spaces, cell layers, and cell size. Scattering occurs mainly due to multiple refractions and reflections at the boundary between hydrated cellular walls and air spaces (Guyot, 1990).

The *red edge* is located between the absorption minimum in the red domain and the reflectance plateau in the near-IR region. This abrupt increase in reflectance, defined by the point of maximum slope, is generally referred to as the red edge (Horler et al., 1983). The wavelength position of the red edge, named *red edge inflection point* (REIP), occurs between 680 and 740 nm. The REIP depends on the amount of chlorophyll seen by the sensor (Dawson & Curran, 1998). The chlorophyll amount present in a vegetation canopy is characterised by the chlorophyll concentration of the leaves and the leaf area index (LAI). On a leaf level, solely the chlorophyll concentration determines the amount of chlorophyll. An increase in chlorophyll amount increases the chlorophyll absorption and broadens the associated chlorophyll-a absorption feature located at about 680 nm (Salisbury et al., 1987). As a consequence, the point of maximum slope (REIP) is moved towards longer wavelengths and a so-called red-shift of the inflection point is observed. Consequently, a decrease in chlorophyll amount will lead to a decrease of the chlorophyll absorption and will shift the REIP towards shorter wavelengths (blue shift).

In the *mid-infrared domain* (mid-IR: 1300-2500 nm), also called shortwave-infrared (SWIR), leaf optical properties are mainly affected by water and other foliar constituents. The major water absorption bands occur at 1450, 1940, and 2700 nm and secondary features at 960, 1120, 1540, 1670, and 2200 nm (Ustin et al, 1999). Water largely influences the overall reflectance in the mid-IR domain but also has an indirect effect on the visible and near-IR reflectances. Protein, cellulose, lignin, and starch also influence leaf reflectance in the mid-IR.

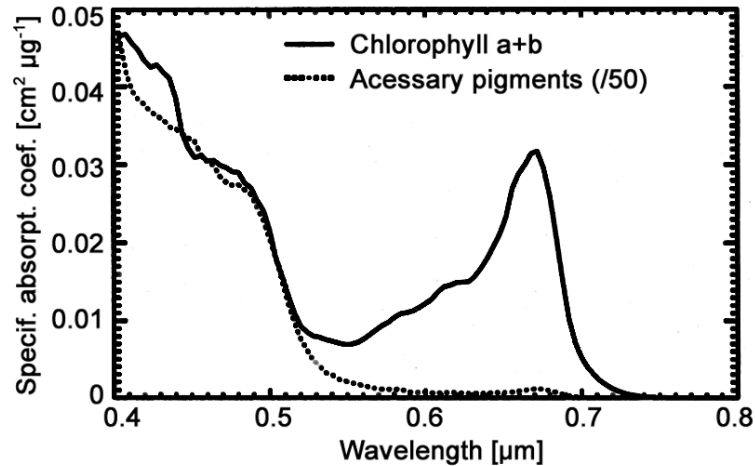


Figure 2.5: Spectrum of specific absorption coefficients of *in vivo* chlorophyll a+b and *in vivo* carotenoids (from Jacquemoud & Baret, 1990).

However, the absorption peaks of those organic substances are rather weak as they result from overtones or combinations related to fundamental molecular absorptions in the region 5 to 8 μm (Curran, 1989; section 2.2.1). The molecular absorptions are associated with certain chemical bonds, such as C-H, N-H, C-O, and O-H. In fresh leaves, spectral features related to organic substances are masked by the leaf water, so that estimation of leaf constituents is difficult (Verdebout et al, 1994).

Indirect factors, such as plant type, leaf age, and leaf health also determine the leaf optical properties as they can affect the leaf structure and the concentrations of absorbers. The leaf structure varies for different plant types (genera and species). Gymnosperms are mainly characterised by needle-shaped leaves. Angiosperms can be divided into the monocotyledons and the dicotyledons. Leaves from dicotyledon species reflect and transmit greater amounts of radiation than leaves of monocotyledon species of the same thickness (Guyot, 1990). Within a certain species, differences in structure occur between sun leaves and shade leaves (Howard, 1991). Leaf age strongly affects the optical properties of conifer needles as the chlorophyll content increases from year to year. Leaves of deciduous trees or annual plants, apart from the juvenile stage and senescence, have practically constant optical properties throughout the major part of their life (Guyot, 1990). Leaf health may be affected by mineral deficiencies, drought, pests and diseases. Drought can reduce the leaf water content; however, in natural conditions, it is necessary to have an extremely severe water stress to affect the leaf optical properties. Nitrogen deficiency reduces the chlorophyll content, the number of cell layers and thus, changes the whole reflectance spectrum (Guyot, 1990). Chlorosis, caused by conditions that prevent the formation of chlorophyll (e.g. lack of light or a deficiency of iron or magnesium) mainly affects leaf reflectance in the visible domain (Oxford Reference Online, 2005a). Plants affected by chlorosis are typically pale green or even yellow.

Leaf reflectance also exhibits directional characteristics. For incidence angles normal to the leaf surface the reflectance is diffuse. For large incidence angles, reflectance is formed by a diffuse and a specular component; the latter is reflected by the cuticle and increases with increasing incidence angles. The specular component is practically the same in the visible and near-IR, whereas the diffuse component is low in the visible and high in the near-IR. This implies, that the relative portion of specular reflected radiation at the total reflected radiation is much lower in the near-IR than in the visible. Consequently, in the near-IR leaves can be considered Lambertian reflectors but in the visible they show strong directional effects (Guyot, 1990). Specularly reflected radiation will not contain any information on the internal biochemical composition of the leaf since no interaction has been occurred.

2.2.3 Soil optical properties

Apart from the leaf optical properties, soil optical properties also affect the reflectance of a forest canopy. In general, the reflectance of a bare soil increases progressively from the visible to the mid-IR and then decreases in the mid-IR with deep valleys at the water absorption bands. The main factors affecting soil reflectance are moisture content, soil texture, surface roughness, iron content, and organic matter content (Guyot, 1990).

With increasing soil moisture content the reflectance decreases for the whole spectrum due to the trapping effect. When particle size increases the soil reflectance increases for all the wavelengths, but the effect is weaker than that of moisture. Both soil moisture and soil texture are strongly related to each other: coarse, sandy soils are usually well drained, resulting in low moisture content and relatively high reflectances; fine, poorly drained clays typically have lower reflectances (Lillesand & Kiefer, 2000).

As a bare soil is not a Lambertian reflector, reflectance depends on the illumination and viewing geometry: reflectance values observed in the direction of the sun are enhanced (hot spot effect) whereas it is reduced in the direction opposite to the sun, because of the shadows

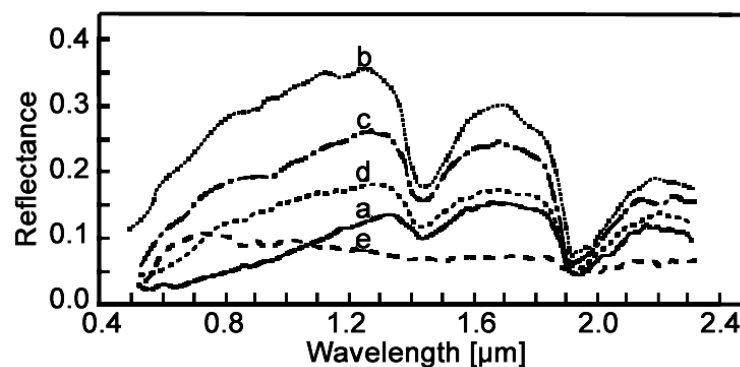


Figure 2.6: Classification of soil spectral curves into five general types (from Baumgardner et al., 1985).

recorded. With increasing soil roughness reflectance decreases in the whole spectrum due to an enlarged occurrence of shadows (Baret, 1991).

Based on their spectral curve forms soils can be divided into 5 main types (Figure 2.6): organic dominated (a), minimally altered (b), iron affected (c), organic affected (d), iron dominated (e) (Baumgardner et al., 1985). Although dense forest canopies may mask the effect of the soil spectral curve on canopy reflectance spectra, factors such as fertility, drainage, and moisture-holding-capacity tend to influence the vegetation growth on a soil (Baumgardner et al., 1985) and thus, forest canopy reflectance.

2.2.4 The canopy level

The optical properties of a forest canopy depend mainly on the optical properties of the canopy constituents and on the canopy structure. The most important canopy elements are the leaves and the underlying soil. Optical properties of other parts of the plants, such as bark, flowers, fruit, etc. will not be considered in the following elaborations. When a plant canopy grows, the contribution of the soil to the observed total signal progressively decreases as the reflectance spectrum of the bare soil is gradually replaced by that of the plant. As a consequence, during growth the visible and middle-infrared (mid-IR) reflectances decrease and the near-infrared (near-IR) reflectances increase (Figure 2.7); the reverse phenomenon is observed during senescence or selective cutting of trees (Guyot, 1990). This behaviour is mainly due to the contrast between leaf and soil optical properties. In the red domain, soil

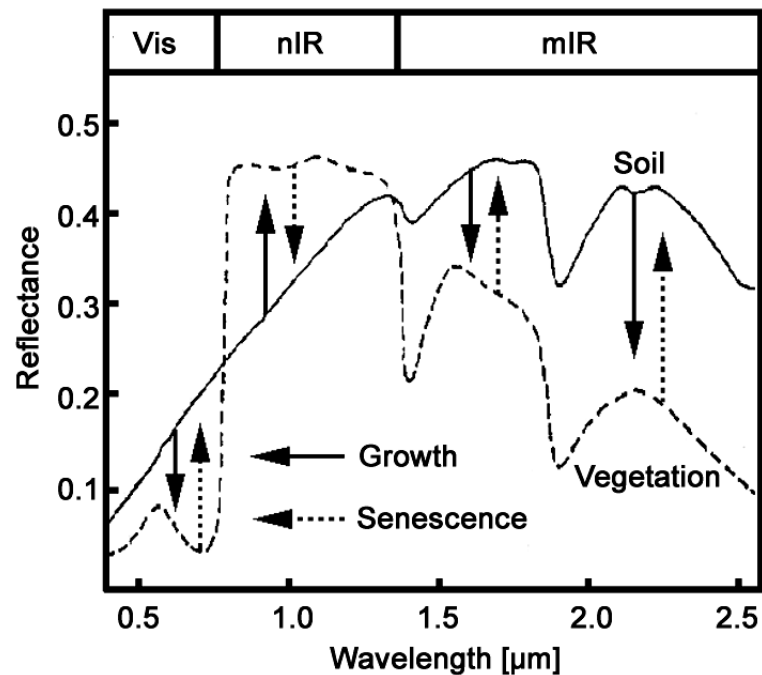


Figure 2.7: Schematic representation of the changes in canopy reflectance during growth and senescence (after Guyot, 1990). See text for details.

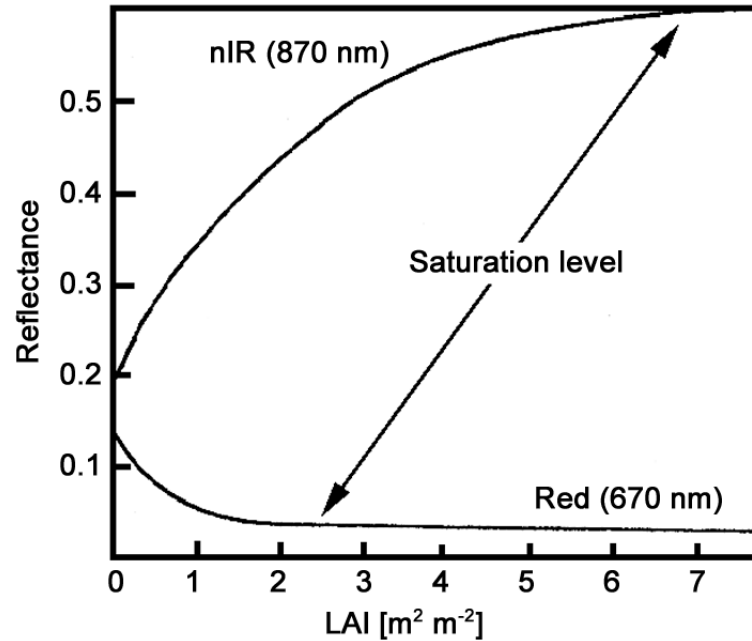


Figure 2.8: Schematic variation of canopy reflectance as a function of leaf area index for the red and near-IR domain (after Guyot, 1990; from Atzberger, 1998).

reflectance is generally higher than leaf reflectance whereas the reverse case is true in the near-IR domain (Baret, 1991). Under a dense forest canopy, the soil will be completely covered by tree crowns, understorey vegetation, and litter and is unlikely to contribute to the recorded signal. With a sparse tree canopy, the soil can be expected to contribute significantly (Howard, 1991).

The canopy structure is primarily defined by the *leaf area index (LAI)* and the *leaf angle distribution (LAD)*. The LAI is defined as the total one-sided leaf area per unit ground area and represents the leaf amount of a canopy. When the amount of vegetation increases during growth, the canopy reflectance can reach saturation levels (Figure 2.8). In the case of annual crops, plots of reflectance as a function of the LAI show that in the visible the saturation level is reached for LAI of about 2 to 3, and in the near-IR for LAI around 5 to 6. These differences are mainly an effect of leaf transmittance, which is low in the visible and mid-IR while it is high in the near-IR (Guyot, 1990). In the near-IR, a number of leaf layers are required to obtain full extinction of the incident radiation while in the red domain almost no radiation penetrates through a single leaf layer (Baret, 1991). The value of LAI where saturation occurs also depends on the LAD: Plants with erect leaves need higher LAI values to saturate than plants having horizontal leaves (Guyot, 1990). For conifers, different observations were made. Peterson et al. (1987) found that the saturation level was reached at an LAI of approximately 8 in the red domain. Other results suggest a saturation of the NDVI at an LAI of about 5 (Chen & Cihlar, 1996) or no saturation effect at all in the case of the RVI (Chen et al., 2002). A possible explanation for these findings is that conifer stands with high LAI generally have

large tree crowns and large crown shadow fractions and thus appear dark in the red domain but bright in the near-IR domain due to strong multiple scattering, causing large RVI values (Chen et al., 2002).

LAD, the main factor characterizing the geometry of a plant canopy, is described by the leaf inclination and azimuth angles. The leaf inclination is the angle between the leaf normal (the perpendicular to the leaf surface) and the vertical axis. It generally changes from 0° for



Figure 2.9: Oblique (left) and nadir (right) view of black spruce (*Picea mariana*) demonstrating the gap effect. See text for details. From Sandmeier (2004). Photos by D. W. Deering.

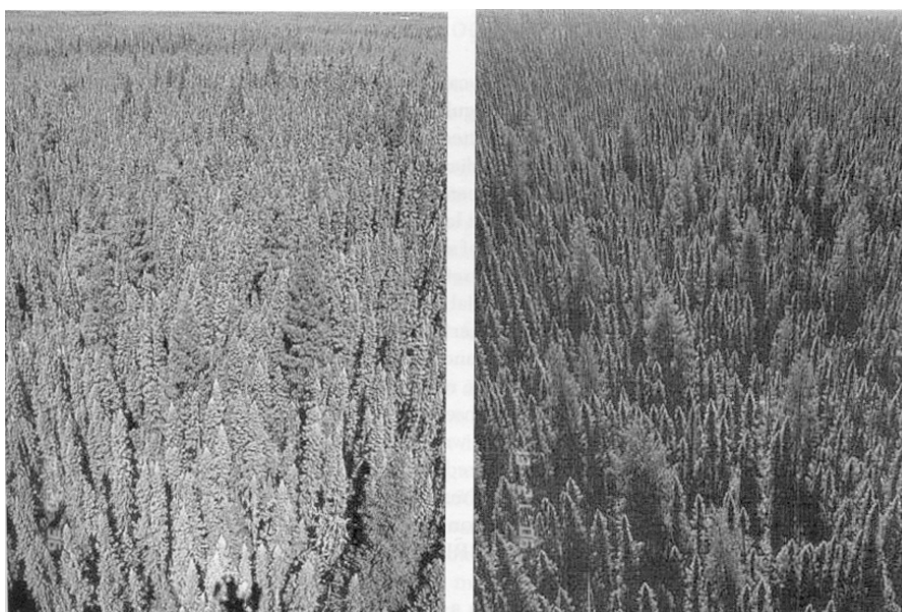


Figure 2.10: Black spruce (*Picea mariana*) observed in backward scattering (left) and forward scattering (right) direction. See text for details. From Sandmeier (2004). Photos by D. W. Deering.

horizontal leaves (planophile) to 90° for vertical leaves (erectophile). The leaf azimuth angle is the orientation of the leaf towards a horizontal reference axis (e.g. north direction) and varies between 0° and 360° . The LAD changes the probability of gap through the entire canopy, which determines if the incident and outgoing radiation will be intercepted by the vegetation. LAD also determines the magnitude of the hot spot effect, which is the peak in the reflectance when the sun is directly behind the sensor. Another effect of canopy geometry occurs when leaves are clumped together rather than uniformly distributed. The clumping increases the probability of a gap which increases the influence of the vegetation in lower layers and of the soil. The reflectance of a forest canopy will also be influenced by the shape and size of the tree crowns (Goel, 1988).

As vegetation canopies are not perfect Lambertian reflectors the bi-directional reflectance of a canopy is affected by the illumination-viewing geometry. The illumination zenith angle is defined as the angle between the surface normal and the sun direction. It controls the amount of shadow present in a scene. The view zenith angle is defined as the angle between the surface normal and the sensor direction. It controls the relative portions of green vegetation and background seen by the sensor.

Bi-directional reflectance effects in vegetation canopies are primarily caused by the distribution of shadows. The amount of shadows observed under specific illumination and viewing angles is controlled the canopy architecture (LAI, LAD, and other structural

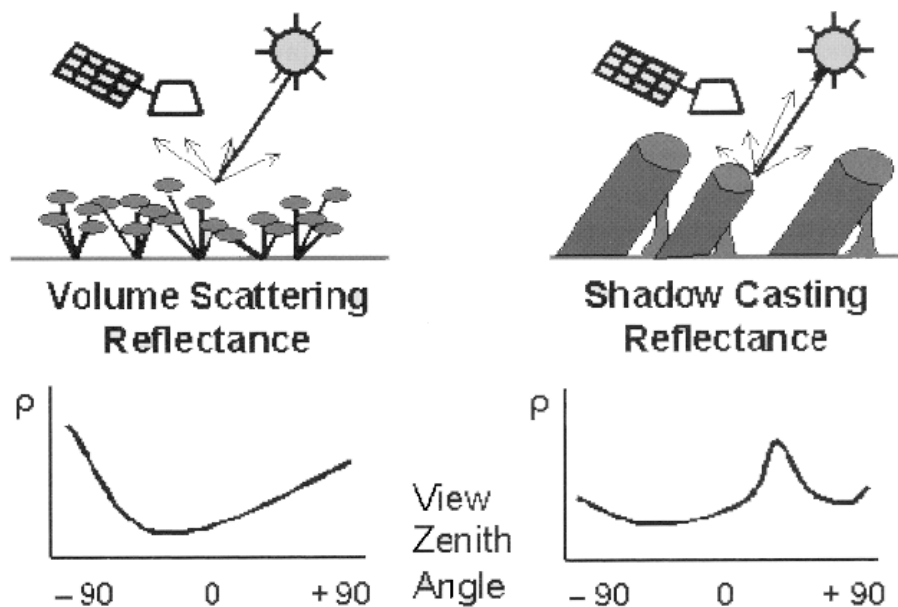


Figure 2.11: Causes for directional reflectance anisotropy of vegetation canopies and the associated typical shapes of the BRDF on the principal solar plane. From Lucht (2004).

attributes) which are influenced by plant species, phenology and health conditions. The influence of the canopy architecture on spectral BRDF data can be explained by the gap and backshadow effects and multiple scattering (Kimes, 1983; Sandmeier et al., 1998). The gap effect (Figure 2.9) occurs particularly in canopies with a vertically oriented (erectophile) structure such as grass lawns or conifer forests. At low view zenith angles, the lower less illuminated canopy levels are visible whereas at large view zenith angles, the well illuminated top layers of the canopy are seen. The *gap effect* alone leads to an azimuthally symmetric bowl shape centred around the nadir view angle (Sandmeier, 2004). The *backshadow effect* (Figure 2.10) causes the sensor to see the unilluminated shadowed vegetation surfaces in forward scattering direction. If only this effect was present in a scene, the lowest reflectance in a conifer forest would occur in the largest view zenith angle in forward scattering direction. In reality, the transmittance of leaves reduces the backshadow effect and under extreme viewing angles, the gap effect becomes dominant, shifting the minimum reflectance to small view zenith angles in forward scattering direction (Sandmeier, 2004). From the combination of gap and backshadow effect, densely vegetated erectophile canopies show i) the minimum reflectance near nadir view angles in the forward direction, ii) maximum reflectance (hot spot) in the backscatter direction at view zenith angle equal to the illumination zenith angle and iii) a general bowl shape of the BRDF (Figure 2.11). The bowl shape (a rise of reflectance with increasing view zenith angles) is caused by the gap effect and in dense forests, by mutual shadowing and obscuring of neighbouring trees (Meister et al. 2004).

The forward scattering component is increased by some specular reflection in most vegetation canopies. Both, gap and backshadow effects, are more pronounced at large illumination zenith angles and show stronger effects in spectral domains with lack of multiple scattering (e.g. red wavebands). The amount of *multiple scattering* regulates the darkness of the shadow in a vegetation canopy. In the near-IR and also the green, radiance reflected or transmitted by the leaves generates a diffuse secondary irradiance that brightens the shadow fractions and reduces the contrast between illuminated and shadowed fractions. Consequently, BRDF effects are less pronounced in the green and near-IR wavebands and strong in red and blue bands (Sandmeier, 2004).

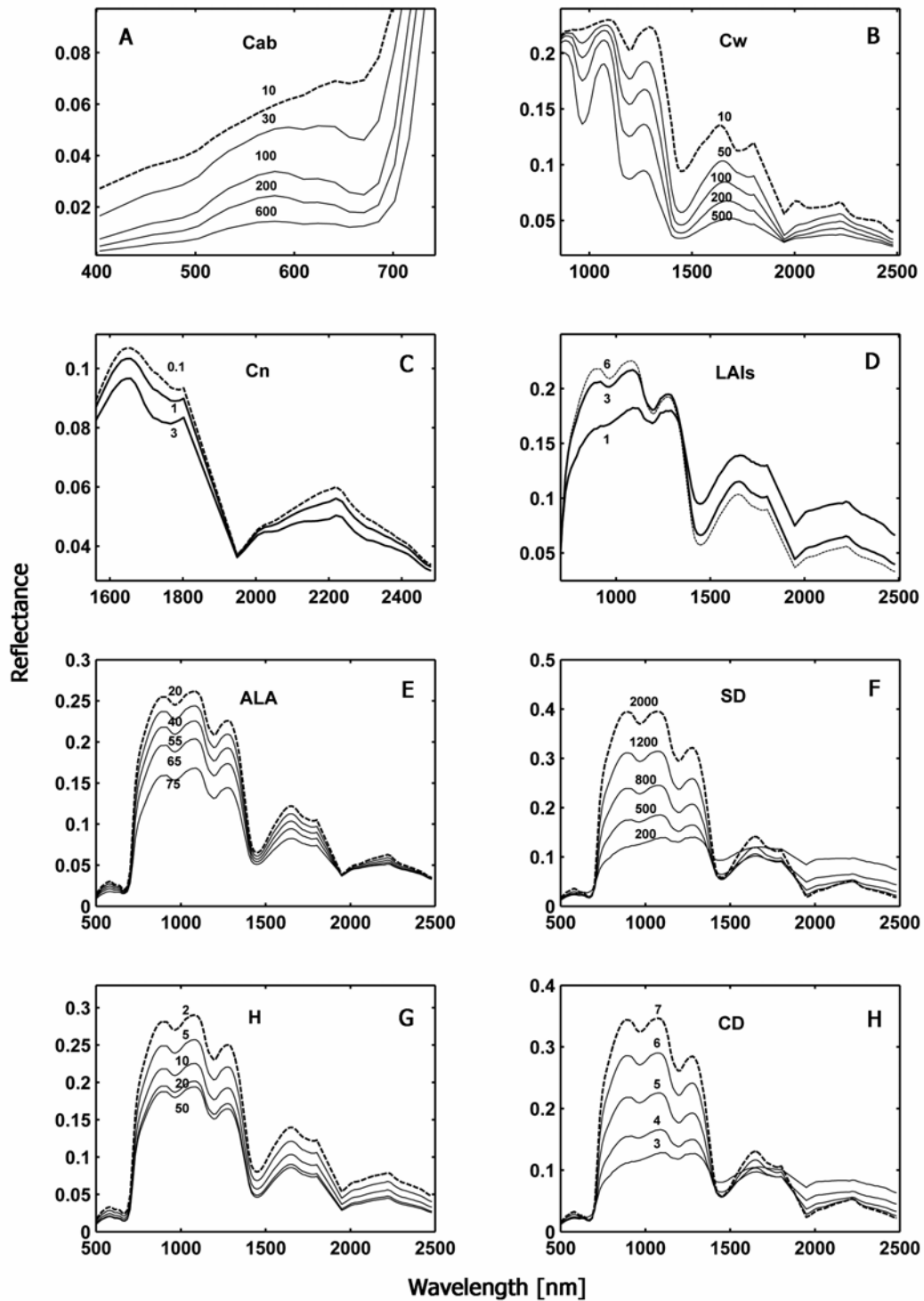


Figure 2.12: Variation of simulated forest canopy reflectance as a function of: A) leaf chlorophyll a+b content (mg m^{-2}), B) leaf water content (g m^{-2}), C) nitrogen content (g m^{-2}), D) single tree leaf area index ($\text{m}^2 \text{m}^{-2}$), E) average leaf inclination angle ($^\circ$), F) stem density (ha^{-1}), G) tree height (m), H) crown diameter (m). Spectral reflectances were simulated by the INFORM model using the following parameter values: $C_{AB} = 200 \text{ mg m}^{-2}$, $C_W = 50 \text{ g m}^{-2}$, $C_N = 1 \text{ g m}^{-2}$, $\text{LAIs} = 6 \text{ m}^2 \text{m}^{-2}$, $\text{ALA} = 55^\circ$, $\text{SD} = 700 \text{ ha}^{-1}$, $H = 10 \text{ m}$, $\text{CD} = 5 \text{ m}$, $\theta_s = 35^\circ$, $\theta_o = 0^\circ$, $\psi = 0^\circ$, $\text{skyl} = 0.1$.

Reflectance models are useful tools for analysing the effects of forest canopy attributes on reflectance signatures. By analysing the sensitivity of forest reflectance to the input variables, one can assess the error that may be caused by inaccurate input data. The variation of forest canopy reflectance with changes in certain canopy attributes as modelled by the INFORM model is shown in Figure 2.12.

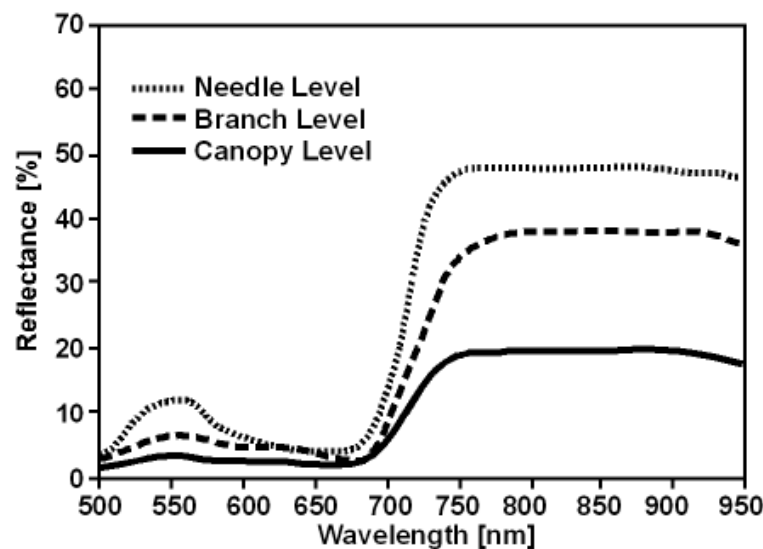


Figure 2.13: Measured reflectance spectra of Norway spruce at the needle, branch, and canopy level (modified from Williams, 1991).

2.2.5 Spectral reflectance properties of Norway spruce

Spectra of Norway spruce and other tree species show a dramatic decrease of reflectance from the needle to the branch to the canopy level in the near-IR and visible domain (Figure 2.13). In the visible changes in reflectance can be attributed to the influence of increased shadowing within the total scene from the needle to the canopy level. In the near-IR region, although reflectance generally increases with increasing canopy density or LAI due to the high reflectance and transmittance, four significant factors may account for a reduction in near-IR reflectance at the branch and canopy level: i) shadowing; ii) absorption of radiation by the twigs, branches, bark, and litter; iii) needle age; and iv) the clustering of needles on the branches which may enhance the trapping of radiation (Williams, 1991). With increasing LAI (or number of branches), reflectance in the near-IR domain is increasing; saturation occurs at an LAI of about 7-9 (Figure 2.14).

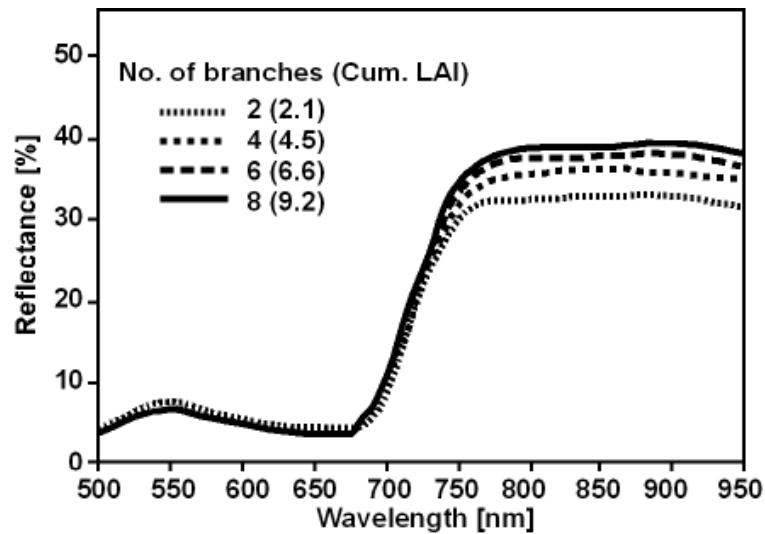


Figure 2.14: Measured reflectance spectra of Norway spruce for changing numbers of branches and corresponding values of cumulative LAI (modified from Williams, 1991).

2.2.6 Age dependence of forest reflectance

Forest age largely controls the structural parameters that determine the spectral reflectance of a forest stand. The age dependence of Norway spruce forest reflectance has been derived from airborne reflectance measurements and through forest reflectance model simulations by Nilson & Peterson (1994). The analysis of airborne data revealed a relatively fast reflectance decrease up to a saturation point at 20 years and 80 years for red and near-IR reflectances, respectively (Figure 2.15). This behaviour was explained by the fact that the amount of shade increases with stand age as the roughness of the forest canopy is increasing. Generally, simulated reflectances agreed with measured reflectances; however, some essential differences were observed by the authors: i) simulated reflectance slightly increased from an age of 30 onwards (red and near-IR domain), ii) in the near-IR domain, simulated reflectance increased during the first 10 years of stand development. Despite a certain disagreement between measured and simulated reflectances, simulated age courses of the scene component proportions (sunlit crowns, shaded crowns, sunlit ground, and shaded ground) largely explained the observed temporal reflectance variation: During the first 20-30 years of stand development, where a fast decrease in reflectance was observed (particularly in the red domain), the proportion of sunlit crowns increased (with increasing canopy cover), whereas the proportion of sunlit ground dramatically decreased. The proportion of shaded ground was constantly increasing with stand age and could be responsible for the observed reflectance decrease in the near-IR domain up to the end of the succession (Nilson & Peterson, 1994). However, the proportion of the shaded crowns did not increase between 40 and 100 years in

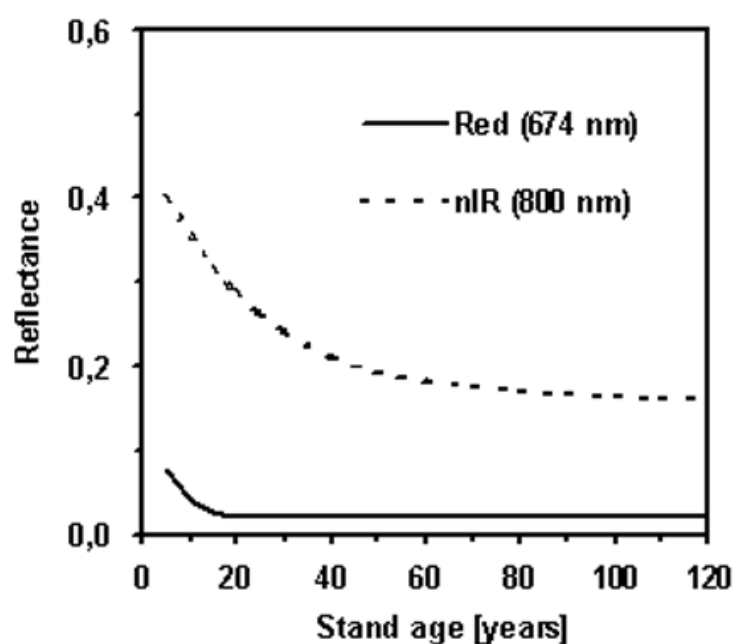


Figure 2.15: Canopy reflectance of Norway spruce as a function of stand age. Regression lines of type $y=a+b\exp(-cx)$ were fitted through measured reflectance data (not shown) with $R^2>0.8$ (modified after Nilson & Peterson, 1994).

the simulation, which is not in harmony with the theory of the increasing shade within the crowns.

Nilson & Peterson (1994) identified the following driving factors of the reflectance age course of a forest stand from their simulation studies: species composition of the main tree storey, canopy cover, tree-storey LAI, understory vegetation, leaf/supporting tissue ratio in the tree storey. According to the authors, also the height distribution of the tree layer (shade effects) and the needle age distribution (effect of different needle optical properties) contribute to the temporal reflectance changes.

2.3 Remote sensing of forest attributes

2.3.1 Classes of forest attributes

There are several classes of attributes to be remotely sensed in forests that share related mechanisms of, and limitations on, their remote estimation. Lefsky & Cohen (2003) defined classes of attributes related to: canopy cover, stand structure, stand composition, and disturbance. *Attributes related to canopy cover* include foliage or canopy cover, fraction of absorbed photosynthetically active radiation (F_{APAR}), and leaf area index (LAI). The attributes related to cover, although their formal definition and their estimation in the field differ, have a

similar, clear link with the remotely sensed signal: An increase of a cover related attribute will be indicated by decreased reflectance in the red and increased reflectance in the near-IR. However, the relationship between canopy cover and LAI is asymptotic; with each additional layer of leaves the amount of additional cover becomes smaller. As changes in reflectance are mostly driven by change in cover, the relationship between reflectance and LAI is also asymptotic (Lefsky & Cohen, 2003; Figure 2.8). Attributes related to cover have been most frequently the target of research in terrestrial remote sensing (section 2.3.3). *Attributes related to canopy height* or stand age include tree volume, aboveground biomass, basal area, diameter-at-breast-height, and stem density. With the exception of very low productivity stands, canopy closure occurs early in most stands while attributes related to canopy height continue to change. Estimation of these attributes is limited to the period of changing canopy cover. Thus, accurate estimation of height-related attributes is one of the most difficult tasks in the remote sensing of moderate to high biomass forests. In some conifer stands, the structural canopy properties that can be observed continue throughout stand development, and determination of height-related variables is more successful (Lefsky & Cohen, 2003). *Attributes related to composition* comprise physiognomy (e.g. trees, shrubs, and herbs), phenological types (deciduous and evergreen), species composition, and various cover type classifications (such as stand age classes). *Attributes related to disturbance* include attributes useful to monitor stand replacement, fires, thinning, etc.

Within this research work the classification proposed by Lefsky & Cohen (2003) was modified. Compositional attributes were denoted as *attributes related to forest type*. Both, attributes related to cover and attributes related to canopy height, were combined to *structural forest attributes*. Additionally, a class denominated *chemical forest attributes* comprising concentrations or contents of leaf constituents was created. Attributes related to disturbance involve the analysis of multitemporal data sets and were not considered.

2.3.2 Attributes related to forest type

Multispectral satellite data have shown a good capability for mapping broad forest type classes, such as hardwoods, softwoods, mixed woods, open wetlands and clearcuts (Bryant et al., 1980). Some conifer species discrimination capabilities have been reported, but consistent discrimination has not been possible (Leckie, 1990). For instance, Walsh (1980) identified seven classes of coniferous tree species through the use of Landsat MSS data with an average accuracy of 88.8 percent. Results obtained by Coleman et al. (1990) revealed that TM imagery was inadequate for differentiating among pine species, but suitable to differentiate five pine age classes (four age classes out of the five age classes had a class mean of less than 20 years, overall classification accuracy was 59.2 percent and 44.6 percent for two sites). Separation of age classes in spruce stands younger than 50 years was achieved by Vohland (1997) using TM data, but discrimination of older stands proved to be problematic.

Few studies have reported on the use of hyperspectral data in mapping forest species. Franklin (1994) compared panchromatic SPOT, multispectral TM and hyperspectral CASI data for discrimination of 9 types of forest species; the obtained overall classification accuracy were 49.2 percent using SPOT data and about 81 percent for both TM and CASI data. In attempting to discriminate age classes of Douglas fir with CASI data, Niemann (1995) concluded that a limited separation based on age is feasible but that discrimination of stands older than 40 years is not possible. Image classification of 11 forest cover types, including pure and mixed stands of deciduous and conifer species using AVIRIS data yielded an overall classification accuracy of 75 percent (Martin et al., 1998). The study used 11 spectral bands for species classification which were closely correlated with field measured canopy nitrogen and lignin concentrations. Prediction of forest age from TM data and additional topographic information using neural networks resulted in rms errors about 5 years for 50 year old stands (Kimes et al., 1996). *In situ* hyperspectral data has also been explored to discriminate conifer (Gong et al., 1997) and tropical species (Cochrane, 2000).

It can be concluded that detailed information suitable for forest inventories can only partly be derived from remote sensing data. While discrimination of young to medium aged forest stands was shown to be possible with both, multi- and hyperspectral data, separation of medium aged to old stands could not be achieved.

2.3.3 Structural attributes

Field estimation of leaf area index

To derive LAI maps from remote sensing data accurate field estimation of LAI is essential. Canopy LAI is difficult to assess in forests through direct methods, such as stratified clipping techniques, litter collections, and allometric relationships. These methods are often site specific and have a limited spatial and temporal validity (Soudani et al, 2002). For instance, allometric relationships between LAI and diameter at breast height are inherently unresponsive to seasonal change, as they are typically derived from variables collected at various times throughout the growing season (Lucas, 1995). To overcome such difficulties, indirect optical methods have been developed. Ground-based LAI measurements using optical instruments have become a standard as they allow for intensive spatial and temporal sampling over large areas (Soudani et al, 2002). The LAI-2000 plant canopy analyser (Li-Cor Inc., Lincoln, USA) (Welles & Norman, 1991) has an optical sensor that consists of five detectors, arranged in concentric rings, which measure radiation (below 490 nm) from different sections of the sky. Canopy transmittance for these different sections is calculated as the ratio between below-canopy and above-canopy readings for each detector ring (Stenberg, 1996). From these transmittance values (gap fraction) LAI is estimated using an approximation of the Lambert-Beer law (see section 2.1.2). This estimation is based on the assumption of randomly

distributed leaves in the crown and does not consider other shading elements such as stems. In reality however, conifer stands show a non-random leaf distribution, as needles are grouped (clumped) first in shoots and shoots are further grouped into branches and crowns (Chen et al., 2002). Therefore, LAI estimates from optical methods are effective plant area indices (LAI_{eff}), which account neither for clumping nor for separating leaves from non-green material, nor for distinguishing species (Soudani et al., 2002). LAI_{eff} represents the equivalent leaf area of a canopy with a random foliage distribution to produce the same light interception as the true LAI (Fernandes et al., 2002). LAI_{eff} generally differs considerably from the true LAI. An underestimation of the true LAI results from clumping as it increases the canopy gap fraction for a given leaf area. An overestimation can be attributed to the fact that the instrument considers not only the leaves but also woody canopy parts such as stems (Stenberg, 1996). Several correction factors were developed to derive the true LAI from LAI_{eff} in forests (Fassnacht et al., 1994; Stenberg, 1996; Chen, 1996). According to Chen & Cihlar (1996), from a remote sensing perspective LAI_{eff} has several advantages over the true LAI: first, the effective LAI was better correlated to vegetation indices (RVI, NDVI) than the true LAI (Chen & Cihlar, 1996); second, the true LAI varied by about 10-30% while LAI_{eff} remained virtually unchanged in the course of a year as the new needles grew on top of the old needles and did not reduce the canopy gap fraction significantly (Chen, 1996). Therefore, in this research work the focus is on mapping LAI_{eff} instead of the true LAI. As suggested by Fernandes et al. (2002) it is possible to convert maps of LAI_{eff} to true LAI using correction factors estimated at the site or given in the literature. For simplicity, in this study the term LAI is used when referring to either effective or true LAI.

Empirical approaches

The majority of studies for extracting structural attributes from remotely sensed data have used empirical techniques to relate the spectral measurements to the variable of interest (Treitz & Howarth, 1999). Spectral measurements are usually converted to spectral vegetation indices (VIs) as these simple transformations are more closely related with plant biophysical properties. If structural parameters are strongly correlated with remotely sensed VIs, the remote sensing imagery can be used to predict those structural characteristics over large areas. A lot of research has been done on the estimation of forest LAI from remote sensing data within about the last 15 years. A selection of literature results is presented in Table 2.2. Most of the studies on forests have used broadband VIs to derive LAI of conifer forest stands; however, with varying success. Several authors found good correlations between the normalized difference vegetation index (NDVI) or the ratio vegetation index (RVI) derived from TM or AVHRR images and field-measured LAI (Running et al., 1986; Peterson et al., 1987; Spanner et al., 1990a; Curran et al., 1992a; White et al., 1997; Franklin et al., 1997). In all of these studies the range in canopy LAI was very large. Those studies where the LAI

range was rather limited generally show a smaller correlation or no relationship (Badhwar et al., 1986; Spanner et al., 1990; Herwitz et al., 1990; Hall et al., 1995; Chen & Cihlar, 1996). Better relationships were found even for small variations in canopy LAI when using modified VIs, such as the reduced simple ratio or the normalised difference between near-IR and mid-IR (Brown et al., 2000; Chen et al., 2002; Boyd et al., 2000) or when multiple linear regression was employed (Fassnacht et al., 1997).

Few studies looked at the suitability of high spectral resolution remote sensing data to derive the LAI of conifer forests. Gong et al. (1995) tested CASI data using univariate and multivariate regression and a VI based algorithm and found strong relationships with reasonable low errors. Danson & Plummer (1995) tested if the red edge inflection point (REIP) is primarily controlled by forest canopy LAI using helicopter-borne spectroradiometer data and found a strong non-linear correlation between plot LAI and the REIP for Sitka spruce (*Picea sitchensis*). For the same tree species, forest LAI was recently related to the canopy REIP computed from imaging spectrometer data (CASI) with success (Lucas et al., 2000).

A systematic investigation on the performance of various broadband multispectral and narrow band hyperspectral vegetation indices has been done on agricultural crops (Boegh et al., 2002; Broge & Mortensen, 2002) and very recently, also in forests. For instance, Gong et al. (2003) estimated forest LAI using vegetation indices derived from Hyperion hyperspectral data. Lee et al. (2004) performed a comparative analysis of hyperspectral versus multispectral data for estimating LAI in four different biomes. Using canonical correlation analysis, the authors found that individual, narrow bands of AVIRIS data yielded better relationships with LAI than broadband data for grassland and forest biomes. Given the few studies undertaken, it is still not sufficiently investigated whether the high spectral resolution data offer advantages over broadband data.

Generally, relationships between the reflectance of a vegetation canopy and its LAI can suffer from effects of internal and external variables. For instance, Spanner et al. (1990; 1990a) found linear and strongly positive relationships between near-IR radiance and LAI only for stands with a canopy cover greater 89% whereas old growth stands with incomplete overstories had low near-IR radiances as a result of less reflective forest litter and shadows. However, in more open stands the exhibition of highly reflective understorey vegetation could also increase near-IR radiance. Soudani et al. (2002) found that the understorey LAI contributed 37-42% to the total LAI in pine forests. Chen & Cihlar (1996) observed that late spring TM images were superior to summer images for determining overstorey LAI in boreal conifer stands because the effect of the understorey was minimized in the spring before the full growth of the understorey and moss cover. On semi-natural forest sites with a wide range of green vegetation amount, canopy cover or LAI was considered the most important variable to control canopy reflectance, even with variable understorey (e.g., Spanner et al., 1990a). On

the contrary, in coniferous forest plantations, which are managed to maintain a large amount of green vegetation with little spatial variation (and thus, low ranges in LAI) the relation between LAI and canopy reflectance may be weaker, as also other structural stand characteristics (stem density, tree height) determine the stand spectral response (Danson & Curran, 1993; Treitz & Howarth, 1999).

To overcome these problems various strategies were suggested. Through stratification by forest cover type, Franklin et al. (1997) yielded more precise LAI estimates from TM data. They also found that the GIS-based implementation of additional information on stem density

Table 2.2: Selected literature results on the estimation of forest structural attributes. Sensors: ATM = Airborne Thematic Mapper, TM = Thematic Mapper, AVHRR = Advanced Very High Resolution Radiometer, CASI = Compact Airborne Spectral Imager, DAIS = Digital Airborne Imaging Spectrometer; Vegetation Index (VI): RVI = Ratio Vegetation Index, NDVI = Normalised Difference Vegetation Index, RSR = Reduced Simple Ratio, REIP = Red edge inflection point, VI3 = (near-IR – mid-IR) / (near-IR + mid-IR); Method: BRA = Bivariate regression analysis, MLR = Multiple linear regression, IRM = Inversion of reflectance model, CCA = Canonical correlation analysis

Sensor	VI/ Method	Variable	Range	N	Relation	Reference
ATM	RVI/BRA	LAI (various conifers)	1-16	18	$R^2 = 0.82$	Running et al., 1986, Peterson et al., 1987
TM	$\frac{\rho_{red} - \rho_{near-IR}}{BRA}$	LAI (aspen)	0.5-3.5	29	No relation	Badhwar et al., 1986
AVHRR	NDVI/BRA	LAI (various conifers)	1-13	19	$R^2 = 0.70-0.79$	Spanner et al., 1990
TM	NDVI/BRA	LAI (various conifers)	1-16	73	$r = 0.60$	Spanner et al., 1990a
TM	RVI/BRA	LAI (pine)	4-7	15	No relation	Herwitz et al., 1990
TM	NDVI/BRA	LAI (pine)	2-10	16	$R^2 = 0.35-0.86$, rmse = 0.74	Curran et al., 1992
CASI	NDVI/MLR	LAI (various conifers)	1-12	30	$R^2 > 0.80$, rmse < 1.0	Gong et al., 1995
Helicopter-borne data	REIP/BRA	LAI (spruce)	5-11	14	$r = 0.91$	Danson & Plummer, 1995
TM	NDVI/BRA RVI/BRA	LAI Cover (various conif.)	0.5-3.5 0.05-0.85	22	$R^2 = 0.38-0.66$ $R^2 = 0.26-0.63$	Chen & Cihlar, 1996
TM	RVI/MLR NDVI/MLR	LAI (various conifers)	1.0-4.5	10	$R^2 = 0.71$ $R^2 = 0.91$	Fassnacht et al., 1997
TM	RVI, NDVI /BRA	LAI (various vegetation types)	2-15	39	$R^2 = 0.65-0.90$	White et al., 1997
TM	NDVI/BRA	LAI (various forest types)	Not specified	17	$R^2 = 0.15$ (all spec.) $R^2 = 0.93$ (conifers)	Franklin et al., 1997
TM	IRM	LAI (various vegetation types)	0-7	Not specified	LAI pattern in good accordance to the land use map	Kuusku, 1998

Table 2.2 (continued)

TM	RSR/BRA	LAI (pine, spruce)	0.5-6.0	35	$R^2 = 0.55-0.70$	Brown et al., 2000
AVHRR	NDVI/BRA VI3/BRA	LAI (pine, aspen, spruce)	2.0-4.0	10	$R^2 = 0.46$ $R^2 = 0.76$	Boyd et al., 2000
CASI	REIP/BRA	LAI (spruce, pine)	3-12	16	$r = 0.94$	Lucas et al., 2000
CASI	IRM	LAI (various conifers)	1.0-3.0	20	$R^2 = 0.51-0.86$	Hu et al., 2000
CASI	IRM	LAI (pine)	1.0-3.0	20	$R^2 = 0.16-0.67$	Fernandes et al., 2002
TM	IRM	Cover (pine)	0.1-1.0	33	$R = 0.33-0.38$	Gemmell et al., 2002
AVHRR	RSR/BRA	LAI (various conifers)	0.5-10.5	> 50	$R^2 = 0.62$ rmse = 1.48	Chen et al., 2002
Hyperion	VI	LAI	Not specified	Not specified	Not specified	Gong et al., 2003
AVIRIS	CCA	LAI (various biomes)	1.9-5.1	Not specified	Not specified	Lee et al., 2004
CASI	IRM	LAI (pine, spruce)	1-6	46	Relative rmse = 14% (spruce)	Fernandes et al., 2004
DAIS	IRM	LAI (poplar)	1.0-3.5	26	rmse = 0.40	Meroni et al., 2004
DAIS	IRM	LAI (pine)	2-4	4	rmse = 0.5	Kötz et al., 2004

increased the accuracy of the LAI estimates and that multiple linear regressions using NDVI and stem density improved correlations with LAI in comparison to the simple correlations. Chen et al. (2002) identified accurate information about subpixel mixture of the various cover types as a key to improving the accuracy of LAI estimates. Badhwar et al. (1986) recommended the use of canopy reflectance models to understand the understory effects on forest reflectance.

Physically based approaches

It is believed that simple empirical relationships need to be replaced by physically based forest reflectance models as a model inversion approach may provide a more robust method for estimating structural characteristics (Gemmell et al. 2002, Treitz & Howarth, 1999). The effects of internal and external variables might be taken into account in the inversion process if such information is available.

In particular in the case of forests, physically based approaches have not yet been widely tested. In the forward mode the CR model computes the spectral reflectance for a certain set of leaf or canopy parameters. Forward modeling provides an efficient way to investigate the effects of forest canopy variables on reflectance signatures and may improve the understanding of how the canopy structure influences the radiation field (e.g., Rautiainen et al., 2004; Schlerf & Atzberger, 2002). For the retrieval of those canopy attributes from measured signals it is necessary to invert the model. Inversion has been mostly considered as

a way to validate radiative transfer models but has rarely been used as an alternative to extract canopy attributes from measured reflectance (Jacquemoud et al., 2000). Most of these works concern the retrieval of canopy structural attributes (LAI, leaf angle distribution) by using multi-angle reflectances (Goel & Thompson, 1984; Goel & Deering, 1985; Iaquina et al., 1997; Bicheron & Leroy, 1999). Recently, hyperspectral reflectances have been increasingly used as an input to model inversion for estimation of structural and chemical vegetation attributes (Jacquemoud et al., 2000; Hu et al. 2000; Zarco-Tejada et al., 2001; Meroni et al., 2004; Fernandes et al., 2004; Kötz et al., 2004).

The majority of the aforementioned and other inversion studies focused on agricultural crops but only some on forests. According to Zarco-Tejada et al (2001), until recent, no validation has been found in the literature reporting results in forest canopies from airborne or satellite-measured reflectance with ground truth. For instance, Woodcock et al. (1994) estimated tree size and cover from TM data using the Li-Strahler model but results were not validated with measured field data. Kuusk (1998) inverted the MCRM model on reflectance in five TM bands to estimate LAI, average leaf angle, and chlorophyll content for various vegetation types. Ground truth data was not available. He found the estimated LAI to be in good accordance with the land use map but had to concede that the LAI particularly of conifer forests was probably underestimated by the model.

For the past five years, an increasing number of successful LAI and crown cover estimation results were reported. Gemmell & Varjo (1999) were unable to provide accurate estimates of LAI and canopy cover in boreal forests; when background reflectance was considered, estimation of canopy cover succeeded with good accuracy (Gemmell, 1999). The use of multi-angle ASAS data further improved estimates of forest canopy cover (Gemmell, 2000). Hu et al. (2000) derived LAI of boreal forest canopies through inversion of a modified FLIM model using hyperspectral CASI data. Validation results showed moderate to high correlations between estimated and field-measured canopy LAI; increased correlations were found when the understorey reflectance was allowed to vary within the range of variability as determined by field measurements. In combination with a multispectral clustering approach, the modified FLIM was used to map spatial patterns of effective LAI within boreal forest stands. Depending on the site, correlations between estimated and measured LAI were poor to moderate (Fernandes et al., 2002). Zarco-Tejada et al. (2001) found acceptable relations between estimated and measured leaf pigment content of closed forest canopies using CASI data and coupled SAILH and PROSPECT models. Meroni et al. (2004) estimated LAI of poplar plantations from DAIS data using the SAIL model coupled with the PROSPECT model and obtained an rmse of 0.40-0.45 against ground truth. Fernandes et al. (2004) report a relative rmse of 14% for black spruce sites using CASI data and the FLIM-CLUS algorithm. Kötz et al. (2004) report an rmse of 0.5 for estimating LAI in pine stands from DAIS data through inversion of a coupled GeoSAIL and PROSPECT models.

Due to the complex character of a CR model an analytical solution is not possible and inversion strategies had to be developed. A successful inversion of a reflectance model requires three factors: a good model, an appropriate inversion procedure, and a set of calibrated reflectances (Jacquemoud et al., 2000). Traditional inversion of reflectance models employs an optimisation technique to estimate the model parameters by minimising a merit function (Goel, 1989). An iterative process is necessary to find the optimal estimates of these parameters. The main drawbacks of this method are i) difficulty in achieving globally optimal and stable results, ii) difficulty in retrieving more than 2 parameters simultaneously (Gong et al., 1999), and iii) computational inefficiencies that prohibit an operational application on a per-pixel basis for regional or global studies (Kimes et al., 2002).

Recently, Artificial Neural Networks (ANN) have been employed for reflectance model inversion (Gong et al., 1999; Udelhoven et al., 2000; Kimes et al., 2002) in order to overcome the above mentioned limitations. Gong et al. (1999) found the Coupled Atmosphere and Canopy (CAC) model extremely difficult to use for the retrieval of structural parameters with ordinary (numerical or look-up table) inversion methods. They employed an ANN on simulated multi-angle reflectances and were able to retrieve many parameters simultaneously; this is usually a problem with numerical inversion methods. It was further concluded that the LAI retrieval could be done accurately with only one directional reflectance, while eight or more directional reflectances were required to accurately retrieve the LAD (leaf angle distribution) parameters. Kimes et al. (2002) inverted a complex 3D model (DART) for a wide range of simulated forest canopies. They compared a traditional inversion approach with the neural network method and found the ANN method to be more accurate. The ANN approach proved to be computationally efficient when inverting a complex reflectance model and could be applied on a per-pixel basis. Udelhoven et al. (2000) inverted the INFORM model using hyperspectral DAIS data and found the estimated structural forest attributes to have reasonable values.

2.3.4 Chemical attributes

Assuming no constraints related to climatic conditions, water availability, nutrient availability or other potentially limiting factors, many of the biogeochemical processes in terrestrial ecosystems are related to the content of chemicals in leaves (Waring & Running, 1998). For instance, net primary production depends strongly on the availability of nitrogen (Vitousek, 1982). Litter decomposition is governed by the leaf C/N ratio (Melillo et al., 1982) and also by the leaf lignin content. Photosynthesis is largely controlled by chlorophyll pigments. Therefore, quantifying foliar chemicals within vegetation should help assessing the physiological status of vegetation, monitoring phenological characteristics, and estimating productivity (Blackburn, 1998).

Leaves are the most important plant surface interacting with solar energy. Besides canopy structure, the concentrations of the leaf chemical constituents (pigments, water, protein, cellulose, and lignin) shape the canopy reflectance spectra (section 2.2). Reflectance spectra can be recorded by airborne or spaceborne spectrometers and converted to information on foliar chemical constituents. This information can then be used to model forest ecosystem processes. Estimation of foliar biochemicals can be done at three different levels based on reflectance spectra either from dried leaves, fresh leaves, or canopies. An overview of literature results on the estimation of foliar chemicals from spectral variables using different

Table 2.3: Selected literature results on the estimation of foliar chemicals from spectral variables using different methodologies. Chemical attributes: L = Lignin, N = Nitrogen, P = Protein, C = Cellulose, W = Water, DM = Dry matter, Chl = Chlorophyll; Level: D = Dried, ground leaves, F = Fresh, whole leaves, C = Canopy, G = Ground, A = Airborne, S = Synthetic; Methodology: MSR = Multiple stepwise regression, BLR = Bivariate linear regression, IRM = Inversion of reflectance model, ANN = Artificial neural network; Spectral variable: R = Reflectance, R' = First derivative of reflectance, diff = Reflectance differences at neighbouring bands, REIP = Red edge inflection point, BDN = Band depth normalization, VI = Vegetation index

Chemical	Species	Level	Methodology	Spectral Variable	Wavelengths [nm] and/or relation (MSR: $R^2 > 0.5$, if not specified)	Reference
N, L	Deciduous	D F C (A)	MSR	$\log(1/R)$	various (N); various (L) 1240 (N) ; 1225, 2305, 2365 (L) none (N), 1500-1700 (L)	Peterson et al., 1988
L	Various	C (A)	MSR	$\log(1/R)'$	1256, 1311, 1555 (L)	Wessman et al., 1988
N ; L	Deciduous	C (A)	MSR	diff'	1265, 1555 (N) ; 1256, 1592 (L)	Wessman et al., 1989
Chl	Amaranthus	F	MSR	R'	710, 718, 724	Curran et al., 1992a
Chl	Sugar beet	C (G)	IRM	R	Good accuracy	Jacquemoud & Baret, 1993
Chl, W	Sunflower	F	BLR	R-ratios	680, 430 (Chl) ; 979, 900 (W)	Penuelas et al., 1994
N, Chl, L	Conifers	C (A)	MSR	R'	552, 1184, 2164 (N); 1069, 1683, 858 (Chl)	Johnson et al., 1994
N, L	Pine	D C (A)	MSR	$\log(1/R)$	2180, 2230 (N); Validation on AVIRIS-spectra: $r=0.74$ (N), $r=0.55$ (L)	Gastellu-Etchegorry et al., 1995
P, C, L	Various	D, F	MSR	R', $\log(1/R)$	5 λ ; no typical wavelengths associated with absorption features; dry samples performed better than fresh material	Jacquemoud et al., 1995
Chl, C+L	Various	D F	IRM	R	$R^2=0.84$ (C+L) $R^2=0.50$ (C+L); 0.65 (Chl)	Jacquemoud et al., 1996
DM	Various	D	IRM	R	DM (g per unit leaf area) is the only accurately retrieved parameter	Fourty et al., 1996
N, L, C	Various	D, F	MSR	$\log(1/R)'$, $\log(1/R)''$	6 bands selected were not related to known absorption features; R^2 were not significantly higher than for randomized N- $\log(1/R)'$ datasets	Grossman et al., 1996

Table 2.3 (continued)

DM, W	Synthetic	C (S)	MSR ANN	R	Selection of 5-8 wavelengths not related to known absorption features; ANN performed better than MSR	Fourty & Baret, 1997
DM, W	Various	F	MSR	log(1/R), log(1/T)	1910, 1380, 900 (W); 2310, 2160, 1870 (DM); P, L, C not accessible from fresh leaf reflectance or transmittance	Fourty & Baret, 1998
L+C, N	Pine	F	ANN	R	1240, 1720 (L+C); 1510, 2180 (N)	Dawson et al., 1998a
Chl	Eucalypt	F	BLR	R ratios	550, 672, 708	Datt, 1998
Chl	Bracken	C (G)	Exp. Regr.	R ratios	800, 680, 635, 470	Blackburn, 1998
Chl	Grassland	C (A)	BLR	REIP	$r=0.71$, $rmse=0.42 \text{ mg g}^{-1}$	Jago et al., 1999
N, L, C	Various	D	MSR	BDN	1730, 2100, 2300 (N, L, C)	Kokaly & Clark, 1999
Chl	Maize Synthetic	F, C (S)	BLR	R ratios	Slopes of near-IR / red vs. near-IR / green	Daughtry et al., 2000
Chl	Synthetic	C (S)	BLR	REIP	No further specifications	Demarez & Gastellu-Etchegorry, 2000
Chl, L, N, C, P, W	Pine	D	MSR	BDN	1496, 680, 648, 2352, 2172 (N); 648, 478, 1124, 1486, 2318 (L)	Curran et al., 2001
N, L	Chaparral vegetation	C (A)	MSR	R ²	Nit : 1609, 1748, 480	Serrano et al., 2002
N	Grass	C (A)	ANN	BDN, REIP	$R^2=0.60$, $rmse=0.13$, relative $rmse$ of mean=8.3%	Mutanga & Skidmore, 2004
Chl	Pine	C (A)	IRM	R	$R^2=0.4$, $rmse=8.1 \mu\text{g cm}^{-2}$	Zarco-Tejada et al., 2004
Chl	Olive trees	C (A)	BLR	Various VI	$R^2>0.6$	Zarco-Tejada et al., 2004a

methodologies is given in Table 2.3.

Dry leaf level

Remote sensing of chemical attributes started with spectrometric laboratory analysis of dried ground foliage. The methodology has been used to successfully derive protein, lignin, and other leaf constituents (Norris et al., 1976). Strong relationships between the concentration of foliar chemicals and reflectance were also found by other researchers for dry and ground leaves using multiple regression techniques (Card et al., 1988; Elvidge, 1990). More reliable results were obtained when normalised band depths were used instead of reflectance values (Kokaly & Clark, 1999; Curran et al., 2001). The inversion of a leaf reflectance model (PROSPECT) showed results of varying success. While Jacquemoud et al. (1996) obtained reasonable estimates on dry (but not on fresh) leaves, Fourty et al. (1996) were not able to

retrieve any of the single biochemical compounds within dry leaves; total amount of dry matter per unit leaf area was the only variable to be accurately retrieved.

Fresh leaf level

To bridge the gap between established laboratory methods and remote sensing, controlled experiments on fresh whole leaves have been undertaken by various researchers. However, the influence of water is strong throughout the near infrared region where most of the sought biochemicals have their absorption features. Consequently, leaf water can obscure absorption features related to foliar chemicals, such as protein, lignin, and cellulose in green leaf materials with considerable consequences for their estimation from reflectance spectra. For instance, Kokaly & Clark (1999) concluded that their method and those using $\log(1/R)$ derivatives would be sensitive to variations in leaf reflectance that may be solely caused by changes in leaf water content. Elvidge (1990) draws the conclusion, that remote sensing techniques for estimating canopy protein or canopy nitrogen content have to be based on indirect rather than direct measurements. Curran et al. (1992a) found good relationships between estimated and measured chemical concentrations for water, chlorophyll and starch (all $R^2 > 0.80$). A study undertaken by Fourty & Baret (1998) showed that the detailed biochemistry (protein, lignin, cellulose) was not accessible in an accurate way when observing a large range of species; they recommended working on a limited set of species. Grossman et al. (1996) found stepwise multiple regression relating chemistry data and derivative reflectance spectra to give relatively large coefficients of determination even for randomised data sets. The bands selected in their study lacked correspondence to those reported in other studies. Inversion of a reflectance model (PROSPECT) on the basis of fresh leaves worked out rather poor for cellulose and lignin, but reasonable for chlorophyll (Jacquemoud et al., 1996).

Canopy level

In the transition from the leaf to the canopy level, strong disturbing effects are introduced, such as canopy architecture (leaf area index, leaf angle distribution) and influence of soil background. Compared to controlled laboratory conditions, airborne or spaceborne studies bring in further disturbances, such as variable solar illumination and atmospheric conditions, along with instrument characteristics (signal-to-noise ratio, spectral bandwidth, geometric field of view). Together, these factors cause a number of problems in the usage of remote sensing data to the determination of foliar biochemistry. Despite these problems it has been attempted to derive chemical attributes related to forest canopies from the analysis of imaging spectrometry data (Peterson et al., 1988; Wessman et al., 1988, 1994a; Johnson et al., 1994; Gastellu-Etchegorry et al., 1995). Results suggested that spectroradiometric measurements of plant canopies can be correlated with variations in canopy chemistry, involving lignin,

nitrogen and cellulose concentrations. However, wavebands selected by multiple linear regression were often not consistent with the absorption features of the chemicals within the leaves. Furthermore, relationships from one forest site showed poor predictive performances when applied to another site (Grossman et al., 1996). Estimation of chlorophyll from remotely sensed imagery can generally be achieved more reliably than the other chemicals, as the prominent chlorophyll absorption feature is not masked by leaf water. For instance, Jago et al. (1999) related the red edge inflection point derived from hyperspectral image data to the mean chlorophyll concentration of grassland and winter wheat sites with moderate success. Various authors successfully estimated chlorophyll from leaf reflectance spectra (Curran et al., 1992a; Penuelas et al., 1994; Jacquemoud et al., 1996; Datt, 1998; Atzberger & Werner, 1998; Daughtry et al., 2000; Schlerf et al., 2003a) and canopy reflectance spectra (Jacquemoud & Baret, 1993; Blackburn, 1998; Demarez & Gastellu-Etchegorry, 2000) using different approaches. Since a large amount of leaf nitrogen is contained in chlorophyll molecules, attempts were made to estimate LNC from reflectances in the chlorophyll absorption feature or the red edge inflection point (Lilienthal et al., 2000; Lamb et al., 2002).

There are many other examples, where data acquired by imaging spectrometers have been related to foliar chemicals, with varying success (e.g., Kupiec, 1994; Kupiec & Curran, 1995; Gholz et al., 1996; Lucas et al., 2000; Zarco-Tejada et al., 2001; 2004). However, there is still a long way to go before canopy chemical concentration can be estimated reliably to drive ecosystem simulation models (Curran, 1994a; Wessman, 1994).

One important limiting factor to reliably estimate foliar chemicals is the signal-to-noise ratio of imaging spectrometry data. Of all the applications of imaging spectroscopy in recent years, the estimation of foliar chemical concentration has proved to be one of the most demanding in terms of signal-to-noise ratio (Peterson and Hubbard, 1992). Specifications given in the literature on required SNRs for chemical estimates vary considerably. Gholz et al. (1996) compared minimum SNRs from a laboratory study (Nitrogen 37:1, Cellulose 65:1) with the approximate SNRs at vegetation reflectance given by the Jet Propulsion Laboratory and assessed data provided by the AVIRIS sensor to be sufficient for the estimation of foliar chemical concentrations. The minimum required SNR for this purpose has also been estimated by Smith and Curran (1996). From modeling the SNR, they showed that the required SNRs at nitrogen absorption features were always the smallest due to close relationships of spectral reflectance to protein and nitrogen concentrations. They suggest that out of three chemicals studied (nitrogen, lignin and cellulose) nitrogen could be estimated most successfully with remotely sensed data. Inflight SNR for the AVIRIS sensor was also determined by Smith and Curran (1996). They concluded that at the beginning of the 1993 flight season the AVIRIS was close to the threshold SNR required to estimate accurately the concentration of foliar chemicals in vegetation canopies (from 1995 SNR was set to double) but conceded that the use of more than one waveband when converting reflectance to

chemical concentration might reduce the SNR requirement slightly. Nonetheless, the former statement questions the validity of results obtained from early studies using AVIRIS data for estimation of foliar biochemistry (e.g., Peterson et al., 1988; Wessman et al., 1988).

Chapter 3 Material

Remote sensing in the geosciences is dealing with many kinds of material such as study sites, sensors, field and laboratory data, and imagery. These aspects are described in this chapter including the radiometric and geometric correction of the HyMap data.

3.1 Study sites

The fieldwork for this research was conducted at two sites, Idarwald and Gerolstein, both located in south-western Germany (Figure 3.1). HyMap images were acquired at both test sites at points in time close to the field data acquisition. The study on the determination of forest cover type and structural attributes was carried out at Idarwald. The research on the estimation of foliar chemicals was conducted at Gerolstein test site. The reason for this split was, that Idarwald offers a great number of homogenous spruce stands with a wide range of age classes and structural attributes but a rather limited variability in foliar chemicals due to its spatially invariable underlying geology. The Gerolstein area, on the other hand, hosts spruce forest standing on soils from very poor to very rich in nutrient availability which gives reasons to expect a relatively large variability in foliar chemicals.

3.1.1 Idarwald

The Idarwald forest (49°45'N, 7°10'E) is located on the north-western slopes of the Hunsrück mountain ridge. It covers an area of about 7,500 ha. Climatically the area is dominated by oceanic influences with primarily westerly winds. Luv effects at the west side of the ridges cause a relatively high mean annual precipitation of about 800-1000 mm. Low stratus above the mountain ridges give rise to additional precipitation during the winter term. The mean annual air temperature is 6.5°C with a summer maximum in July and the minimum temperatures occurring in January. In the winter months frost and snowfall are frequent (Arbeitskreis Standortkartierung, 1985). Topographically the area is characterised by remnants of peneplains, and quartzite ridges reaching a height of up to 770 m above mean sea level. Geologically the area is underlain by Devonian quartzite (Taunusquartzit) and

Devonian shale (Hunsrückschiefer). Taunusquarzit consists to 98 percent of quartzitic sand grains cemented by silicic acid and is characterised by an enormous weathering resistance. Weathering products of Taunusquarzit are almost pure sands while the Hunsrückschiefer weathers to sandy loam. Loess sedimentation and solifluction during the Pleistocene had a major influence on the soil formation. The predominant soil types are rankers, podzols, and dystric cambisols (podsolige Braunerde). The soils range from well to poorly drained. They are generally low in nutrient status and are partially acidified (Reichert & Stets, 1980; Arbeitskreis Standortkartierung, 1985).

The dominant forest species are Norway spruce (*Picea abies* L. Karst.), beech (*Fagus sylvatica*), oak (*Quercus petraea*) and Douglas fir (*Pseudotsuga menziesii*). They cover 53, 18, 11, and 5 percent of the forested area, respectively. The predominant natural forest community in the area is *Luzulo-Fagetum typicum*, but afforestation starting at the end of the 18th century lead to a wide spreading of Norway spruce (Vohland, 1997; Arbeitskreis Standortkartierung, 1985).

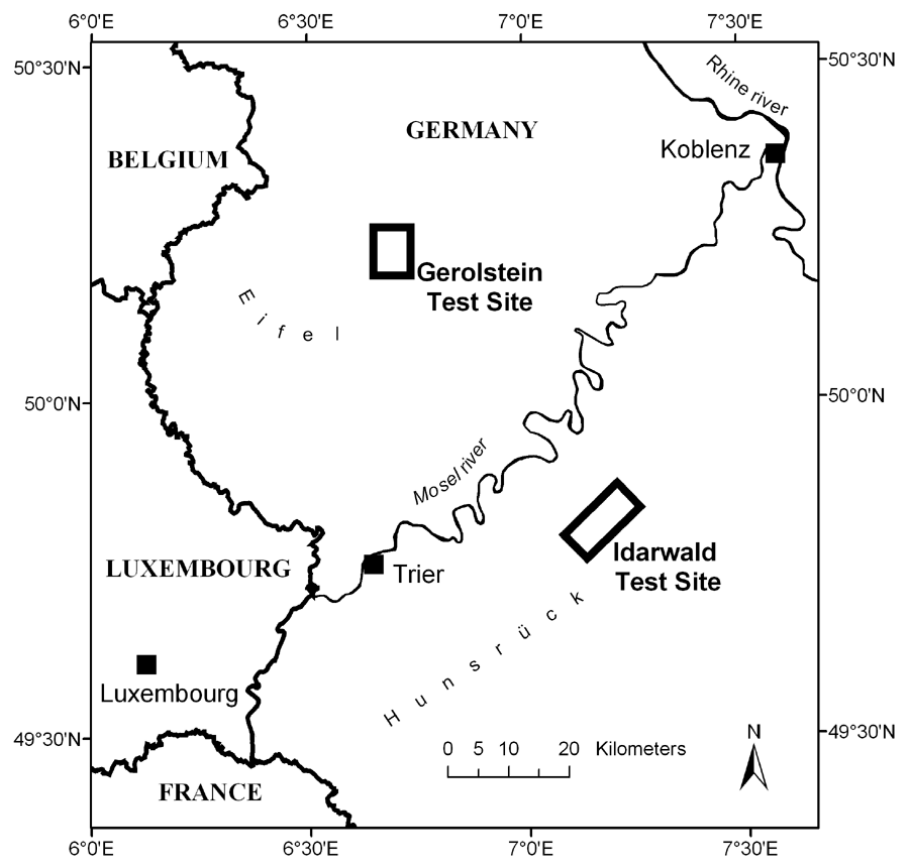


Figure 3.1: Location of study sites. Data sources: ATKIS-Geobasisdaten (Landesvermessungsamt Rheinland-Pfalz), ESRI data (U.S. Geological Survey).

Besides natural factors forest stand structure is largely determined by actual management practices. The timber forest or high forest (“Hochwald”) is a forest with trees that have evolved from seeds. There are two management types of high forest: forest with cutting areas, and single-tree selection forest (“Plenterwald”). Timber forest with cutting areas denotes a forested area that is subdivided into cutting areas (stands, divisions), in which the composition of the tree stock is rather uniform, especially in terms of age. Silvicultural measures comprise regeneration, tending, and thinning. Thinning is the extraction of some of the young trees in a forest so that the remainder grow and develop fully. The aim is to remove as much timber as possible while maintaining output to maximise the profitability of a site. Thinning has a major influence on the temporal LAI dynamic. At Idarwald, after a maximum LAI value at an age of 20-30 years is reached, stands of Norway spruce are usually thinned at an age of 30-50. After 60-70 years an increase in LAI may take place up to an age of 100 where logging can

Table 3.1: Soil substrates occurring at the Gerolstein test site (from Schwind & Schüler, 2001 and Schwind, personal communication). German denominations appear in brackets. For definition of the term “Soil substrate” refer to text.

Abbreviation	Soil substrate	Underlying geology (epoch)	Typical soil type (FAO classification)	Base saturation
VLdu	Loam formed from quartzite, sandstone and shale (Verwitterungslehme unterdev. Quarzit-Sandstein-Tonschiefer Böden)	Lower Devonian (Unterdevon)	Eutric Cambisole (Skelettreiche Braunerde)	low-medium
wDLT	Wet loam cover above clay loam (Staunasse Decklehme über Tonlehm)	Lower Devonian (Unterdevon)	Planosole-Eutric Cambisole (Pseudogley-Braunerde)	medium
KVLdm	Loam formed from limestone and dolomite (Kalk- und Dolomitverwitterungslehme)	Mid- and Upper Devonian (Mittel- und Oberdevon)	Calcaric Cambisole, Rendzina (Kalkbraunerde, Rendzina)	very high
Ssm	Sands (Sande des Mittleren Buntsandsteins)	Mid-Buntsandstein (Mittlerer Buntsandstein)	Podzol (Podsol)	very low
DLsm	Loam cover above sandstone (Decklehme über Sanden des Mittleren Buntsandsteins)	Mid-Buntsandstein (Mittlerer Buntsandstein)	Podzolic Cambisole (Podsol-Braunerde)	low
BVL	Loam formed from basalt (Basaltverwitterungslehme)	Tertiary-Quaternary (Tertiär-Quartär)	Eutric Cambisole (Braunerde)	high
DLB	Loam cover above basalt (Decklehme über Basalt)	Tertiary-Quaternary (Tertiär-Quartär)	Eutric Cambisole (Braunerde)	high
Kol+	Colluvium (Kolluvium)	Quaternary (Quartär)	Gleysole-Cambisole (Gley-Braunerde)	high

lead to gaps in the canopy cover. Depending on the application of thinning measures, maximum variation of LAI can be expected at age 30-70 (personal communication Wagner, Womelsdorf; cited from Vohland, 1997).

Another method of regeneration is the clear cutting system, which involves clearing an entire area and then replanting it in a uniform and homogeneous fashion. Nowadays, clear cutting measures are restricted by law requiring special permission by the forest authority of the respective federal state if they exceed a certain size. By forest management in cutting areas, the vast majority of the forests in Germany (approximately 97%) have been converted into one-age-cohort plantations. This particular form of management is now considered outdated, but still largely shape the present-day appearance of our forests due to long time-lags (Häusler & Scherer-Lorenzen, 2001).

Soils formed over the quartzite ridges typically show a low buffer capacity as a consequence of the low nutrient availability. As a consequence, soil acidification has become a major problem in the study area during the 80s and early 90s of the last century. At the beginning of the 1990s, measurements in the upper soil layer revealed pH values as low as 3.8, indicating that protons are buffered under release of aluminium ions out of clay minerals (Block et al., 1991). Free Al^{3+} -ions cause damage to plants' fine roots and the mykorrhizha. High soil acidity may initiate additional processes: i) release of heavy metal ions, further increasing aluminium toxicity; ii) wash out of cation bases, such as Ca^{2+} , Mg^{2+} , K^+ and Na^+ resulting in a low cation exchange capacity. From the latter process, a limitation of the plant nutrient supply can be expected (Block, 1993).

Nutrient concentrations from chemical analyses of foliage samples can give evidence towards restricted nutrient supply. Insufficient supply with magnesium (Mg), indicated by yellowing of leaves or needles as a consequence of chlorophyll decomposition has been observed particularly at the mountain ridges of the Idarwald during the 1980s. From 1990 onwards, intensive fertilization measures (3-6 tons of dolomite per hectare) have been carried out at several forest stands in order to increase their Mg-supply and neutralize acids present in the

Table 3.2: Soil chemical indicators for three typical soil profiles occurring at the Gerolstein test site. CEC_{eff} : effective cation exchange capacity. BS: Base saturation. N: concentration of Nitrogen in the soil. C/N: carbon-to-nitrogen ratio (from Schwind & Schüler, 2001).

Soil substrate	Soil profile	CEC_{eff} [mmol kg ⁻¹]	BS [%]	N [mg kg ⁻¹]	C/N of Ah
Vldu	Ah-Bv-Cv	138-52-39	27-5-4	4310-700-380	24
KVLdm	Ah-BvCv- IICv	109-307-482	75-97-98	3480-1300- 650	12
Ssm	Aeh-Bv1- Bv2-Cv	105-83-26-6	8-3-8-27	2320-1230- 200-100	26

soil. As a result, the portion of yellowed trees decreased from 40 percent in 1980 to just 2 percent in 1995 (Ministerium für Umwelt und Forsten Rheinland-Pfalz, 1995). Therefore, yellowing is not anymore considered as a major problem at Idarwald.

Due to the limited spatial variability in soil nutrient availability as a consequence of the relatively uniform substrate characteristics at the Idarwald test site, spatial variability is also low in leaf chemical concentrations. However, remote sensing of foliar biochemistry requires a location where forest grows on both rich and poor sites. Therefore, another test site was established which is characterised by a great small-scale variability in lithology.

3.1.2 Gerolstein

The Gerolstein test site (50°15'N, 6°40'E) is located in the central part of the Eifel mountain. The mean annual precipitation is about 800-900 mm; the mean annual air temperature is 7°C.

The manifold soil types are a product of the extreme diversity of bedrock types that occur in the area. Geologically the area is underlain by lower Devonian quartzite-sandstone-schist formations; middle Devonian limestones (calcite and dolomite), Triassic sandstones, as well as Tertiary and Quaternary basalts. In parts of the area the underlying bedrock was mixed with Pleistocene loess cover or periglacial layers. Small river valleys are covered by colluvial material that has been washed off the slopes and deposited at the foot slopes during the Holocene (Schwind & Schüler, 2001). To classify the complexity of the soil types, the concept of “soil substrates” is used in Germany by the Federal Research Centre for Forestry and Forest Products. The term “soil substrate” (german: Bodensubstrat) describes in a combined manner the grain-size distribution of the soil material, the type of bedrock and the stratification. Eight different soil substrates were identified at the study site (Table 3.1). Despite the extreme range in nutrient availability (Table 3.2), stands of Norway spruce forest are found on all eight substrate types.

3.2 Field and laboratory data

3.2.1 Field data

One way to determine certain characteristics of an entire forest is to measure every single tree in it. For practical reasons, measurements made of some individual trees in the forest are scaled up to estimate what is available from the whole forest. This process of ‘scaling up’ involves two steps. Firstly, measurements of individual trees are made in stands. A stand refers to a more or less homogenous group of trees in a forest. Stand measurements are usually performed on a per unit ground area basis, for instance the number of stems per hectare. Stand measurements can also be recorded as an average for the stand, for example,

the average of tree stem diameters. The second step in scaling up means that many stands scattered throughout the forest are measured to estimate the total amount or the distribution of an attribute across the entire forest (West, 2004).

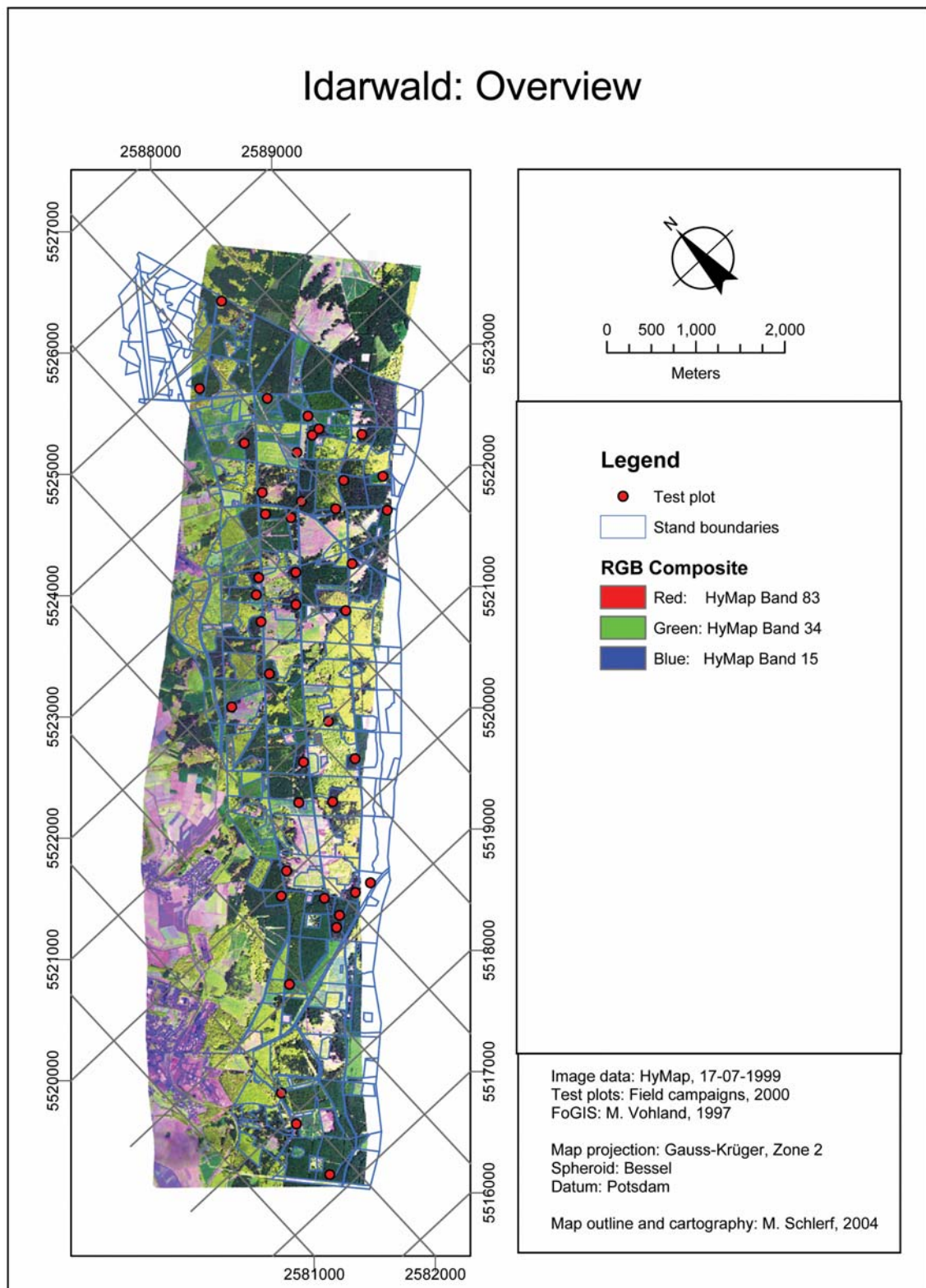


Figure 3.2: General map of Idarwald test site with stand boundaries and locations of test plots.

Idarwald test site

In 2000, 42 relatively homogenous Norway spruce stands were identified at the Idarwald study area (Figure 3.2). Dolomite had been added to 25 of the stands between 1986 and 1995. Within each stand, a square 0.09 ha plot was established. The central location of each ground plot was determined with an accuracy of about ± 5 m using a differential global positioning system (GPS). Signal distortion within the forest stands did not give as high accuracies as specified by the manufacturer. From a total of 42 stands, one was not covered by the HyMap imagery, and another one was thinned in the period between ground data collection and the HyMap overpass. These two stands were excluded from the analysis reducing the dataset to 40 stands.

At each plot, measurements of forest structural attributes were carried out. Attributes that have been measured include leaf area index (LAI), stem density (SD), canopy cover (CO), perimeter-at-breast-height (PBH), stand height (H) and crown diameter (CD). LAI was estimated using a Li-Cor LAI-2000 Plant Canopy Analyser. The LAI-2000 estimates effective LAI using measurements of diffuse solar radiation above and below the forest canopy. Several factors such as sky conditions, topography, foliage clumping, woody materials, and plant phenology all affect LAI estimates (Fournier et al., 2003). The LAI-2000 was only operated under overcast sky conditions during 10-16 hours daytime. A 270-degree view restrictor was used on the sensor. Within each plot, below canopy measurements were taken at 10 regularly spaced points from which the average was calculated. As no second device was available to operate the LAI-2000 in a two-sensor mode, above the canopy measurements were taken in a nearby open field before entering the plots. It was carefully paid attention to stable sky conditions between the open field and plot measurements. None of the outer rings were eliminated in the gap-fraction inversion. Despite the non-random distribution of leaves, no corrections for shoot level clumping and stand level clumping were applied. Also no contributions of woody surfaces were subtracted as the influence of woody components on the measurements is difficult to assess. It was assumed that the underestimation of LAI due to clumping effects was somehow compensated by the overestimation of LAI through woody structures (Fournier et al., 2003). As no corrections were applied, the retrieved LAI-2000 measurements represent an effective plant area index instead of the real leaf area index (see section 3.2.1). In the following sections these measurements are named effective leaf area index and abbreviated as LAI. Stem density (SD) or stocking density, the number of tree stems per unit area, was obtained by counting the number of trees in a plot and dividing the number by the plot area measured in hectare. Canopy cover (CO) or fraction of canopy closure, was

visually estimated in steps of 5 percent. Perimeter-at-breast-height (PBH) is defined as the trunk perimeter at 1.3 m above the forest floor. It is equivalent to diameter-at-breast height

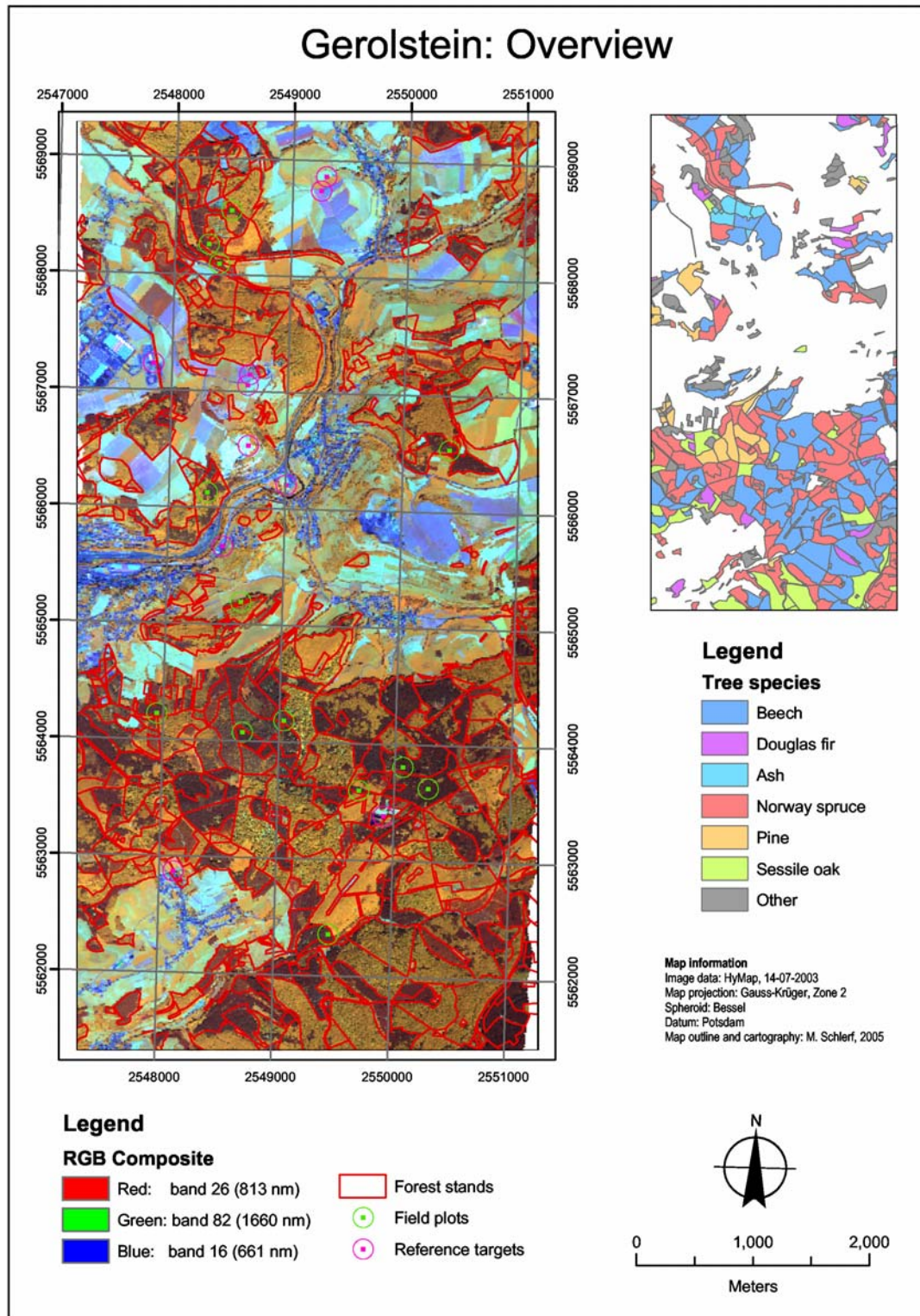


Figure 3.3: General map of Gerolstein test site with stand boundaries, locations of field plots and locations of targets used for radiometric calibration.

(DBH) which is often used instead. PBH was measured for 10 randomly selected trees within each plot and the stand average was calculated. Stand height (H) was calculated from the mean height of three dominant trees that were randomly selected within each plot. The height of each tree (from the ground to the top) was determined from angular measurements. As forest stands at Idarwald consist of trees of the same age, dominant trees within a stand have similar heights. Hence, the selection of three trees to represent H was considered to be appropriate. Crown diameter (CD) was determined as the mean of maximum and minimum crown diameters. From five representative trees per plot the average was calculated. CD was only measured in forest stands older than sixty years ($n = 28$).

Assuming that the volume of a single stem can be approximated by a cone, a new variable stem biomass (SBM, unit: $t \text{ ha}^{-1}$) was calculated from PBH, H, and SD:

$$SBM = \frac{\pi \cdot \left(\frac{PBH}{2 \cdot \pi}\right)^2 \cdot H}{3} \cdot SD \cdot \delta_{WOOD} \quad 3.1$$

where δ_{WOOD} is the density of fresh wood (for Norway spruce: 0.47 g/cm^3 at 12-15% moisture content; Sedlmayer, 2004).



Figure 3.4: Woodman climbing a tree at Idarwald test site (March, 2000).

Gerolstein test site

In August 2003, 13 relatively homogenous Norway spruce stands were identified at the Gerolstein test site (Figure 3.3). Three trees were randomly selected within each stand. Skilled woodsmen climbed the trunks up to the treetop and cut off three branches from the outer part of each crown (Figure 3.4). Foliage from the sampled branches was removed separately by age class (1st and 3rd year) according to their position on the branch, bagged, labelled and placed in cold boxes in the field. As freezing and thawing are known to change the spectral properties of leaves and needles, the foliage samples were stored in refrigerators at +5°C after the transport to the geosciences laboratory of the University of Trier. In total, 78 samples were obtained (13 stands x 3 trees x 2 age classes). From these samples sub-samples were randomly selected and subjected to standard wet chemical analysis to obtain measures of the concentration of chlorophyll a and b, water, nitrogen, and other chemical elements (section 3.2.2). Additional sub-samples were randomly selected for reflectance measurements (section 3.2.3). To validate predictive models developed on the data obtained at Gerolstein (section 7.4.4) foliar samples from Idarwald were used. At Idarwald test site samples had been collected during March 2000 in a same fashion as previously described for the Gerolstein area. In total, 30 samples were obtained (5 stands x 3 trees x 2 age classes). Chemical and spectrometric measurements and pre-processing steps were identical for both sets of data.

3.2.2 Chemical laboratory analysis

To determine leaf water concentration (C_W), approximately 5 g of fresh sample were weighted, dried in an oven at 105 °C to constant weight (24 hrs), and were then re-weighted. Leaf water concentration was calculated as (fresh weight [g] – dry weight [g]) / dry weight [g] x 100.

Chlorophyll concentration (C_{AB}) of the foliage was determined as described by Lichtenthaler (1987). Approximately 0.5 g of fresh sample were weighted and ground by hand in acetone with aid of quartz sand until no green colour was left in the residual material. After the chlorophyll solution was decanted off the residue, filled up to a volume of 50 ml with acetone, centrifuged for 30 minutes, it was measured in a laboratory spectrophotometer. Chlorophyll a was measured at its absorption maximum of 663 nm and chlorophyll b at 646 nm. Concentration of chlorophyll a+b (C_{AB}) was converted from unit “grams per litre” to “milligrams per gram of dry weight”: $C_{AB} [\text{mg g}^{-1}] = C_{AB} [\text{g l}^{-1}] \times \text{volume [l]} \times 1000 / \text{dry sample weight [g]}$. The extraction of chlorophyll was carried out under cool and totally dark conditions as leaf pigments tend to decompose when exposed to light.

Total nitrogen concentration (C_N) of the foliage was determined through CHN elementary analysis (Wilson, 1990). The samples are broken down into its atomic components and are then separated. To break the sample down it is combusted in an oxygen atmosphere at 980°C. At this temperature all of the elements to be detected react with oxygen to form CO_2 , H_2O , and N_xO_y . The gas is then led over copper granulate material where the nitrogen oxides are reduced to N_2 . Next, the gases are carried via a He-stream to a detector. The detector reports a value to the computer which compares it to the known value of a standard. These values are calculated based on the sample weight. Results are reported in percent element by weight.

3.2.3 Spectral reflectance measurements

The directional-hemispherical spectral reflectance and transmittance of plant leaves are typically measured by laboratory spectroradiometers equipped with an integrating sphere to average the signal reflected or transmitted in all directions. Problems typically occur with needles as their size is generally shorter than the diameter of the sample port of integrating spheres. As a consequence, alternative techniques consist of measuring the reflectance of a mat of needles arranged side-by-side into a single layer or measuring the reflectance of an infinite number of needles, e.g. a layer stack (Despan & Jacquemoud, 2004).

Reflectance spectra were measured using a Field-Spec-II spectroradiometer under laboratory conditions. The target was illuminated by a 1000 W halogen light source at a zenith angle of 45° and a distance of approximately 60 cm. The optical head of the Field-Spec-II was positioned at nadir (0° viewing angle) at a distance of 10 cm above the target. It was made sure that the instrument's field of view lay well within the target's perimeter. The target consisted of needles arranged in an optical dense layer of about 1 cm thickness over a matt black background. Relative spectral radiances between 350 and 2500 nm were recorded at

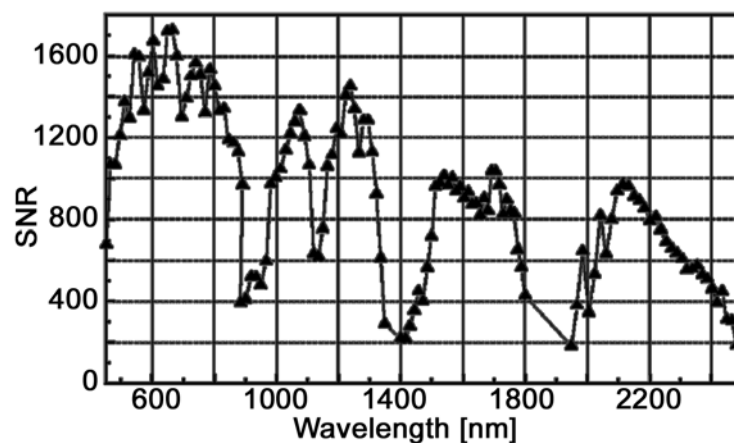


Figure 3.5: Signal-to-noise ratio measured while viewing a 50% reflectance target at a solar zenith angle of 30 degrees; the pixel integration time was equivalent to operation at 14 lines per second (from Cocks et al., 1998).

Table 3.3: Spectral configuration of the HyMap sensor (from Cocks et al., 1998)

Module	Spectral range	Bandwidth across module	Average spectral sampling interval
Visible	0.45–0.89 μm	15–16 nm	15 nm
near-IR	0.89–1.35 μm	15–16 nm	15 nm
SWIR1	1.40–1.80 μm	15–16 nm	13 nm
SWIR2	1.95–2.48 μm	18–20 nm	17 nm

1 nm steps in 2151 spectral wavebands. Each sample measurement comprised 50 single measurements of the target and was repeated four times thereby rotating the target to average out any possible directional effects. The reference panel (Spectralon) was measured before and after the target measurements. The absolute spectral reflectance (ρ_{target}) for each waveband was calculated from the radiance counts of measurements of the target ($\text{DN}_{\text{target}}$) and the reference ($\text{DN}_{\text{reference}}$) and the reflectance of the reference ($\rho_{\text{reference}}$) as $\rho_{\text{target}} = \text{DN}_{\text{target}} / \text{DN}_{\text{reference}} * \rho_{\text{reference}}$. The 5 spectra recorded for each sample were averaged to produce a single spectrum. The resulting spectra were smoothed using a 31 nm wide moving Savitzky-Golay filter to reduce instrument noise.

3.3 HyMap image data

The estimation of quantitative forest properties from remote sensing data requires acquisition and preprocessing of image data. This section outlines the design and operation of the Hyperspectral Mapper (HyMap) and describes the radiometric and geometric correction that has been applied to the HyMap data.

3.3.1 The HyMap sensor

HyMap was designed and built by Integrated Spectronics, Australia, and operated by HyVista. It has become operational for scientific and commercial tasks in 1998. The spatial configuration is as follows: The instrument collects data in across-track direction by mechanical scanning and in along-track direction by movement of the airborne platform. Its instantaneous field of view (IFOV) is 2.5 mrad along-track and 2.0 mrad across-track and the field of view (FOV) is 60 degrees (512 pixels). Typically, the sensor is flown aboard a light, twin engined aircraft at altitudes of 2000-5000 m above ground level. The swath width at these altitudes is 2.3 to 4.6 km and the ground resolution 5 to 10 m (along-track) (Cocks et al, 1998).

The spectral configuration of HyMap provides contiguous sampling across the spectral range of 0.45–2.48 μm except for gaps in the strong atmospheric water absorption bands near 1.4 μm and 1.9 μm . Additionally, it collects broadband information in the thermal infrared domain. A complete spectrum over the range of 0.45–2.48 μm is recorded in a sampling interval of 13–17 nm by 4 spectrographic modules (Table 3.3). The visible module includes a silicon (Si) detector array operated at ambient temperatures and the near-IR, SWIR1, and SWIR2 modules incorporate indium-antimony (InSb) arrays cooled by liquid nitrogen. Each spectrographic module provides 32 spectral channels giving a total of 128 spectral measurements for each image pixel (Cocks et al, 1998).

Airborne imaging spectrometers have to cope with a relatively weak illumination source (the sun) compared to laboratory illumination sources, sensor-to-object distances of several kilometres, and very short dwell times. Together, these factors suggest that imaging spectrometers generally have a low signal-to-noise ratio (SNR) (Curran & Dungan, cited from Kupiec, 1994). To meet the requirements for the detection of subtle variations in the spectral properties of image objects, sensor technology has been driven to achieve higher SNRs. Ground measurements by Cocks et al. (1998) have shown that in the spectral regions of the atmospheric windows, the HyMap sensor achieves SNRs approaching 1000:1 or better (Figure 3.5). These ground based measurements of SNR are a very good indicator of the sensor's in-flight performance.

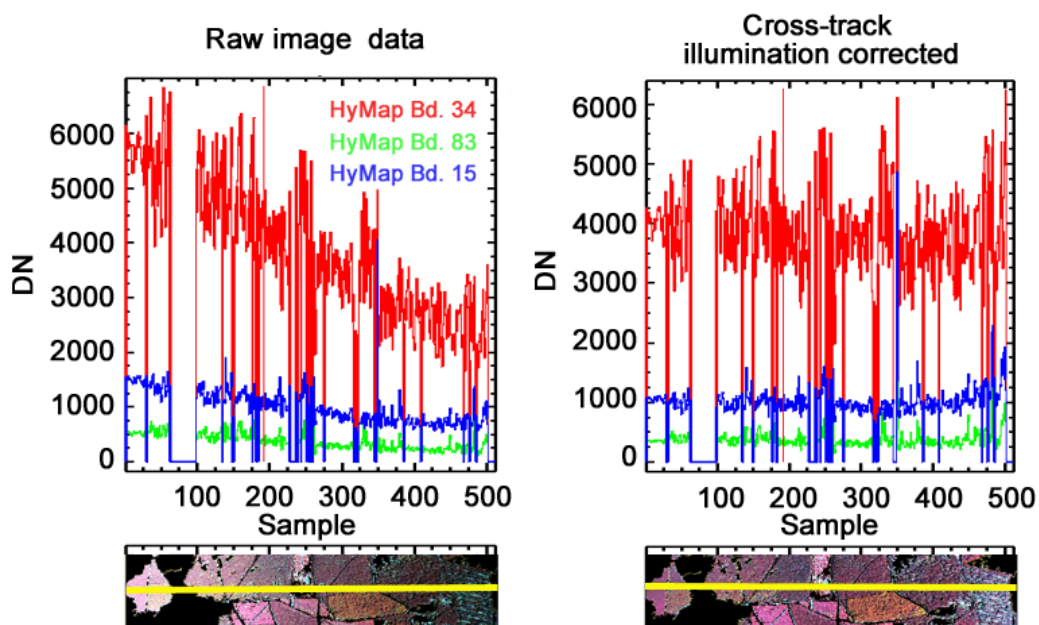


Figure 3.6: Raw (left) and cross-track illumination corrected (right) HyMap image profiles (upper part) and corresponding portions of the HyMap scene (lower part) at Idarwald. The yellow lines in the images indicate the course of the profiles. Profiles are shown for the red (Bd. 15), near-IR (Bd. 34), and mid-IR (Bd. 83) domains. Images are displayed at band combination 34-83-15 (RGB).

3.3.2 The HyMap data sets

HyMap was flown over Idarwald test site at 17th July 1999. The data were recorded at 13:00 hrs CET at an average flying height of 1980 m above ground level. The resulting ground resolution was about 5 m with a full scene covering approximately 3 km x 10 km. The flight line was run in a NE–SW direction parallel to the mountain ridge. The acquired single scene was free of cloud cover. A number of 14 HyMap spectral channels with high noise were identified as bad bands and removed from the dataset. After removing these channels, a total of 114 wavebands remained out of the original 128. All subsequent data analyses were carried out on the 114-band dataset.

HyMap was flown over Gerolstein test site at 14th July 2003. The data were recorded at 12:40 hrs CET at an average flying height of 3400 m above ground level. The resulting ground resolution was about 7 m with a full scene covering about 4 km x 13 km. The flight line was run in almost N-S direction. The acquired scene was free of cloud cover. A number of 16 HyMap spectral channels with high noise were identified as bad bands and removed from the dataset. After removing these channels, a total of 110 wavebands remained out of the original 126. All subsequent data analyses were carried out on the 110-band dataset.

3.3.3 Radiometric correction

Radiometric correction of image data is exceptionally important to remote sensing of coniferous forests, as the small reflectance signal generated by conifer canopies is strongly influenced by terrain and atmospheric effects (Peterson & Running, 1989). When quantitative attributes are to be estimated from remote sensing data, surface reflectance is the preferred or

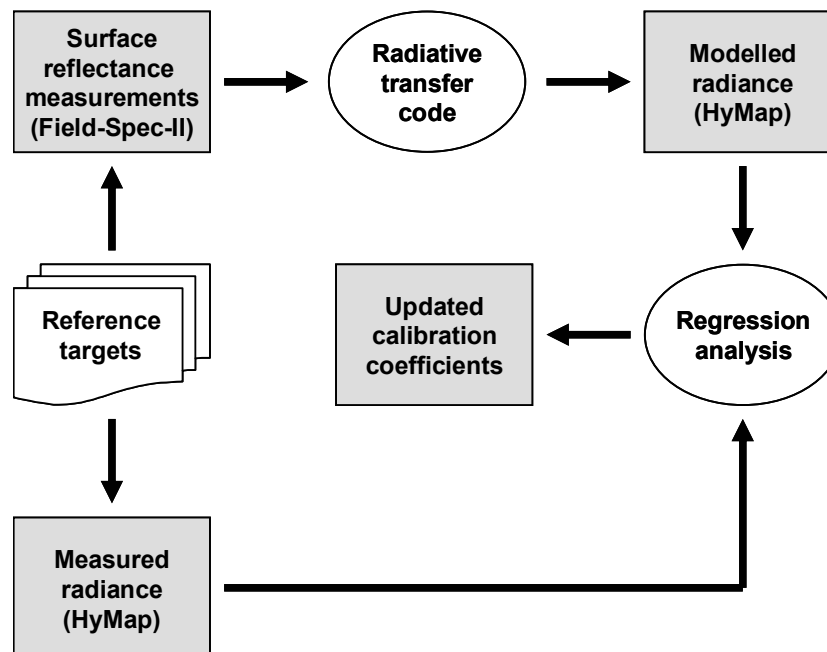


Figure 3.7: Schematic representation of the sensor recalibration.

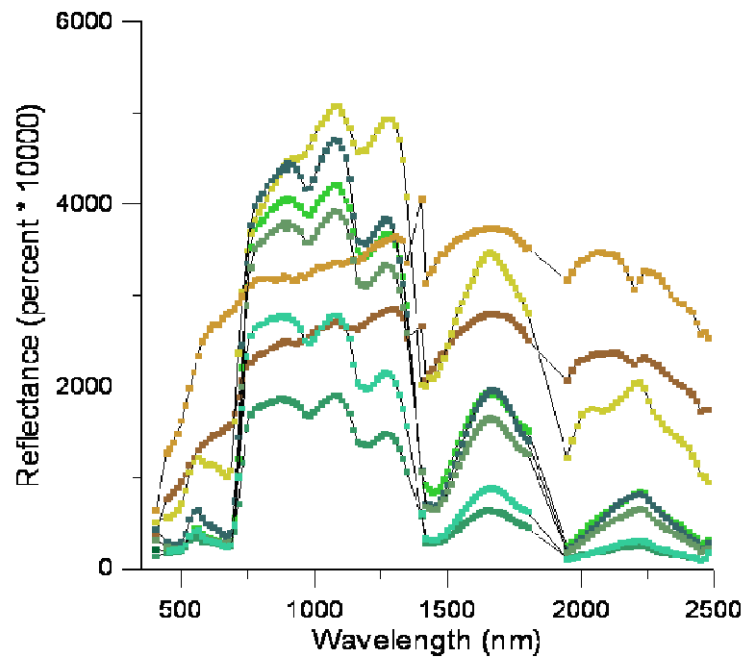


Figure 3.8: Atmospherically corrected HyMap reflectance spectra from various forested and non-forested areas at Idarwald study site (from Hill, 2002).

required data type (Peddle et al., 2003). Radiometric correction of the HyMap data set acquired over both test sites consisted of i) an across-track illumination correction and ii) additional radiometric correction involving atmospheric correction, correction for illumination effects caused by topography, and in-flight calibration of the HyMap sensor system. The vicarious calibration of the instrument implies the computation of updated calibration coefficients (illustrated in Figure 3.7). From reflectance measurements collected at several reference targets on the ground, at-sensor radiance is modelled using a radiative transfer code. Modelled radiance is then related to measured image radiance through a linear regression to obtain a set of updated in-flight calibration coefficients.

Atmospheric correction of the HyMap data sets was achieved with an in-house developed software package (AtCPro 3.01) which is originally based on the formulation of radiative transfer in 5S and 6S (e.g., Tanré et al., 1990) (section 2.1.2). This code has been modified to account for atmospheric extinction processes as a function of sensor and terrain altitude (Hill & Sturm, 1991). It has been further extended for the ability to estimate the aerosol optical thickness directly from dark objects in the satellite image (Hill, 1993). A topographic correction module has been integrated where targets are assumed to have Lambertian reflectance characteristics (Hill et al., 1995). Recently, the method has been extended to cope with specific requirements of airborne hyperspectral image data by adding a module that produces spatially distributed maps of atmospheric water vapour to be included into the atmospheric correction (Hill & Mehl, 2003).

HyMap at Idarwald test site

Across-track illumination correction was applied to correct for the effects of change in sensor view angle that typically affect sensors with a large total field of view (Kennedy et al., 1997). To determine the magnitude of these effects, values of digital numbers (DN) representing conifer forest were plotted against image pixel number in the across scan direction. A systematic increase in values of DNs with view angle in the down-Sun viewing direction and a decrease in the opposite-Sun viewing direction was observed (Figure 3.6). This well known trend can be attributed to the effect of anisotropy and canopy shadow. As most vegetation canopies show a backward scattering characteristic the opposite-Sun side of the scanned image receives less reflected energy than the down-Sun side (Hildebrandt, 1996; section 2.2.4). To correct this view angle effect an across track illumination correction was applied to each spectral band independently (ENVI 3.4, Research Systems). For this purpose, a second-order polynomial was fitted to the data. Based on the fitted polynomials, a normalization procedure was applied.

The atmospheric correction of the HyMap data set used additional field data collected for a specific calibration flight performed during the same day in a different area only 30 km away from the Idarwald study site. There, measurements of atmospheric beam transmittance were conducted with a CIMEL photometer during the time of both flights. Their evaluation yielded an aerosol optical depth of $\tau_a = 0.33$ at $\lambda = 0.55 \mu\text{m}$ representing a horizontal visibility of approximately 15 km. Contemporarily, bi-directional reflectances of several reference targets with different surface characteristics (gravel, asphalt, grass and water) were measured at the ground with an ASD Field-Spec-II instrument. From these ground measurements, together with the derived aerosol optical depth and a water vapour concentration of 3.8 g cm^{-2} that was obtained from an iterative approximation based on several MODTRAN runs, the at-sensor radiance was modelled. Modelled radiance and measured digital numbers from the image were then related through a linear regression to obtain a set of updated HyMap in-flight calibration coefficients. It turned out that, except for single noisy bands with limited radiometric performance, the resulting adjustments remained within $\pm 15 \%$ of the HyMap pre-flight calibration values. Using these updated calibration coefficients together with estimates of the water vapour concentration it was possible to reconstruct a spatially differentiated water vapour map for the HyMap scene of Idarwald. Water vapour concentration for each image pixel was estimated from the depth of the water absorption features at $0.94 \mu\text{m}$ and $1.14 \mu\text{m}$. In a final run, the water vapour map was integrated into the atmospheric correction processing of this image. This correction also included a correction for terrain induced illumination effects, for which specific DEM-derivates (slope, aspect, and the proportion of the visible hemispherical sky at each pixel) had been transferred to the geometry of the original HyMap image using the parametric image processing software PARGE developed by Schläpfer et al.(1998). The obtained reflectance spectra (Figure 3.8) point

towards a good data quality and indicate that a sound foundation has been laid for subsequent quantitative data exploration using empirical or physical based methods (Hill, 2002).

HyMap at Gerolstein test site

The radiometric correction procedure of HyMap imagery acquired over Gerolstein test site was similar to the procedure applied to the Idarwald image that was described in the previous section. Just a few aspects are mentioned where the procedure differs from the one applied to the Idarwald image.

To correct for across track illumination effects, a first order polynomial was fitted to the data followed by a normalisation procedure. The aerosol optical depth was derived from estimates of the horizontal visibility that was provided by three meteorological stations located in the region (mean horizontal visibility: 35 km). At the day of the overflight, several reference targets were measured at the ground with an ASD Field-Spec-II spectroradiometer. The targets covered a wide range of surface characteristics and included short grass (football ground), long grass (pasture), cereals (grain field), asphalt (parking lot), calcareous material (mining dump) and water (pond). From these ground measurements, together with the derived aerosol optical depth and the iteratively derived water vapour concentration the at-sensor radiance was modelled. Modelled radiance and measured digital numbers from the image were then related through a linear regression (Figure 3.9) to obtain a set of updated HyMap in-flight calibration coefficients. The relations between measured and modelled radiances lie close to the 1:1 lines and have values of r^2 between 0.91 and 0.98 with best relations in visible and near-IR wavebands. The resulting adjustments remained within $\pm 10\%$ of the HyMap pre-flight calibration values except for single noisy bands. The obtained reflectance spectra exhibited an excellent data quality which is an important pre-requisite for mapping of foliar chemicals.

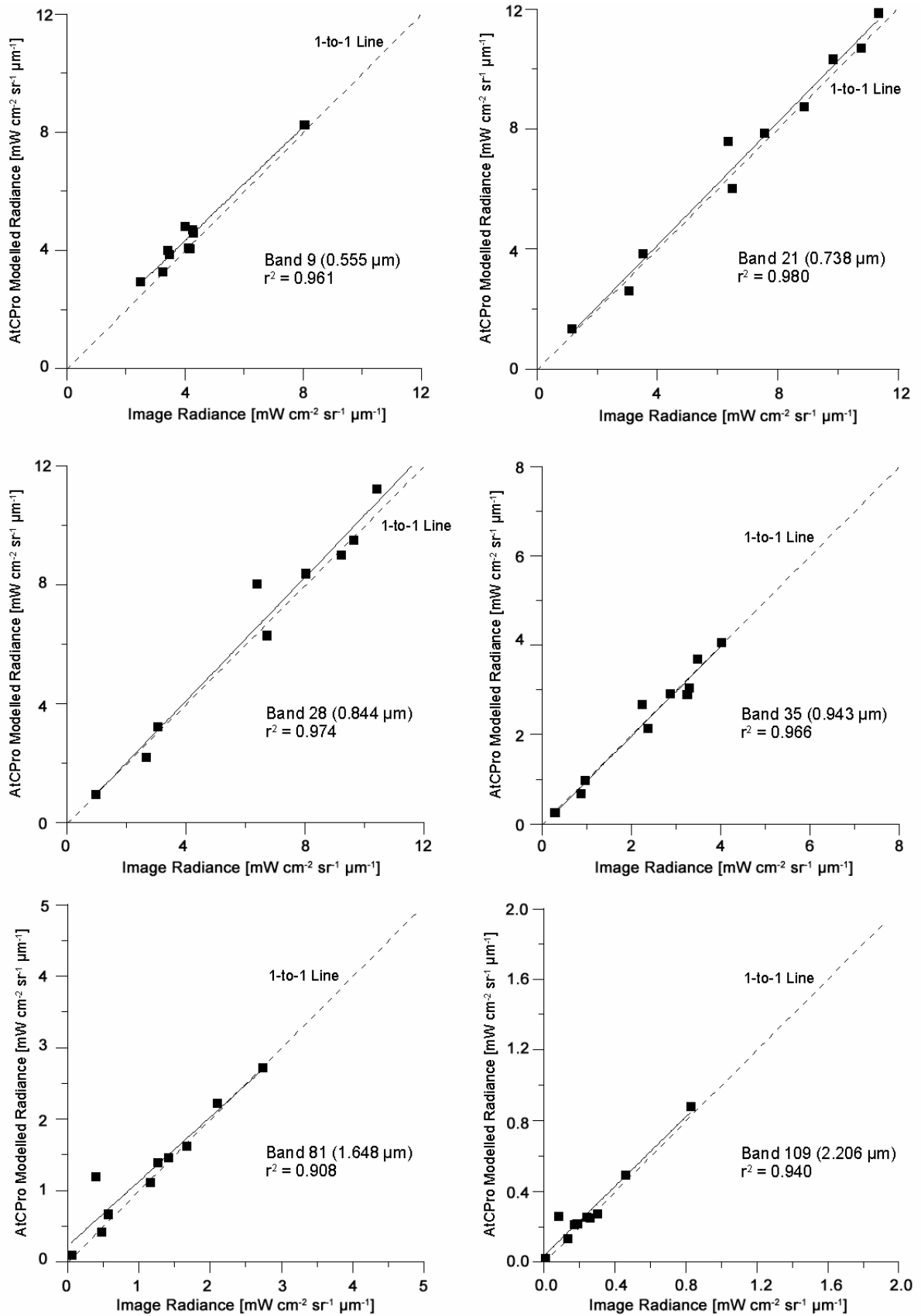


Figure 3.9: Modelled against measured radiance in six wavebands based on ten reference targets at Gerolstein test site.

3.3.4 Geometric correction

The image data were geometrically corrected to the local coordinate system (Gauss Krüger, Zone 2, Ellipsoid: Bessel 1841, Datum: Potsdam) using the parametric geocoding software PARGE (Schläpfer et al., 1998). For this purpose, the required DEM with an original pixel size of 20 m was resampled to the image pixel size (Idarwald: 5 m; Gerolstein: 7 m) using bilinear interpolation. In the case of the Idarwald image, 30 ground control points (GCPs) measured in the field by differential GPS were used to calibrate the in-flight auxiliary data. For the Gerolstein image, 53 GCPs were obtained from an orthophoto mosaic. Image resampling was performed using triangulation coding from centre pixels (Schläpfer et al., 1998). The root mean squared error of the geometric correction was 4.3 m in x-direction and 4.8 m in y-direction (Idarwald image) and 4.9 m in x-direction and 5.6 m in y-direction (Gerolstein image). With an image pixels size of 5 m and 7 m, respectively, the geometric correction of both data sets was accurate to within a pixel.

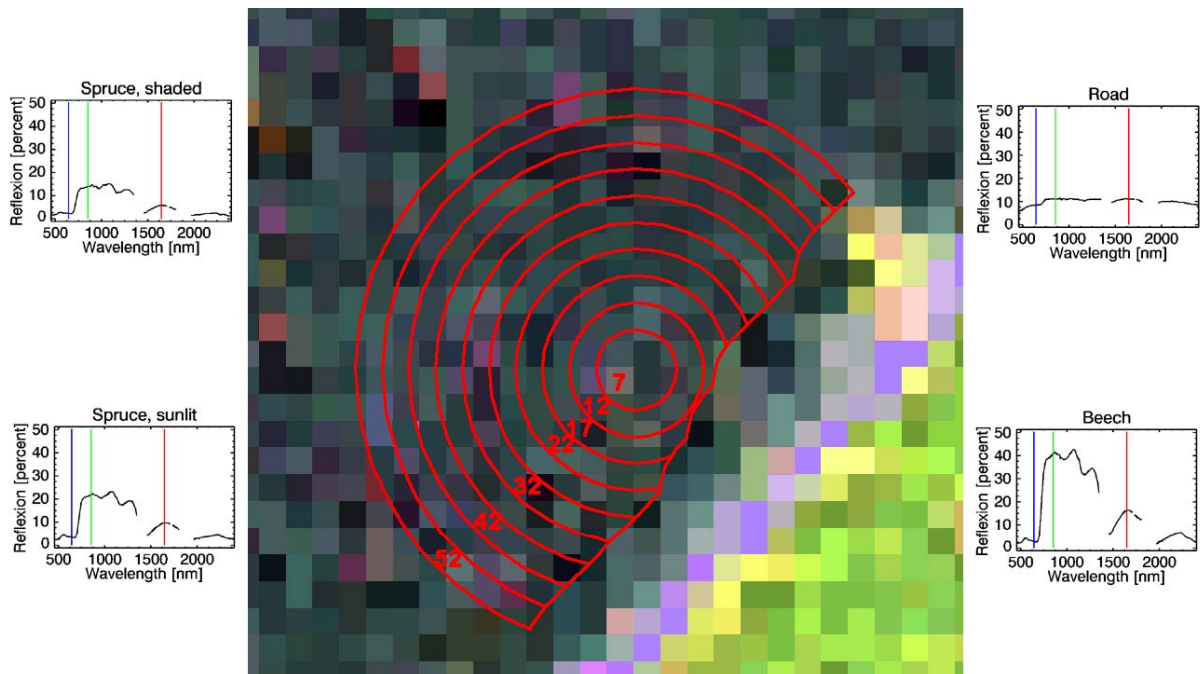


Figure 3.10: Extraction of spectra for various radii. Circle segments were obtained through buffering around the GPS-measured central plot position and subsequent masking using the conifer forest mask. Image pixels representing shaded spruce crown appear in a very dark green tone, sunlit spruce crowns appear in dark green, beech in bright green and road in purple tones.

3.3.5 Extraction of reflectance spectra from HyMap imagery

Idarwald image

Reflectance spectra have been extracted from the image data for all 40 forest stands under investigation. To collect representative image spectra in each plot, average reflectance spectra were computed from image pixels within certain radii around the central plot position. Average spectra were derived from radii of 7 m, 12 m, 17 m, 22 m, 32 m, 42 m, and 52 m. Pixels not representing spruce forest were cut out from the circles through a GIS operation resulting in circle segments (Figure 3.10). Mean and standard deviation of spectral reflectance were extracted. Mean reflectance was plotted against wavelengths for a typical forest stand for the near-IR wavelength region (Figure 3.11A) and the visible wavelength region (Figure 3.11B). It is evident that a critical value of reflectance is reached with increasing radius and stabilisation occurs. The plateau where reflectance remains constant lasts from a radius of 32 m until 52 m in both the visible and the near-infrared wavelength region. Therefore, the central position of the plateau at a radius of 42 m was considered to be the critical size from where local heterogeneity is not further increasing. The other forest stands essentially show similar patterns. Sometimes, values of reflectance plateau already at a smaller radius, but

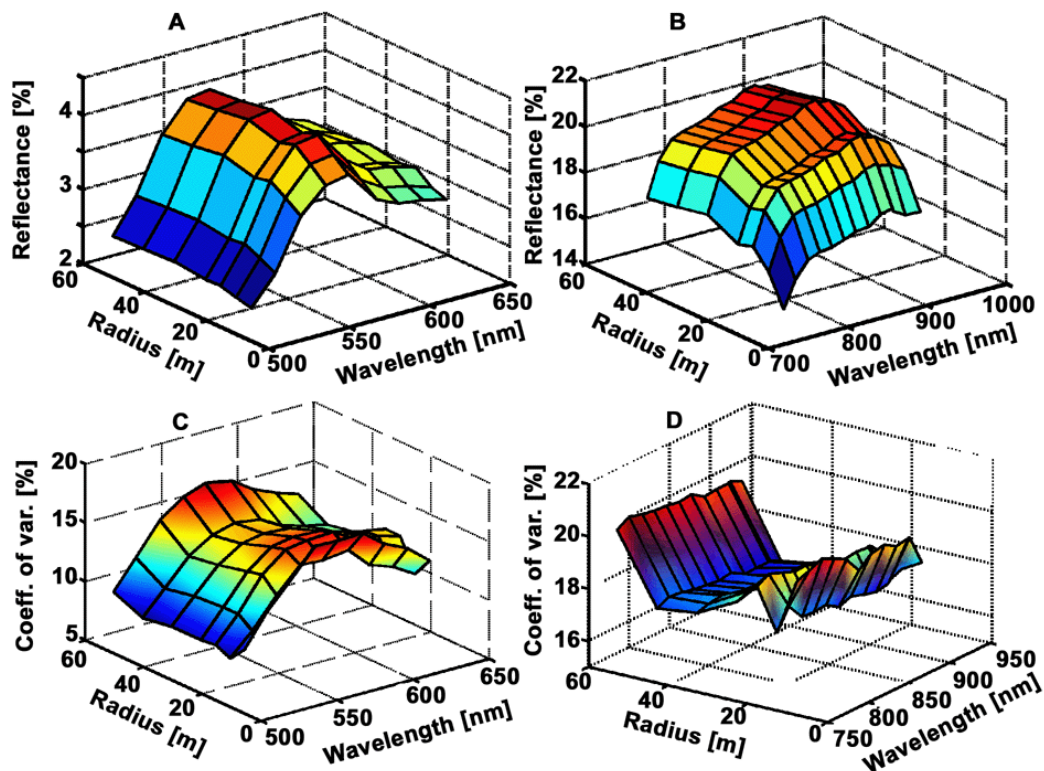


Figure 3.11: (A) Change of reflectance with increasing circle radius across the visible region (HyMap-bands 4-12) and (B) the near-infrared region (HyMap-bands 20-32). (C) Change of the coefficient of variation with increasing circle radius across the visible region (HyMap-bands 4-12) and (D) the near-infrared region (HyMap-bands 20-32).

never a decrease in reflectance with increasing circle size is observed. A sharp decrease of reflectance in the near-IR region would indicate that the boundary of the stand is crossed, incorporating gaps in the forest cover. A sharp increase of reflectance in the near-IR region would indicate incorporation of broad-leaf forest which shows a considerably higher reflectance at the near-IR plateau (Figure 3.10).

In a similar fashion, the coefficient of variation (standard deviation of spectral reflectance divided by the mean spectral reflectance) was plotted against wavelength for the visible (Figure 3.11C) and the near-infrared (Figure 3.11D) region. As can be seen, the lowest variation occurs at radii of 42 m for both wavelengths regions.

Gerolstein image

As many of the investigated forest stands at Gerolstein test site were relatively small in relation to the image pixel size, a systematic investigation of the number of extracted pixels was not feasible. Instead, reflectance spectra were extracted from the image using the region growing tool under the image processing software ENVI (version 4.0). At each field plot in the image, four pixels were defined as a “region of interest” (ROI). Growing of ROIs was done in 4 directions (neighbours) with a standard deviation multiplier of 1 resulting in ROIs of 8 to 31 image pixels. From the selected image pixels mean reflectance spectra were computed and used for further analysis.

3.4 Forest Geographic Information System

A Forest Geographic Information System (FoGIS) was available for Idarwald test site. It contained the current forest inventory information (cutoff date: 01.10.1994) as had been made available by the regional forest authority (Forstdirektion Koblenz). The forest inventory data listed for each forest type present in a particular forest stand information about tree species, age, form of mixing, productivity, etc. This information was aggregated into a stand average in order to link attribute data to geographic data (stand polygons) by a 1:1 relation (Vohland, 1997). With the help of FoGIS it was possible to find suitable training and validation areas for image classification (Chapter 5) and to identify useful plots for field data sampling (section 3.2.1).

Chapter 4 Statistical and physical methods

4.1 Overview

Generally, it can be distinguished between empirical-statistical and analytical techniques for the derivation of leaf and canopy properties from reflectance data. The following main approaches exist for the utilization of remotely sensed spectral information to identify and characterize plant canopies (Ustin et al., 1999; Baret & Jacquemoud, 1994):

- Data analysis to determine the spatial extent of cover types based on their spectral response. Mapping of cover types is typically achieved through image classification. In classification, a statistically based decision rule is applied to categorize all pixels in an image to one of several cover classes (Lillesand & Kiefer, 2000). Image classification techniques (section 4.2) were used to map tree species and age classes.
- Empirical models that relate the spectral measurement through regression analysis to the variable of interest. Regression techniques comprise bivariate regression, multiple stepwise regression, partial least squares regression, and others. The spectral measurement is often manipulated in such a way, that it can be related to a given canopy property (Verstraete & Pinty, 1996). These so-called vegetation indices (VIs) include band ratios, spectral derivatives, spectral shifts, and others. One objective of using VIs is to enhance spectral features while minimizing confounding factors, such as soil optical properties or atmospheric effects (Demetriades-Shah et al., 1990). Empirical techniques are described in section 4.3.
- Analytical models. Radiative transfer models describe the interaction of radiation with leaves and vegetation canopies based on physical principles. Such a leaf or canopy reflectance model relates the spectral information via a complex mathematical function to leaf and canopy variables (Goel, 1988). A good model will simulate a realistic spectral signature from a given set of variables. Once a model is developed, estimates of these variables can be retrieved from reflectance spectra through inversion (Goel, 1989). One of the main problems with model inversion is the so-called ill-posed problem. It states that a given reflectance signal could be generated by more than one set of combinations of variable values, because different variables may affect the canopy reflectance in the same way. Consequently, a unique set of parameter

combination would not exist (Combal et al., 2000). Physically-based techniques are described in section 4.4.

- Spectral mixture analysis can be considered a simple reflectance model. In spectral mixture analysis, the reflectance spectrum of a given target is considered as composed of a small number of elementary objects called end-members. The (linear) combination of single end-member spectra is determined that describes best the observed spectrum. It provides an estimate of the relative coverage of the elementary surface types (e.g., vegetation) in the observed pixels. However, this approach assumes that radiative transfer processes involved are additive which is not valid for dense vegetation canopies (Smith et al., 1994). Therefore, spectral mixture analysis was not used in this research work.

The structural and chemical properties of a vegetation canopy control its spectral signature (section 2.2) and can in general be derived from remote sensing (section 2.3). The reflectance (ρ_λ) of a vegetation canopy at wavelength λ is determined by the vegetation parameters (V) plus more or less variable side conditions (S):

$$\rho_\lambda = f(V_1, \dots, V_n, S) \quad 4.1$$

To find the function f that relates the parameters of interest to the recorded signal is the fundamental goal in quantitative remote sensing (Verstraete et al., 1996). However, the side conditions comprise a number of variables that describe the atmosphere, illumination and viewing geometry, environmental conditions, etc. that are very difficult to measure. Therefore, finding f is not trivial. It is the overall objective of this research to compare different methods that can find transfer functions that relate remote sensing data of certain spectral properties to various forest attributes in order to enable their reliable estimation from operational sensors in the future.

The following sections describe general aspects of the methodology that were used in this research work. Information on how the methods were implemented in detail are given in Chapter 5, Chapter 6 and Chapter 7 as processing strategies and results are often strongly interrelated.

4.2 Image classification

4.2.1 Introduction

Classification has been an important tool in digital image analysis for land resources applications since early Landsat missions when multispectral image data was regarded as a composition of multivariate measurement vectors for each image pixel. In classification, the

thousands or millions of such vectors that form an image are treated as class descriptors, and the spectral bands as explanatory variables related to these classes. The underlying assumption is that each class exhibits a unique multi- or hyperspectral signature. In the classification process, image pixels with similar signatures are grouped into classes which are pre-defined in supervised classification approaches. The result is a simplified image where pixels are labelled with their appropriate class type (Franklin et al., 2003).

Therefore, classification is the most logical approach for the prediction of the class membership of an image pixel when categorical attributes (e.g. forest type, tree species) are mapped. Yet, classification can also be used to map continuous forest attributes, such as cover, biomass or stand age, when those attributes are divided into ordinal categories (Franklin et al., 2003). For instance, the attribute ‘stand age’ with unit years can be divided into distinct age classes.

4.2.2 Spectral Angle Mapper

A number of classification methods exist that have been used in forest mapping from remote sensing data (Franklin et al., 2003). Most often described in the literature and implemented into imaging processing software packages are Minimum Distance, Box or Parallelepiped and Maximum Likelihood Classifier. These classifiers were all designed to cope with data of multispectral type. Other, more advanced classifiers, include Artificial Neural Networks and Decision Tree Classifiers. The availability of hyperspectral data has led to the development of new classifiers that could better handle large numbers of wavebands. For instance, the Spectral Angle Mapper (SAM) determines the spectral similarity between two spectra by calculating the angle between the spectra, treating them as vectors in a space with dimensionality equal to the number of bands. SAM compares the angle between the spectrum vector of the known class and each pixel vector (unknown class) in n-dimensional space. In the classification stage, the class with the smallest angle is assigned to the corresponding image pixel. Because this method uses only the direction and not the length of the vector, it is insensitive to illumination (Kruse et al, 1993). The angle α between the test spectrum t and the reference spectrum r is calculated as

$$\alpha = \cos^{-1} \left(\frac{\sum_{i=1}^n t_i r_i}{\left(\sum_{i=1}^n t_i^2 \right)^{0.5} \left(\sum_{i=1}^n r_i^2 \right)^{0.5}} \right) \quad 4.2$$

where n is the number of spectral bands.

4.3 Statistical methods

Empirical quantitative analysis in spectroscopy and in other scientific fields is based on the assumption that the amounts or concentrations of the constituents of interest in the samples are in some way related to the spectral measurement of those samples. The aim is to find a calibration equation that can be applied to data of unknown samples in order to predict their amounts of the constituents. Calculation of these equations requires a set of samples that span the expected range of amounts in the unknown samples. Calibration (known) and unknown samples have to be measured under exactly the same conditions using the same measurement technique. The measurements of the calibration samples, together with their amounts or concentrations, form the calibration data set from which the calibration equation (the model) is calculated. The model can then be applied to the unknown samples (validation data set) in order to predict their amounts or concentrations or to test the model's validity (Duckworth, 1998).

4.3.1 Correlation analysis

The *correlation coefficient* (product-moment correlation coefficient or Pearson's correlation coefficient) is a measurement of the strength of a relationship between two variables. It is defined as the covariance of the two variables divided by the product of their standard deviations; hence it may be thought of as a measure of standardised covariance. It is symbolized by r , and it ranges from 1.00 for perfect positive correlation, through zero for uncorrelated variables, to -1.00 for perfect negative correlation. Correlation coefficients may also be calculated for multiple regressions. Then it is an index of how well a dependent variable can be predicted from a linear combination of independent variables. It ranges from 0 (zero multiple correlation) to 1 (perfect multiple correlation) (Colman, 2001). When one variable is being used to predict another, the *coefficient of determination* (R^2) indicates the proportion of variance in one variable that is explained by the other (given certain linear assumptions), or the proportion of variance shared by the two variables: if $r = 0.50$, then $R^2 = 0.25$, indicating that 25 per cent of the variance in one of the variables is explained by the other, or that 25 per cent of the variance is shared by the two variables. It is measure of the goodness of fit of a set of scores to a linear model and can range in value from 0 to 1, with 1 indicating perfect fit (Colman, 2001).

4.3.2 Regression analysis

Bivariate linear regression

Bivariate linear regression (BLR) is the analysis of the relationship between a predictor variable (also called independent variable), such as a vegetation index and a dependent variable, e.g. a forest canopy attribute. The relationship is usually expressed as a linear model in which the value of the dependent variable is equal to a weighted value of the independent variable plus a constant:

$$Y = b_0 + b_1X \quad 4.3$$

When more than one predictor variable is involved, it is called multiple regression.

Multiple linear regression

The spectrum of a sample measured by a spectrometer has many spectral data points that can be used to generate the calibration model. The problem is to find those wavebands that have a relationship to the concentration of the constituents of interest. Mostly multivariate models are used to find the best relation between the independent variables (spectral reflectances or absorbances) and the dependent data (concentrations or contents). A technique called least squares regression is employed to solve for the model equation; it calculates the coefficients of a given equation such that the differences between the known spectral responses and the predicted spectral responses are minimized. The classical least squares model (CLS) calculates reflectance at a single wavelength as an additive function of the constituent concentrations. The main drawback of CLS is that it can be only applied to systems in which the concentration of every constituent in the sample is known. The inverse least squares model (ILS) or multiple linear regression (MLR) assumes that the concentration of a constituent is a function of the reflectances at a series of given wavelengths. The advantage of the MLR is that it can accurately build models for complex mixtures when only some of the constituent concentrations are known; the only requirement is selecting wavelengths that correspond to the reflectances of the desired constituents (Duckworth, 1998).

Multiple linear regression (MLR) is a statistical method for analysing the joint and separate influences of two or more predictor variables on a dependent variable, usually through a linear model. The form of a multiple regression equation for k independent variables is a weighted sum:

$$Y = b_0 + b_1X_1 + b_2X_2 + \dots + b_kX_k \quad 4.4$$

where Y is the estimated value of the dependent variable, b_0 is the Y intercept, X_1 is the value of the first independent variable, X_2 the value of the second independent variable, b_1 the slope associated with X_1 , and b_2 the slope associated with X_2 . The slope is a standardised regression

coefficient indicating the relative importance of the corresponding independent variable in determining the predicted value of the dependent variable (Colman, 2001). In this research and typically in spectroscopy or imaging spectrometry, spectra of a leaf or canopy target recorded at a large number of wavebands serve as the independent variables and are used to predict structural and chemical variables of that target.

Stepwise multiple linear regression

Stepwise multiple linear regression (SMR) is a technique for choosing wavebands to include into a regression model. An important underlying assumption is that only some, but not all wavebands do have an important explanatory effect on the leaf chemistry. Forward SMR starts with no variables in the regression equation; at each step, the most statistically significant variable is added, as specified by the entry criteria (highest F-value or lowest p-value); at the same time the procedure computes the removal statistic for each variable and removes variables if possible (as determined by the removal criteria). Stepping is terminated when neither entry nor removal of variables can be performed (StatSoft, Inc., 2002).

Statistical significance is a property of the results of an empirical investigation suggesting that they are not due to chance alone. The 5 per cent level of significance has become conventional in the empirical sciences; this means that results are normally considered to be statistically significant if statistical tests show that the probability of obtaining, by chance alone, results at least as extreme as those obtained is less than 5 percent, usually written $p < 0.05$. If the significance test indicates that the probability is sufficiently small, the investigator is justified in rejecting the null hypothesis and therefore also in accepting its logical negation, namely the alternative hypothesis. If the probability is not sufficiently small, then the correct interpretation is that there is no evidence of an effect, not that there is evidence of no effect (Colman, 2001).

SMR, although very useful to estimate leaf chemicals from foliar spectra, can be criticised in three points (Curran, 1989): I) Overfitting of wavebands in the calibration equation can occur when the number of samples is smaller than the number of wavebands. When the number of wavebands increases in the calibration model, the chance that unknown samples will vary in exactly the same way decreases, because the model starts to include the spectral noise unique to the training data set. Therefore, only those wavebands that have a causal relationship with the chemical of interest should be included in the calibration equation. II) Intercorrelation of chemicals may result in the selection of a waveband in the calibration model that is not related to a chemical bond of the constituent A but to the chemical bond of another constituent B that is highly correlated with A. III) It is difficult to explain why a particular waveband was included into the model while another waveband equally suited in terms of its relationship to chemical bonds was omitted.

Multiple regression is based on four main assumptions that can be easily violated when adapting the approach to remote sensing (Curran, 1989): I) The assumption that the relationships between reflectance and chemical concentration are near-linear is reasonable. II) The assumption that we can extract the vegetation spectra of interest from imaging spectrometry data is reasonable if continuous vegetation stands are studied. III) The assumption that the relationship between spectra and foliar chemicals is not disturbed by canopy geometry or phenology is reasonable if stands of a single species of vegetation are studied. IV) The assumption of accuracy in the measurements of chemical concentrations in the vegetation canopy is difficult to fulfil. It consists of two additional assumptions: i) the chemical composition of a canopy does not vary within a given volume; ii) the concentrations of a chemical measured in the laboratory does not differ from its concentration in the field due to a) transformation of the chemicals during the isolation process, b) the occurrence of many different forms of one single chemical, e.g. lignin, and c) the method chosen to measure the chemical.

4.3.3 Artificial neural networks

Neural networks are very sophisticated modeling techniques capable of modeling extremely complex, nonlinear functions. For many years linear modeling has been the commonly used technique for most modeling tasks, but where the linear approximation was not valid the models suffered accordingly.

Multilayer Perceptrons (MLP) (or multi layer feed forward networks) are perhaps the most popular network architecture in use today. In MLP, signals flow from inputs, forward through any hidden units and reach the output units. The units (or neurons) each perform a biased weighted sum of their inputs and pass this activation level through a transfer function to produce their output. The hidden and output layer neurons are each connected to all of the units in the preceding layer. The network has a simple interpretation as a form of input-output model, with the weights and biases the free parameters of the model. Such networks can model functions of almost arbitrary complexity, with the number of layers, and the number of units in each layer, determining the function complexity (Haykin, 1994; Bishop, 1995).

In supervised learning, the network learns to infer the relationship between the examples of inputs together with the corresponding outputs. Training data is usually taken from historical records or from simulations. The neural network is then trained using one of the supervised learning algorithms (e.g. back propagation), which uses the data to adjust the network's weights and thresholds in such a way that the error in its predictions on the training set is minimised. If the network is properly trained, it has then learned to model the (unknown) function that relates the input variables to the output variables, and can subsequently be used to make predictions where the output is not known (StatSoft, Inc., 2002).

The best-known example of a neural network training algorithm is back propagation (Rumelhart et. al., 1986). In back propagation, the gradient vector of the error surface is calculated. This vector points along the line of steepest descent from the current point. A sequence of moves in the direction of the vector will eventually find a minimum. The step size is proportional to the slope and to a special constant, the learning rate. The correct setting for the learning rate is application-dependent, and is typically chosen by experiment. The algorithm progresses iteratively, through a number of epochs. On each epoch, the training cases are each submitted in turn to the network, and target and actual outputs compared and the error calculated. This error, together with the error surface gradient, is used to adjust the weights, and then the process repeats. The initial network configuration is random and training stops when a given number of epochs elapses or when the error reaches an acceptable level (StatSoft, Inc., 2002).

The training data set includes a number of cases, each containing values for a range of input and output variables. Gathering cases and selecting input variables are critical issues of neural network design. The number of cases required for neural network training is related to the (unknown) complexity of the underlying function which the network is trying to model. For most practical applications, the number of cases required will be hundreds or thousands. As the number of variables increases, the number of cases required increases nonlinearly. (StatSoft, Inc., 2002). Problems of over-learning (or over-fitting) and selection of input variables are discussed in section 6.3.6.

4.3.4 Ratio-based and orthogonal vegetation indices

Broadband vegetation indices are based on discrete bands, usually located in red and near-IR wavelengths (Table 4.1). They are generally divided into ratio-based indices (RVI, NDVI, MVI, RSR) and orthogonal indices (PVI, SAVI, TSAVI). Ratio-based indices are calculated independently of soil reflectance properties, whereas orthogonal indices include parameters referring to the soil line. Ratio-based VIs tend to minimize the effects of illumination conditions while enhancing the contrast between vegetation and soil (Baret & Guyot, 1991). Orthogonal VIs aim to compensate for soil and background effects.

Most of the VIs are based on the reflectance in the red and near-IR part of the spectrum. With hyperspectral data, VIs can generally be calculated for all possible two-band combinations:

$$RVI = \frac{\rho_{Bd1}}{\rho_{Bd2}} \quad 4.5$$

$$PVI = \frac{\rho_{Bd1} - a\rho_{Bd2} - b}{\sqrt{1 + a^2}} \quad 4.6$$

Table 4.1: Broadband vegetation indices investigated in this study. ρ =reflectance, TM=Thematic Mapper

Name	Abbreviation	Equation	Reference
Ratio vegetation index	RVI	$\frac{\rho_{TM4}}{\rho_{TM3}}$	Pearson & Miller, 1972
Normalised difference vegetation index	NDVI	$\frac{\rho_{TM4} - \rho_{TM3}}{\rho_{TM4} + \rho_{TM3}}$	Rouse et al., 1974
Perpendicular vegetation index	PVI	$\frac{\rho_{TM4} - a\rho_{TM3} - b}{\sqrt{1 + a^2}}$ $a = 0.9, b = 0.1$	Richardson & Wiegand, 1977
Transformed soil-adjusted vegetation index	TSAVI	$\frac{a(\rho_{TM4} - a\rho_{TM3} - b)}{a\rho_{TM4} + \rho_{TM3} - ab}$ $a = 0.9, b = 0.1$	Baret et al., 1989
Mid-infrared vegetation index	MVI	$\frac{\rho_{TM4}}{\rho_{TM5}}$	Fassnacht et al., 1997
Greenness vegetation index	GVI	$-0.2848\rho_{TM1} - 0.2435\rho_{TM2}$ $-0.5436\rho_{TM3} + 0.7243\rho_{TM4}$ $+0.0840\rho_{TM5} - 0.1800\rho_{TM7}$	Christ and Cicone, 1984
Reduced simple ratio	RSR	$RVI \cdot \left[1 - \frac{\rho_{TM5} - \min \rho_{TM5}}{\max \rho_{TM5} - \min \rho_{TM5}} \right]$	Brown et al., 2000

It is then assumed that the soil line concept, originally defined for the red–near-IR feature space, can be transferred into other spectral domains (Thenkabail et al., 2000). Hence, it is supposed that soil lines exist between all wavebands.

4.3.5 The red edge inflection point

As the red edge inflection point (REIP) is defined as the point of maximum slope in the reflectance spectrum it may be determined using the first derivative of the reflectance. This approach will yield precise calculations of the REIP on data acquired by field-spectrometers which collect spectra with a spectral resolution of about 1 nm. However, in the case of imaging spectrometer data with a spectral resolution of usually about 10 to 20 nm, the subtle shifts of the REIP may not be recognized as the vegetation spectrum is sampled in a limited number of points. Therefore, a function has to be fitted through the measured data points of the reflectance spectrum. Several methods have been developed for interpolation in the

wavelength region of the red edge. An approach suggested by Guyot et al. (1992) calculates in a first step the reflectance at the red edge inflection point by linear interpolation. More sophisticated approaches are the inverted Gaussian model (IGM) and the La Grange interpolation (LGI) technique.

Inverted Gaussian model

The inverted Gauss model (IGM) (Bonham-Carter, 1988) fits a Gaussian normal function to the reflectance at the red edge

$$R_{est}(\lambda) = R_s - (R_s - R_0) \cdot e^{-\frac{(\lambda - \lambda_0)^2}{2\sigma^2}} \quad 4.7$$

where R_{est} is the estimated reflectance at wavelength λ , R_s is the reflectance maximum (“shoulder” reflectance), usually at approximately 780-800 nm; R_0 is the reflectance minimum, usually at about 670-690 nm; λ_0 is the wavelength of the reflectance minimum; σ is the Gaussian shape parameter with unit nm. The estimated $REIP_{IGM}$ is then the midpoint on the ascending part of the modelled curve:

$$REIP_{IGM} = \lambda_0 + \sigma \quad 4.8$$

The function is fitted through the measured reflectance data points $R_{mes}(\lambda)$ by adjusting the values of R_s , R_0 , λ_0 and σ in such a way that the root mean square error (*rmse*) is minimized according to:

$$RMSE = \sqrt{\frac{\sum_{i=1}^N (R_{mes}(\lambda_i) - R_{est}(\lambda_i))^2}{N}} \quad 4.9$$

where N is the number of data points recorded in the N corresponding wavebands.

Lagrangian model

Another approach, the Lagrangian interpolation (LGI), has been proposed by Dawson & Curran (1998). The technique is applied to the approximate first-derivative of the reflectance spectrum, which is computed as follows:

$$D_{mes}(\lambda_j + \Delta\lambda) = \frac{R(\lambda_j) - R(\lambda_{j-1})}{\lambda_j - \lambda_{j-1}} \quad 4.10$$

where $D_{mes}(\lambda_j + \Delta\lambda)$ is the measured first-derivative transformation at the midpoint with wavelength $\lambda_j + \Delta\lambda$ between the wavebands $j-1$ and j ; $R(\lambda_{j-1})$ and $R(\lambda_j)$ are the reflectances at the bands $j-1$ and j , respectively. A second order polynomial is fitted directly to three bands of the first-order derivative spectrum:

$$\begin{aligned}
D_{est}(\lambda) &= \frac{(\lambda - \lambda_i) \cdot (\lambda - \lambda_{i+1})}{(\lambda_{i-1} - \lambda_i) \cdot (\lambda_{i-1} - \lambda_{i+1})} \cdot D_{mes}(\lambda_{i-1}) \\
&+ \frac{(\lambda - \lambda_{i-1}) \cdot (\lambda - \lambda_{i+1})}{(\lambda_i - \lambda_{i-1}) \cdot (\lambda_i - \lambda_{i+1})} \cdot D_{mes}(\lambda_i) \\
&+ \frac{(\lambda - \lambda_{i-1}) \cdot (\lambda - \lambda_i)}{(\lambda_{i+1} - \lambda_{i-1}) \cdot (\lambda_{i+1} - \lambda_i)} \cdot D_{mes}(\lambda_{i+1})
\end{aligned} \tag{4.11}$$

where $D_{est}(\lambda)$ is the first derivative estimated by the LGI model at any wavelength λ ; λ_i is the band having the maximum first derivative; λ_{i-1} and λ_{i+1} are the bands on the left and right side of λ_i , respectively; $D_{mes}(\lambda_i)$, $D_{mes}(\lambda_{i-1})$ and $D_{mes}(\lambda_{i+1})$ are the measured first derivative values. The REIP is located at the wavelength $REIP_{LGI}$ where $D_{est}(\lambda)$ is maximum; to determine this position (and thus, the position of maximum slope of reflectance), the first derivation on $D_{est}(\lambda)$ 4.11 is performed, representing the second derivative of the reflectance. The equation is resolved, for when the first derivative of $D_{est}(\lambda)$ is zero, giving:

$$REIP_{LGI} = \frac{A \cdot (\lambda_i + \lambda_{i+1}) + B \cdot (\lambda_{i-1} + \lambda_{i+1}) + C \cdot (\lambda_{i-1} + \lambda_i)}{2 \cdot (A + B + C)} \tag{4.12}$$

where

$$A = \frac{D_{mes}(\lambda_{i-1})}{(\lambda_{i-1} - \lambda_i) \cdot (\lambda_{i-1} - \lambda_{i+1})}, B = \frac{D_{mes}(\lambda_i)}{(\lambda_i - \lambda_{i-1}) \cdot (\lambda_i - \lambda_{i+1})}, C = \frac{D_{mes}(\lambda_{i+1})}{(\lambda_{i+1} - \lambda_{i-1}) \cdot (\lambda_{i+1} - \lambda_i)} \tag{4.13}$$

The characteristics of both methods for the calculation of the red edge inflection point were compared by Dawson & Curran (1998): In the case of the linear and the inverted Gaussian model, certain parameters such as R_s and R_0 have to be predefined. These parameters depend, apart from the leaf optical properties, on canopy optical properties which are unknown. The Lagrangian model, on the other hand, does not need *a priori* knowledge of the spectrum and is therefore better suited to be used on canopy spectra than the other approaches. Furthermore, it forces the interpolation curve through the measured data points, thus taking into account the curvature of the function, whereas the IGM ignores the curvature as it fits a normal curve. The drawback of the Lagrangian method is the higher sensitivity to spectral noise as it is calculating the REIP from the derivative spectra.

4.3.6 Derivative spectra

The derivative of a spectrum is the rate of change of reflectance with respect to wavelength. The approximate first-order derivatives can be calculated according to

$$D(\lambda_j + \Delta\lambda) = \frac{R(\lambda_j) - R(\lambda_{j-1})}{\lambda_j - \lambda_{j-1}} \tag{4.14}$$

where $D(\lambda_j + \Delta\lambda)$ is the first-derivative transformation at the midpoint with wavelength $\lambda_j + \Delta\lambda$ between the wavebands $j-1$ and j ; $R(\lambda_{j-1})$ and $R(\lambda_j)$ are the reflectances at the bands $j-1$ and j , respectively. Derivative spectra have been widely used in spectroscopy and remote sensing. Reflectance spectra may suffer from background signals and albedo effects. In contrast, derivatives were shown to be less sensitive to variations of soil background, illumination, and surface albedo (Demetriades-Shah et al., 1990). The main disadvantage of derivatives is their sensitivity to sensor noise. The decrease in the signal-to-noise ratio (SNR) with increasing derivative order often limits the usage of higher order derivatives.

4.3.7 Continuum-removal and band-depth normalisation

Absorptions in a spectrum are composed of the continuum and individual features, where the continuum is the background absorption onto which other absorption features are placed over. The continuum is simply an estimate of the other absorptions present in the spectrum, not including the one of interest (Clark & Roush, 1984). In practice, linear segments can be used to approximate the continuum line. Once this line is established, the continuum removed spectra (CR) are calculated by dividing the original reflectance values (ρ_{or}) by the values of the continuum line (ρ_{cl}) at the corresponding wavelength (Kokaly & Clark, 1999) as $CR = \rho_{or} / \rho_{cl}$. As non-linear multiplicative effects shape reflectance spectra, the continuum

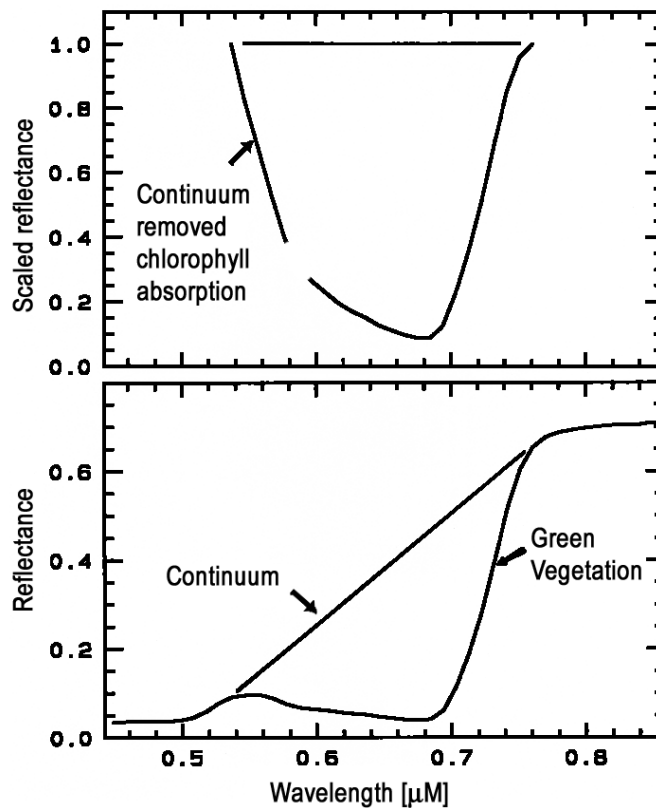


Figure 4.1: Continuum-removal for chlorophyll absorption in vegetation (from Clark, 1999).

should be removed by division and only by subtraction when working with absorption coefficients (Clark, 1999). The removal of the continuum isolates spectral features and makes them comparable. Continuum removal, for instance, for the chlorophyll feature of green vegetation (Figure 4.1) may reveal detailed spectral variations of absorption that are not obvious in the original reflectance spectra (Clark, 1999).

Continuum-removed absorption features can be compared by scaling them to the same depth at the band centre. The band depth (ρ_D) at each wavelength in the absorption feature is computed from the continuum-removed reflectance (ρ_{CR}) as $\rho_D = I - \rho_{CR}$. The normalized band depths (ρ_{DN}) are calculated by dividing the band depth of each waveband (ρ_D) by the band-depth at the band centre (ρ_{Dc}) as $\rho_{DN} = \rho_D / \rho_{Dc}$ (Kokaly & Clark, 1999). The main purpose of continuum-removal and band-depth-normalization is the minimization of effects that extraneous factors may have on reflectance spectra to highlight shape differences of absorption features. Shape differences are then correlated with variations in foliar biochemistry through multiple stepwise linear regression.

4.3.8 Non-linear least-squares spectral matching

Gao & Goetz (1994, 1995) developed the non-linear least squares spectrum-matching technique to determine whether reflectance spectra of green leaves in the 1.0-2.5 μm region contain only liquid water absorption features or contain both the absorption features of liquid water and that of other leaf compounds. This method attempts to calculate a fresh leaf spectrum as a non-linear combination of a measured leaf water spectrum and a measured dry leaf spectrum. The leaf water spectrum was obtained by measuring reflectances of glass beads mixed with liquid water. The dry leaf spectrum was obtained by measuring reflectances of dried ground leaves. Approximate absorption coefficients (k_λ) of liquid water and of dry leaves were calculated from reflectance R_λ as $k_\lambda = -\log(R_\lambda)$. The authors found that besides water, dry leaf components, such as lignin and cellulose, control the reflectance spectra of green vegetation (oak and cotton leaves) in that spectral domain.

The approach by Gao & Goetz (1994) was modified to estimate protein concentration in Norway spruce needles. Absorption coefficients of leaf water and protein were obtained from Dawson et al. (1998). The spectral reflectance of fresh needles $R_{Fmod}(\lambda)$ was modeled from the spectral absorption coefficients of liquid water $k_W(\lambda)$ and protein $k_P(\lambda)$ as

$$R_{Fmod}(\lambda) = (A + B\lambda)e^{-(C_W k_W(\lambda) + C_P k_P(\lambda))} \quad 4.15$$

where C_W and C_P represent concentrations of water and protein, respectively, and the term $(A + B\lambda)$ represents the background level of the calculated spectrum. A , B , C_W and C_P were iteratively adjusted in such a way that the sum of the squared differences between the measured reflectance $R_{Fmes}(\lambda)$ and the modeled reflectance $R_{Fmod}(\lambda)$ for each given waveband

was minimized. The spectral reflectance of water $R_{W\text{mod}}(\lambda)$ was calculated by setting the parameter $C_P(\lambda)$ to zero in equation 4.15), giving:

$$R_{W\text{mod}}(\lambda) = (A + B\lambda)e^{-(C_W k_W(\lambda))} \quad 4.16$$

4.4 Physically-based reflectance modeling

4.4.1 Canopy reflectance models

Starting from the 1970's a number of radiative transfer models, so-called canopy reflectance (CR) models have been developed. There are four broad categories of CR models (Goel, 1988; Roberts, 2001; Atzberger, 2003): *Geometrical models* (e.g., Li & Strahler, 1985) describe the vegetation canopy using opaque geometric shapes (cones or cylinders), which cast shadows on the ground; crown transparency is not considered. They are used to describe forests or shrublands, where shadowing plays an important role. *Turbid medium or analytical models* (e.g. Suits, 1972; Verhoef, 1984) describe the canopy as a horizontally homogenous and transparent layer that contain small vegetation elements which are treated as absorbing and scattering particles of a given geometry and density. These models are better suited to describe dense leafy canopies such as crops, but shadowing is not taken into account. *Hybrid models* are combinations of geometrical and turbid medium models. The geometric shapes representing, for instance, tree crowns, are not considered as being opaque but are treated as a turbid medium. This model type is often more complex but also closer to reality. FLIM

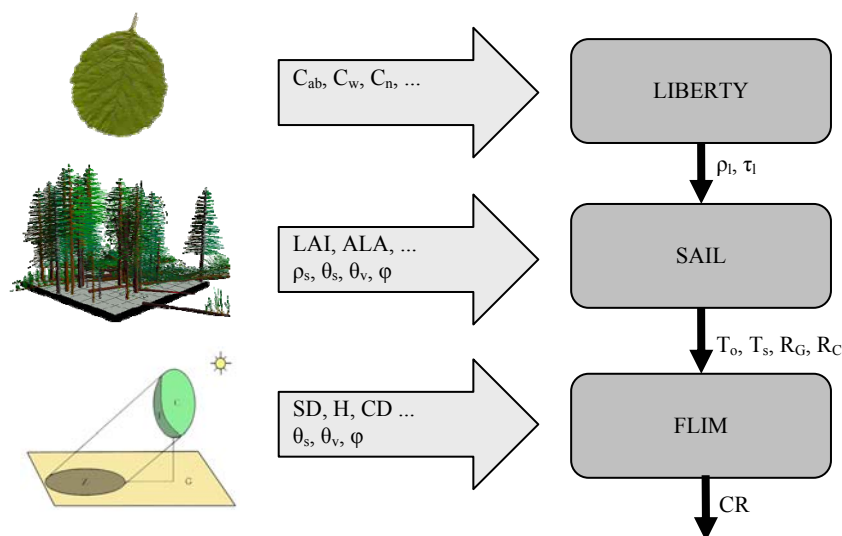


Figure 4.2: Schematic view of the link between LIBERTY, SAIL, and FLIM models showing the input variables used for the simulation. Modified after Zarco-Tejada et al. (2004a).

(Rosema et al, 1992) can be considered a very simple hybrid model, whereas INFORM (Atzberger, 2000) is of more sophisticated nature. *Ray-tracing or computer simulation models* (e.g., Gastellu-Etchegorry et al., 1996) compute the path of each photon through the canopy using random numbers to determine the direction of the incident rays, the location of the vegetation elements, the direction of scattering, and so on. Due to the complex structure and the large number of input parameters required, these models are difficult to invert (Goel, 1988; Roberts, 2001; Atzberger, 2003).

4.4.2 The Invertible Forest Reflectance Model

The Invertible Forest Reflectance Model (INFORM) (Atzberger, 2000) simulates the bi-directional reflectance of forest stands between 400 and 2500 nm. INFORM is essentially a combination of FLIM (Rosema et al., 1992), SAIL (Verhoef, 1984), and PROSPECT (Jacquemoud & Baret, 1990) or LIBERTY (Dawson et al., 1998). A schematic view of the link between the models is given in Figure 4.2.

The Forest Light Interaction Model (FLIM) takes into account both, the effects of shadowing and crown transmittance (Rosema et al., 1992). In this model, the forest is considered as a discontinuous canopy layer with tree crowns and gaps. The underlying assumption is that canopy reflectance is primarily controlled by coverage and crown transmittance (computed from LAI), and that background characteristics, spatial distribution of trees, and stand structure are of secondary importance (Gemmell & Varjo, 1999). FLIM calculates stand reflectance R in a given spectral band as

$$R = R_C \cdot C + R_G \cdot G \quad 4.17$$

where R_C is the crown reflectance at infinite crown depth and R_G is the background reflectance. C is the “crown factor”:

$$C = (1 - T_s \cdot T_o) \cdot c_s \cdot c_o \quad 4.18$$

where T_s is the average crown transmittance in sun direction and T_o is the average crown transmittance in observation direction; both T_s and T_o are exponentially related to LAI; c_o is the ground coverage by crowns in observation direction; c_s is the ground coverage by shadow in sun direction.

G is the “ground factor”:

$$G = F_a \cdot T_s \cdot T_o + F_b \cdot T_o + F_c \cdot T_s + F_d \quad 4.19$$

where F_x are ground surface fractions; F_a represents tree crowns with shadowed background, F_b tree crowns with sunlit background, F_c shadowed open space, and F_d sunlit open space. The fractions in equation 4.19 are calculated from c_o and c_s and additionally take into account

the correlation between c_o and c_s which is in turn calculated from geometrical considerations using the tree height (H) and the crown diameter (Rosema et al., 1992).

The observed ground coverage by crowns c_o under an observation zenith angle θ_o is given by

$$c_o = 1 - e^{\frac{-k \cdot SD}{\cos \theta_o}} \quad 4.20$$

where SD is the tree or stem density [ha^{-1}] and k is a constant representing the average tree crown horizontal area [ha]. Similarly to the observed ground coverage by crowns, the ground coverage by shadow c_s under a solar zenith angle θ_s is defined as

$$c_s = 1 - e^{\frac{-k \cdot SD}{\cos \theta_s}} \quad 4.21$$

The constant k representing the average horizontal area of a single tree crown [ha] can be derived from

$$k = \frac{\pi \cdot (0.5 \cdot CD)^2}{10000} \quad 4.22$$

where CD is the crown diameter [m].

In FLIM, crown transmittance terms (T_s and T_o) are assumed to be exponentially related to LAI; this neglects the effects of leaf geometry and leaf optical properties on the transmittance. Therefore in INFORM crown transmittance is calculated by the SAIL model (Verhoef, 1984). To compute crown transmittance for observation T_o and sun direction T_s (for a given leaf transmittance τ and leaf reflectance ρ), leaf area index (LAI), average leaf inclination angle (ALA), observation angle (θ_o), sun angle (θ_s), the relative azimuth angle between sun and sensor (ψ) and the fraction of diffuse radiation ($skyl$) have to be specified:

$$T_o = f_{SAIL}(LAI, ALA, \tau, \rho, \theta_o, \psi, skyl) \quad 4.23$$

$$T_s = f_{SAIL}(LAI, ALA, \tau, \rho, \theta_s, \psi, skyl) \quad 4.24$$

The original version of INFORM accounted for the reduction of transmittance by woody components within the canopy; the transmittance calculated by the SAIL model was reduced by a wood factor that represented the shadow cast on the ground by woody parts in a leafless crown (Atzberger, 2000). The correction for woody components was not applied in the present research as their influence is difficult to quantify.

In the FLIM model, the crown reflectance at infinite crown depth R_C and the background reflectance R_G (equation 1) are both derived empirically from the image data itself. INFORM, conversely, computes both terms using the SAIL model. For a given illumination and observation geometry, R_G is derived as

$$R_G = f_{SAIL}(LAI_U, ALA_U, \tau, \rho, \rho_{soil}, \theta_o, \theta_s, \psi, skyl) \quad 4.25$$

where LAI_U and ALA_U are the LAI and the ALA, respectively, of the understorey vegetation and ρ_{soil} is the soil reflectance. A soil reflectance spectrum must be provided from measurements. For a given illumination and observation geometry, R_C is computed as

$$R_C = f_{SAIL}(LAI_{inf}, ALA, \tau, \rho, \rho_{soil}, \theta_o, \theta_s, \psi, skyl) \quad 4.26$$

where LAI_{inf} is the LAI at infinite crown depth.

In the initial version of INFORM (Atzberger, 2000), leaf spectral reflectance and transmittance were computed by the PROSPECT model (Jacquemoud & Baret, 1990) since only deciduous forests were considered. However, PROSPECT does not very well represent the optical properties of needle shaped leaves of conifer forest stands. Consequently, the LIBERTY model (Dawson et al, 1998) has been used as a replacement for PROSPECT. LIBERTY (Leaf Incorporating Biochemistry Exhibiting Reflectance and Transmittance Yields) is a general purpose radiative transfer model for simulating the reflectance and transmittance spectra of a conifer needle, or a stacked layer of needles between 400 and 2500 nm. It treats a needle as an aggregation of cells and calculates multiple scattering between cells. In LIBERTY, needle transmittance (τ) and reflectance (ρ) are computed as a function of three structural parameters (cell diameter (d), intercellular air space (i), leaf thickness (t)) and the combined absorption coefficients of leaf chemicals (chlorophyll (c_{AB}), water (c_W), lignin and cellulose (c_L), and protein (c_P)):

$$\tau = f_{LIBERTY}(d, i, t, c_{AB}, c_W, c_L, c_P) \quad 4.27$$

$$\rho = f_{LIBERTY}(d, i, t, c_{AB}, c_W, c_L, c_P) \quad 4.28$$

In a summary, INFORM calculates forest reflectance R as a function of internal canopy parameters, internal leaf parameters and external parameters:

$$R = f_{INFORM}(SD, CD, H, LAI, ALA, LAI_{inf}, LAI_U, ALA_U, \rho_{soil}, d, i, t, c_{AB}, c_W, c_L, c_P, \theta_o, \theta_s, \psi, skyl) \quad 4.29$$

4.4.3 Inversion of reflectance models

In the forward mode the CR model computes the spectral reflectance for a certain set of leaf or canopy parameters. Forward modeling provides an efficient way to investigate the effects of forest canopy attributes on reflectance signatures and may improve the understanding of how the canopy structure influences the radiation field. For the retrieval of those canopy variables from measured signals it is necessary to invert the model. Few studies exist, where CR models were inverted to estimate forest characteristics from remote sensing observations (section 2.3.3).

Due to the complex character of a CR model, an analytical solution is not possible and numerical approaches have been developed to successfully invert CR models. Traditional inversion of reflectance models employs an optimisation technique to estimate the model parameters by minimising a merit function (Goel, 1989). An iterative process is necessary to find the optimal estimates of these parameters. The main drawbacks of this method are i) difficulty in achieving globally optimal and stable results, ii) difficulty in retrieving more than 2 parameters simultaneously and iii) requirement of substantial computation time (Gong et al., 1999).

Recently, Artificial Neural Networks (ANN) have been employed for reflectance model inversion (Gong et al., 1999; Udelhoven et al., 2000; Kimes et al., 2002) in order to overcome the above mentioned limitations. To invert a reflectance model using an ANN the following steps have to be carried out (Gong et al., 1999): A) Determination of the structure of the ANN, in particular the number of nodes in the input, hidden, and output layer; each spectral band to be used corresponds to a node in the input layer; the number of parameters to be retrieved is the same as the number of nodes in the output layer. B) Simulation of the reflectance spectra from known parameter sets using the reflectance model. C) Presentation of known parameter sets and their corresponding reflectance spectra to the ANN; during the training step an algorithm is used to adjust weights and biases of the ANN in such a way that the root mean squared error (rmse) between estimated and true parameters is minimal. D) Input of measured reflectance spectra to the previously trained ANN and comparison of parameters estimated by the ANN to measured ones.

4.5 Validation

Cross-validation is a method of assessing the accuracy and validity of a calibration model. From the available data set one sample is selected and its spectrum and the corresponding attribute data are removed. The remaining training set samples are used to perform the calibration calculations. The calibration model is then used to predict the attribute of interest (e.g. concentration) of the removed sample. The previously left out sample is placed back into the training data set and a different sample is selected. Each sample is left out once and predicted by the training samples. Because the predicted samples are not the same as the samples used to build the model the cross-validated root mean squared error (rmse) is a good indicator of the accuracy of the model in predicting unknown samples (Duckworth, 1998). The rmse is the square root of the mean squared error; it is calculated from the differences between estimated values (Y_{est}) and measured (Y_{mes}) values and has the same units as the original data:

$$rmse = \sqrt{\frac{\sum_{i=1}^n (Y_{est} - Y_{mes})^2}{n}} \quad 4.30$$

Another advantage of cross-validation is its ability to detect outliers. If the predicted concentration for a single sample is far off the measured concentration, the sample is probably an outlier (Duckworth, 1998).

Validation set prediction tests the predictive model on a validation data set. The validation set can come either from a new set of samples measured under the same conditions as the calibration samples or a large set of training data can be split into two groups: a set of calibration data and a set of validation data, where the split could be 80/20, 50/50, etc. depending on the total number of samples. The main advantage of this validation technique is the ability to test the model's performance with a completely different and independent data set which is most important to determine the model's long term stability (Duckworth, 1998).

Chapter 5 Mapping forest cover type through image classification

5.1 Introduction

Despite the large amount of spectral bands in data collected from imaging spectrometers, it has frequently been found, that the forest categorical variables considered do not have unique spectral signatures that allow forest classes to be distinguished without confusion. From this point of view it is still an open issue if hyperspectral data contain more information relevant to the classification of forest cover than broadband multispectral data. It is also not clear if a large spatial resolution of a few meters allow a better forest mapping compared to a pixel size of a few tens of meters typical to most earth observation satellite system, such as Landsat TM.

Forest types as defined by species composition and age class have spectral reflectance characteristics that may be strongly influenced by variations in the structural attributes of the forest stand (Franklin et al., 2003). For instance, variations in a stand structural attribute, such as stem density (the number of trees or stems per hectare) may have a greater effect on forest reflectance than tree species composition. Therefore, other mapped environmental variables that control forest vegetation distributions, such as terrain variables or geology, or structural attributes, can be combined with image data in the classification process to aid discrimination of forest type.

Classification should be applied to remotely sensed data of the appropriate spatial, spectral and temporal resolution for the required forest attribute information. Until recently, the choice of remote sensing data to map forests was limited to available operational sensor types. With airborne imaging spectrometers that were successfully operated in recent years, data with high spatial and high spectral resolution has become available. This data type offers the opportunity to systematically investigate the selection of optimal remote sensing data for forest mapping.

Based on the previous outline, the objectives of this study were to (i) compare the classification performance of four different remote sensing datasets of different spectral and spatial resolution (Figure 5.1) to map forest species and age classes and (ii) to investigate if additional information on stem density can improve the classification results.

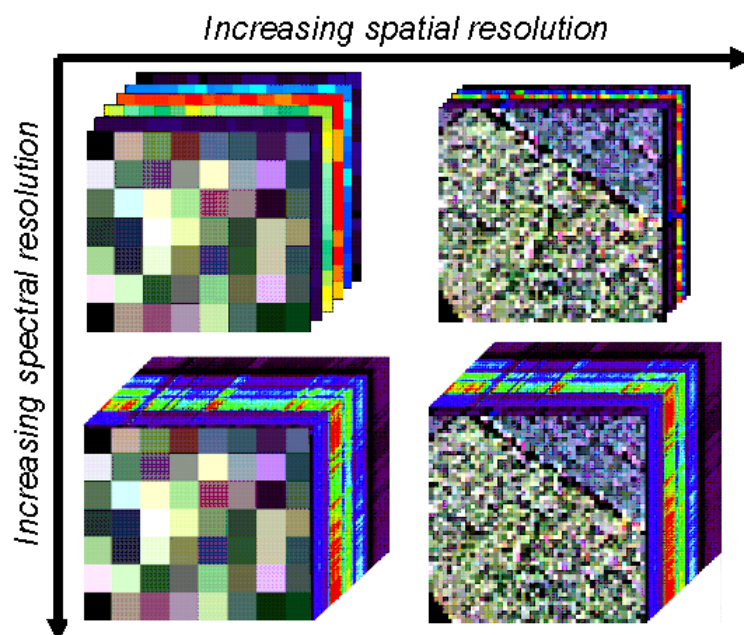


Figure 5.1: Four datasets of varying spectral and spatial resolution. Upper left: TM, 30m; upper right: TM, 5m; lower left: HyMap, 30m; lower right: HyMap, 5m.

5.2 Implementation of additional information

Information about forest parameters that have an influence on the signal recorded from the forest canopy by a sensor can support the estimation of other (unknown) parameters. The aim was to use spatial information on an important structural attribute, stem density (number of stems per hectare) as an ancillary layer in the classification process of the HyMap data in order to better distinguish between certain classes of forest cover type. Stem density information was derived from black/white aerial orthophotos by an approach described in Atzberger & Schlerf (2002). The procedure was based on thresholds of the digital numbers in the image data followed by morphological operations (erosion and dilation) and tree crown identification using a moving window. The method proved to be capable of estimating stem density with an accuracy of approximately 63 trees per hectare for stem densities varying between 200 and 800 stems per hectare (Figure 5.2). Stem density was estimated for the entire area of the Idarwald test site. On a stand basis, the mean stem density and the standard deviation were calculated. The resulting image of the Idarwald test site (25 m x 25 m ground resolution) is shown in Figure 5.3a). From this image, per-field mean and standard deviation of the reference stem densities have been calculated (Figure 5.3b, c) and integrated into the FoGIS of Idarwald.

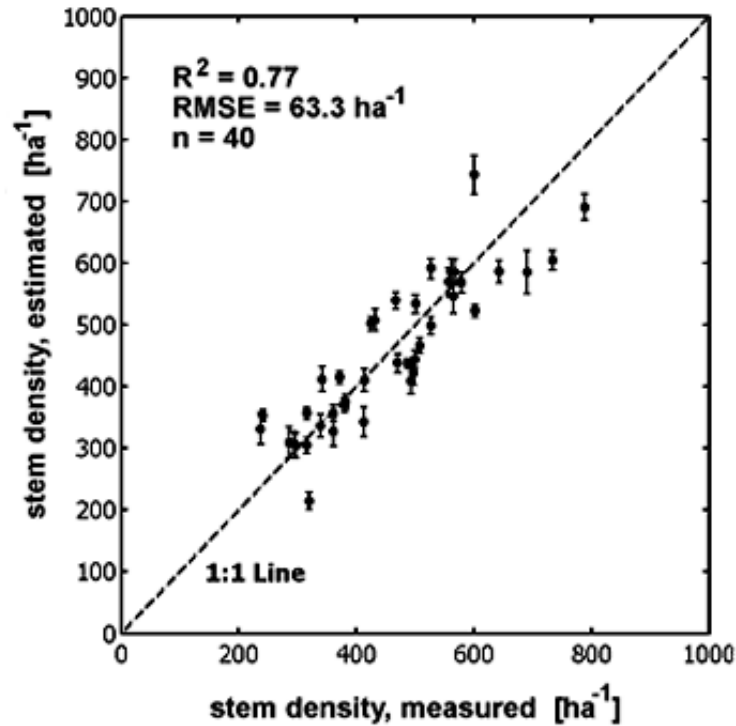


Figure 5.2: Estimated against field-measured stem density (cross-validated) at Idarwald test site. From Atzberger & Schlerf (2002).

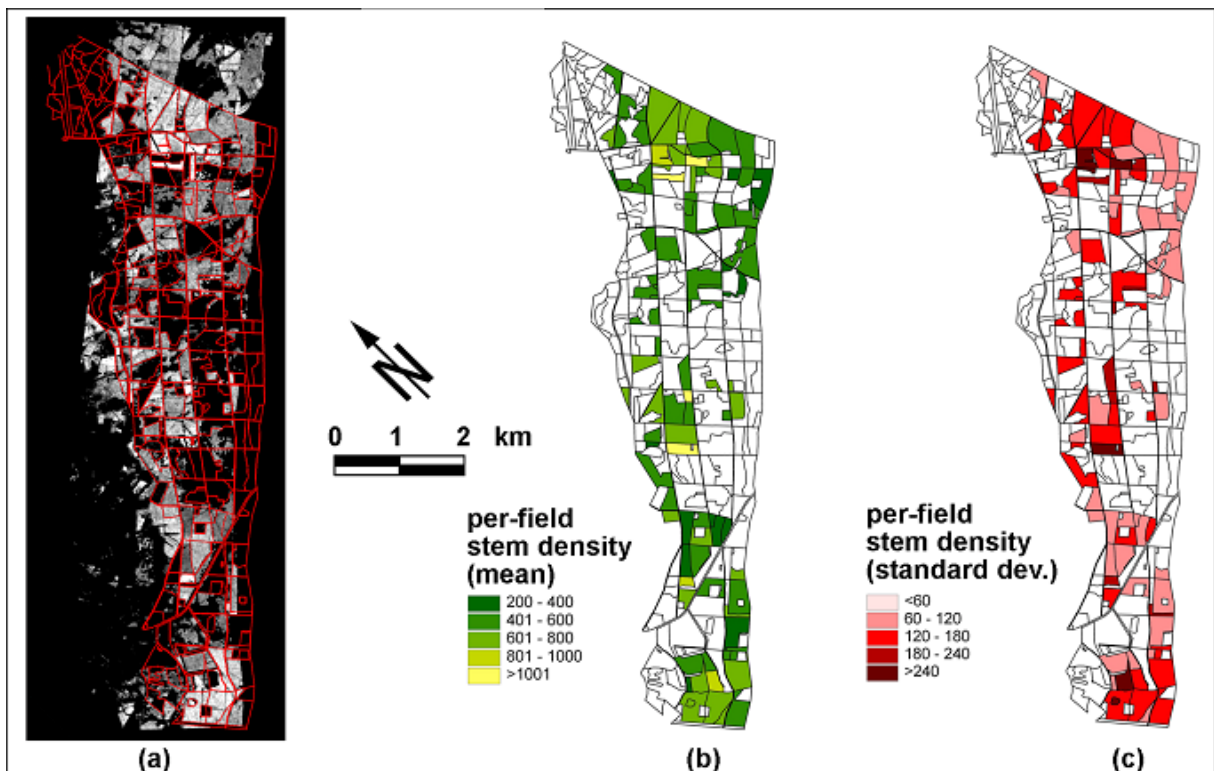


Figure 5.3: Stem density (unit: ha^{-1}) at the Idarwald obtained from black/white orthophotos. (a) pixel resolution, (b) per-stand mean, (c) per-stand standard deviation. Stand borders are shown for clarity. From Atzberger & Schlerf (2002).

Table 5.1: Training data used in the forest classification

Forest class	Number of stands used for training
Spruce, >80 yrs	11
Spruce, 50-80 yrs	16
Spruce, 30-50 yrs	11
Spruce, 10-30 yrs	10
Douglas fir, 30-50 yrs	5
Douglas fir, 10-30 yrs	5

5.3 Image classification

Since the classification was restricted to conifers, deciduous forest was masked out using a forest mask, which had been generated through an unsupervised classification of the HyMap data using the isodata algorithm. All subsequent processing steps are restricted to coniferous forest.

5.3.1 Data preprocessing

From the available wavebands, usually a best minimum subset is selected for classification. This holds in particular for hyperspectral data as classification algorithms may suffer from redundancy (e.g. highly correlated wavebands). Two different types of spectral preprocessing were carried out, generation of multispectral data and compression of hyperspectral data. To generate synthetic, multispectral broadband data, the radiometrically and geometrically corrected HyMap image was spectrally resampled to Landsat TM wavebands using the appropriate sensor function. Hyperspectral data was compressed because an important requirement for a successful classification is the reduction of the spectral dimensions of the data without losing information. In the present study, the minimum noise fraction (MNF) transformation was used to achieve the data compression. The MNF transformation is similar to the Principal Component Analysis (PCA), but orders the data according to decreasing signal-to-noise ratio instead of decreasing variance (Green et al., 1988; Lee et al., 1990). The MNF transformation was used to partition the data space into two parts: one associated with large eigenvalues containing a large amount of information and a second with low eigenvalues and a large amount of noise. By using only the first portion of the data, the noise is separated from the data, thus reducing the number of bands and improving spectral processing results (Kruse, 1999). The first 19 MNF fractions were separated from the remaining fractions and used for further analysis.

Spatial degradation of the high spatial resolution data (5 m) was done by calculating the mean pixel value within a 30 m x 30 m array for each waveband.

5.3.2 Training

Discrimination of forest types from classification of remote sensing imagery requires that each category (forest types) has unique reflectance properties that are different from the other categories (Franklin et al., 2003). While this concept of unique spectral signatures has been successfully applied in hyperspectral applications for mineral mapping, it has been less successful in forest applications due to the similar spectral response of vegetation canopies. Despite expected difficulties, it was attempted within this research to separate different forest types as defined by tree species and stand age.

A number of multivariate classification techniques (also called pattern recognition) have been successfully used in the remote sensing of forests. In supervised (opposed to unsupervised) classification, the predefined classes (e.g. forest types) are described from observations of the independent variables (reflectances and ancillary data), and then an algorithm is used to assign new observations (e.g. pixel of unknown forest type) to classes. This process assumes that the distribution of forest types to be mapped is known beforehand, at least for some part of the area of interest. This information is typically derived from field sampling or from ancillary data, such as a Geographic Information System.

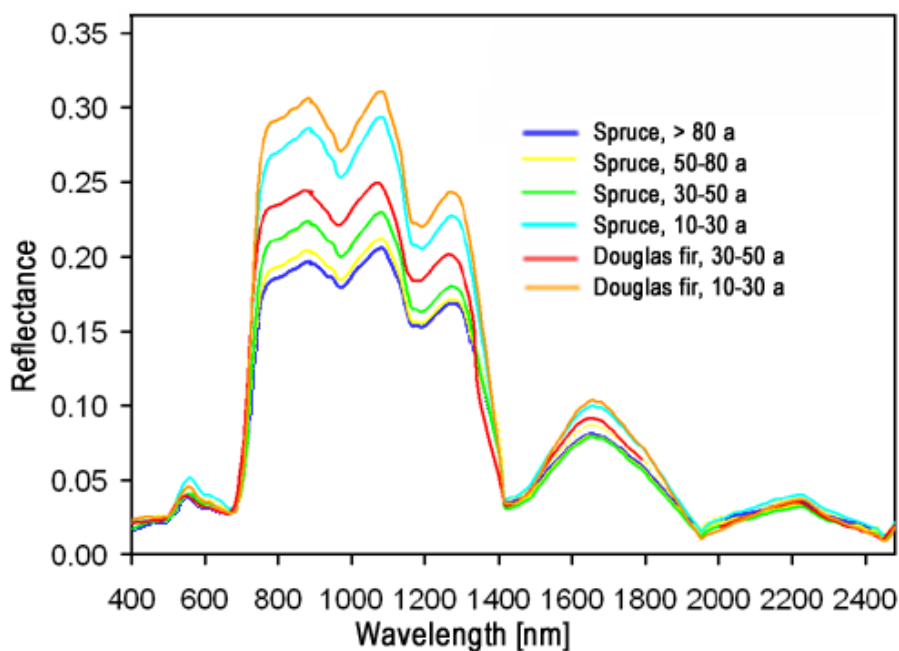


Figure 5.4: Reflectance spectra of forest types considered in the classification process. Note: point measurements of reflectance at discrete waveband positions were connected with lines for clarity.

Table 5.2: Summary of accuracies

Dataset	Overall Accuracy	Kappa Coefficient
A: HyMap 5m	81.4	0.78
B: HyMap 30m	95.0	0.94
C: TM 5 m	55.9	0.47
D: TM 30 m	69.5	0.64
E: HyMap 5 m + Stem density	83.5	0.81

The available FoGIS of Idarwald (section 3.4) was used to collect training data. The aim of the training stage is to collect a set of statistics that describe the spectral response pattern for each forest class. It was decided to consider only forest types in the classification that were represented by a minimum of three forest stands. Each of the six forest types that were considered represented a unique combination of a tree species (Norway spruce or Douglas fir) with an age class (Table 5.1). Other conifer tree species, such as fir and pine were very scarce in the study area and could not be considered in forest mapping. Age classes represent the stand development of Norway spruce that is observed at Idarwald test site and were defined by Womelsdorf, the local forest manager (personal communication, cited from Vohland, 1997). For Douglas fir, no definition of age classes was available and the lower and upper boundaries used to define age classes of Norway spruce were applied. The polygons in the FoGIS representing the forest stands were used to extract spectral signatures for each class. Within each forest type class, subclasses were defined. Each forest stand (polygon) that was available in the FoGIS was considered as a subclass. The generation of training data involved collecting 5-15 polygons per class, each polygon consisting of 100-1000 pixels. In total, 44 subclasses and 52.844 pixels were obtained. Training data were divided randomly into three sets of pixels: 10 percent were used for training (training pixels), 25 percent for validation of the classification result (validation pixels) and the remaining 65 percent pixels were not used. The training setup was designed this way to reflect the small amount of ground truth commonly available in reality. A visual interpretation of the collected spectra revealed considerable overlap of reflectance values for certain classes. Figure 5.4 shows the mean spectra of the considered forest types computed from all training pixels available.

5.3.3 Classification

Only Spectral Angle Mapper (SAM) algorithm (section 4.2.2) was employed for supervised classification as the focus of the study was on the information content of various types of data rather than the performance of different classifiers. After the classification, the 44 subclasses obtained were condensed into the 6 main classes. Then post-classification smoothing was performed to remove single isolated image pixels (sieve and clump).

5.3.4 Validation

To assess the accuracy the validation pixels were used. A confusion matrix was generated from the validation pixels for each classification. Two measures of classification accuracy are reported. Overall accuracy (OAA) quantifies the percentage of cases correctly classified:

$$OAA = \frac{\sum_{k=1}^q n_{kk}}{n} * 100 \quad 5.1$$

where n_{kk} is the number of correctly classified validation pixels (confusion matrix diagonals), q is the number of classes, and n is the total number of validation pixels used. The kappa coefficient accommodates for the effects of chance agreement:

$$KAPPA = \frac{n \sum_{k=1}^q n_{kk} - \sum_{k=1}^q n_{k+} n_{+k}}{n^2 - \sum_{k=1}^q n_{k+} n_{+k}} \quad 5.2$$

where n_{k+} is the sum of the validation pixels in a class and n_{+k} is the sum of the classified pixels in that class.

5.4 Results and discussion

Table 5.2 lists overall accuracies and kappa coefficients obtained from classifying each of the 5 sets of data (2 types of spectral resolution x 2 types of spatial resolution plus 1 type high spectral and high spatial resolution combined with stem density). Table 5.3 lists detailed confusion matrices for all datasets.

The overall accuracy (OAA) and Kappa coefficient using the HyMap datasets (A and C) were considerable larger than using the TM datasets (B and D). These results confirm that hyperspectral data contain more information relevant to the mapping of forest type than broadband multispectral data. Contrary to broadband data analysis techniques, hyperspectral data offer the use of full-spectrum analysis techniques that exploit all the inherent information. As an example, it has already been shown that the estimation of canopy LAI using hyperspectral imagery can be achieved with accuracy greater than with a broadband sensor (Gong et al, 1992, see also Chapter 6).

Table 5.3 (continued)

D) Class	Ground Truth (Percent)						Total
	Spr. >80	Spr. 50-80	Spr. 30-50	Spr. 10-30	Dou. 30-50	Dou. 10-30	
Unclassified	8.0	6.4	10.8	17.8	4.8	3.3	7.9
Spr. >80	44.1	10.6	1.1	0.0	0.0	0.5	11.2
Spr. 50-80	41.9	83.0	41.1	0.0	0.0	0.0	38.9
Spr. 30-50	6.0	0.0	45.7	5.0	0.0	0.0	11.9
Spr. 10-30	0.0	0.0	1.3	77.2	0.2	3.2	5.6
Dou. 30-50	0.0	0.0	0.0	0.0	94.3	2.3	15.4
Dou. 10-30	0.0	0.0	0.0	0.0	0.7	90.8	9.2
Total	100.0	100.0	100.0	100.0	100.0	100.0	100.0

E) Class	Ground Truth (Percent)						Total
	Spr. >80	Spr. 50-80	Spr. 30-50	Spr. 10-30	Dou. 30-50	Dou. 10-30	
Unclassified	3.5	3.6	5.5	0.5	2.1	1.5	3.3
Spr. >80	90.0	10.3	4.1	0.0	0.4	0.0	18.4
Spr. 50-80	5.6	84.3	25.4	0.1	3.4	0.1	30.2
Spr. 30-50	0.6	1.7	64.3	0.1	2.8	0.4	16.5
Spr. 10-30	0.4	0.1	0.6	99.3	0.5	2.4	9.1
Dou. 30-50	0.0	0.0	0.1	0.0	89.9	0.7	14.6
Dou. 10-30	0.0	0.0	0.1	0.0	0.9	94.9	7.9
Total	100.0	100.0	100.0	100.0	100.0	100.0	100.0

1990; Schlerf et al., 2003). Foody (2002) claimed that accuracies larger than 85 percent are required from remote sensing image classification. The requirement is not fulfilled by most of the datasets except the hyperspectral data low spatial resolution data which can be explained by the fact, that the classification problem encountered is not trivial. Forest classes, such as clearings have spectral reflectance characteristics that differ very much from the closed canopy stands considered in the study and are relatively easy to discriminate from the other forest types. Including such forest classes probably would have increased the accuracy of the classification.

The type of post-classification smoothing applied to the classified image considerably influenced the classification accuracy. Also the design of the validation procedure controlled the classification results to a certain amount. Buddenbaum (2004) used a modified validation approach. In this approach the forest stands were divided into spatially separated training and validation areas. The received accuracies were somewhat lower.

The OAA using the full set of HyMap 5 m data and stem density information (dataset E) was 83 percent and thus 2 percent larger than the OAA using HyMap 5 m (dataset A) alone. This result confirms that the classification of forest cover may be improved through addition of orthophoto derived stem densities into the classification process. However, the increase in classification accuracy was rather limited. Various other types of ancillary information have already been utilized in multispectral classification of vegetation cover: Wulder (1998), for instance, used texture and Franklin (1994) used digital elevation models as additional

information and observed an increase of overall classification accuracy compared to using remote sensing data on a pixel basis alone. Buddenbaum (2004) computed texture parameters from hyperspectral image data by means of geostatistics and used both, hyperspectral wavebands and texture channels together for mapping conifer forest. The results pointed towards an increase in classification accuracy.

In contrast to difficulties reported in the literature (Niemann, 1995; Vohland, 1997; Köhl & Lautner, 2001), discrimination of medium aged to old stands was feasible using the outlined classification strategy. Identification of old forest stands that hold large amounts of biomass is of particular interest to forest authorities to determine the time of harvest. The resulting forest type map is presented in Figure 5.5.

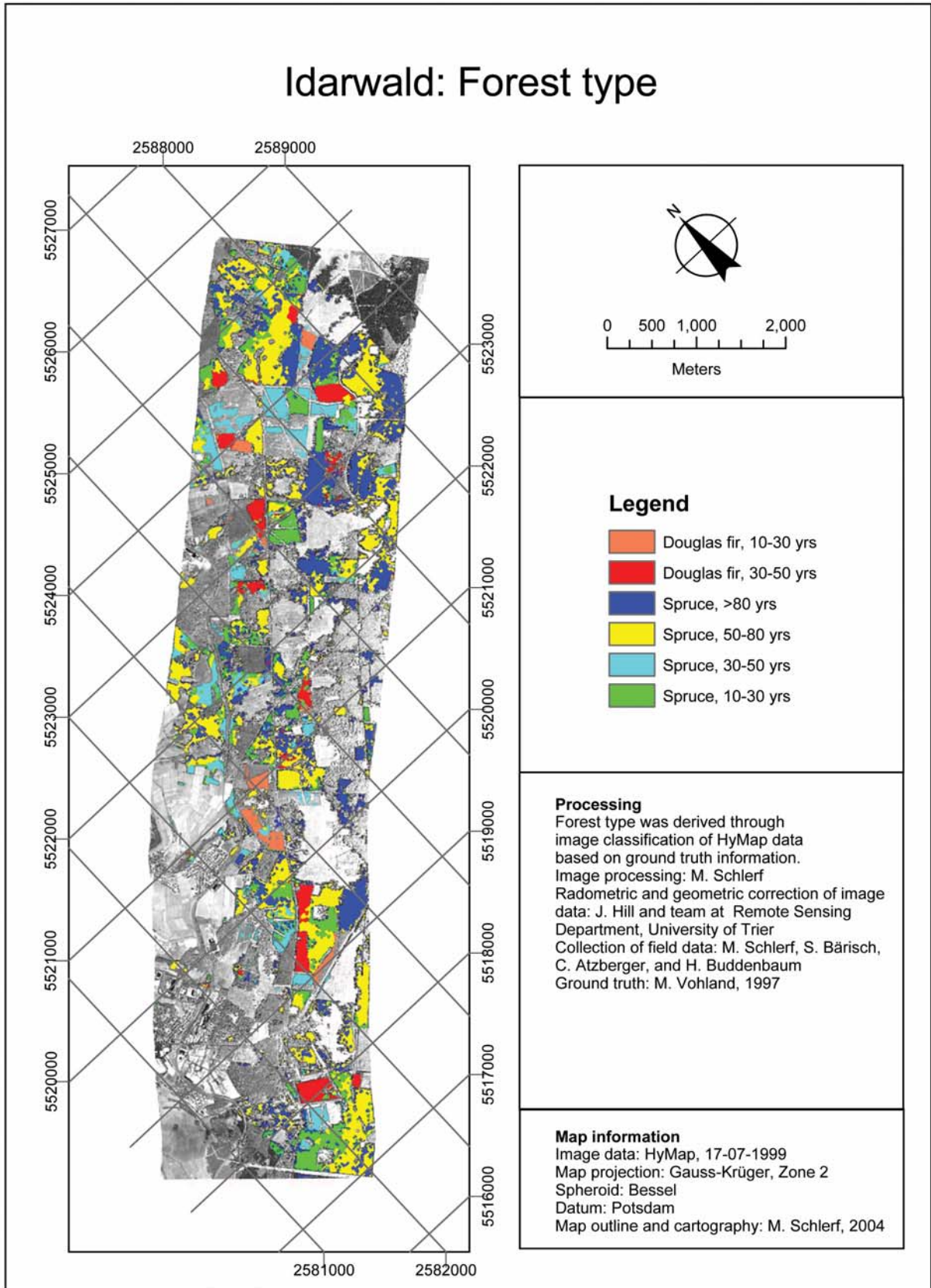


Figure 5.5: Map of forest type at Idarwald.

Chapter 6 Determination of forest structural attributes

6.1 Introduction

Estimation of structural and chemical forest characteristics from remotely sensed data can be generally achieved by empirical or physical approaches (Asner et al., 2003; Chapter 4). Empirical models relate a measure of reflectance (e.g., a vegetation index, VI) to the variable of interest through a regression equation. In a physically based approach, a forest reflectance model is inverted to estimate the structural characteristics of a forest canopy. Both approaches do have certain advantages and disadvantages. For instance, reflectance models can take into account effects of shadowing and multiple scattering while those effects represent major challenges to vegetation indices. On the other hand, empirical models though they need costly field work data are easy to apply.

The main objective of this chapter was to compare empirical and physically-based approaches in terms of their capability to determine forest structural attributes from hyperspectral remote sensing imagery. Another commonly used concept, spectral unmixing, was not implemented within this study, as spectral mixture models can be considered as simple reflectance models which are better suited for sparse vegetation canopies than for dense forests.

Table 6.1: Resulting subsets after stratification according to forest stand age

Subset	Designation	Abbreviation	Age	n
1	total (pooled dataset)	t	10-148	40
2	medium to old	mo	30-148	35
3	old	o	80-148	17
4	medium	m	30-79	18
5	young	y	10-29	5

Table 6.2: Summary statistics for forest stand attributes (n=40)

Stand variable	Mean	Standard deviation	Maximum	Minimum	Range	Coefficient of variation
Perimeter-at-breast height (PBH) [m]	1.09	0.32	1.63	0.27	1.36	0.294
Stem density (SD) [ha ⁻¹]	640	458	2444	244	2200	0.716
Canopy cover (CO) [%]	48	11	70	30	40	0.229
Canopy height (H) [m]	25.1	7.9	39.1	5.0	34.1	0.315
Leaf area index (LAI) [m ² m ⁻²]	3.24	0.97	5.47	1.66	3.81	0.299
Stem biomass (SBM) [m ³ ha ⁻¹]	201	109	654	11	643	0.540

6.2 Developing predictive models

6.2.1 Introduction

The overall aim of this part of the study was to develop linear predictive models between vegetation indices and forest structural variables. More specific objectives were (i) to identify useful stand variables out of the measured ones or generate new stand variables that could be correlated with reflectance measured by the HyMap sensor, (ii) to determine spectral vegetation indices that are best suited for characterising those stand variables, and (iii) to compare and contrast traditional broad-band and hyperspectral VIs in terms of basic statistical characteristics of the predicted stand variables relative to the observed stand variables.

To improve LAI mapping it has been suggested to derive land cover specific VI-LAI

Table 6.3: Linear correlation between forest stand variables (n=40); ** correlation coefficient significant at P<0.01.

Stand variable	PBH	SD	CO	H	LAI	SBM
PBH	1.00					
SD	-0.87**	1.00				
CO	-0.55**	0.72**	1.00			
H	0.88**	-0.86**	-0.58**	1.00		
LAI	-0.72**	0.70**	0.68**	-0.70**	1.00	
SBM	0.81**	-0.59**	-0.20	0.80**	-0.48**	1.00
AGE	0.85**	-0.72**	-0.49**	0.82**	-0.66**	0.77**

relationships using land cover maps (Franklin et al., 1997; Chen et al., 2002; Cohen et al., 2003). This statistical stratification process is usually based on the species type. As in the present study just one single species is considered, it was decided to stratify the dataset according to stand age (Table 6.1). Information about stand age was provided by a Forest Geographic Information System (FoGIS) that had been compiled for the Idarwald (section 3.4).

6.2.2 Computation of vegetation indices

Both, hyperspectral and broadband VIs (section 4.3.4) were computed from the radiometrically and geometrically corrected HyMap spectra after reflectance spectra had been extracted from the HyMap imagery (section 3.3). Ratio-based and orthogonal broadband VIs (Table 4.1) were calculated after the HyMap data had been resampled to Landsat TM spectral bands involving the appropriate Landsat TM filter functions; the ratio-based VIs were RVI and NDVI; the orthogonal VIs were PVI and TSAVI; additional VIs were MVI and GVI. Narrowband RVI and PVI (section 4.3.4) were systematically calculated for all possible $114 \times 114 = 12,996$ band combinations. PVI requires site-specific soil line slopes (a) and intercepts (b). As no soil spectral data was available, standard values ($a=0.9$; $b=0.1$) were used. Additionally, the REIP was calculated using two different methods, the IGM and the LGI (section 4.3.5). Bivariate linear regression (section 4.3.2) was employed to evaluate the relationships between structural stand attributes and VIs. A cross-validation (leave one out) procedure (section 4.5) was used to validate the regression models.

6.2.3 Analysis of forest stand variables

From the summary statistics (Table 6.2) it can be seen that the attributes perimeter-at-breast height (PBH), canopy height (H), and leaf area index (LAI) have a similar variability, whereas canopy cover (CO) is less variable and stem density (SD) and stem biomass (SBM) are more variable. The large variability of SD can be attributed to the extraordinary large density values of young forest stands.

Table 6.3 lists linear correlation coefficients between forest stand attributes. Strong relationships between stand attributes were found for perimeter-at-breast height, stem density, and canopy height. These variables are closely related to stand age; with increasing age trees grow in height and diameter and perimeter-at-breast height and canopy height increase, while stem density is reduced due to thinning. An inverse relationship can be observed between LAI and age. The inverse relation between LAI and stand age seems to be related to the fact that during stand development, crowns of individual trees expand and increase utilization of available growing space. The point at which crowns of different trees begin to interact is considered as being the peak LAI after which a rapid decrease takes place due to competition

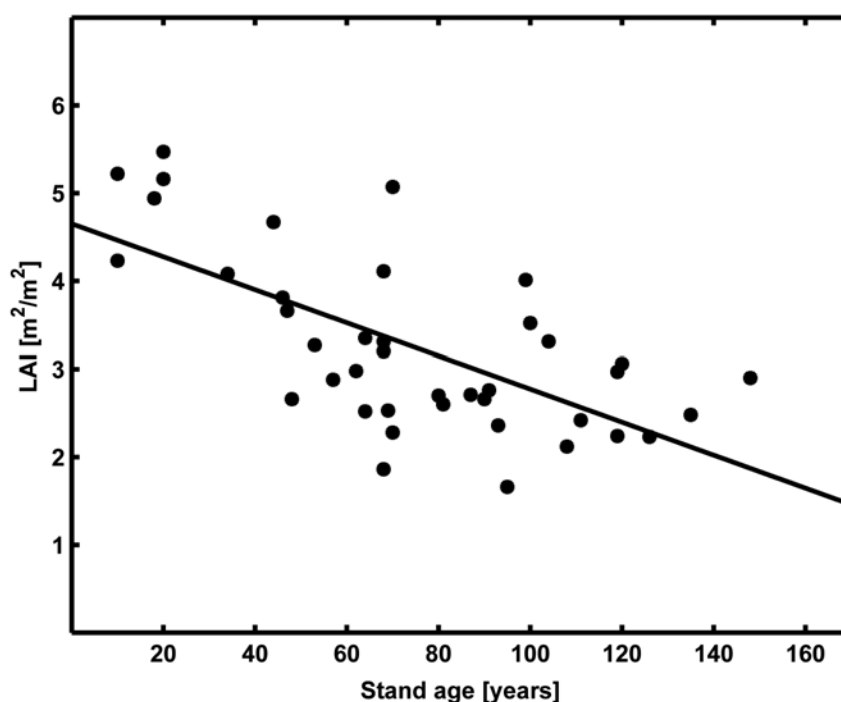


Figure 6.1: LAI as a function of stand age for Norway spruce stands at Idarwald test site (n=40).

between the individual trees (Vose et al., 1994). It has been shown that stands of slow growing species (*Pinus contora*) reached its maximum LAI at age 40 and that it lasted for about 30 years (Long & Smith, 1992; cited from Vose et al., 1994).

Prevalent forestry practices in Germany aim to maximise the profitability of a site. Thinning, the extraction of some of the young trees in a forest so that the remainder grow and develop fully, has an additional, major influence on the temporal LAI dynamic. At Idarwald, after a maximum LAI value at an age of 20-30 years is reached, stands of Norway spruce are usually thinned at an age of 30-50. Therefore, relatively low LAI values can be expected. After 60-70 years an increase in LAI may take place up to an age of 100 where logging can lead to gaps in

Table 6.4: Linear correlation between forest stand attributes and HyMap reflectance resampled to TM spectral bands (n=40); ** correlation coefficient significant at $P < 0.01$, * correlation coefficient significant at $P < 0.05$

Stand variable	TM3	TM4	TM5
Perimeter-at-breast height	-0.60**	-0.80**	-0.55**
Stem density	0.72**	0.86**	0.66**
Canopy cover	0.41**	0.69**	0.38*
Canopy height	-0.57**	-0.84**	-0.57**
Leaf area index	0.36*	0.76**	0.33*
Stem biomass	-0.50**	-0.64**	-0.51**

the canopy cover. Depending on the application of thinning measures, maximum variation of LAI can be expected at age 30-70 (personal communication Wagner, Womelsdorf; cited from Vohland, 1997).

In Figure 6.1, LAI is plotted against stand age for the probed Norway spruce stands of Idarwald test site. Here, a peak LAI can be assumed at an age of 20. From an age of 20 onwards, a gradual decline in LAI from up to age 150 is evident. Maximum variation of LAI occurs at age 60-70. Obviously, some stands have been thinned lately whereas others have been thinned long time ago. After an increase of LAI up to age 100 a decrease of LAI is caused by gaps related to logging measures. It can be concluded that the observed age course of Norway spruce based on the probed sample is a result of both natural circumstances and actual management practices. Concurrently, regeneration of leaf area index subsequent to thinning measures is also determined by the water and nutrient supply of a particular site. It is also clear from Figure 6.1, that LAI can vary considerably within a single age class and thus, information on LAI can not simply be derived from an age class map.

At first, relationships between the forest stand attributes and single band reflectance were examined (Table 6.4). The stand attributes were most strongly correlated with TM4 and less correlated with TM3 and TM5. Correlations were positive for stem density (SD), canopy cover (CO), and LAI and negative for perimeter-at-breast height (PBH), canopy height (H) and stem biomass (SBM). PBH, SD, and H were more strongly correlated with reflectance whereas CO, LAI, and SBM were less correlated with reflectance. Attributes related to canopy cover (LAI, CO) are usually expected to have negative correlations with red reflectance. At Idarwald, we found weak positive correlations between LAI and red reflectance (TM3). However, red reflectance varied only between 2.7 and 3.0 percent and possibly, saturation in the red has already occurred at low LAI values. Another explanation could be, that green leaves and the underlying soil and litter have similar reflectances in the red and that an increase in LAI or CO would not have an influence on red reflectance. Finally, effects of shading could be responsible that old stands of relatively low LAI also have low reflectances in the red domain. One could also expect negative correlations between LAI and reflectance in the mid-IR (TM5) (Brown et al., 2000). Although we found such negative correlations for wavebands located in the water absorption features, we observed positive correlations for wavebands located at the reflectance maximum between the 1.4 μm and 1.9 μm water absorption features. Again, shading could be a possible explanation for these findings.

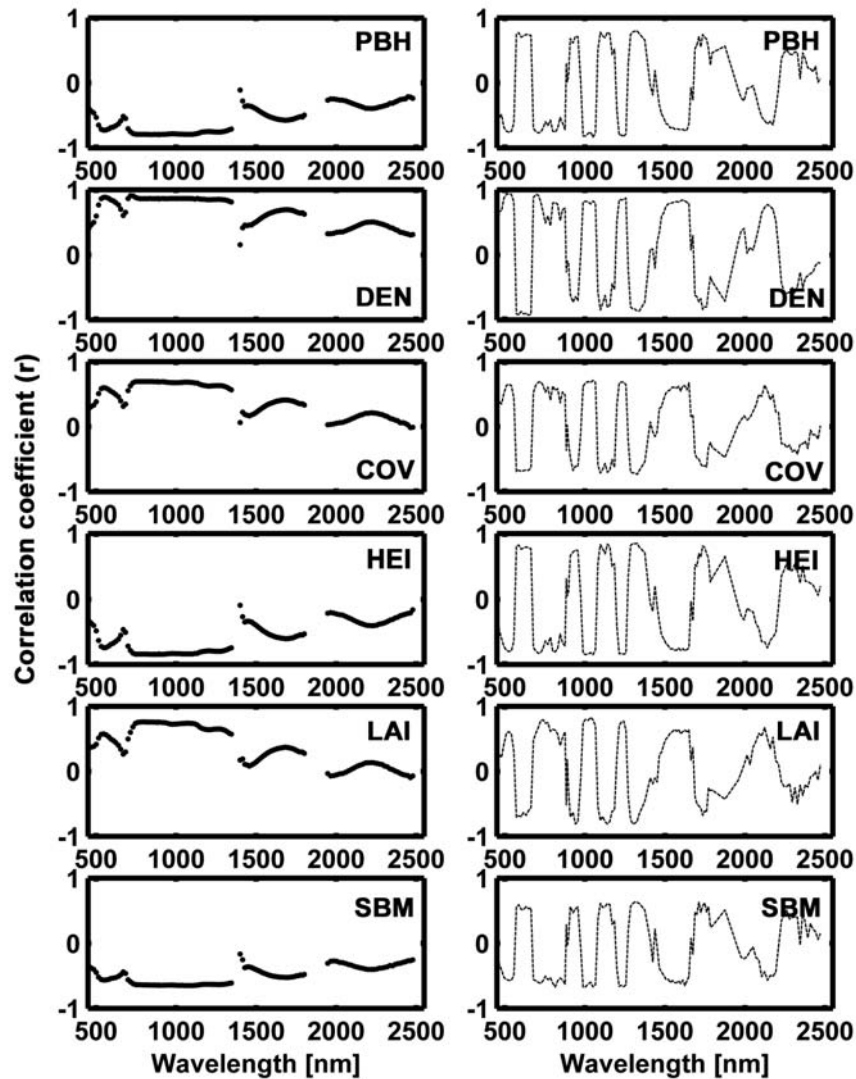


Figure 6.2: Correlograms for six stand attributes and both reflectances (left) and first derivative reflectance spectra (right) ($n=40$). Data points in first derivative reflectance correlograms are plotted as lines for clarity.

The correlation coefficients (r) between structural attributes and both reflectance and first derivative reflectance spectra are presented as correlograms (Figure 6.2). The strength of the relation generally decreased from near infrared (near-IR) to mid infrared (mid-IR) wavebands and was greater for first derivative reflectance spectra in opposition to reflectance spectra. The decreasing r values with increasing wavelength from the near-IR to the mid-IR reflected the decrease in signal-to-noise ratio of the data. In this respect the correlograms were similar to those reported in other studies (e.g., Curran et al., 2001). Correlations were positive throughout all wavelength regions for stem density, canopy cover, and LAI and negative for stem perimeter (PBH), canopy height, and stem biomass. The near-IR region of reflectance spectra revealed strongest correlations followed by the green peak, the mid-IR region, and the chlorophyll absorption features in the red and blue wavebands. For the correlation between

Table 6.5: Statistics of the first component factor of the varimax rotation (CF1) compared to the Eigenvector of the first principal component PC1 (n=40)

Stand variable	Specific variance CF1	Loading CF1	Loading PC1
Perimeter-at-breast height	0.1268	-0.9345	0.4638
Stem density	0.1275	0.9341	-0.4757
Canopy cover	0.5400	0.6782	-0.3972
Canopy height	0.1417	-0.9265	0.4633
Leaf area index	0.4107	0.7677	-0.4315

reflectance and LAI, similar curves were obtained in other studies (Thenkabail et al., 2000). However, one major difference was the positive correlation between LAI and reflectance in the red which has been already discussed in the previous paragraph.

From the strong intercorrelations between the stand attributes (Table 6.3) it is evident that no single variable could be regarded as causal to the reflectance in the TM bands. Therefore, the principal components (PC) were computed on the forest stand variables in order to reduce the data and generate new variables that could be correlated with reflectance. The input variables were standardized to zero mean and unit standard deviation. From the five original variables (all variables except SBM) five PC were derived. The first 3 PC explained more than 95 percent of the variability of the original dataset (not shown). The eigenvectors are vectors which define the principal component axes in terms of the original coordinate axes (Richards, 1993). The eigenvectors of PC1 revealed moderately large positive loadings on PBH and H and a moderately large negative loading on SD (not shown). While principal components analysis is often preferred as a method for data reduction, principal factors analysis is often chosen when the goal of the analysis is to detect structure. In principal components analysis we assume that all variability in a stand variable should be used in the analysis. In principal factors analysis we only use the variability in a stand variable that it has in common with the other stand variables. The goal of the various existing rotational strategies is to obtain a clear pattern of loadings, explicitly, factors that are clearly marked by high loadings for some variables and low loadings for others (Stat Soft, Inc., 2004; Harman, 1976).

Table 6.6: Linear correlation between principal components and HyMap reflectance resampled to TM spectral bands (n=40); ** correlation coefficient significant at P<0.01

Component	TM3	TM4	TM5
CF1	0.65**	0.88**	0.61**
PC1	-0.61**	-0.89**	-0.57**
PC2	-0.18	-0.02	-0.19
PC3	-0.29	-0.02	-0.28

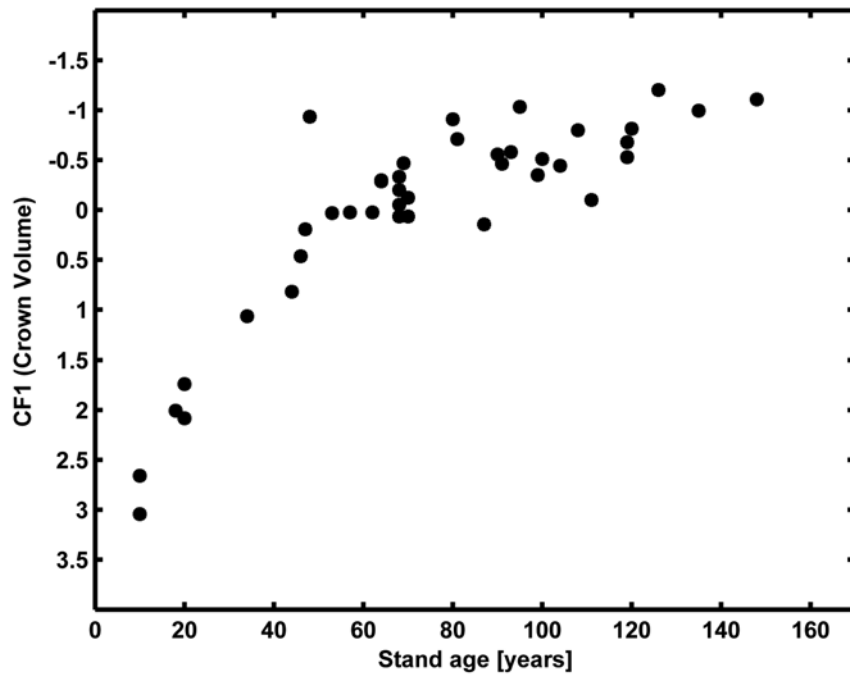


Figure 6.3: Crown volume (VOL) as a function of stand age for Norway spruce stands at Idarwald test site (n=40). A low value of CF1 corresponds to a large crown volume.

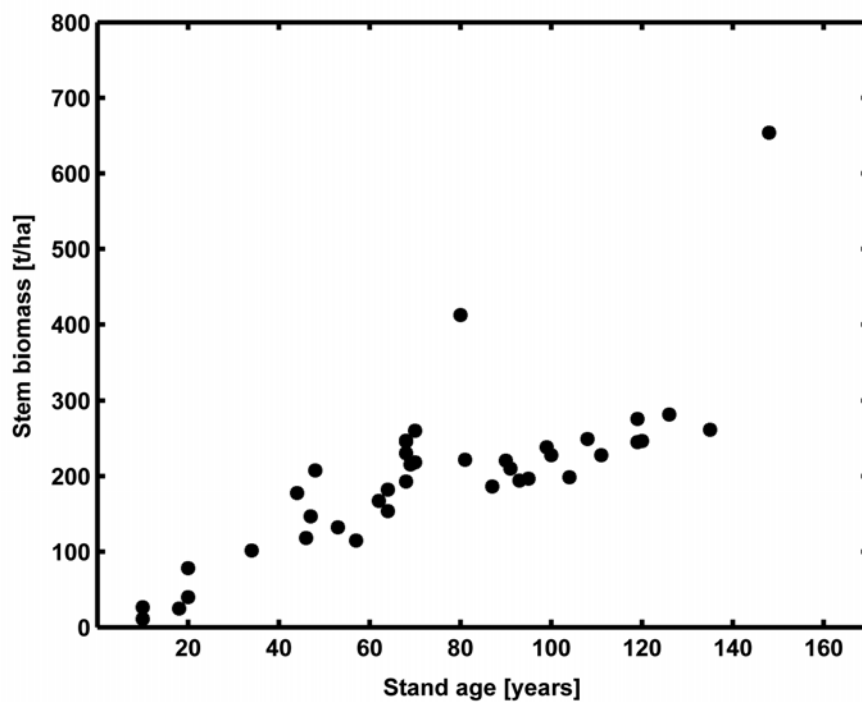


Figure 6.4: Stem biomass (SBM) as a function of stand age for Norway spruce stands at Idarwald test site (n=40).

The factor analysis was computed using the *varimax* rotation. Again, the input variables were standardized to zero mean and unit variance. After standardisation, one common factor (CF)

was computed from the five original stand attributes (Table 6.5). The p-value of 0.08 failed to reject the null hypothesis of one common factor suggesting that this model provides a satisfactory explanation of the covariation in these data. A specific variance of 1 would indicate that there is no common factor component in that attribute while a specific variance of 0 would indicate that the attribute is entirely determined by common factors. The estimated specific variances indicated that the stand attributes PBH, SD, and H are determined by the common factor. However, the common factor did not clearly represent the attributes LAI and CO. For interpretation of the common factor, its loading has to be examined (Table 6.5). CF1 has very high loadings on the variables PBH, SD, and H, but only moderately high loadings on LAI and CO. The loadings obtained by CF1 reveal a much clearer pattern than those obtained by PC1. According to the loadings of CF1, old stands consisting of large trees at low density would have low scores on CF1. It was obvious, to interpret CF1 as a variable that is inversely related to stand age. The correlation between CF1 and stem biomass was moderately strong ($r = -0.74$). Following an interpretation by Danson & Curran (1993), CF1 was regarded as a variable inversely related to crown volume (VOL).

In a next step, the common factor and the principal components were correlated with the reflectance data in the TM bands (Table 6.6). Statistically significant positive relationships were found between VOL and TM reflectance. This indicated, that stands for which a high reflectance was recorded had a high score on CF1 and thus, a low canopy volume. Also PC1 showed a close relationship to TM reflectance. No correlations were observed between PC of higher order and reflectance. From Figure 6.3 it is evident, that VOL is closely related to stand age. While up to stand age 60 a linear relationship can be observed, saturation starts at higher age.

A similar increase with stand age has also been observed for total biomass in boreal spruce (*Picea abies*) forests (Kazimirov & Morozova, 1973; cited from Schultz, 2000) but saturation did not occur before age 120. This relationship between stand age and total biomass was compared to the relationship between stand age and stem biomass (SBM). When SBM is plotted against stand age, apart from two extreme observations a curvilinear relationship is observed, but even at high age no saturation occurs (Figure 6.4). The outlier in the upper part of the plot is the oldest of all sampled stands (age = 148 years). In this stands very large values of canopy height and PBH and moderately large values of stem density were measured resulting in very large values of SBM. Despite a relatively large correlation coefficient between crown volume (VOL) and SBM of -0.74, VOL and SBM were considered as dissimilar variables in the subsequent analysis mainly due to their different dependence on stand age.

6.2.4 Relationships between vegetation indices and forest variables

Most of the linear regression models indicated that the best relationships were obtained using LAI or VOL; the regression with perimeter-at-breast height, canopy height, and stem density also provided several good relations but were not considered due to their strong intercorrelation; canopy cover was not further considered due to the strong relation to LAI. Thus, the results presented restrict to LAI, VOL, and SBM.

Narrowband VIs

To determine optimal narrowband VIs, coefficients of determination (R^2) between all possible two-band VIs and forest stand variables were computed. The results are illustrated in 2D-

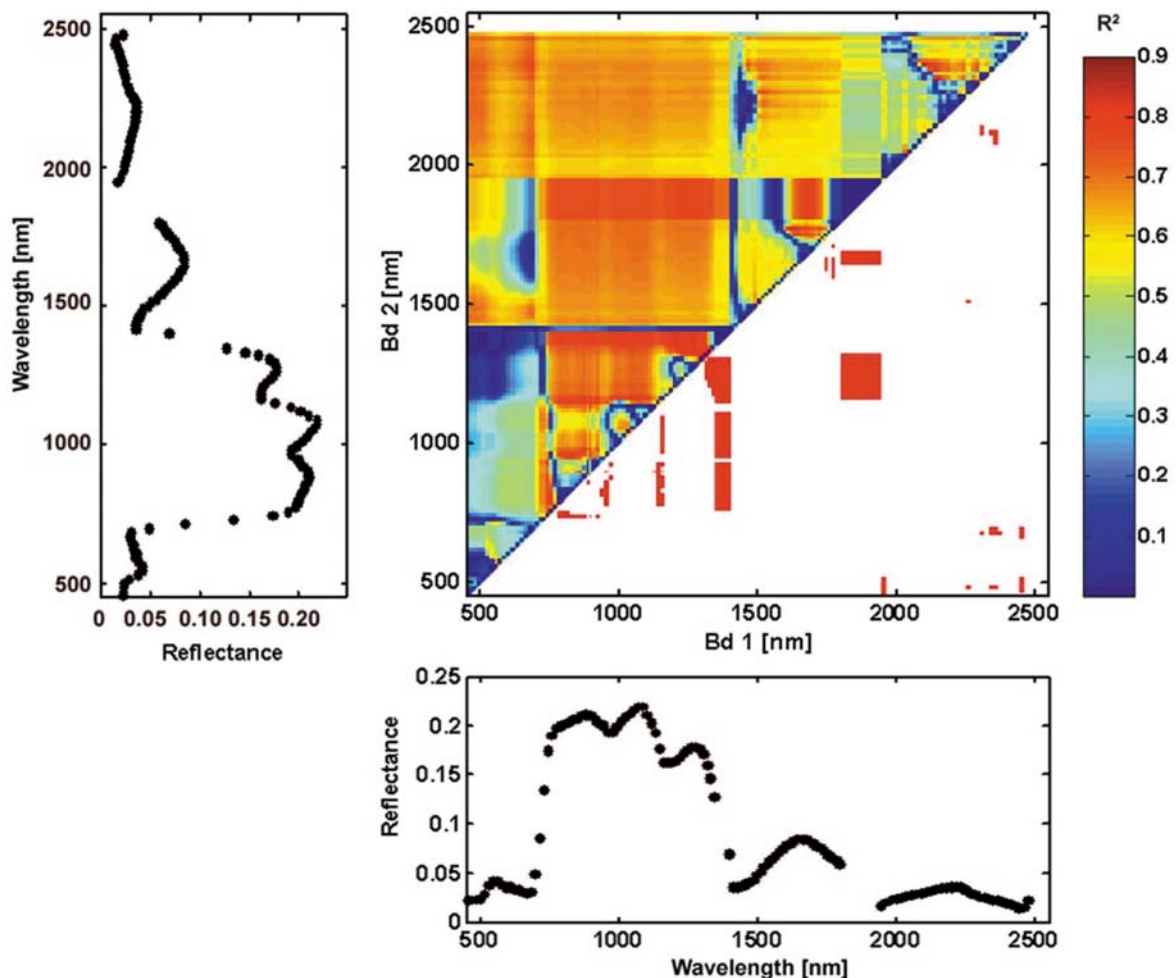


Figure 6.5: 2D-correlation plot that shows the correlation (R^2) between LAI and narrow band RVI values (subset m). The matrix is symmetrical, therefore just values above the diagonal are displayed. Below the diagonal, band combinations are marked in red where $R^2 > 0.75$. The displayed average reflectance spectrum of all measured forest plots eases the interpretation of the 2D-correlation plot.

correlation plots (Figure 6.5). Each point at position (band 1, band 2) in the upper triangle of Figure 6.5 represents the R^2 value between LAI and the RVI calculated from the reflectance values in that two wavebands. The lower triangle highlights band combinations where R^2 was larger than 0.75. Similar correlation plots to the one in Figure 6.5 were computed for the other biophysical variables. Based on the R^2 values in the 2D-correlation plots band combinations that form the best indices were determined for LAI, VOL, and SBM. These were considered as optimal indices and were named RVI_opt and PVI_opt. Up to three best performing indices were considered when they occurred in different wavelength regions. For example, in Figure 6.5, the indices that have highest correlation with LAI were extracted from the 2D-correlation plot range above 0.75; the three most dominant indices occur in the regions around 1346nm/1207nm, 1134nm/920nm, and 1802nm/1163nm. The band positions were then tabulated in Table 6.7. For the best performing narrow band index, cross-validated R^2 and rmse were computed (Table 6.8).

Broadband VIs

The first step in the analysis of broadband VIs was to compare ratio to soil-adjusted VIs and

Table 6.7: Best narrow band RVI and PVI derived from 2D-correlation plots for different subsets. Subset y was excluded from the analysis due to the small number of samples

	Pooled dataset (t) (10-148 years)		Medium-old (mo) (30-148 years)		Old (o) (80-148 years)		Medium (m) (30-79 years)		
	λ [nm]	R^2	λ [nm]	R^2	λ [nm]	R^2	λ [nm]	R^2	
LAI	RVI_opt	918/965	.65	896/965	.68			1346/1207	.85
		850/680	.55	1802/1043	.65	747/807	.60	1134/920	.85
		1165/750	.60	1346/1119	.65			1802/1163	.80
	PVI_opt	1088/1148	.70					918/1134	.83
		1148/807	.70	895/1134	.64	1445/2060	.56	1320/1220	.82
								2220/457	.72
SBM	RVI_opt	472/1119	.31	933/747	.31	2354/2337	.50	1279/1264	.53
	PVI_opt	777/900	.46	933/747	.32	2337/2354	.41	948/747	.46
VOL	RVI_opt	671/702	.74	996/1058	.60	2385/2042	.51	1011/1028	.74
	PVI_opt	981/1058	.82						
		1417/1070	.82	1073/981	.60	2320/2449	.41	1073/996	.69
		948/885	.82						
		747/457	.82						

to compare VIs based on visible and near-IR reflectance to those based on mid-IR and near-IR reflectance. Broadband ratio VIs (RVI and NDVI) generally showed relatively low values of R^2 and relatively high values of rmse for all subsets. The soil-adjusted broadband models (PVI and TSAVI) performed significantly better for the pooled data set; obviously, background effects related to soil and litter were reduced. Whereas younger stands revealed a denser canopy with little background contribution to the signal, in older stands with gaps and a more open canopy the background may have a larger influence on reflectance. Hence, when the total age dynamic is considered, TSAVI and PVI performed better than RVI or NDVI but when age classes are considered separately no performance increase was observed. The findings of Brown et al. (2000), that soil-adjusted VIs compared to the RVI have a decreased sensitivity to forest LAI, could not be confirmed.

Broadband MVI was closer related to LAI and VOL than broadband RVI and NDVI (subset *m* and *mo*). The mid-IR band in combination with the near-IR band seemed to contain more information relevant to the characterisation of forest canopies than the combination of red and near-IR bands. Recently, a closer relation of forest-LAI to radiation in the mid-IR than to radiation in the visible was found by Boyd et al. (2000) for tropical vegetation; the authors put forward that this could be the case also with boreal forests. The results found in the present study also support the suggestion by Fassnacht et al. (1997) that mid-IR bands may improve LAI estimation, particularly in more open forest stands. Recently, Lee et al. (2004) stretched the importance of spectral channels in the red-edge and mid-IR regions in predicting LAI of different biomes.

Broadband versus hyperspectral VIs

In the second step of the analysis, the broadband VIs were compared to the hyperspectral VIs to see if hyperspectral indices improve the prediction accuracy. All best narrowband RVI (RVI_{opt}) and PVI (PVI_{opt}) performed better than the corresponding broadband VIs. Values of rmse of about $1 \text{ m}^2 \text{ m}^{-2}$ or larger for regression models between broadband RVI and LAI (medium-old (*mo*), old (*o*), and medium (*m*) aged stands) decreased to values as low as $0.5 \text{ m}^2 \text{ m}^{-2}$ for the optimal narrowband RVI. The improvement of the narrowband models compared to the broadband models was not that distinct in the case of the PVI. Regression between PVI and VOL over all age classes (pooled dataset) revealed almost similar results for broadband and narrowband indices. The reason that some of the broadband results were high could be from having a very high signal-to-noise ratio (SNR). However, this does not mean that sensors like Thematic Mapper could be able to reproduce these results as they would have a much lower SNR.

Table 6.8: Cross-validated R^2 (first line) and cross-validated rmse (second line) for linear regression between broadband and hyperspectral (narrowband VIs and REIP) indices and forest stand variables LAI and VOL. The best broadband and hyperspectral VIs are typed in bold. Relations with SBM were generally poor and are not listed. Subset y was excluded from the analysis due to the small number of samples

		LAI				VOL			
Subset		t	mo	m	o	t	mo	m	o
n		40	35	17	18	40	35	17	18
Broadband VI	RVI	.40	.42	.40	.17	.23	.38	.35	.26
		1.23	.92	1.05	1.67	1.9	1.7	2.9	1.9
	NDVI	.43	.44	.44	.17	.24	.34	.31	.25
		1.13	.86	.95	1.72	1.8	1.7	2.8	1.9
	PVI	.57	.29	.23	.22	.76	.35	.35	.10
		.87	1.29	1.7	1.7	.58	2.2	4.9	3.1
	TSAVI	.61	.36	.30	.24	.68	.37	.36	.07
		.80	1.06	1.35	1.55	.69	1.8	3.6	3.9
	MVI	.38	.54	.58	.35	.19	.51	.45	.15
		1.3	.71	.71	1.83	2.3	1.1	1.3	85.5
	GVI	.58	.31	.24	.24	.75	.36	.35	.07
		.85	1.2	1.62	1.55	.59	2.1	4.7	3.8
Hyperspectral VI	RVI _opt	.62	.64	.77	.57	.70	.59	.70	.45
		.78	.58	.45	.57	.68	.91	.65	1.1
	PVI _opt	.67	.45	.41	.52	.79	.58	.64	.38
		.69	.86	1.02	.58	.52	.98	.78	1.4
	LGI	.01	.58	.75	.44	.26	.46	.33	.05
		400	.64	.49	.66	5.8	1.1	1.6	16.2
	IGM	.00	.58	.72	.47	.27	.43	.27	.00
		45	.65	.53	.66	4.0	1.2	1.8	8.7

Comparing narrowband orthogonal VIs with ratio VIs revealed that PVI_opt performed better than RVI_opt (pooled dataset); for subsets *mo*, *m*, and *o*, however, RVI_opt showed lower rmse values than PVI_opt for LAI and VOL. No correlation was observed between the red edge inflection point (REIP) computed from Lagrange interpolation (LGI) or inverted Gauss model (IGM) and LAI over the total age dynamic, but for subset *m*, LGI showed an rmse value of less than $0.5 \text{ m}^2 \text{ m}^{-2}$. This value is comparable to the rmse value obtained between RVI_opt and LAI. These findings were partly supported by results obtained from other studies. Danson & Plummer (1995) found a strong non-linear correlation between plot LAI and the REIP for Sitka spruce (*Picea sitchensis*) using helicopter-borne spectroradiometer data. For the same tree species, forest LAI was recently related to the canopy REIP computed

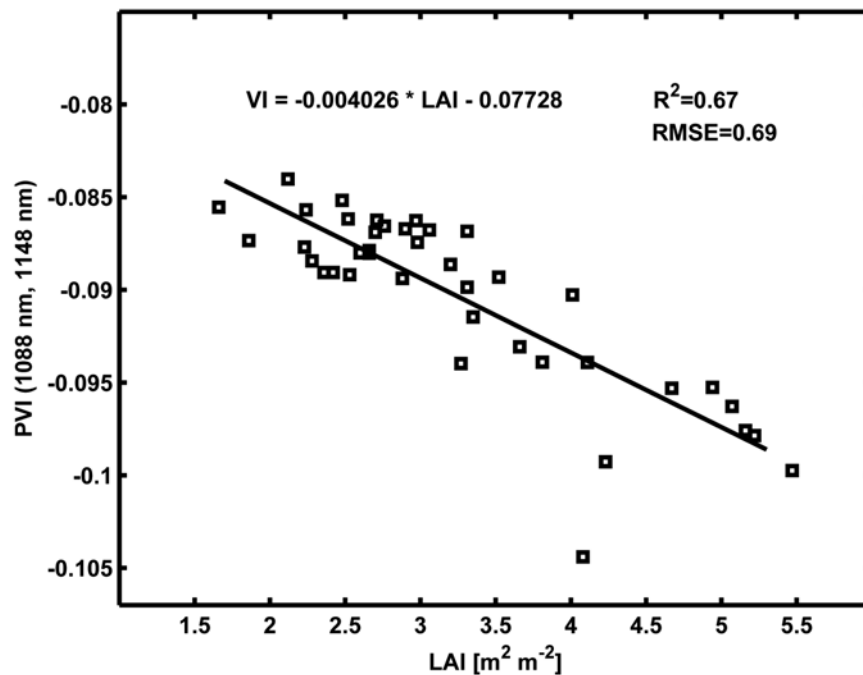


Figure 6.6: Linear regression between best narrow band PVI and LAI. Values of R^2 and rmse are cross-validated. When the outlier at position 4.1/-0.104 is removed, cross-validated R^2 increases to 0.77 and rmse decreases to $0.54 \text{ m}^2 \text{ m}^{-2}$.

from imaging spectrometer data (CASI) with success (Lucas et al., 2000). Attempts to relate the chlorophyll content of canopies to the REIP were successful for grass canopies (Pinar & Curran, 1996), but only partially successful for forest canopies (Curran et al., 1991). Blackburn (2002) found no relation between REIP and LAI for coniferous stands using CASI data.

In a summary, it was concluded that the best relationships between remotely sensed reflectance and forest stand variables were found using LAI and crown volume (VOL). In a study on agricultural crops, Thenkabail et al. (2000) also found the closest relations between hyperspectral VIs and LAI or biomass, whereas relationships with crop height, and canopy cover were generally not as good. The major result of the present study was that the hyperspectral dataset contained more information relevant to the estimation of the forest stand variables LAI and VOL than multispectral data. Lee et al. (2004) came to the conclusion that regression models using AVIRIS channels performed better to predict LAI than those based on broadband data. However, the advantage of hyperspectral over multispectral data does not always seem to be the case: For instance, Broge & Mortensen (2002) came to the conclusion, that hyperspectral VIs derived from field spectral measurements were not better at estimating green crop area index (a variable related to LAI) than traditional broadband VIs. Then again, these authors found that the prediction of canopy chlorophyll density was improved using narrow bands across the red edge. Results of the present study concerning old stands show,

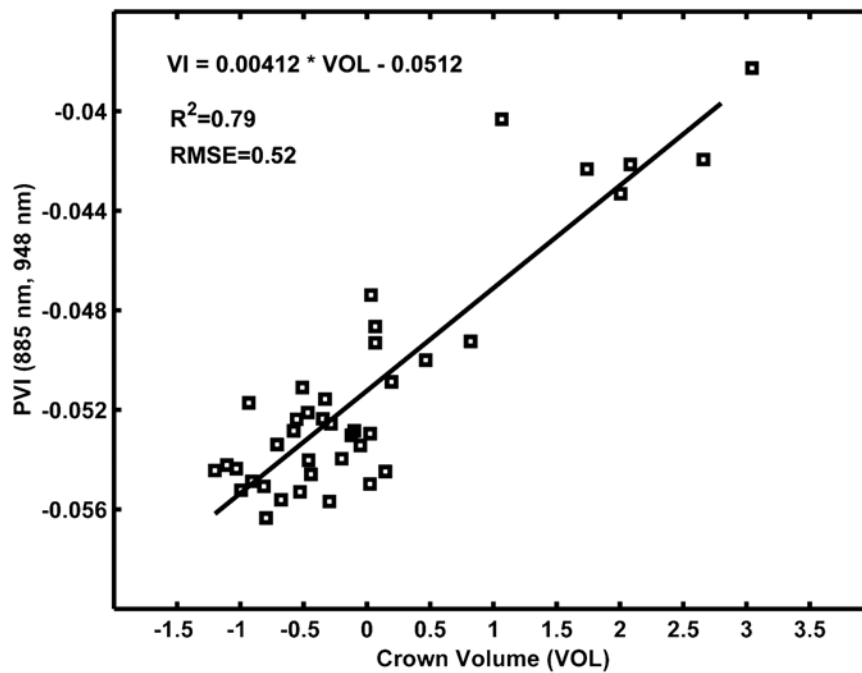


Figure 6.7: Linear regression between best narrow band PVI and crown volume. Values of R^2 and rmse are cross-validated. A high value of VOL corresponds to a low crown volume and vice versa.

that relatively poor relationships were found in particularly for the broadband VIs. Also other studies reported problems with old stands that have been ascribed to shadow effects and a relatively dark background in the near-IR (Spanner et al., 1990a).

In the scatter plot between PVI_{opt} and LAI (Figure 6.6), even at high values of LAI no saturation is evident. A closer look reveals an outlier at position 4.1/-0.104. The corresponding forest stand of age 34 was identified in the image data. Whereas the 1999 image showed no abnormality in reflectance, in recently acquired HyMap data of 2003, a striped pattern was detected. From the spectral reflectance properties, the image pixels representing stripes could be identified as a mixture between tree crowns and forest litter. The striping pattern was caused by open strips that had been cut into the forest between the image acquisition and field measurements. Open strips allowed for the employment of harvesters in order to remove trees that had been exposed to game bite (Womelsdorf, G., personal communication).

Also the relationship between PVI_{opt} and VOL (Figure 6.7) is linear. In contrast to Figure 6.6, two main clusters of data points can be identified. Those data points with a value of VOL larger than 1 refer to forest stands of an age less than 40 years.

6.2.5 Absorption features related to leaf area index and crown volume

The best relations between both LAI and VOL and the optimal narrowband VIs used PVIs based on wavelength positions related to water absorption features. One of the two wavebands forming PVI_opt typically lay at the shoulder of the absorption feature, the other waveband at the absorption minimum (Figure 6.8). Obviously, PVI_opt based on such wavebands is a measure of the total amount of canopy water (M_{H_2O}) seen by the sensor. M_{H_2O} (unit: kg water per m^2 ground area) depends on both leaf water content (LWC; unit: mg water per cm^2 leaf area) and leaf area index (LAI):

$$M_{H_2O} = LWC \cdot LAI \quad 6.1$$

When LWC does not vary between forest stands, PVI_opt reflects spatial patterns of LAI (Schlerf et al., 2005).

6.2.6 Maps of forest attributes

The best regression models that have been found for the estimation of LAI (Figure 6.9) and VOL (Figure 6.10) were applied to the HyMap image. Only image pixels representing conifer forest were considered. Estimated values of LAI were generally in a reasonable range. LAI values were classified into five classes for cartographic reasons. Although most of the forest stands in the LAI map appear rather homogenous, certain variation within the stands can be observed. This reflects the fact that even in highly managed forests stands do not develop evenly in space. From the interpretation of the spatial patterns prevalent in both parameter maps it can be seen that the values of the crown volume map are in general inversely related to the values of the LAI map. Young stands with low crown volume have not undergone clearing measures and reveal large LAI values. Old stands with relatively low values of LAI have built up large tree crowns. Medium old stands show the largest variability depending on to what extent clearing measures have been carried out.

From the resulting LAI map and the Forest Geographic Information System, average values

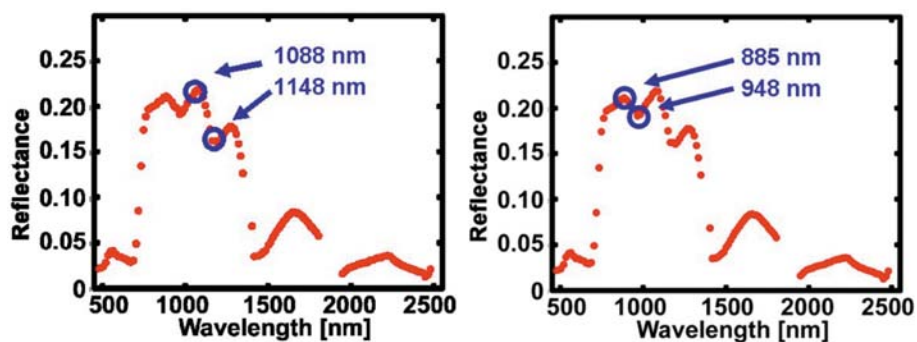


Figure 6.8: Wavelength position of selected optimal narrowband VIs for LAI (left) and VOL (right). Wavebands are associated with typical water absorption features.

Table 6.9: Summary statistics for leaf area index in five age classes

Stand age [years]	n	Leaf area index [$\text{m}^2 \text{m}^{-2}$]			
		Mean	Standard deviation	Minimum	Maximum
11-30	24	5.2	0.7	3.3	6.8
31-50	46	3.7	0.9	1.9	6.7
51-80	41	3.1	0.6	2.2	4.6
≥ 81	45	2.6	0.4	1.7	3.9

of LAI were computed for 156 forest stands (Figure 6.11). Stand average LAI was summarised into four age classes (Table 6.9). Mean LAI is generally decreasing with increasing stand age. All forest stands in the map support the age course of LAI observed for the 40 stands that have been used to calibrate the regression model (Figure 6.1) and that were then used to compute the map. Standard deviation of LAI is particularly large for the age class of 31-50 year old stands. This class also shows low minimum and large maximum values. The reason for the large variability of the 31-50 year old stands is that some stands of this age may be subjected to thinning measures while others may remain undisturbed and thinned at a later stage (Section 6.2.3).

The LAI map is a valuable resource. It was integrated into the local Forest-GIS of Idarwald. Stand LAI may serve to parameterise coarse scale ecological models (e.g., Biome-BGC) that are used to simulate net primary production and carbon, nutrient, and water cycling. The crown volume map may help to assess the amount of standing biomass in support of forest inventory procedures. Although remote sensing methods rarely play a role in operational inventory procedures, it may overcome certain limitations of traditional inventory practices.

6.2.7 Conclusions

This research intended to explore whether hyperspectral data may improve estimation of forest attributes compared to multispectral data using empirical statistical approaches. Several narrowband and broadband vegetation indices were compared. The following conclusions were drawn from this study:

- Forest leaf area index (LAI) and crown volume (VOL) were estimated with good accuracy from hyperspectral remote sensing data; stembiomass did not show relations with any vegetation index
- Orthogonal compared to ratio VIs were better suited to characterise forest LAI and crown volume
- Hyperspectral data contains more information relevant to the estimation of the forest stand attributes than multispectral data

- Best hyperspectral VIs in relation with LAI were typically based on wavebands related to prominent water absorption features. However, more investigations are necessary to confirm this result.

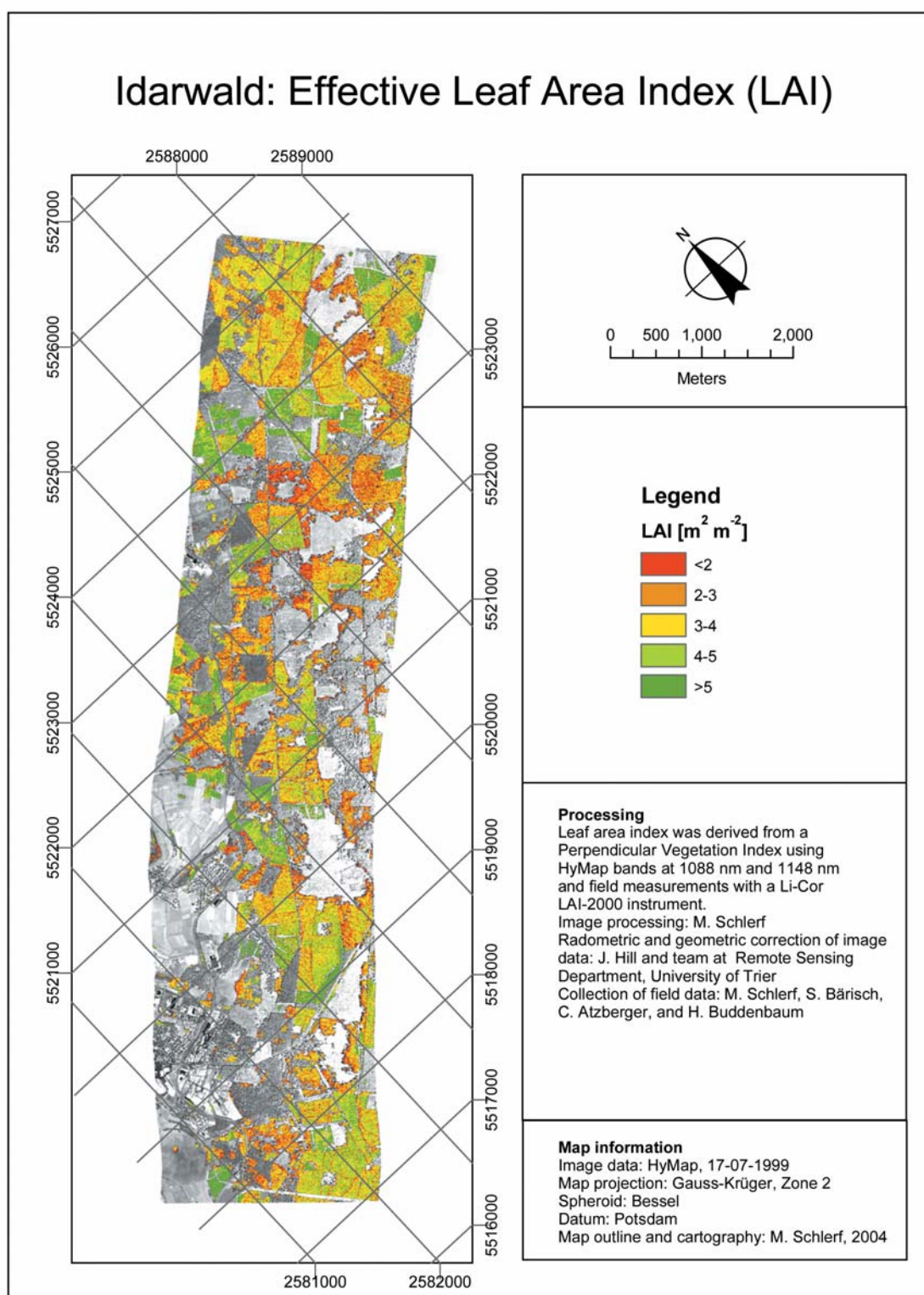


Figure 6.9: Map of effective leaf area index at Idarwald obtained from an empirically derived predictive equation.

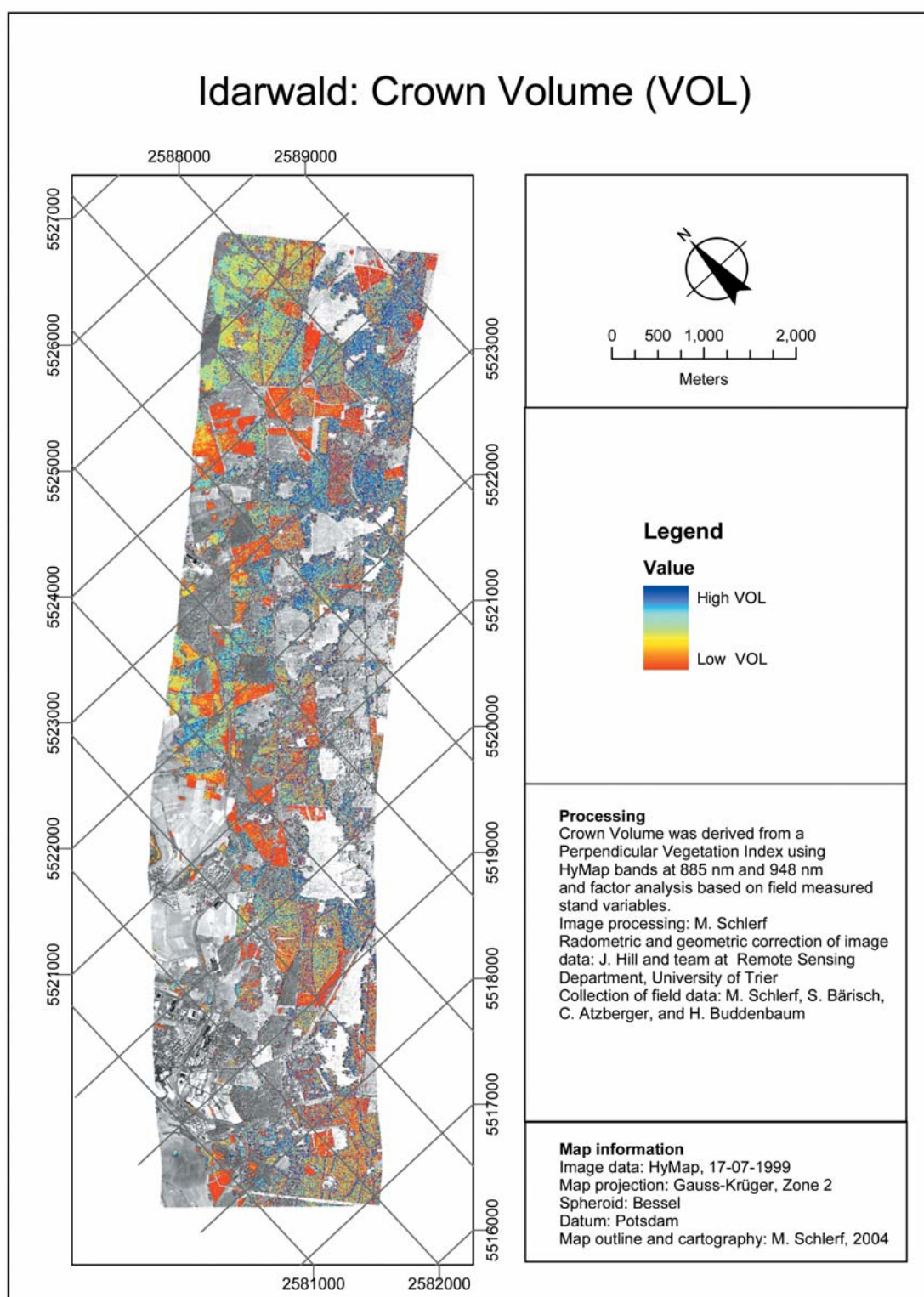


Figure 6.10: Map of crown volume at Idarwald obtained from an empirically derived predictive equation.

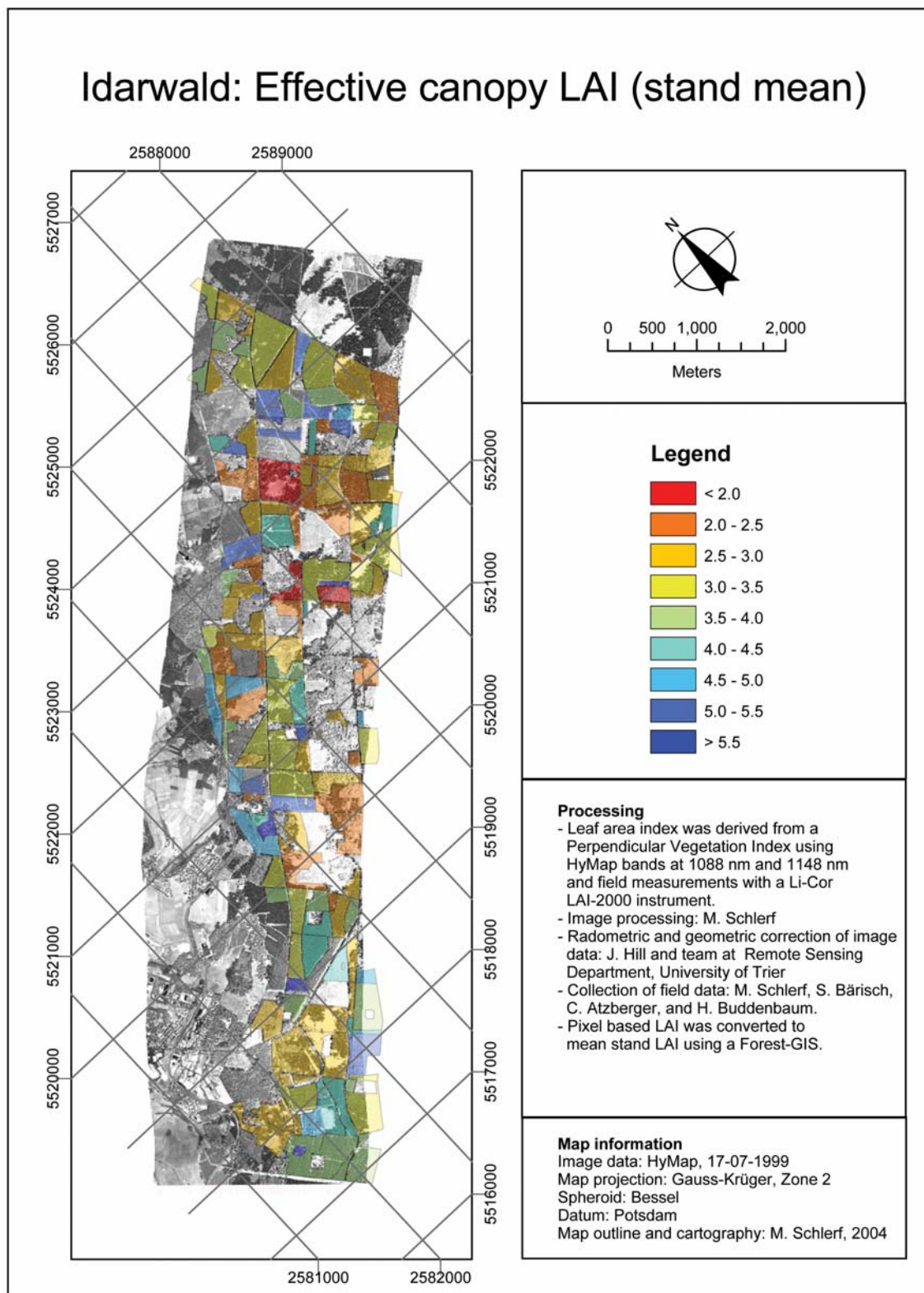


Figure 6.11: Map of stand mean leaf area index at Idarwald.

6.3 Inversion of a forest reflectance model

6.3.1 Introduction

The literature review (section 2.3.3) reveals that neural network approaches for the inversion of forest reflectance models using satellite or airborne remote sensing data that include a validation with ground truth data, are non-existing or rare. This investigation attempts to estimate forest structural characteristics from HyMap data through inversion of the hybrid-type reflectance model INFORM (Atzberger, 2000). The objectives were to i) assess if the reflectance signatures simulated by the model are consistent with the remotely sensed canopy spectra, ii) assess if the model can be inverted to provide reasonable estimates of forest leaf area index (LAI), crown cover and stem density, iii) identify the most suitable spectral bands for use in the neural network inversion procedure, and iv) and to compare inversion accuracies obtained with HyMap reflectances to those retrieved with HyMap data that had been resampled to Landsat TM wavebands.

6.3.2 Parameterisation of the forest reflectance model

A fundamental prerequisite to reflectance model inversion is a valid model that is capable of representing radiative transfer within the complex forest structure. To make sure that the model outputs were realistic, modelled reflectance was compared to reflectance measured by the HyMap sensor. Spectra were compared for canopy LAI (LAI_c) classes of 1.5, 2.5, 3.5, 4.5, 5.5, and 6.5. The LAI map developed in section 6.2.6 was used to extract mean reflectance spectra from the HyMap imagery for a certain LAI_c class value ± 0.5 . For instance, for LAI_c of 1.5, all pixels where the map showed LAI values from 1.0 to 2.0 were averaged to form a single reflectance spectrum. The LAI map had been previously derived through linear regression between a perpendicular vegetation index and field measured LAI at 40 plots; LAI had been estimated with a cross-validated R^2 of 0.77 ($n = 39$) and a cross-validated rmse of $0.54 \text{ m}^2 \text{ m}^{-2}$ (17 percent of the mean) between estimated and measured LAI. The INFORM model requires the provision of a soil spectrum (ρ_{soil}). For that purpose a soil spectrum representing the forest floor (soil and litter, no understorey vegetation) was extracted from the HyMap dataset where the LAI map showed values around zero. The contribution of understorey vegetation is modelled by INFORM. A spectrum of infinite canopy depth was extracted from image pixels with LAI values above 10 according to the aforementioned LAI map. It well agreed with the modelled spectrum of infinite canopy depth.

In INFORM LAI is a single tree LAI (LAI_s). Canopy LAI (LAI_c) can be expressed as the product of LAI_s and canopy cover (CO). CO was denoted “observed ground coverage by

Table 6.10: Relationships between canopy leaf area index and the attributes canopy cover, stem density and canopy height

Forest attribute	Regression equation	R ²	n
SD [ha ⁻¹]	140.76*exp(0.4127*LAI _c)	0.58	40
CO	0.0778*LAI _c +0.2259	0.46	40
H [m]	-5.7413*LAI _c +43.847	0.49	40

crowns (c_o)” in section 4.4.2 (Equation 4.20) and is now simply referred to as “canopy cover”. CO is calculated as a function of stem density (SD) and crown diameter (CD) (Equations 4.20 and 4.22). To model forest reflectance of a certain LAI_c, the values of LAI_s, SD, and CD and also the canopy height (H) had to be defined. Site specific information was used to parameterise the model correctly and to model corresponding forest reflectance spectra. Field plot data (section 3.2.1) was used to establish relationships between LAI_c and attributes SD, CO and H (Table 6.10). Regression equations were used to compute values of SD, H and CO for the six LAI_c classes (Table 6.11). Single tree leaf area index (LAI_s) was computed as LAI_s = LAI_c / CO.

CD was measured only in forest stands older than 60 years (n = 28) and from this data no relationship could be found with LAI_c. Typical values of CD ranged between 4 m for 60-80 year old trees up to 6.5 m for 80-100 year old trees. Generally, the size of tree crowns increases with increasing age and, due to the negative relationship between age and LAI_c found at Idarwald (section 6.2), it decreases with increasing LAI_c. To represent this relationship and to extent it to forest stands younger than 60 years, values of CD ranging from 3.5 m to 6.5 m in steps of 0.6 m were assigned to the six LAI_c classes. All attribute values used to model canopy reflectance that were directly or indirectly derived from field work are listed in Table 6.11.

The remaining external, leaf and canopy parameters were kept constant for all simulations.

Table 6.11: Inputs to the INFORM model used to compare modelled with measured reflectance spectra derived from field data and modelled values of CO and LAI_c

LAI _c	LAI _s	SD [ha ⁻¹]	CO	CD [m]	H [m]	Modelled CO	Modelled LAI _c
1.5	4.4	261	0.34	6.5	35.2	0.41	1.78
2.5	5.9	395	0.42	5.9	29.5	0.48	2.81
3.5	7.0	597	0.50	5.3	23.8	0.55	3.82
4.5	7.8	902	0.58	4.7	18.0	0.61	4.75
5.5	8.4	1362	0.65	4.1	12.3	0.66	5.54
6.5	8.9	2058	0.73	3.5	6.5	0.70	6.19

Table 6.12: Important parameters that were kept constant during all model simulations. Type of variable: E = External, C = Canopy, L = Leaf

Type of variable	Variable	Designation	Unit	Value
E	Sun zenith angle	θ_s	deg	30
E	Observation zenith angle	θ_o	deg	0
E	Azimuth angle	ψ	deg	0
E	Fraction of diffuse radiation	skyl	fraction	0.1
C	Average leaf angle of tree canopy	ALA	deg	55
C	Leaf area index of understorey	LAI _U	m ² m ⁻²	0.1
C	Average leaf angle of understorey	ALA _U	deg	45
L	Cell diameter	d	μm	40
L	Intercellular air space	i	arbitrary	0.045
L	Leaf thickness	t	arbitrary	1.6
L	Baseline absorption	b	arbitrary	0.0006
L	Albino absorption	a	arbitrary	2
L	Chlorophyll content	c _{AB}	g m ⁻²	200
L	Water content	c _W	g m ⁻²	100
L	Lignin and cellulose content	c _L	g m ⁻²	40
L	Nitrogen content	c _P	g m ⁻²	1

Leaf variables as input to LIBERTY were set to default values as proposed by Dawson et al. (1998). Average leaf angle and variables related to the understorey were set to values as suggested by Atzberger (2000). The most important parameters are listed in Table 6.12.

Six forest reflectance spectra were simulated in 128 spectral HyMap wavebands using the INFORM model. As can be seen from Table 6.11, the modelled values of CO differed to a certain extent from those that were derived from field data through regression equations. If the field values of CO were taken as an absolute reference, the model overestimated small CO values and slightly underestimated large CO values. However, field values of CO were visually estimated and a relative, but no absolute accuracy could be expected. There was also a slight difference between modelled and field measured canopy LAI but it was generally smaller than for CO.

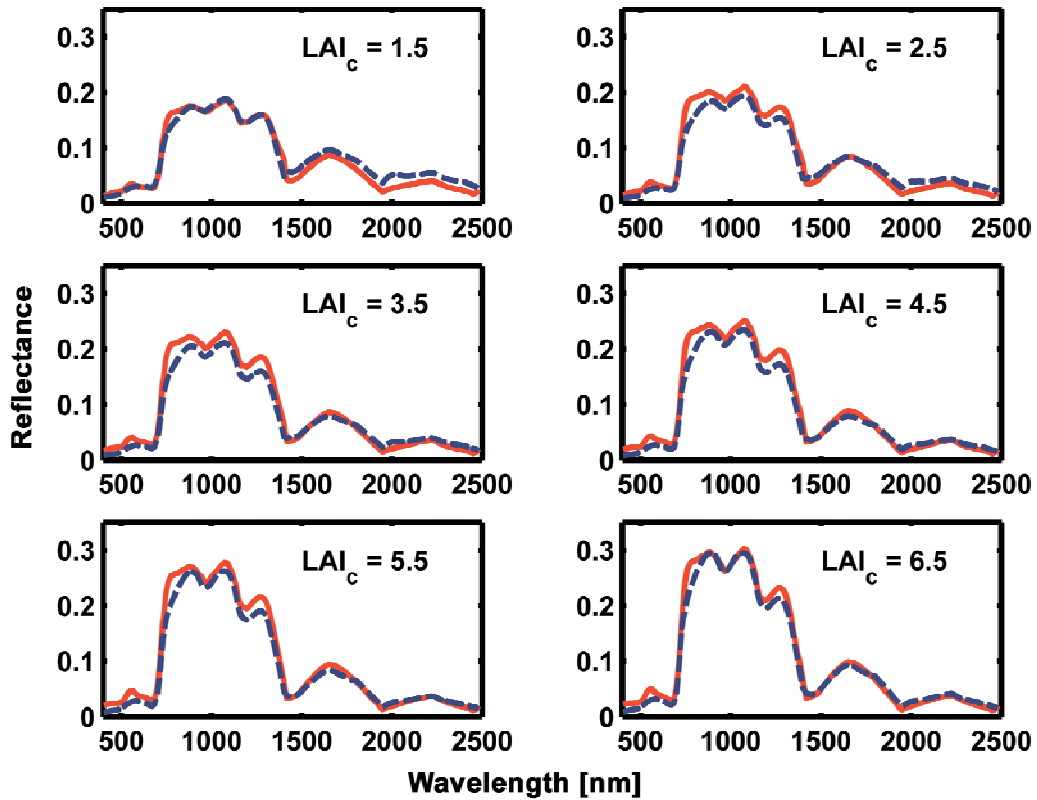


Figure 6.12: Measured (red) and modelled (blue) forest canopy reflectance for certain values of canopy LAI.

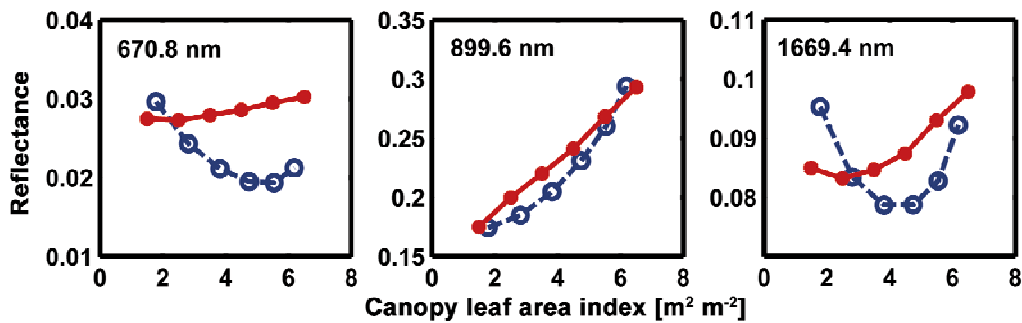


Figure 6.13: Measured (red) and modelled (blue) forest canopy reflectance against canopy LAI.

Modelled and measured reflectance spectra are generally in good agreement (Figure 6.12). In the near-IR region both types of spectra show an increase in reflectance with increasing LAI_c. Differences between modelled and measured spectra occur along the shoulder of the near-IR plateau, in the visible domain at large LAI_c-values and in the mid-IR wavebands at low values of canopy LAI. In the near-IR, both modelled and measured reflectances linearly increase with increasing LAI_c and no saturation effect can be observed (Figure 6.13, centre). Positive relationships between near-IR reflectance or NDVI and forest LAI or canopy cover were also

found in other studies that used forward reflectance modeling (Asner, 1998; McDonald et al., 1998; Eklundh et al., 2001). In the red, a decrease of reflectance with increasing LAI is expected from theoretical considerations which are confirmed by the modelled spectra (Figure 6.13, left). Here, saturation occurs at an LAI of about 4. Measured reflectance, in contrast, increases with increasing values of LAI_c in a linear fashion. The reason for this behaviour of the measured reflectances is that an increase of LAI comes along with a decrease of stand age and thus, less shadowing takes place. For the same reason, measured reflectance increases with increasing LAI in the mid-IR for values of LAI larger than 2 (Figure 6.13, right).

Up to an LAI of 4, modelled reflectance decreases with increasing LAI as expected but then increases for larger LAI values. Positive relationships between near-IR reflectance or NDVI and forest LAI or canopy cover were also found in other studies that used forward reflectance modeling (Asner, 1998; McDonald et al., 1998; Eklundh et al., 2001). For instance, model results using the Kuusk-Nilson model indicated that for dense forest stands, reflectance in the red decrease and in the near-IR increase with increasing LAI (Eklundh et al., 2001), but relations to measured reflectance were rather weak in all TM channels. However, in another study using the same model, negative relations between LAI and spectral reflectances in the red, near-IR and mid-IR were found (Rautiainen et al., 2004).

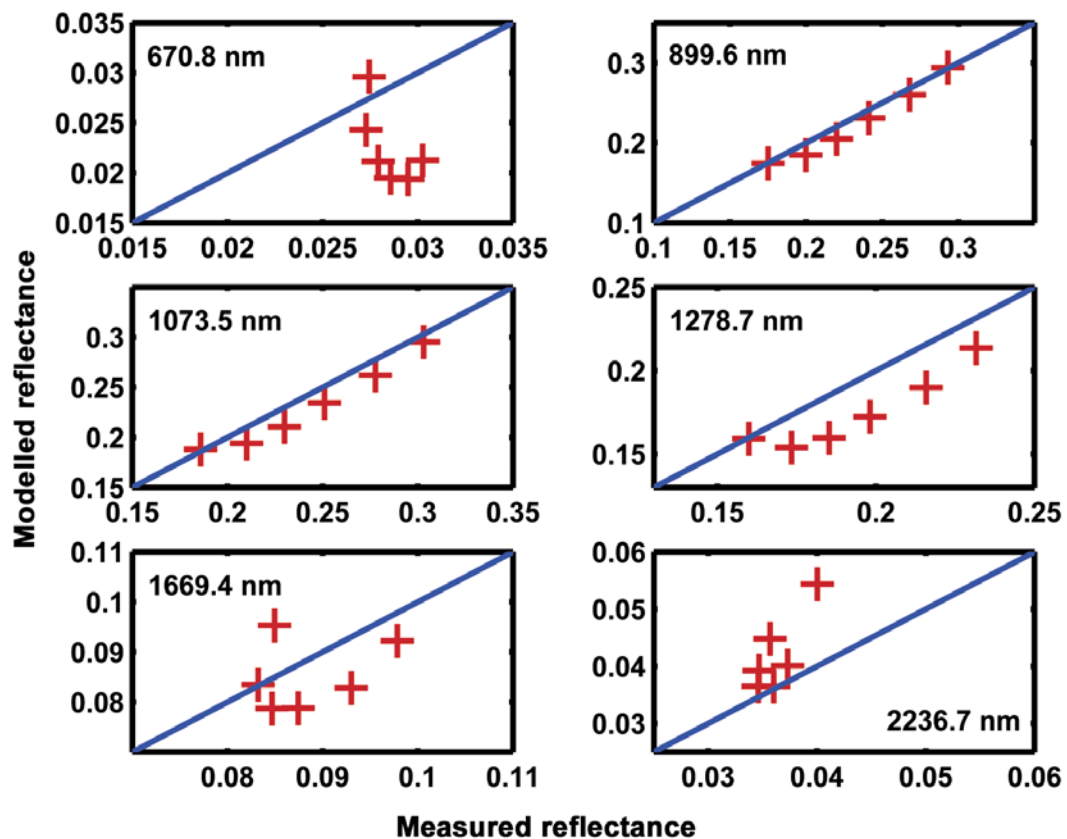


Figure 6.14: Modelled versus measured forest canopy reflectance for certain values of canopy LAI in different wavebands. The one-to-one line is shown for orientation.

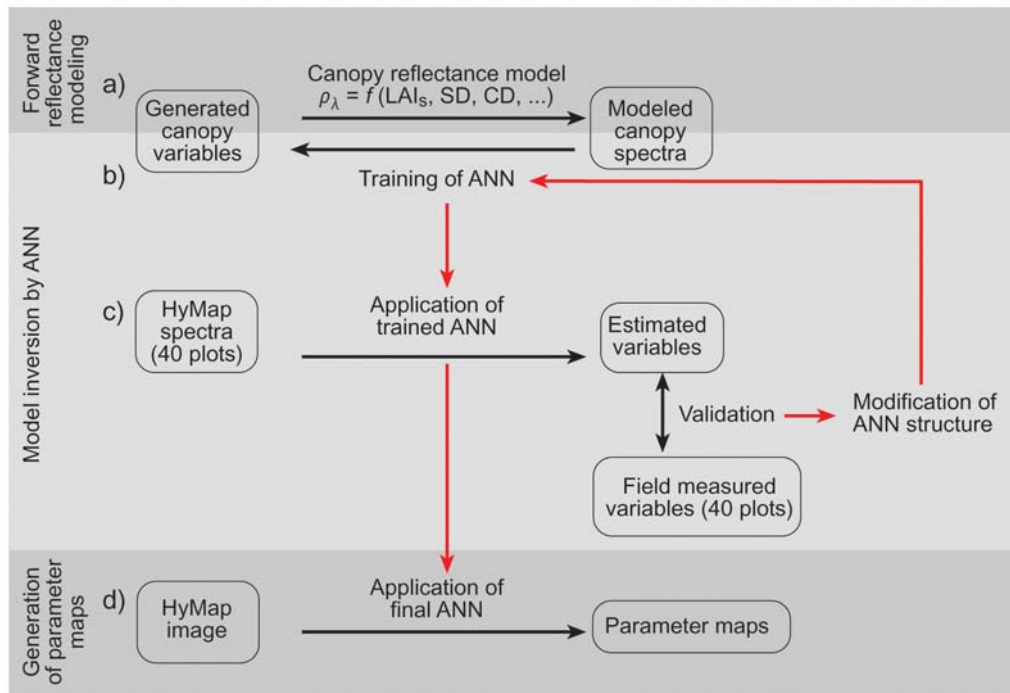


Figure 6.15: General procedure for estimating canopy attributes from remote sensing data through inversion of a forest reflectance model. See text for details.

Modelled were compared to measured reflectances in certain wavebands (Figure 6.14). The closest relation between modelled and measured reflectances occurred in the near-IR, followed by mid-IR and visible wavebands. Wavebands with best relationships were selected and used in the inversion process (section 6.3.7).

6.3.3 Overview of the inversion procedure

The general procedure for the estimation of forest attributes from remote sensing data through inversion of the reflectance model consisted of four major steps (Figure 6.15): Forward modeling to generate synthetic canopy spectra (a), training of the Artificial Neural Network (ANN) using the modelled data (b), application of the trained ANN to measured HyMap spectra to estimate forest canopy attributes (c), and the application of the ANN to the whole image to generate parameter maps (d). Details of the procedure are given in the following sections.

6.3.4 Forward reflectance modeling

Sets of input variables had to be generated to simulate forest reflectance spectra with INFORM. External parameters, leaf parameters and certain canopy parameters were assigned fixed standard values as defined in Table 6.12. Values of the canopy variables LAI_s , SD, CD,

Table 6.13: Statistics of canopy variables used to simulate forest reflectance

Variable	Mean	Std. dev.	Min.	Max.
LAI _s	6.49	1.42	4	9
SD	1217	576	200	2200
CD	5.01	0.57	4	6
H	20.42	9.26	5	37

and H were chosen randomly within the range of values observed at the study site. Their statistics are given in Table 6.13. 5000 sets of input variables were generated and the corresponding forest reflectance spectra were modelled in 128 HyMap wavebands.

6.3.5 Spectral sampling

Given a multi- or hyperspectral remote sensing data set, a selection of the bands to be used in the inversion process is recommended because those bands with larger model and measurement uncertainties would bias the retrieval (Meroni et al., 2004). However, an optimal spectral sampling is a very complex problem and is still an open issue for the remote sensing community. Recently, Genetic Algorithms have been used to find the optimal set of spectral variables to include into a model.

To compare the suitability of broadband multispectral and narrowband hyperspectral data in model inversion, simulated and measured HyMap reflectances were spectrally resampled to Landsat TM wavebands using the appropriate sensor functions. We tested all two-band and three-band combinations in TM wavebands. More than three wavebands were not considered to avoid usage of highly correlated data. It turned out that two wavebands were sufficient to invert the model. To save computation time, in HyMap wavebands just all two-band combinations were assessed, which meant to 114x113/2 times invert the model.

6.3.6 Network architecture and training

The Neural Network approach was realised within the Matlab software environment (www.mathworks.com). Training of the network was done by presenting modelled spectra and canopy variables to the ANN. During the training process, the values of the weights and biases in the network are iteratively adjusted in such a way that the error between the network outputs and the target outputs (the canopy variables) is minimised. Before the modelled canopy variables and spectra could be presented as training data to the ANN, two preprocessing steps were performed: Band selection and data normalisation.

To ensure that the training data was consistent with the real data, wavebands were selected where measured and modelled reflectances agreed best (Figure 6.14). Selection of input bands involved testing all 2-band combinations of wavebands at 899.6 nm, 1073.5 nm, 1278.7 nm, and 1669.4 nm on how well the network performed on the validation data (section 6.3.7). From the available wavebands, two were selected: one in the near-IR at 1073.5 nm and another one in the mid-IR at 1669.4 nm. More than two wavebands were not considered to avoid usage of highly correlated data. Spectra and canopy variables were normalised by a forward z-transformation. Statistical parameters of the z-transformation (mean and standard deviation) were later used to normalise the measured data in exactly the same way.

The 5000 sets of reflectance data in the selected wavebands together with the corresponding input variables were divided into a training dataset and a test dataset. The measured HyMap spectra and the field-measured canopy variables were used as validation dataset. All following assessments concerning the performance of the ANN are based on the results obtained with the validation set. Details of the validation procedure are given in section 6.3.7. The structure of the used ANN was relatively simple (Figure 6.16). It had two input neurons (equal to the number of used wavebands), one neuron in the hidden layer, and three output neurons (one for

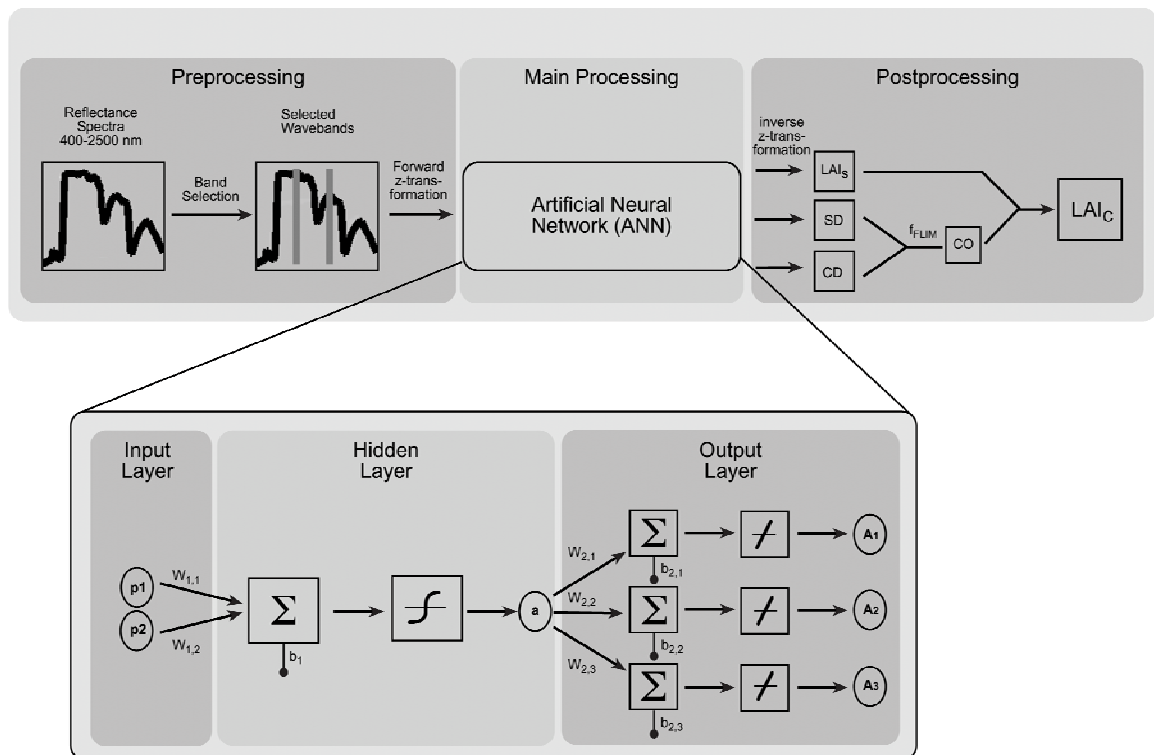


Figure 6.16: Structure of the Artificial Neural Network used to invert the INFORM model. The employed three layer feed-forward backpropagation network had two input neurons, one neuron in the hidden layer, and three output neurons. A tan-sigmoidal transfer function in the hidden layer and a linear transfer function in the output layer was used. See text for further details.

each variable to be estimated). A three layer feed-forward backpropagation network with a tan-sigmoidal transfer function in the hidden layer and a linear transfer function in the output layer was employed. The layer with the nonlinear transfer function allowed the network to learn nonlinear and linear relationships between input and output vectors. The linear output layer enabled the network to generate values outside the range -1 to 1. The employed network type can approximate any function, given sufficient neurons in the hidden layer (Demuth & Beale, 2003).

For training the resilient backpropagation algorithm was applied. The purpose of this training algorithm is to eliminate harmful effects of the magnitudes of the partial derivatives that may be caused when using steepest descent to train a multilayer network with sigmoid functions. Only the sign of the derivative is used to determine the direction of the weight changes; the magnitude of the derivative has no effect on the weight changes (Demuth & Beale, 2003). Other faster training algorithms, the Levenberg-Marquardt backpropagation and the scaled conjugate gradient backpropagation algorithm were also tested but not further considered, as the resilient backpropagation algorithm produced the best results on the validation data.

One of the main problems that typically occur during ANN training is overfitting. This phenomenon describes the situation that the error on the training data is driven to a very small value, but when new data is presented to the network the error is large (Demuth & Beale, 2003). This lack of generalisation can be avoided by using a network that is just large enough to provide an adequate fit. The complexity of a network is mainly determined by the number of neurons in the hidden layer. To find the appropriate dimension of the hidden layer, the performance of the algorithm was systematically investigated with the number of neurons in the hidden layer varying between 1 and 10; it turned out that one neuron in the hidden layer was sufficient to approximate the function between input and output vectors of the validation data.

To further improve generalisation of the network the early stopping technique (Demuth & Beale, 2003) was applied. The patterns generated with INFORM were divided into two subsets. 2500 datasets were used for training, and 2500 were used as a test dataset to prevent

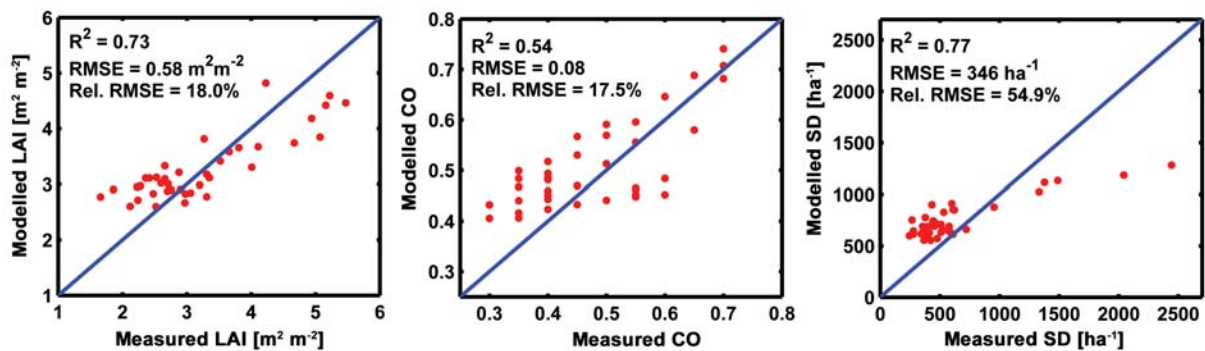


Figure 6.17: Modelled against measured forest canopy variables (n = 39).

overfitting. The training set was used for computing the gradient and updating the weights and biases. The error on the test set was monitored during the training process. During the initial training phase, both, training and test set error decreased. When the network began to overfit the data, the test set error started to rise. At this point the training was stopped and the actual weights at the minimum of the test error were returned. These weights and biases were then used to estimate the independent variables of the validation dataset.

6.3.7 Validation of inversion results and modification of network architecture

Only data from 39 plots were used for validation since one of the originally 40 plots had been thinned between the image acquisition and field measurements (section 6.2.4). The validation data (i.e. the HyMap spectra and the structural attribute data) was preprocessed in exactly the same way as the training set. That means the same wavebands were selected from the measured HyMap spectra. Both reflectances and attribute data were normalised with the same statistical parameters that had been previously used for the z-transformation of the training data. After the HyMap spectra were sent through the network, the resulting network outputs were subjected to an inverse z-transformation and from the estimated values of LAI_s , SD, and CD, estimated values of CO and LAI_c were computed using equations 4.20 and 4.22 (Figure 6.16). The coefficient of determination and the root mean squared error between estimated and field-measured forest canopy variables were calculated. Both parameters served as a measure of accuracy of the model inversion. The number of hidden neurons and input bands were systematically analysed (section 6.3.6). To generate biophysical parameter maps the trained ANN yielding the highest overall accuracy was finally applied to the radiometrically and geometrically corrected HyMap image.

Using two HyMap wavebands at 837 nm and 1148 nm, model estimated and ground LAI show relatively good agreement as indicated by the close position of most data points along 1:1 line (Figure 6.17). Low values of ground LAI are slightly overestimated whereas relatively large values of ground LAI are somewhat underestimated. The obtained accuracy of the LAI map amounts to an rmse of 0.58 (relative rmse 18 % of mean) and a coefficient of determination (R^2) of 0.73. As expected, canopy cover and stem density (both considerably determine canopy LAI in the INFORM model) behave similar with LAI with respect to the 1:1 line. Canopy cover was estimated with reasonable accuracy (rmse 17.5 % of mean). However, model outputs of stem density considerably underestimate the ground measurements for large values (rmse 55 % of mean). With HyMap data resampled to Landsat TM spectral bands and using two bands at 840 nm and 1650 nm, rmse was 0.66 and relative rmse 21 % against ground measured LAI.

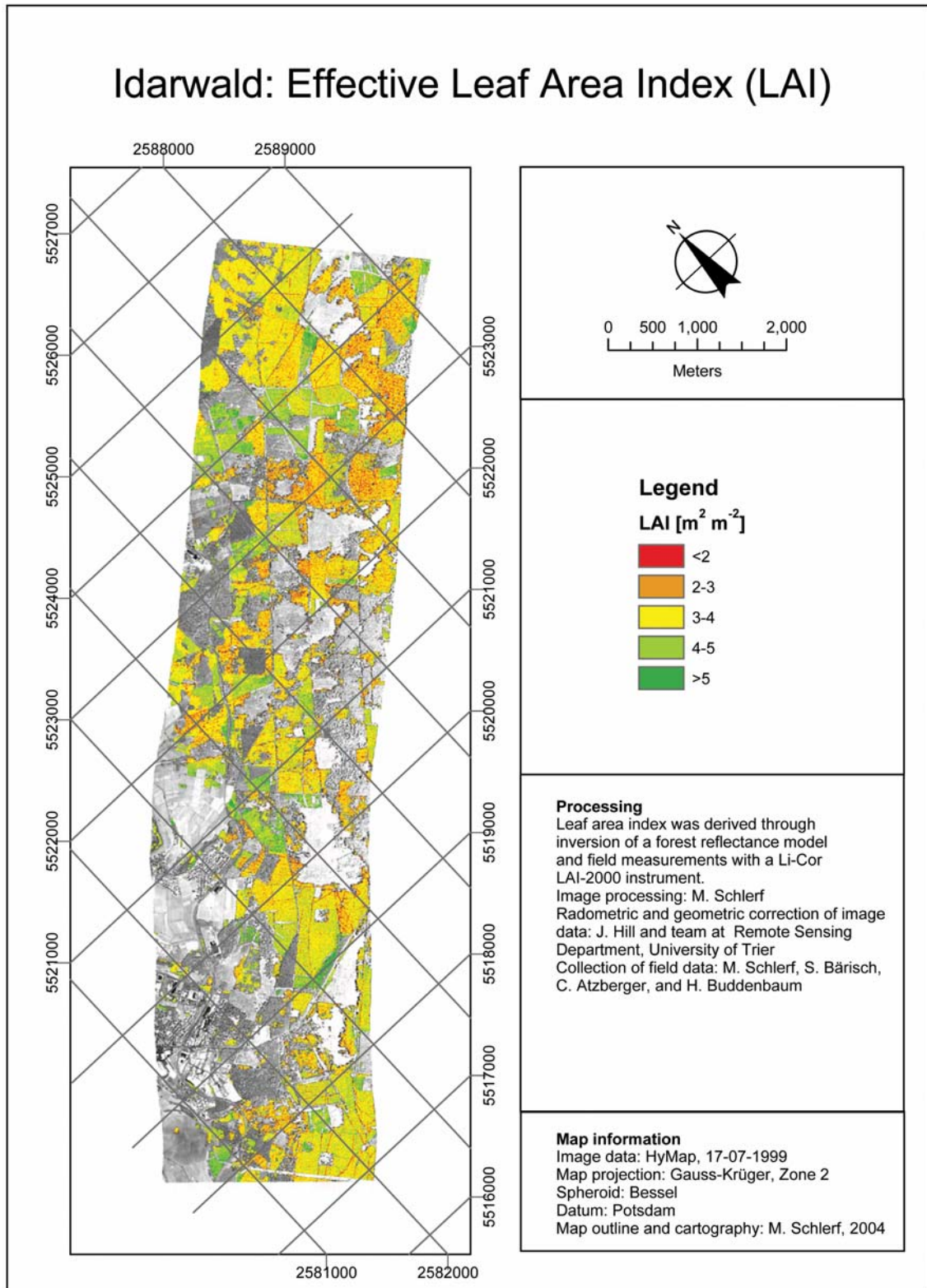


Figure 6.18: Map of effective leaf area index at Idarwald obtained through inversion of a forest reflectance model.

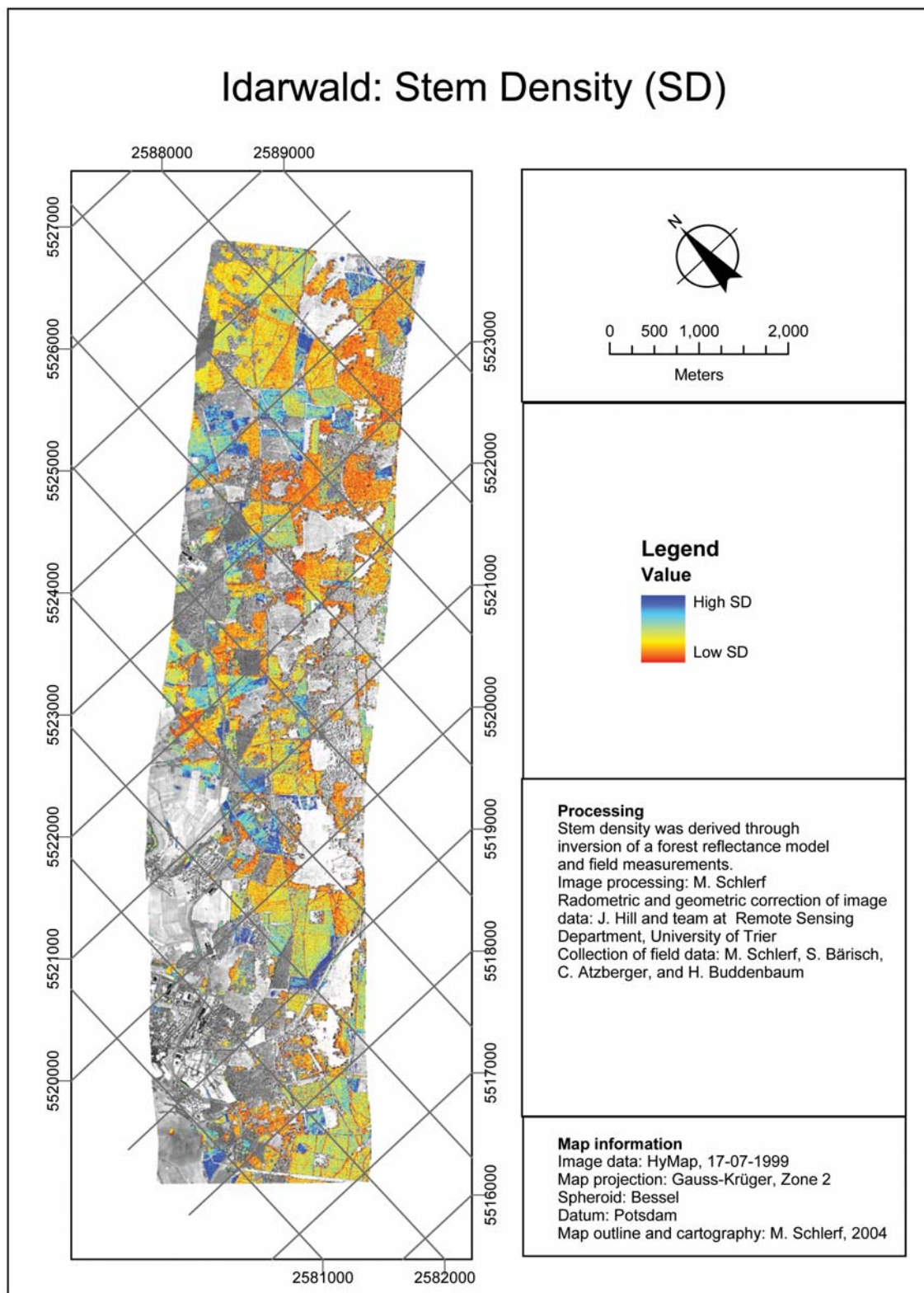


Figure 6.19: Map of stem density at Idarwald obtained through inversion of a forest reflectance model.

The main result of this research is that forest leaf area index could be estimated through inversion of a reflectance model with accuracy comparable to that of VI based approaches. These findings are supported by other studies. For instance, LAI of different vegetation types was estimated with fair accuracy (rmse = 0.70) by inversion of the Kuusk reflectance model, better than that obtained with an empirical LAI-VI relation (Bicheron & Leroy, 1999). In another work, inversion of the hybrid-type Kuusk-Nilson model performed better than NDVI when estimating forest cover from TM data, though accurate estimates on a per-stand basis were not possible (Gemmell et al., 2002). Whereas empirical approaches rely on a calibration function between a certain vegetation index and a ground measured forest variable, calibration of the reflectance model is based on synthetic data and the ground truth serves as an independent validation base. In opposition to empirically derived prediction functions that are generally limited to the local conditions at a certain point in time and to a specified sensor type, the calibrated reflectance model can be applied more easily to different optical remote sensing data acquired at landscape to regional scales (Schlerf & Atzberger, 2006).

6.3.8 Maps of forest attributes

The final neural network was applied to the entire HyMap image. Again, only image pixels representing conifer forest were considered. Estimated values of LAI were generally in a reasonable range (Figure 6.18). LAI values were classified into five classes for cartographic reasons. Stem density is presented in values ranging from low to high as estimated absolute values did not well agree with those that had been measured in the field (Figure 6.19).

6.3.9 Conclusions

If correctly parameterized, the INFORM model simulates forest reflectance spectra comparable to those measured by an imaging spectrometer (HyMap). There is a good agreement between modelled and measured spectral reflectance in the near-IR wavebands and an acceptable agreement in the mid-IR. In the visible, however, model outputs and HyMap reflectances disagree and the model has to be further improved. Our results further show that INFORM can be inverted with a neural network approach to give estimates of important structural forest characteristics. Relatively simple network architecture with just one hidden neuron proved to be suitable to solve the inversion problem. By systematically evaluating all 2-band combinations of HyMap spectral bands, the optimum band combination could be identified. Estimates of forest LAI and percent coverage show relative good agreement with ground truth data ($n = 39$). In contrast, the spectrally much less important stem density could only be estimated with fair quality. Using HyMap reflectances resampled to Landsat TM spectral bands it could be shown, that two spectral bands were sufficient to properly invert the model; usage of more spectral bands did not further improve the inversion. Compared to the results using the HyMap data, Landsat TM performed less well.

Chapter 7 Estimation of forest chemical attributes

7.1 Introduction

This chapter focuses on the estimation of foliar concentrations of chlorophyll, nitrogen and water from high spectral resolution data. The research systematically compared predictive models between different types of spectral data and foliar chemical concentrations. It is based on the spectral reflectance measurements (section 3.2.3) and chemical analyses (section 3.2.2) of Norway spruce needles collected at Gerolstein and Idarwald test sites (section 3.2.1) and the HyMap image acquired over the Gerolstein area in 2003 (section 3.3.2). Whereas chemical data from Gerolstein was used to develop predictive models, chemical data from Idarwald was used to test the predictive models. In a first step, the approach was tested on needle spectra (layer stack) measured in the laboratory and afterwards applied to forest canopy spectra measured by the HyMap sensor.

The overall aim of the work was to evaluate the information content of hyperspectral remote sensing data for the estimation of foliar chemical concentrations in forests. More specific objectives were (i) to find predictive models by stepwise multiple linear regression technique (section 4.3.2) using characteristic absorption features to estimate chemical concentrations, (ii) to systematically compare different types of derivatives of spectral reflectance regarding the accuracy of the predictive models and (iii) to examine the effects of sensor bandwidth and sensor noise on the estimations of chemical concentrations from laboratory reflectance data to assess the transferability of the techniques to remote sensing data.

Different types of derivatives of spectral reflectance have been used in combination with stepwise multiple regression (SMR) to estimate foliar chemical concentrations, such as first-derivative of reflectance (section 4.3.6), continuum-removed (CR) spectra and band-depth normalised (BDN) spectra (section 4.3.7) among others. Most of these derivatives aim to enhance the absorption feature present in vegetation spectra in the first step and SMR in the second step tries to find wavebands located in these absorption features that are related to the investigated chemicals. CR and BDN spectra were most often applied to reflectance spectra of dry leaf samples or to absorption features that are not masked by water (section 2.3.4), for instance the chlorophyll features. A technique that explicitly attempts to remove the influence

Table 7.1: Summary of data for three chemicals at two sites. C_{AB} = Chlorophyll a+b concentration, C_N = Nitrogen concentration, C_W = Water concentration

Chemical	Training data, Gerolstein test site August 2002, n=78					Validation data, Idarwald test site March 2000, n=30				
	Mean	Std. dev.	Min.	Max.	Var. coef.	Mean	Std. dev.	Min.	Max.	Var. coef.
C_{AB} [mg g ⁻¹ dry matter]	3.21	0.64	1.80	4.94	0.20	1.96	0.48	1.12	3.43	0.24
C_N [% dry matter]	1.19	0.11	0.88	1.46	0.09	1.21	0.12	1.01	1.43	0.10
C_W [% dry matter]	136.5	17.0	107.9	170.8	0.12	101.8	9.3	87.6	135.0	0.09

of leaf water from a fresh vegetation reflectance spectrum is least-squares spectral matching (LSM). LSM was modified (section 4.3.8) and combined with SMR to investigate if it allows for a better estimation of leaf nitrogen than the other derivatives mentioned before. The following types of derivative of reflectance were compared:

- Spectral reflectance (RFL)
- First-difference of spectral reflectance (DRFL)
- Continuum-removed spectra (CR)
- Band-depth normalised spectra (BDN)
- First-difference of water removed spectra (DWRS)

The following leaf chemical concentrations were investigated:

- Chlorophyll a+b concentration (C_{AB})
- Nitrogen concentration (C_N)
- Water concentration (C_W)

The next section briefly explains the general procedure of developing predictive models, that is, how the absorption features relevant to the determination of the chemicals were extracted and how the SMR method and the validation procedure were implemented. The third section shows the results obtained with the modified LSM technique to derive an additional derivative of reflectance and how it was coupled with SMR. The fourth section shows the results obtained with the laboratory spectra and the fifth section shows the results achieved with the HyMap image. The chapter ends with the conclusion drawn from this study.

Table 7.2: Five absorption features used in the regression analysis.

Denotation of absorption feature (nm)	Relation to chemical	Start [nm]	Centre [nm]	End [nm]
670	Chlorophyll a+b	548	669	760
1200	Water	1080	1201	1270
1800	Protein	1680	1790	1820
2100	Protein	2100	2145	2200
2300	Protein	2240	2308	2370

Summary statistics of chemical data from both test sites are listed in Table 7.1. From the summary statistics, it can be seen that C_{AB} has a larger variability than C_N and C_W at both test sites. Mean values of C_{AB} and C_W were significantly larger at Gerolstein than at Idarwald whereas mean C_N showed no marked difference. First year needles have higher water and concentrations but lower chlorophyll a+b concentrations than third year needles. Nitrogen concentration does not show a marked difference between first and third year needles.

A complete list of the chemical analysis data is given in Appendix B. Linear correlation coefficients between C_{AB} and C_W ($n=78$) indicate a low negative relation ($r = -0.39$) and between C_{AB} and C_N a moderate positive relation ($r = 0.58$). The closest relation is found between C_N and C_W ($r = 0.73$). To examine the potential of the method at the fresh leaf level to cope with remote sensing measurements of forest canopies, the influence of sensor bandwidth and sensor noise were considered. To do so, two additional sets of reflectance were computed from the reflectance measured by the Field-Spec-II device (F-data). Reflectance spectra of 1 nm spectral resolution were degraded to HyMap spectral bands using the appropriate sensor function (FH-data). To the degraded spectra a normally distributed noise component ($\sigma=0.002$) was added (FHN-data).

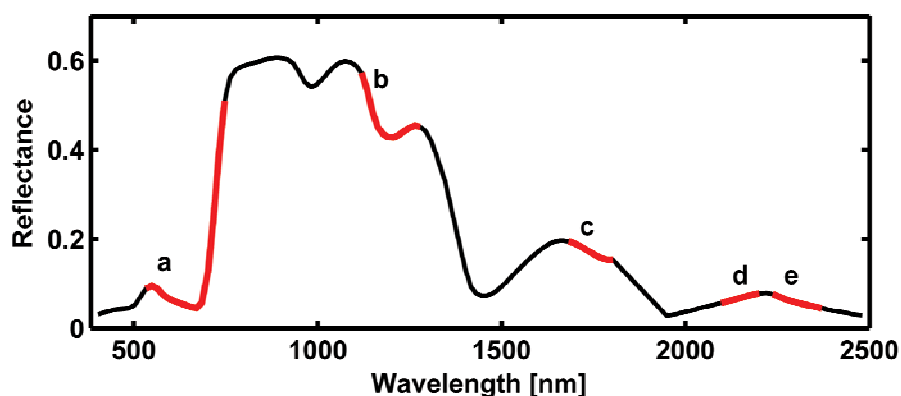


Figure 7.1: Location of absorption features related to total chlorophyll (a), water (b), and protein (c, d, e) used in the regression analysis.

7.2 Developing predictive models

7.2.1 Selection of absorption features

Kokaly & Clark (1999) used three absorption features located around 1730 nm, 2100 nm, and 2300 nm to estimate nitrogen, lignin, and cellulose concentrations. Curran et al. (2001) increased the number of chemicals under investigation and included additional absorption features into their analysis. Following both approaches, the chlorophyll absorption feature at 670 nm and the water absorption feature at 1200 nm, and three absorption features related to protein at 1800 nm, 2100 nm, and 2300 nm were included into the regression analysis in order to estimate concentrations of nitrogen, chlorophyll and water (Table 7.2, Figure 7.1). Calculation of the derivatives involved either computation of the derivative followed by an extraction of the features (RFL, DRFL) or extraction of the features followed by the computation of the derivative (CR, BDN). The five features of a single type of derivative were then re-combined into one single data set, normalised band wise to mean of zero and standard deviation of one, and subjected to regression analysis. SMR was run separately for 1st year, 3rd year, and both 1st and 3rd year needle samples. The idea was that each data set contained all information necessary to estimate all of the three chemical substances and to see if the appropriate wavebands were selected from the available bands.

7.2.2 Developing regression equations

Forward SMR was used to develop relationships between chemical concentration and a

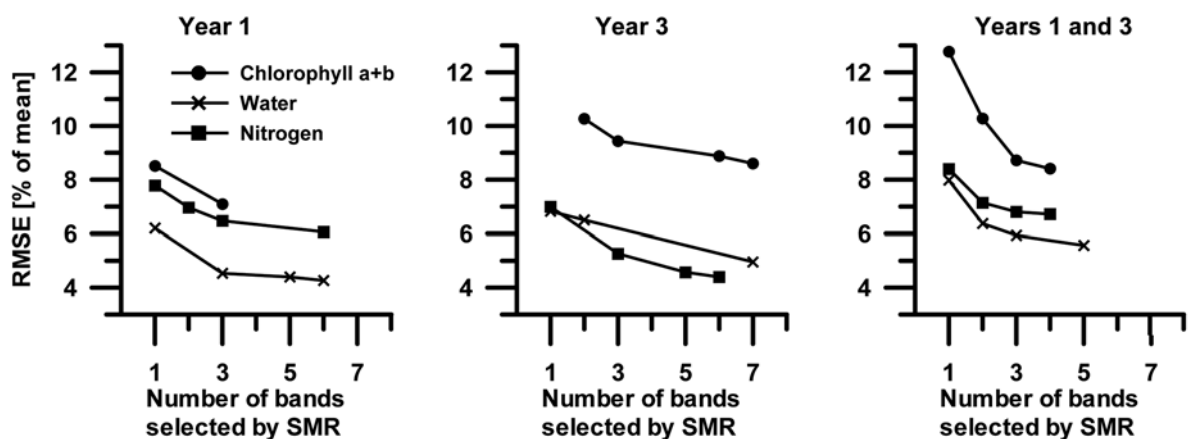


Figure 7.2: Cross-validated rmse against number of wavebands selected by stepwise multiple regression for the Field-Spec-II data resampled to HyMap spectral bands (DWRS data set). Some number of bands did not occur as a consequence of the used enter and removal criteria. DWRS refers to first-difference of water removed spectra (see section 7.3).

measure of reflectance for certain wavebands. Cross-validation was employed to assess the accuracy and validity of the regression models. This required for each regression variant to develop n (n = sample number) separate models, each time with data from $n-1$ observations. The calibration model was then used to predict the observation that was left out. Cross-validated coefficient of determination (R^2) and cross-validated root mean squared error (rmse) as well as relative rmse (rmse divided by the mean) provide performance measures for each chemical. Forward SMR was run repetitively with multiple pairs of p -values to enter (p_{in}) and remove (p_{out}) on the spectral data and the chemical data. Larger p -values often resulted in a larger number of wavebands included into the regression models. With increasing number of wavebands in the regression model, overfitting of the model can occur (Curran, 1989). If overfitting occurs, SMR may find false patterns in the data. For instance, Grossman et al. (1996) found SMR relating chemistry data and derivative reflectance spectra to give relatively large coefficients of determination even for randomised data sets. To avoid overfitting of the models, two control measures were implemented: i) cross validated values of rmse were plotted against the number of bands selected (Figure 7.2). Optimal numbers of bands were determined visually by only including a maximum number of bands where the rmse values were above the break in slope. For instance, for the estimation of C_w from DWRS data (year 1 needles), three wavebands were considered to be appropriate. An increase in the number of selected bands would not have noticeably decreased rmse. Entry and removal criteria were modified in such a way that the optimal number of bands that had been previously determined was included into the model. ii) Control runs were done with chemical data that had been brought into random order. When a control run for a particular model achieved values of R^2 larger than zero, p -values for entry and removal were decreased in such a way, that no correlation between spectral data and randomized chemical data was observed any longer. These criteria were then used in the actual model run. After taking into account both control measures, models typically included between 2 and 7 wavebands in case of the needle spectra ($n=78$ for 1st and 3rd year samples) and between 1 and 3 wavebands in case of the canopy spectra ($n=13$).

7.3 Removing water from absorption features in the mid infrared

7.3.1 Testing the modified least squares spectral matching approach

In reliably estimating leaf nitrogen concentration from fresh vegetation spectra, as main limiting factors have to be considered the leaf water that obscures absorption features related to protein and other chemical substances. If a refined methodology was developed to remove the disturbing effects of leaf water on the estimation of protein from reflectance data then it would have potential to better estimate leaf nitrogen concentration. Such a technique, least-squares spectral matching (LSM), was published by Gao & Goetz (1994, 1995, section 4.3.8).

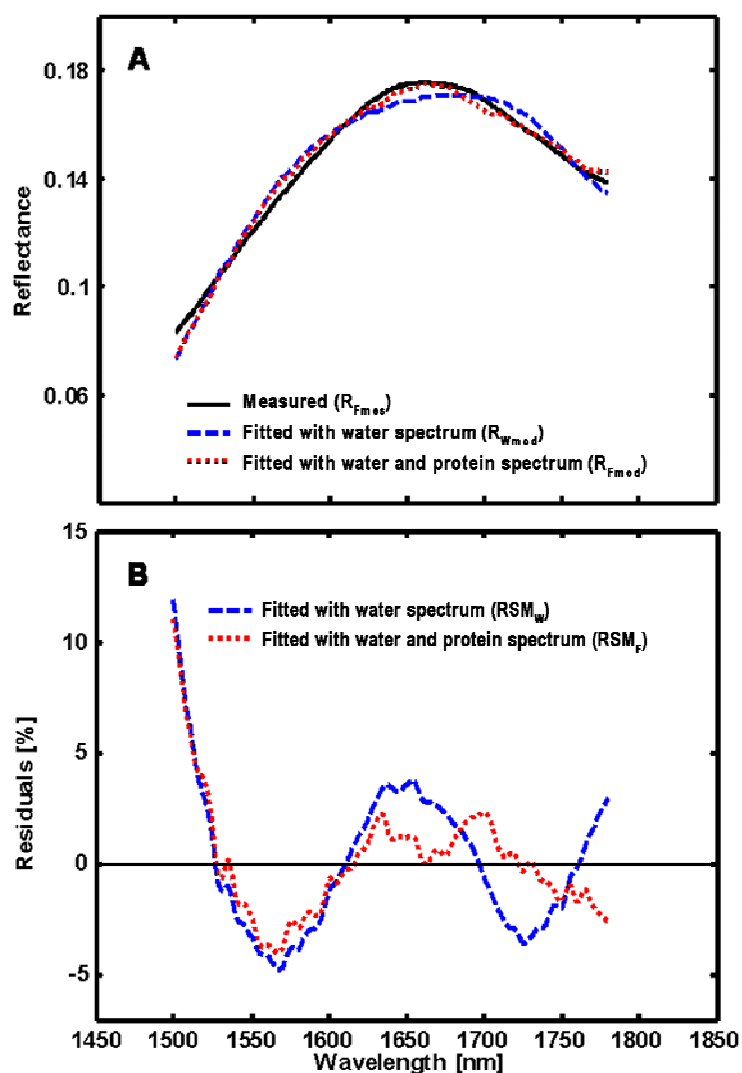


Figure 7.3: A) Matching of fresh needle (stack layer) spectrum in the 1500-1780 nm region with the water spectrum and with a combination of the water and the protein spectrum, B) residual spectra between the measured and the modeled spectra.

Table 7.3: The cross-validated coefficient of determination (R^2) and the cross-validated rmse between two sets of spectral data (features at 1800 nm, 2100 nm, and 2300 nm) and nitrogen and water for 1st year needle reflectance spectra resampled to HyMap spectral bands ($n=39$); bands: number of wavebands selected by SMR ($p_{in} = 0.10$, $p_{out} = 0.15$); units of rmse: % dry matter

Spectral data	Leaf chemical	R^2	rmse	Bands
DRFL	C_N	0.29	0.10	2
	C_W	0.53	7.37	3
DWRS	C_N	0.54	0.08	5
	C_W	0.06	10.49	2

To test the LSM technique on the measured laboratory spectra, the matching was made over a narrow spectral range between 1.50 μm and 1.78 μm located between the major atmospheric water absorption bands as suggested by Gao & Goetz (1994). To compare the goodness of the matching, the residual spectrum (Residual of Spectral Matching, RSM) was calculated which is defined as the difference between the measured fresh needle spectrum R_{Fmes} and the modelled spectrum R_{Fmod} or R_{Wmod} divided by the measured spectrum R_{Fmes} (Figure 7.3). The dashed line shows the matching of the measured spectrum of fresh spruce needles with the leaf water spectrum R_{Wmod} . Obvious differences between both spectra occur near 1570 nm, 1650 nm, and 1725 nm. The dotted line in Figure 7.3 shows the match of the measured fresh needle spectrum R_{Fmes} with a combination of the leaf water and the protein spectrum R_{Fmod} . The values of RSM at 1650 nm and 1725 nm are considerably decreased for the fresh needle spectrum compared to the water spectrum. Obviously, the reflectance spectra of spruce needles or green vegetation in general in the 1.50 μm to 1.78 μm region are both controlled by leaf water and protein. The remaining differences between the modelled fresh needle spectrum and the measured spectrum can probably be attributed to other chemicals, such as lignin and cellulose, as they also influence the reflectance spectra in that spectral region (Gao & Goetz, 1994). It could be followed that the residual of the matching of the fresh needle spectrum with the leaf water spectrum in the 1.50-1.78 μm spectral region contains information about the needle's protein concentration. As many protein absorption features are located in the 2.1-2.3 μm spectral region it was assumed that the residual in the 2.1-2.3 μm spectral region could also contain relevant information about protein. In a next step the RSM spectra were subjected to a stepwise regression procedure.

7.3.2 Coupling least squares spectral matching with stepwise multiple regression

LSM was run on the investigated absorption features at 1800 nm, 2100 nm, and 2300 nm using equation 4.16 to produce water removed spectra (WRS). To examine if LSM could remove the influence of water on reflectance spectra in this wavebands, SMR was run on the first difference of WRS (DWRS) and the first difference of reflectance (DRFL) data and concentrations of nitrogen and water. First difference of reflectance approximates the slope of reflectance (first derivative) which has a closer relation to absorption features than absolute values of reflectance (Dixit & Ram, 1985). Results of the analysis (Table 7.3) showed that for 1st year needles the R^2 between DRFL and water was larger than between DRFL and nitrogen. However, after the application of LSM to the spectra, the R^2 between DWRS and nitrogen was larger than between DWRS and water. The R^2 between spectral data and nitrogen increased from 0.29 with DRFL data to 0.54 with DWRS data. For 3rd year needles the difference between DRFL and DWRS in estimating nitrogen was less pronounced. Nevertheless, it was concluded that LSM can remove the influence of leaf water on the reflectance in relevant wavebands of the mid-IR region. At the same time, LSM may enhance absorption features related to nitrogen containing leaf constituents such as protein.

Table 7.4: The cross-validated coefficient of determination (R^2) and the cross-validated rmse between spectral data (DWRS) and concentrations of chlorophyll, nitrogen and water (year 1: n=39, year 3: n=39, year 1+3: n=78); bands: number of wavebands selected by SMR; units of rmse: % dry matter (C_W , C_N), mg g⁻¹ dm (C_{AB})

		Field-Spec-II data (F-data)			Field-Spec-II data resampled to HyMap spectral bands (FH-data)			Field-Spec-II data resampled to HyMap spectral bands plus noise (FHN-data)		
		707 wavebands			49 wavebands			49 wavebands		
		R^2	rmse	Bands	R^2	rmse	Bands	R^2	rmse	Bands
Year 1	C_{AB}	0.82	0.19	3	0.81	0.20	3	0.69	0.24	3
	C_W	0.74	5.5	6	0.60	6.8	3	0.32	8.9	3
	C_N	0.76	0.059	6	0.63	0.074	6	0.44	0.089	3
Year 3	C_{AB}	0.68	0.32	3	0.63	0.34	3	0.66	0.33	3
	C_W	0.73	5.2	7	0.63	6.1	7	0.26	8.56	2
	C_N	0.82	0.043	7	0.72	0.053	5	0.54	0.068	2
Year 1+3	C_{AB}	0.83	0.26	3	0.81	0.28	3	0.75	0.32	3
	C_W	0.78	8.0	3	0.77	8.1	3	0.57	11.1	2
	C_N	0.56	0.076	4	0.52	0.080	4	0.47	0.083	2

To compare DWRS with the other derivatives spectral data representing the chlorophyll and the water absorption features had to be used. However, for these two features water removal did not make sense (as no water effect is present in the chlorophyll absorption feature at 670 nm and water influence was not to be removed from the main water feature at 1200 nm). Thus, for the chlorophyll and water absorption features, first derivative of reflectance (DRFL) and for the protein absorption features, first derivative of water removed spectra (DWRS) were used and combined into a single data set. The dataset was denoted DWRS. By this, all spectral datasets consisted of the same number of bands (F-data: 707 wavebands, FH-data and FHN-data: 49 wavebands).

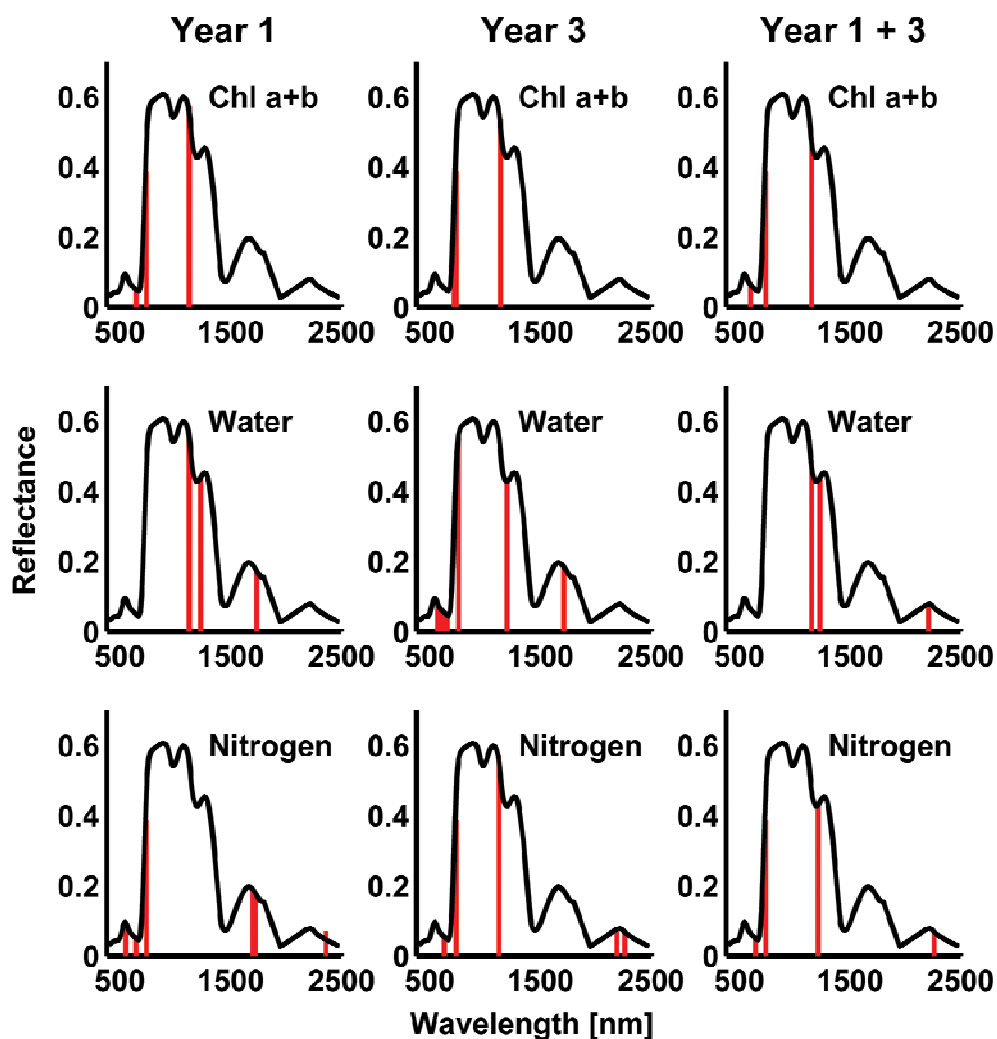


Figure 7.4: Positions of wavebands that have been selected by SMR between DWRS spectral data (resampled to HyMap wavebands) and three leaf chemicals.

7.4 Estimating leaf chemicals from laboratory reflectance data

7.4.1 Effects of sensor bandwidth and sensor noise

The first part of the analysis exemplarily used DWRS spectra to compare the performance of laboratory data (F-data), laboratory data resampled to HyMap spectral bands (FH-data), and noisy resample laboratory data (FHN-data) (see introduction in section 7.1) in estimating foliar chemicals. Cross-validated coefficients of determination (R^2) for all samples (Year 1+3) were generally largest between F-data and total chlorophyll (C_{AB}), second largest between F-data and water (C_W) and lowest for F-data and nitrogen (C_N) (Table 7.4). R^2 were generally largest between F-data and chemical concentrations and lowest for FHN-data and chemical attributes. Inversely, cross-validated values of rmse were generally lower between F-data and

Table 7.5: Wavebands that have been selected by SMR between DWRS spectral data (resampled to HyMap wavebands) and three leaf chemicals; bold: wavebands directly related to known absorption features of the chemical of interest; italic: wavebands related to known absorption features of a chemical with which the chemical of interest was correlated (indirectly related); Interpretation consists of the related absorption feature (if present) and its location (in nm) or describes the spectral region where the selected waveband is located; Wavebands appear in the order of selection by SMR

Leaf chemical	Year	Selected wavebands [nm] and interpretation
Chlorophyll a+b	1	648.5 : Chlorophyll b at 640, 739: Red edge, <i>1126.5</i> : Lignin at 1120
	3	<i>723.5</i> : Red edge, 739: Red edge, <i>1141</i> : Lignin at 1120
	1+3	601.5: Edge of chlorophyll absorption feature, 739: Red edge, 1155.5: Edge of water absorption band
Water	1	<i>1126.5</i> : Lignin at 1120, 1229 : Water at 1200, <i>1737</i> : Protein at 1730
	3	571.5: Edge of chlorophyll absorption feature, 601.5: Edge of chlorophyll absorption feature, <i>648.5</i> : Chlorophyll b at 640, <i>663.5</i> : Chlorophyll a at 660
		1199.5 : Water at 1200, <i>1712.5</i> : Protein at 1730, 761: none
	1+3	1155.5: Edge of water absorption band, 1229 : Water at 1200, <i>2210.5</i> : Protein at 2240
Nitrogen	1	556: Green peak, 648.5 : Chlorophyll b at 640, 739 nm: Red edge, 1700 : Protein at 1690, 1725 : Protein at 1730, 2362 : Protein at 2350
	3	632.5 : Chlorophyll b at 640, 739: Red edge, <i>1126.5</i> : Lignin at 1120, 2192.5 : Protein at 2180, 2262.5 : Protein at 2240
	1+3	648.5 : Chlorophyll b at 640, 739: Red edge, <i>1214.5</i> : Water, Cellulose, Starch, Lignin at 1200, 2262.5 : Protein at 2240

foliar chemicals and largest for FHN-data and leaf constituents. However, the effects of spectral resolution and noise were not the same for all chemical attributes. A decrease of spectral resolution had a minor influence on the estimation of both C_{AB} and C_W . Adding noise to the data, on the other side, strongly decreased the accuracy for the estimation of C_W , but only slightly decreased the accuracy for the estimation of C_{AB} .

Estimation accuracy for nitrogen (C_N) decreased from F-data over FH-data to FHN-data for Year 1 and Year 3 needles but remained almost constant for Year 1+3 samples. The number of bands included into the models was only slightly lower for FH-data than for F-data, but considerably lower for FHN-data. Whereas models to estimate C_{AB} always included 3 wavebands, the number of bands included into a model considerably decreased after adding noise to the data in the case of C_W and C_N . In a summary, when looking on all samples ($n=78$), C_{AB} was well estimated and just slightly affected by a decrease of the spectral resolution or adding of noise, C_N was moderately well estimated and just slightly affected by a decrease of the spectral resolution or adding of noise and C_W was well estimated with F-data and FH-data but strongly affected by noise addition. For subsequent analyses, only FH-data were considered.

7.4.2 Selected wavebands by stepwise multiple regression

The wavebands selected by stepwise multiple regression (SMR) between FH-data (DWRS spectra) and concentration of foliar chemicals are presented in Table 7.5 and Figure 7.4. Of the wavebands selected to estimate C_{AB} , only one was directly related, only two were indirectly related, and six were not related to known absorption features listed in Table 2.1. Wavebands located in the red edge region and along the edge of the chlorophyll absorption feature played an important role in the estimation of C_{AB} concentration from spectral data. This result is in agreement with a general understanding that the maximum correlations occur on the edge of absorption features as the central wavelengths become saturated (O'Neill et al., 2002; Curran, 1989). Of the wavebands selected to estimate C_W , three were directly related, six were indirectly related, and four were not related to known absorption features (Table 7.5). Regression models to estimate C_W often employed wavebands related to C_{AB} (year 3) or other chemicals (year 1) or made use of wavebands located at the edge of water absorption features (year 1+3). Of the wavebands selected to estimate C_N , nine were directly, two indirectly, and four not related to known absorption features. The first waveband selected in a regression model was often related to the chlorophyll absorption feature and the second was always located in the red edge region, reflecting the fact that chlorophyll is a major nitrogen bearing leaf constituent. The wavebands selected afterwards were often directly related to known protein absorption features as protein is the second most abundant constituent containing nitrogen.

The results demonstrate that nitrogen concentration can be moderately well estimated from reflectance spectra using wavebands related to chlorophyll and protein absorption features. Previous studies have also used statistical methods to link reflectance in certain wavebands to changes in nitrogen, protein or chlorophyll concentration. Table 7.6 presents the selection of wavebands in previous studies. Wavelengths close to protein features at 1730 nm, 2180 nm, and 2350 nm that have been repeatedly selected in these studies were also selected in the present work (Table 7.5). As in the present work, a combined selection of both, wavebands related to chlorophyll and protein absorption features in one model to estimate nitrogen concentration, had also occurred in previous studies (Johnson et al., 1994; Curran et al., 2001; Serrano et al., 2002).

Table 7.6: Wavelengths correlated with nitrogen (Nit), protein (Pro), total chlorophyll (Chl) and water (Wat) by multivariate statistical measures; Level: D = Dried, ground leaves, F = Fresh, whole leaves, CA = Canopy measured from airborne sensor; Spectral Variable: RFL = Reflectance, DRFL = First derivative of reflectance, NBA = Normalised to band area; bold: wavebands directly related to known absorption features of the chemical of interest; italic: wavebands related to known absorption features of a chemical with which the chemical of interest was correlated (indirectly related)

Authors	Species	Level	Spectral Variable	Wavelengths [nm]
Card et al., 1988	Various tree species	D	Log (1/RFL)	Pro: 2220 , <i>2110</i> , 1730 , <i>1460</i> , <i>1740</i> , 2170 Chl: 680 , <i>2110</i>
Wessman et al., 1989	Deciduous	CA	DRFL	Nit: <i>1265</i> , <i>1555</i>
Curran et al., 1992a	Amaranthus	F	DRFL	Pro: 2322 Chl: <i>724</i> Wat: <i>1752</i> , <i>1268</i> , <i>550</i> , <i>2148</i> , 1172
Johnson et al., 1994	Various conifer species	CA	DRFL	Nit: <i>552</i> , <i>1184</i> , 2164 Chl: <i>1069</i> , <i>1683</i> , <i>858</i>
Curran et al., 1997	Slash pine	CA	DRFL	Nit: 1031 , 925 , <i>1223</i> , 2341 , 916
Kokaly & Clark, 1999	Various tree species	D	NBA	Nit: <i>2036</i> , 2050 , <i>2078</i> , <i>2152</i> , 2180
Curran et al., 2001	Pine	D	DRFL	Nit: 1496 , <i>680</i> , <i>648</i> , 2352 , 2172 Pro: 1496 , 1008 , <i>1800</i> , 2352 , <i>1308</i> Chl: 622 , <i>2172</i> , <i>1496</i> , 418 , <i>2352</i> Wat: 1936 , 1216 , <i>2172</i> , 1182 , 1920
Serrano et al., 2002	Mediterranean vegetation	CA	DRFL	Nit: <i>1609</i> , 1748 , <i>480</i>

Table 7.7: The cross-validated coefficient of determination (R^2) and the cross-validated rmse between three types of spectral data (resampled to HyMap wavebands) and three leaf chemicals (year 1: $n=39$, year 3: $n=39$, year 1+3: $n=78$); DWRS: first-difference of reflectance for chlorophyll and water absorption features and first-difference of water removed spectra for protein absorption features; RFL: reflectance for all absorption features; BDN: band-depth normalized reflectance spectra for all absorption features; bands: number of wavebands selected by SMR; unit of relative rmse: % of mean

		DWRS			RFL			BDN		
		R^2	rel. rmse	Bands	R^2	rel. rmse	Bands	R^2	rel. rmse	Bands
Year 1	C _{AB}	0.81	7.1	3	0.83	6.4	3	0.81	7.1	4
	C _W	0.60	4.5	3	0.53	4.9	6	0.59	4.6	4
	C _N	0.63	6.1	6	0.54	6.6	3	0.50	7.0	4
Year 3	C _{AB}	0.63	9.7	3	0.58	10.3	3	0.39	11.1	4
	C _W	0.63	5.1	7	0.39	6.5	3	0.54	5.6	2
	C _N	0.72	4.7	5	0.64	5.2	4	0.53	6.1	2
Year 1+3	C _{AB}	0.81	8.7	3	0.80	9.0	3	0.76	9.6	6
	C _W	0.77	5.9	3	0.75	6.2	5	0.79	5.7	3
	C _N	0.52	6.7	4	0.49	6.8	5	0.52	6.6	4

Table 7.8: Wavebands selected by SMR using three sets of spectral data (resampled to HyMap wavebands) and three leaf chemicals. DWRS: first-difference of reflectance for chlorophyll and water absorption features and first-difference of water removed spectra for protein absorption features; RFL: reflectance for all absorption features; BDN: band-depth normalized reflectance spectra for all absorption features; Directly related: ± 30 nm of the chemical of interest; Indirectly related: ± 30 nm of a chemical with which the chemical of interest was correlated (approach adapted from Curran et al., 2001)

Spectral data	Leaf chemical	Number of wavebands (percent of total in brackets)			
		Total number of wavebands selected	Directly related	Indirectly related	Unattributed
DWRS	C _{AB}	9 (100)	1 (11)	2 (22)	6 (67)
	C _W	13 (100)	3 (23)	6 (46)	4 (31)
	C _N	15 (100)	9 (60)	2 (13)	4 (27)
RFL	C _{AB}	9 (100)	1 (11)	1 (11)	7 (78)
	C _W	14 (100)	0 (0)	8 (57)	6 (43)
	C _N	12 (100)	0 (0)	0 (0)	12 (100)
BDN	C _{AB}	14 (100)	2 (14)	1 (7)	11 (79)
	C _W	9 (100)	0 (0)	1 (11)	8 (89)
	C _N	10 (100)	5 (50)	0 (0)	5 (50)

7.4.3 Comparing different sets of spectral data

Three methods were compared on laboratory reflectance data. All three methodologies used SMR to develop relationships between chemical concentrations and a measure of reflectance in HyMap bands. The methods differed only in the spectral data used: First derivative of water removed spectra (DWRS), reflectance spectra (RFL), and band-depth normalised spectra (BDN). The spectra had been generated from the same five absorption features previously described. Between three and seven wavebands were selected with no marked differences in the accuracy of estimating chemical concentrations between the three data sets (Table 7.7). For year 1+3 samples, R^2 were uniformly high (>0.75) between all three forms of data and C_{AB} and C_W . R^2 were moderate (about 0.50) between all three forms of data and C_N for year 1+3 samples, but considerably larger between DWRS data and C_N than between RFL data or BDN data and C_N for year 1 and year 3 samples. There was a considerable difference between the three spectral data sets in the relevance of the selected wavebands with respect to known absorption features (Table 7.8). The total number of wavebands within ± 30 nm of the absorption feature of a chemical of interest (directly related) was largest for DWRS spectra and lowest for RFL spectra. For C_N , 73 percent of the selected wavebands were directly or indirectly related with DWRS data, but only 50 percent with BDN data and zero percent with RFL data. For C_{AB} , between 21 percent and 33 percent of the selected wavebands were directly or indirectly related with the three data sets. For C_W , the number of directly or indirectly related wavebands was 69 percent, 57 percent, and 11 percent for DWRS data, RFL data, and BDN data, respectively. The proportion of directly related wavelengths selected was considerably higher and the number of unattributed wavelengths selected was noticeably lower for DWRS data than for both other types of spectra.

7.4.4 Application of regression models to an independent data set

To determine the stability of the models, their performance with a completely different and independent validation data set than the calibration data (Gerolstein data set) was tested. The validation set (Idarwald data set) was a new set of samples measured under the same conditions as the calibration samples, however, from a different geographical site and date. To do so, relationships developed on the Gerolstein data set ($n=78$) were applied to the spectra of the Idarwald data set ($n=30$). The results were generally disappointing (Table 7.9). Coefficients of determination (R^2) between estimated and measured C_{AB} reached 0.70 with F-data and did not considerably decrease with FH-data and FHN-data. However, the relative rmse between measured and estimated C_{AB} values amounted from 25 percent up to 50 percent of the mean. For the other chemical attributes, though the values of relative rmse were comparatively low, values of R^2 were generally very low. A possible explanation for the large errors could be the time of sample collection. Samples used for calibration were collected in summer whereas collection of samples used for validation took place in spring.

Table 7.9: The performance of regression equations developed from the calibration dataset (Gerolstein) that were afterwards applied to the validation data set (Idarwald) for estimation of chemicals. Spectral data used: DWRS resampled to HyMap wavebands; units of rmse: % dry matter (C_W , C_N), mg g^{-1} dm (C_{AB}); unit of relative rmse: % of mean

		Field-Spec-II data (F-data)			Field-Spec-II data resampled to HyMap spectral bands (FH-data)			Field-Spec-II data resampled to HyMap spectral bands plus noise (FHN-data)		
		R^2	Rmse	Rel. rmse	R^2	Rmse	Rel. rmse	R^2	Rmse	Rel. rmse
Year 1	C_{AB}	0.67	0.78	45	0.67	0.47	27	0.54	0.98	57
	C_W	0.03	59.2	56	0.31	20.6	19	0.00	46.0	43
	C_N	0.04	0.16	13	0.18	0.54	44	0.43	0.44	35
Year 3	C_{AB}	0.63	1.18	54	0.46	0.63	29	0.70	0.43	20
	C_W	0.34	19.0	20	0.23	25.9	27	0.00	17.7	18
	C_N	0.23	0.13	11	0.22	0.12	10	0.31	0.24	20
Year 1+3	C_{AB}	0.70	0.92	47	0.67	0.49	25	0.65	0.76	39
	C_W	0.48	15.4	15	0.51	9.0	9	0.16	11.6	11
	C_N	0.08	0.31	26	0.18	0.37	31	0.16	0.40	33

7.5 Estimating chemical forest attributes from HyMap reflectance data

7.5.1 Scaling-up from leaf level to canopy level

Predictions of chlorophyll or other biochemical attributes from airborne or satellite canopy reflectance can be achieved through four different methodologies (Zarco-Tejada et al., 2001):

1. Establishing directly a statistical relationship between ground-measured chemical data and canopy-measured reflectance
2. Applying a leaf-level relationship derived between spectral indices and the chemical concentration to canopy-measured reflectance
3. Scaling up the leaf-level relationships based on spectral indices related to chemical attributes through models of canopy reflectance
4. Inverting the observed canopy reflectance through a canopy reflectance model coupled with a leaf model to estimate the chemical content

Methods 3 and 4 were not considered for estimating foliar chemicals in this work because the available forest reflectance model (INFORM), although it well simulated the variation of forest reflectance with changing canopy structure (section 6.3), did not prove to be very confident in modeling subtle changes of reflectance with change in chemical content in the visible domain and in parts of the mid-IR domain. Method 2 was not further considered as the application of leaf-level relationships developed on one site already showed relatively poor results when applied on another site and no improvement was expected when applying it to the canopy-level. Consequently, it was decided to choose method 1 for predicting chlorophyll, nitrogen and water concentrations from HyMap reflectance data.

To correlate chemical data with reflectances measured by the HyMap imaging spectrometer, chemical data that had been obtained on a leaf level had to be aggregated to stand level. Three different types of aggregation were performed: a) stand mean of year 1 needles, b) stand mean of year 3 needles, and c) stand mean of year 1 and year 3 needles. Canopy reflectance spectra extracted from the HyMap imagery (section 3.3.5) were processed in exactly the same way as the leaf reflectance data as described in section 7.2.1.

7.5.2 Comparing different sets of spectral data

Five methods were compared to develop relationships between chemical concentrations and HyMap reflectance (Table 7.10). Most often, one to three wavebands were selected. Relatively often, no regression model could be established. Differences in the accuracy of estimating attributes between the five types of derivatives were more pronounced than with laboratory data. None of the methods was capable in finding reasonable predictive equations to determine water concentration. Chlorophyll concentration (C_{AB}) for year 1+3 sample sets was well estimated by all methods except reflectance spectra (RFL). The best predictive model to estimate C_{AB} was achieved by band-depth normalisation (BDN) with a cross-validated coefficient of determination (R^2) of 0.90 and a cross-validated relative rmse of 2.8 percent. Continuum-removed spectra (CR) performed less accurate (relative rmse: 4 percent), but used only 2 instead of 3 wavebands in the model. Nitrogen concentration was moderately well estimated by first-difference of water removed spectra (DWRS), CR and first-difference of reflectance spectra (DRFL) using three wavebands with a relative rmse below 5 percent. For year 1 and year 3 just one or two techniques showed good results while the other techniques performed poorly. The results are comparable to accuracies obtained in other studies. For instance, Mutanga & Skidmore (2004) mapped nitrogen concentrations in savanna grass with an rms error of 8.3 percent of the mean observed nitrogen concentration using continuum-removal.

Table 7.10: The cross-validated coefficient of determination (R^2) and the cross-validated rmse between five types of spectral data (HyMap imagery) and three leaf chemicals (n=13); relative rmse: % of mean; bands: number of wavebands selected by SMR; ***: $p_{in}=0.05$, $p_{out}=0.10$; **: $p_{in}=0.10$, $p_{out}=0.15$; *: $p_{in}=0.15$, $p_{out}=0.20$; units of rmse: % dry matter (C_W , C_N), mg g⁻¹ dm (C_{AB}); unit of relative rmse: % of mean

		DWRS			RFL			BDN			CR			DRFL		
		R^2	Rmse (Rel. rmse)	Bands	R^2	Rmse (Rel. rmse)	Bands	R^2	Rmse (Rel. rmse)	Bands	R^2	Rmse (Rel. rmse)	Bands	R^2	Rmse (Rel. rmse)	Bands
Year 1	C_{AB}	0.67 ***	0.18 (6.4)	3	0.88 **	0.10 (3.5)	4	0.44 ***	0.22 (7.8)	1	0.49 ***	0.21 (7.4)	1	0.46 **	0.22 (7.8)	2
	C_W	0.17 ***	7.6 (5.1)	1	-	-	-	-	-	-	-	-	-	-	-	-
	C_N	-	-	-	-	-	-	0.35 ***	0.073 (6.0)	1	0.60 ***	0.068 (5.6)	2	0.71 ***	0.054 (4.4)	4
Year 3	C_{AB}	-	-	-	-	-	-	0.37 ***	0.30 (8.3)	1	0.75 ***	0.19 (5.3)	3	-	-	-
	C_W	0.47 ***	6.2 (5.0)	1	0.49 **	6.7 (5.4)	3	-	-	-	0.22 **	7.6 (6.2)	1	0.38 ***	6.77 (5.5)	2
	C_N	-	-	-	-	-	-	-	-	-	0.19 ***	0.069 (5.9)	1	-	-	-
Year 1+3	C_{AB}	0.72 ***	0.15 (4.7)	3	0.46 **	0.22 (6.9)	3	0.90 ***	0.09 (2.8)	3	0.80 ***	0.13 (4.0)	2	0.79 ***	0.13 (4.0)	3
	C_W	-	-	-	0.45 *	6.7 (4.9)	3	-	-	-	-	-	-	-	-	-
	C_N	0.52 ***	0.058 (4.9)	3	-	-	-	0.34 ***	0.065 (5.5)	1	0.56 **	0.058 (4.9)	3	0.57 ***	0.055 (4.6)	3

Table 7.11: Wavebands selected by SMR using five sets of spectral data (HyMap imagery) and three leaf chemicals. DRFL-DWRS: first derivative of reflectance for chlorophyll and water absorption features and first derivative of water removed spectra for protein absorption features; RFL: reflectance; BDN: band-depth normalized reflectance spectra; CR: continuum-removed spectra; DRFL: first derivative of reflectance; Directly related: ± 30 nm of the chemical of interest; Indirectly related: ± 30 nm of a chemical with which the chemical of interest was correlated (approach adapted from Curran et al., 2001)

Spectral data	Chemical attribute	Number of wavebands (percent of total in brackets)			
		Total number of wavebands selected	Directly related	Indirectly related	Unattributed
DWRS	C _{AB}	6 (100)	0 (0)	2 (33)	4 (67)
	C _W	2 (100)	0 (0)	1 (50)	1 (50)
	C _N	3 (100)	2 (67)	0 (0)	1 (33)
RFL	C _{AB}	7 (100)	0 (0)	0 (0)	7 (100)
	C _W	6 (100)	0 (0)	4 (67)	2 (33)
	C _N	0 (100)	0 (0)	0 (0)	0 (0)
BDN	C _{AB}	5 (100)	0 (0)	0 (0)	5 (100)
	C _W	0 (100)	0 (0)	0 (0)	0 (0)
	C _N	2 (100)	0 (0)	0 (0)	2 (100)
CR	C _{AB}	6 (100)	0 (0)	1 (17)	5 (83)
	C _W	1 (100)	0 (0)	1 (100)	0 (0)
	C _N	6 (100)	2 (33)	0 (0)	4 (67)
DRFL	C _{AB}	5 (100)	0 (0)	1 (20)	4 (80)
	C _W	2 (100)	0 (0)	1 (50)	1 (50)
	C _N	7 (100)	4 (57)	1 (14)	2 (29)

The analysis of the selected wavebands (Table 7.11) revealed that a smaller number of bands could be directly related to known absorption features compared to laboratory reflectance data (Table 7.8). The largest portion of directly related wavebands for estimating nitrogen concentration again showed DWRS (67 percent) followed by DRFL (57 percent) and CR (33 percent). The wavebands chosen by stepwise multiple regression to determine the other leaf chemicals could not be directly related to known absorption features. However, selected wavebands, although not attributable to known features, were often located in spectral regions that are known to be important to detect chlorophyll (Table 7.12). For instance, the predictive model to estimate total chlorophyll concentration found with CR spectra was based on wavebands located along the red edge and along the edge of the green peak. This was also the case with the regression models developed on leaf spectra. Again, maximum correlations

occurred on the edge of absorption features. These findings are in full agreement with the results of other studies where differences in reflectance between healthy and stressed vegetation due to changes in pigment levels have been detected in the green peak and along the red edge (Rock et al., 1988; Gitelson & Merzlyak, 1996; Haboudane et al., 2002).

7.5.3 Maps of leaf chlorophyll concentration and leaf nitrogen concentration

Predictive models developed using CR spectra were applied on the HyMap image to compute maps of C_{AB} and C_N . Only image pixels representing conifer forests were considered. The following predictive models between continuum-removed spectra (CR) and leaf chlorophyll concentration and leaf nitrogen concentration were applied to the HyMap image to derive the respective maps of foliar concentrations:

$$Cab_{est} = -41.7813 \cdot CR_{738} + 16.5392 \cdot CR_{585} + 33.3041 \quad 7.1$$

where Cab_{est} is the estimated chlorophyll a+b concentration and $CR_{wavelength}$ denotes the continuum-removed value of reflectance in the specified waveband (in nm).

$$Cn_{est} = -5.3535 \cdot CR_{738} + 2.7992 \cdot CR_{1157} - 8.9829 \cdot CR_{2373} + 12.724 \quad 7.2$$

where Cn_{est} is the estimated nitrogen concentration.

Table 7.12: Wavebands that have been selected by SMR between CR spectral data (HyMap imagery) and three leaf chemicals; bold: wavebands directly related to known absorption features of the chemical of interest; italic: wavebands related to known absorption features of a leaf chemical with which the chemical of interest was correlated (indirectly related); Interpretation consists of the related absorption feature (if present) and its location (in nm) or describes the spectral region where the selected waveband is located; Wavebands appear in the order of selection by SMR

Leaf chemical	Year	Selected wavebands [nm] and interpretation
Chlorophyll a+b	1	1157: Edge of water absorption band
	3	738: Red edge, 753: Red edge, 2357: Protein at 2350
	1+3	738: Red edge, 585: Edge of chlorophyll absorption feature
Water	1	-
	3	<i>2341</i> : Protein at 2350
	1+3	-
Nitrogen	1	738: Red edge, 2373 : Protein at 2350
	3	738: Red edge
	1+3	738: Red edge, 1157: Edge of water absorption band, 2373 : Protein at 2350

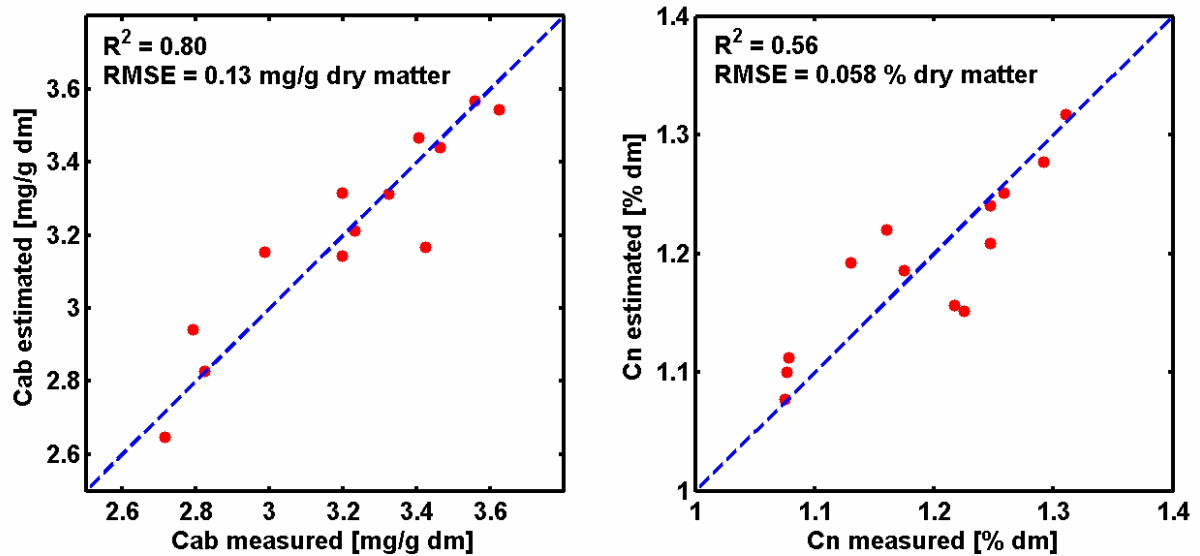


Figure 7.5: Estimated against measured leaf total chlorophyll concentration (C_{AB}) (left) and estimated against measured leaf nitrogen concentration (C_N) (right).

The scatter plots (Figure 7.5) show linear relationships between measured and estimated values of C_{AB} and measured and estimated values of C_N . The points in the scatter diagrams are close to the 1:1 line over the entire range of values indicating that no systematic underestimation or over estimation of the chemical concentrations occur.

In the chlorophyll map (Figure 7.6) and the nitrogen map (Figure 7.7), the observed values are in a reasonable range. C_{AB} values range from 1 mg/g to 6 mg/g and C_N values range from 1 % to 1.7 %. Most of the forest stands in both maps appear rather homogenous but also certain variations within the stands can be observed. From the interpretation of spatial patterns in both maps it can be noticed that C_{AB} and C_N are on the one hand interrelated to a certain extent but that on the other hand individual patterns exist.

7.5.4 Relations of foliar chemicals with other parameters

The maps of chemical forest attributes were integrated into the local Forest-GIS of Gerolstein. The Forest-GIS contained information about the tree species and the age structure on a stand base as well as the underlying geology. Statistical measures of chemicals were computed for zones of stand development phase and zones of geological epochs (Figure 7.8). Stand development phase is strongly related to stand age. Geological epoch stands for the rock types and the associated soil types that occur in the Gerolstein area and can be regarded as a measure of base saturation (Table 3.1) Mean values of chlorophyll concentration (C_{AB}) slightly increase from qualification towards maturation, but the large standard deviations indicate a substantial overlap between those classes. The same holds for zones of geological

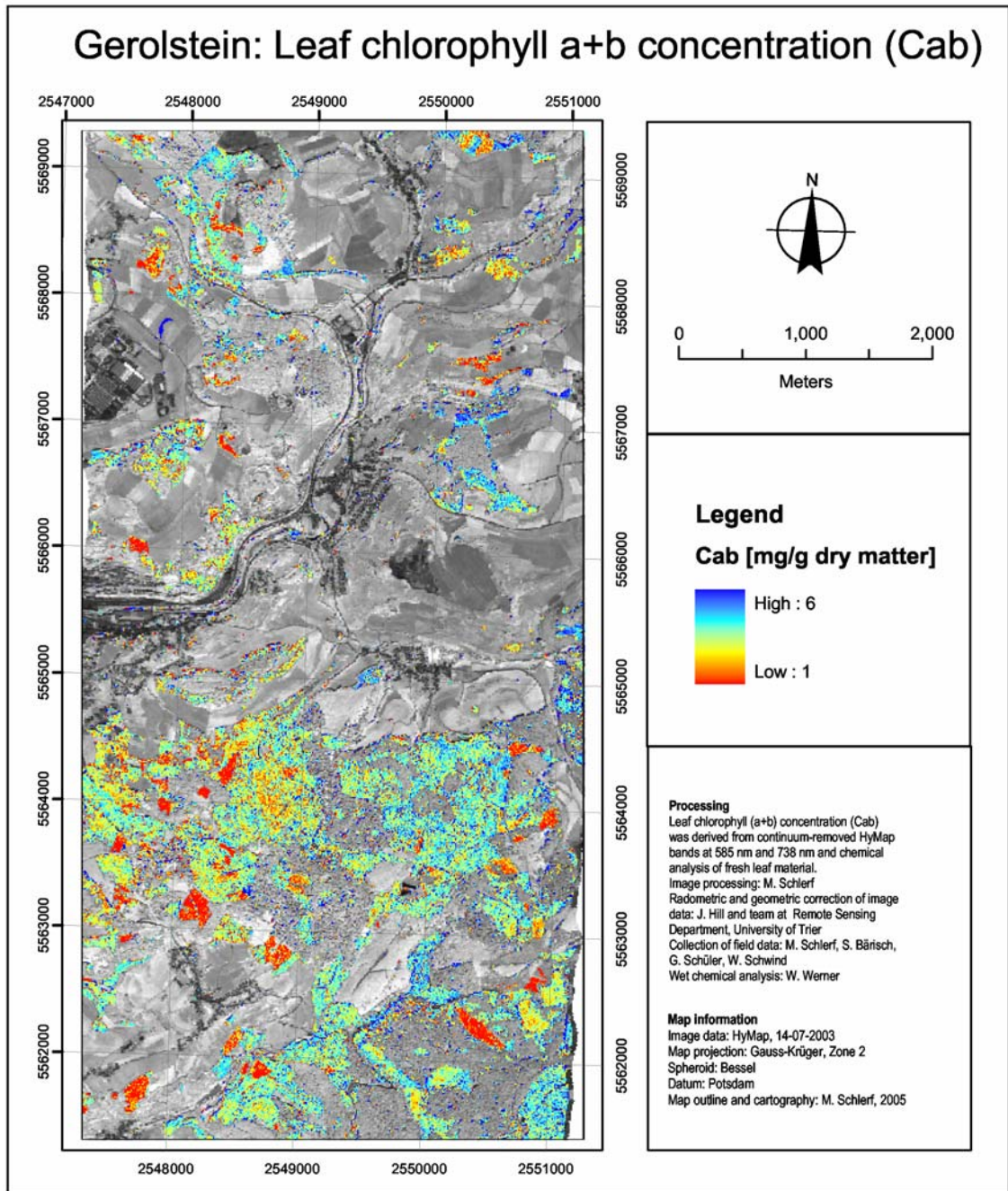


Figure 7.6: Map of leaf chlorophyll concentration at Gerolstein test site.

epochs. At Gerolstein area, each epoch is roughly represented by a single rock type (section 3.1.2). Substrates from the Holocene and Pleistocene with high base saturation showed the largest mean chlorophyll concentrations. Again, large standard deviations pointed towards substantial overlap between the classes. To receive more distinct patterns, the chemical parameter maps were reclassified into three classes of low (class 1), medium (class 2) and high (class 3) concentration. For C_{AB} , the class limits were: <2.8 (class 1), 2.8-3.4 (class 2),

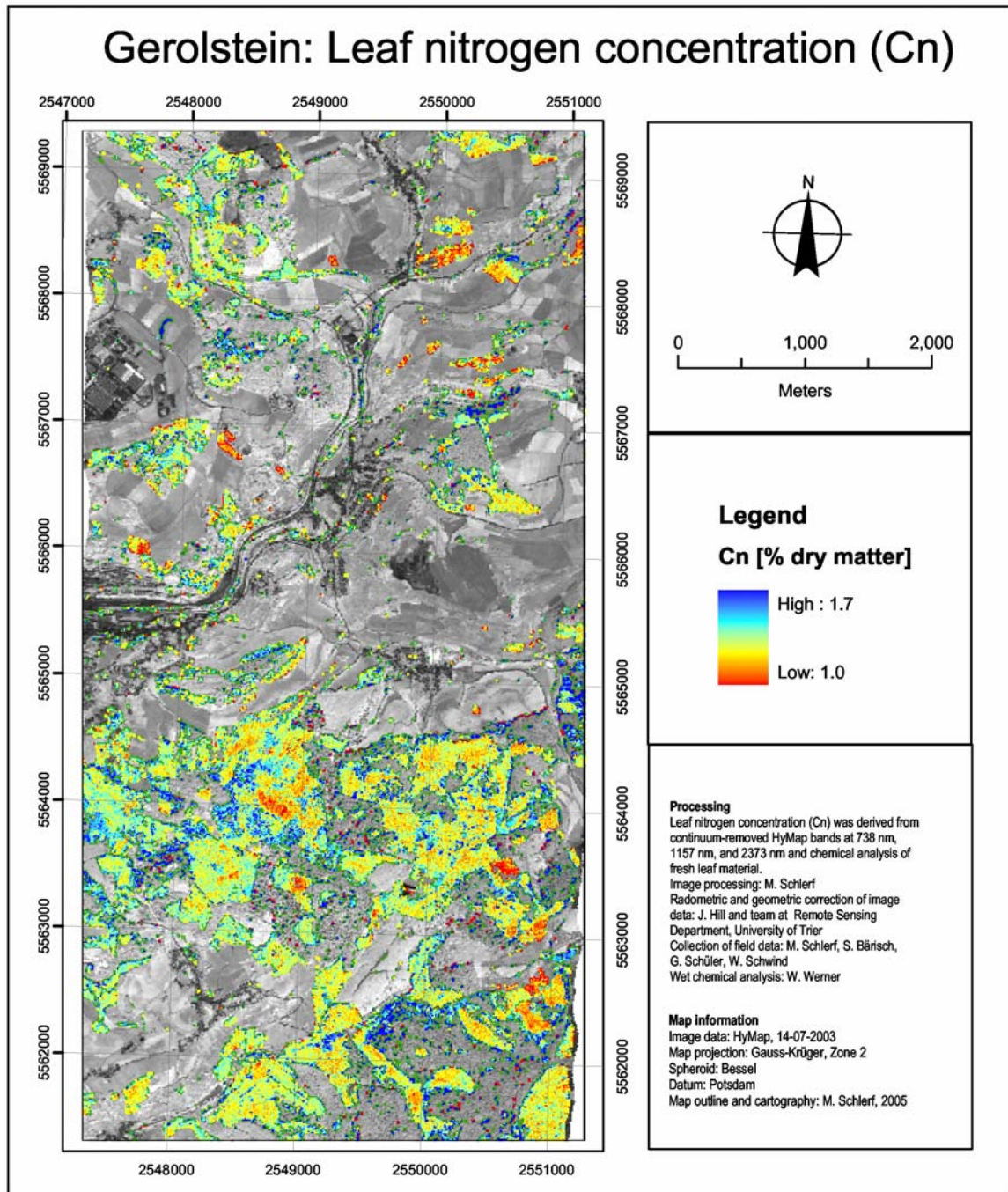


Figure 7.7: Map of leaf nitrogen concentration at Gerolstein test site.

>3.4 (class 3). For nitrogen concentration, the class limits were: <1.15 (class 1), 1.15-1.25 (class 2), >1.25 (class 3). The reclassified parameter maps were then majority filtered using a 3x3 kernel. For each zone, the class majority (the class number that occurred most often) was computed. As can be seen from Figure 7.8, C_{AB} class 3 is the most frequent class over substrates with large base saturation whereas class 1 occurs most often over poorly base saturated soils over rocks from Buntsandstein (sands). For Lower Devonian and Mid

Devonian substrates, no relation between base saturation and C_{AB} is evident. No relations were observed between nitrogen concentration and zones of stand development phase or zones of geological epoch.

An assessment concept for nitrogen and other biochemicals classifies values of nitrogen concentration in spruce needles (*Picea abies*) into five distinct classes (Hüttl, 1992): very low (< 1.3% dm), low (1.3-1.4% dm), medium (1.4-1.5% dm), high (1.5-1.7% dm), very high (> 1.7% dm). At Gerolstein test site, observed minimum nitrogen concentration (stand mean) is 1.08% of dry matter and the observed maximum is 1.31% dm. According to the classification scheme, 12 out of 13 stands have very low nitrogen concentrations. It is concluded that the large variation in base saturation present in the soils at Gerolstein area does is not equalled by corresponding variations in leaf nitrogen concentrations.

7.5.5 Accuracy requirements for ecological applications

Variations in foliar nitrogen occur between and within ecosystems. Foliar nitrogen in forests

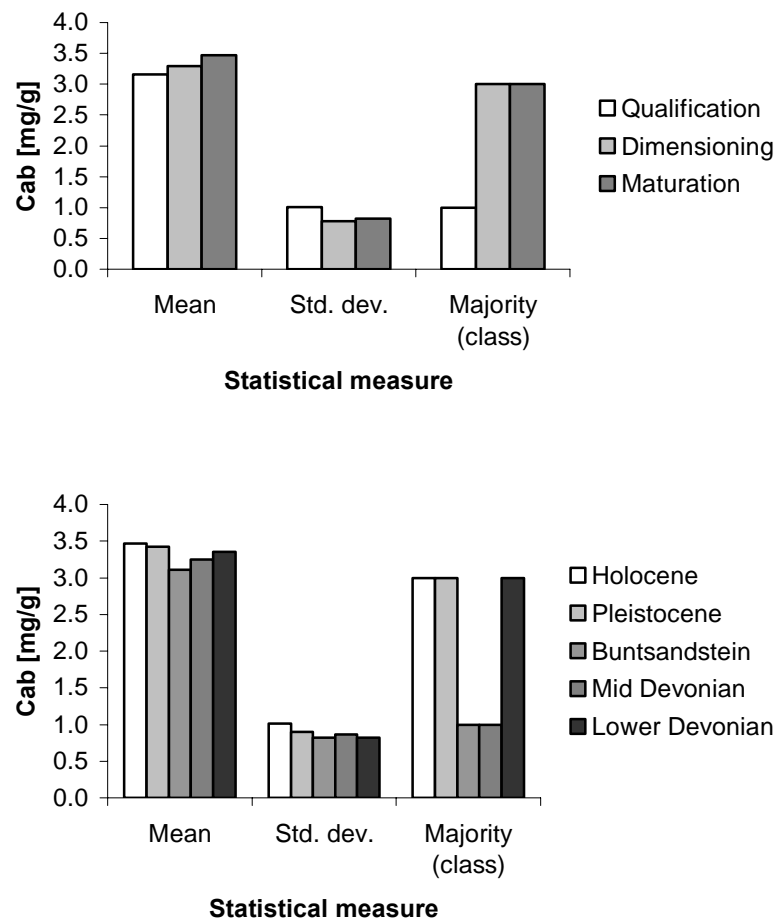


Figure 7.8: Statistical measures for three main phases and five main geological epochs that occur in the study area. Ordinate titles solely refer to mean and standard deviation.

across North America spans a range from 1 to 2.5 percent, as shown by Yin (1993, cited from Schimel, 1995), with foliar nitrogen being broadly correlated with summertime temperatures. Within ecosystems, seasonal variability in leaf nitrogen concentration can be very high; a change from early season nitrogen contents approaching 3 percent to late summer values of 0.8 percent in a tallgrass prairie was reported (Hobbs et al., 1991, cited from Schimel, 1995).

According to Schimel (1995), the following accuracies are required from remote sensing in order to map large scale variations in foliar nitrogen and lignin: Accuracy of 0.5% (absolute) nitrogen is necessary to distinguish between ecosystems with differences in nitrogen large enough to affect photosynthesis. Accuracy of 5% lignin concentration is needed to detect between-system gradients. Higher resolution, 1% lignin, is required to detect changes within a single forest type in order to map changes relevant to decomposition and nutrient cycling. These requirements are based on spatial gradients in nitrogen of 1-3.5 percent that occur between ecosystems. Spatial variations in spruce forest at Gerolstein site are considerably smaller: Stand mean values of C_N (appendix A2) range from 1.08 percent to 1.31 percent. This range of C_N (0.23 percent nitrogen) covers just about one tenth of what has been observed between ecosystems (2.5 percent nitrogen). From the low variation of nitrogen concentration present in Norway spruce needle at Gerolstein area no statement about the spatial variation of photosynthesis can be made. To increase variation in foliar nitrogen, the study has to be extended towards other ecosystems, such as beech forest or grassland.

Kokaly & Clark (1999) specified the required signal-to-noise ratio (SNR) to meet the accuracy requirements of Schimel (1995) as follows: A high SNR of approximately 700 is required to achieve an rmse of 0.5% absolute nitrogen. For RMS error of 5% absolute lignin concentration, the S/N must be only 100. However, the required SNR calculated from the dry leaves measured in the laboratory, with an average reflectance level of 40%, must raise by a factor of 8 for AVIRIS data over vegetation canopies, resulting in requirements for SNR of 800, 4400 and 5600 for lignin, cellulose, and nitrogen, respectively. They observed AVIRIS signal-to-noise ratios of about 360 at 2.10 μm . Their results show further, that it is possible to average two or more channels (bandpasses up to 78 nm) of the AVIRIS data, helping to compensate the lower SNR of the imaging spectrometer relative to laboratory measurements.

The SNR of the HyMap sensor, as specified by Cocks et al. (1998) based on ground measurement of a target with 50 percent reflectance, amount to 1600 at 0.55 μm , 1500 at 0.80 μm , and 900 at 2.10 μm . For a conifer forest target, the obtained SNR add up to 160, 600, and 90 at 0.55 μm (5 percent reflectance), 0.80 μm (20 percent reflectance), and 2.10 μm (5 percent reflectance), respectively. It is obvious, that the requirements as specified by Kokaly & Clark are not fulfilled by the HyMap sensor. Nonetheless, with an error of about 0.06 percent nitrogen (of dry matter) it was shown in the present research that an accurate determination of C_N is possible. This can be attributed to the fact, that the required SNR, as

specified by Kokaly & Clark (1999) are based on absorption features in the mid-IR domain whereas the most important wavebands used in equation 7.2 are located in the red edge. Detection of variations in chlorophyll and thus, nitrogen along the red edge requires much lower SNRs.

Chapter 8 Conclusions and future perspectives

Research overview

It has been the overall aim of this research work to assess the potential of hyperspectral remote sensing data for the determination of forest attributes relevant to forest ecosystem simulation modeling and forest inventory purposes. The research contributes to the fundamental concern of remote sensing; that is, to evaluate to what extent remotely sensed radiation can in fact provide useful information for a specific application and to develop the appropriate retrieval techniques (Verstraete et al., 1996).

The logic applied to the research followed three distinct phases:

1. Attributes that describe the properties of the forest canopy and that are potentially open to remote sensing were identified, appropriate methods for their retrieval were implemented and field, laboratory and image data were acquired over a number of forest plots.
2. The forest plots served as calibration and validation base for deriving relationships between forest attributes and remotely sensed data using image classification techniques, empirical-statistical approaches and physically-based methods.
3. The remotely sensed data were used to extrapolate plot estimates of forest attributes over the entire study area to produce parameter maps; the resulting spatial patterns were analysed with respect to other environmental factors; finally, the accuracies to predict the attributes were compared to those needed for applications in forestry.

Selection of forest attributes

Among the variety of attributes that characterise forest canopies, three requirements were identified to select suitable forest attributes:

- i) the attribute has to be of interest to ecological or economical applications
- ii) the attribute must directly or indirectly affect the transfer of radiation to allow the retrieval of reliable quantitative information on that attribute by remote sensing
- iii) ground measurement of the attribute has to be feasible using widely accepted and operational methods in the field and laboratory. The attributes selected in this research work that affect ecological processes are leaf area index (LAI), leaf chlorophyll a+b concentration (C_{AB}), and leaf nitrogen concentration (C_N). Attributes that are of

concern to forest inventory and management are stem biomass (SBM), crown volume (VOL) and stand age.

Retrieval of forest attributes from hyperspectral data

A number of approaches for the determination of structural and chemical attributes from hyperspectral remote sensing have been applied to the collected data sets. Many of the methods to be found in the literature were

- a) applied to broadband multispectral data
- b) applied to vegetation canopies other than forests
- c) reported to work on the leaf level or with modelled data
- d) not validated with ground truth data or
- e) not systematically compared to other methods.

Mapping of forest type

Age structure and species composition of forest stands are routinely collected in forest inventories every 10 years or longer to assess timber store and to optimise harvesting. Data of many spectral and spatial resolutions can be used for mapping forest type. In this study, the goal is to investigate whether tree species and age classes can be reliably derived from hyperspectral remote sensing data through image classification and to compare the overall information content of fine to broad spectral resolution and small to large spatial resolution data. The results of the image classification show that the overall accuracy and kappa coefficient using hyperspectral data are substantially larger than with multispectral data. These results indicate that hyperspectral data contain more information relevant to the mapping of forest type than broadband data. Remarkably, degradation of the high spatial resolution to coarser image pixels considerably increased the classification accuracies. In hyperspatial data individual trees comprise several pixels, each pixel may represent one of several classes (shadow or sunlit, young foliage or old), and the larger class variance may reduce class discrimination.

For mapping of forest types in Germany where currently the vast majority of the forests are one-age-cohort plantations, a moderate spatial resolution (30 m) optical sensor would be preferable. One-age-cohort management is not sustainable from an ecological point of view and has been abandoned by the forest administrations of all German federal states (Häusler & Scherer-Lorenzen, 2001). It is currently being replaced by alternative management strategies that in the future will increasingly produce forest stands with rather heterogeneous species composition and age structure. From a remote sensing perspective, under these conditions a hyperspatial sensor would be preferable that could detect such small scale variations to avoid the problem of mixed pixels. A hyperspectral would be preferred over a multispectral system to make use of narrow spectral features for discriminating different forest types.

Required classification accuracies from remote sensing, as claimed by Foody (2002), are not fulfilled by most of the datasets except hyperspectral data with low spatial resolution. One possible explanation would be that the classification problem encountered in this study is not trivial. Forest classes, such as clearings have spectral reflectance characteristics that differ very much from the closed canopy stands studied here. Those clearcuts are relatively easy to discriminate from the other forest types and including them in this study would probably have increased the classification accuracy.

Improvement of forest type mapping is often attempted by adding ancillary data into the classification process. The influence of stem density information proves to have a limited effect on classification accuracy. The major disadvantage of this approach is the restricted availability of these data. Other methods overcome traditional pixel-based image analysis and make use of textural information. Using geostatistical parameters derived from the image data itself as demonstrated by Buddenbaum et al. (2005) is another innovative approach to improve classification results.

Determination of leaf area index

Leaf area index (LAI) plays an important role in the quantification of ecosystem process, e.g. absorption of photosynthetically active radiation, canopy conductance and interception of precipitation. LAI, as other attributes related to canopy cover, affects the remotely sensed signal in sparse to medium dense canopies significantly. The goal is to compare empirical and physical approaches to determine LAI and to identify the most suitable hyperspectral and multispectral bands for both methods. The main results obtained from the research are summarised in Table 8.1. Determination of LAI through linear regression between remotely sensed vegetation indices (VIs) and ground measured LAI can be performed best with a narrowband perpendicular vegetation index (PVI) based on wavebands at 1088 nm and 1148 nm ($R^2 = 0.77$, $rmse = 0.54 \text{ m}^2 \text{ m}^{-2}$). LAI determination with NDVI and other broadband ratio vegetation indices based data resampled to Landsat TM wavebands is less successful due to saturation effects, influence of background and understorey vegetation. These effects are partly compensated when soil-line related broadband VIs (e.g. PVI) are used ($R^2 = 0.59$, $rmse = 0.84 \text{ m}^2 \text{ m}^{-2}$). However, problems with old stands are still present that can be ascribed to shadow effects and a relatively dark background in the near-IR.

The physical approach inverts a forest reflectance model using a neural network approach. With wavebands at 837 nm and 1148 nm the obtained accuracy of the retrieved LAI map amounts to an $rmse$ of $0.58 \text{ m}^2 \text{ m}^{-2}$. With HyMap data resampled to Landsat TM spectral bands and using two bands at 840 nm and 1650 nm, an $rmse$ of 0.66 (relative $rmse = 20\%$ of the mean) is achieved. Comparing the performance of both, empirical and physically-based approaches for LAI estimation from hyperspectral data it is concluded that both methods work

Table 8.1: Determination of leaf area index ($n = 39$) using different methods and data. From the original number of 40 stands, one stand subjected to clearing measures has been removed from the analysis (section 6.2).

Method	Data/Index (wavebands)	R^2	Rmse [$\text{m}^2 \text{m}^{-2}$]	Relative rmse [% of mean]
Empirical	Hyperspectral PVI (1088 nm, 1148 nm)	0.77	0.54	17
	Broadband PVI (670 nm, 840 nm)	0.59	0.84	26
	Broadband NDVI (670 nm, 840 nm)	0.47	1.06	33
Physically-based	Hyperspectral (837 nm, 1148 nm)	0.73	0.58	18
	Broadband (670 nm, 840 nm)	0.69	0.85	26
	Broadband (840 nm, 1650 nm)	0.73	0.66	21

equally well. When broadband multispectral data is used, LAI is more accurately predicted by the reflectance model inversion. This is a clear advantage of the physically-based approach over the empirical models. The physical approach explicitly takes into account canopy architecture, multiple scattering and signal contributions of the background and understorey vegetation. Quite different from empirical prediction functions that are generally limited to the local conditions at a certain point of time and a specific sensor type, the calibrated reflectance model can be applied more easily to different optical remote sensing data acquired at landscape to regional scales.

Analysis of the relations between best narrowband PVIs and LAI reveals that the wavebands forming the vegetation indices are either located at the shoulder of a water absorption feature (1088 nm) or at the absorption minimum (1148 nm). The same waveband (1148 nm) is employed to invert the reflectance model and the other waveband is situated on the near-IR plateau (837 nm). Obviously, in both, the empirical and the physical approach, the total amount of canopy water is mapped by the 1148 nm waveband. As the leaf water content is considered to be relatively constant in the study area, variations in LAI are retrieved.

Attributes related to aboveground biomass can not be accurately retrieved by both empirical and physically-based approaches. Poor relations are found between various vegetation indices and stem biomass. However, a synthetic variable is derived from measured structural (biomass related) attributes (stem density, stem diameter, canopy height) through factor analysis. This variable is interpreted as measure of crown volume (VOL) and it is linearly related to a PVI based on wavebands at 885 and 948 nm ($R^2 = 0.79$, $\text{rmse} = 0.52 \text{ m}^2 \text{ m}^{-2}$). Reflectance model inversion considerably underestimates stem density compared to ground data for dense forest stands (rmse 55 % of mean). To retrieve attributes related to aboveground biomass different remote sensing data and techniques have to be employed. For instance, lidar systems can very accurately measure the height of tree canopies and allow determining timber store.

Table 8.2: Determination of chemical forest attributes using laboratory and HyMap data and three types of spectral derivatives; relative rmse: % of mean; percentage of attributable bands: directly or indirectly related to the variable of interest

Data	Chemical	DWRS			RFL			BDN		
		R ²	Rel. rmse	Perc. of attribut. bands	R ²	Rel. rmse	Perc. of attribut. bands	R ²	Rel. rmse	Perc. of attribut. bands
Laboratory resampled to HyMap (n=78)	C _{AB}	0.81	8.7	33	0.80	9.0	22	0.76	9.6	21
	C _W	0.77	5.9	69	0.75	6.2	57	0.79	5.7	11
	C _N	0.52	6.7	73	0.49	6.8	0	0.52	6.6	50
HyMap image (n=13)	C _{AB}	0.72	4.7	33	0.46	6.9	0	0.90	2.8	0
	C _W	-	-	50	0.45	6.7	67	-	-	0
	C _N	0.52	4.9	67	-	-	0	0.34	5.5	0

Determination of chlorophyll, water and nitrogen concentration

The study on chemical forest attributes evaluated the information content of HyMap data for the estimation of chlorophyll (C_{AB}) water (C_W) and nitrogen (C_N) concentration. The aims were to find predictive models to estimate chemical concentrations and to systematically compare different types of derivatives of spectral reflectance regarding the accuracy of prediction. The results of the analysis (Table 8.2) show that C_{AB} can be well estimated from laboratory and canopy reflectance data. The best predictive model to estimate C_{AB} at the laboratory level yielded a cross-validated R² of 0.81 and a relative rmse of 8.7 % (n=78). The best model to estimate C_{AB} at the canopy level was achieved using band depth normalised spectra with a cross-validated R² of 0.90 and a relative rmse of 2.8 %. However, the small sample size at the canopy level (n = 13) is critical. The promising results that are obtained for chlorophyll may be explained by two reasons. First, chlorophyll is a strong absorber of radiation and variations of concentration have a large influence on reflectance. Second, chlorophyll concentration shows the largest variation of all chemicals which may explain the strong statistical correlation between chlorophyll concentration and reflectances. The same factors operating conversely may explain the weaker relations between reflectance and the concentration of nitrogen (R² = 0.57, rel. rmse = 4.6 %). Protein, one of the main nitrogen bearing leaf constituents, is a weak absorber of radiation and had a low variation between samples. Water concentration is well estimated from laboratory reflectance data, but not from noisy laboratory spectra and canopy spectra. This seems to be surprising as leaf water is a strong absorber of radiation. However, the low variation between samples could be the reason for the weak correlation between water concentration and noisy or canopy reflectance data.

The analysis of the selected wavebands reveals that for canopy spectra a smaller number of bands can be directly related to known absorption features compared to laboratory reflectance

data. The wavebands selected to estimate C_{AB} with laboratory and HyMap spectra are typically located in the red edge region and along the edge of the chlorophyll absorption feature. This result coincides with a general understanding that the maximum correlations occur on the edge of absorption features as the central wavelengths become saturated. For C_N , the wavebands selected in the regression models with laboratory data are often related to the chlorophyll absorption feature, the red edge region and to known protein absorption features. However, the portion of selected wavebands attributable to known substance absorption features strongly depends on the type of derivative spectra used. A method called “derivative of water removed spectra” (DWRS) produces the largest percentage of wavebands directly or indirectly related to known absorption features with laboratory and canopy spectra. Using band depth normalised spectra (BDN) the portion of wavebands attributable to known absorption features was relatively large with laboratory data but very low with HyMap spectra. Possibly, DWRS better than BDN preserves its ability to enhance absorption features during the upscaling from leaf to canopy spectra.

Wavelengths close to protein features at 1730 nm, 2180 nm, and 2350 nm that have often been selected in the literature are also selected in this research. As in the present work, a combined selection of wavebands related to both chlorophyll and protein absorption features in a single model to estimate nitrogen concentration is also reported from other studies.

The ability to estimate chemical concentrations from reflectance spectra using a model derived from an independent sample set is fundamental for extrapolating results over large sample sets and for determining of the model’s long term stability. Here, two independent data sets of Norway spruce samples were used. Estimations of all chemicals had large errors and low R^2 values except chlorophyll which showed values of R^2 above 0.65 for noisy laboratory spectra.

A limited data quality was reported for early AVIRIS campaigns (Kupiec, 1994; Niemann & Goodenough, 2003) which did not allow an accurate mapping of foliar chemicals. Contrary, the results of this research indicate that the detection and mapping of variations in chlorophyll and nitrogen concentrations is possible through the use of HyMap data. Obviously, the signal-to-noise ratio of the HyMap sensor is large enough to allow detection of small reflectance variations. Apart from the quality of the raw data, a sound radiometrically calibration to retrieve surface reflectances is an essential requirement for successful mapping of quantitative forest attributes. It can be concluded that the radiometric processing applied to the data fulfils the requirements to allow an accurate mapping of structural and chemical forest attributes.

Reflectance modeling

An essential requirement for model inversion is to ascertain that the reflectance signatures simulated by the model are consistent with the remotely sensed canopy spectra. If correctly

parameterised, the INFORM model simulates forest reflectance spectra comparable to those measured by an imaging spectrometer (HyMap). There is a good agreement between modelled and measured spectral reflectance in the near-IR wavebands and an acceptable agreement in the mid-IR. In the visible, however, model outputs and HyMap reflectances disagree. The disagreement in the visible domain can be explained by the used leaf reflectance model. A possible solution for the problem in this spectral domain could be to replace the LIBERTY by the PROSPECT model which was shown in other studies to work also with conifer needles. Perhaps better agreement between simulated and HyMap spectra in the visible could be obtained if chlorophyll content was changed within the typical range of variation. Also the performance of INFORM in the mid-IR region has to be further improved. The difference between simulated HyMap spectra in the mid-IR could be the reason for the poor estimation of stem density. Future studies will continue to clarify the relative importance of structural factors influencing the remote sensing measurements collected over forests.

A central question of the research on physically-based models was to study a new method to invert the model based on neural networks. The applied network with two input neurons and only one neuron in the hidden layer is of a very simple structure. Presumably, the two input neurons together establish a linear combination of two wavebands, similar to PVI. Next, the hidden neuron transforms the intermediate result in non-linear way, after which three output neurons compute the output to approximate the requested output variables. Finally from three output variables canopy LAI is computed. The assumption that the neural network approach works in comparable manner to PVI is supported by the fact that similar wavebands are used in both, PVI-based and neural network based approaches and that equal accuracies are retrieved by both methods.

Spatial patterns of parameter maps

After the best empirical model was applied to the HyMap image to derive estimates of LAI for each pixel, pixel-based LAI was aggregated to mean stand values. After a peak LAI at an age of 20, mean LAI is decreasing with increasing stand age. The observed age course is a result of both natural circumstances and actual management practices. Concurrently, regeneration of leaf area index subsequent to thinning measures is also determined by the water and nutrient supply of a particular site. Standard deviation of stand LAI is particularly large for the age class of 31-50 year old stands. The reason for the large variability of the 31-50 year old stands is that some stands of this age may be subjected to thinning measures while others may remain undisturbed and thinned at a later stage. LAI can vary considerably within a single age class and thus, information on LAI can not simply be derived from an age class map.

Predictive models were applied on the HyMap image to compute maps of chlorophyll concentration and nitrogen concentration. Results of map overlay operations revealed

coherence between C_{AB} and zones of stand development stage and between C_{AB} and zones of soil type. Larger values of C_{AB} occurred over soils with large base saturation (formed of basalt and colluvium) whereas poorly base saturated soils over sandstone showed lower C_{AB} values. However, the large variation in base saturation present in the soils at Gerolstein area is not equalled by corresponding variations in leaf nitrogen concentrations. From the low variation of nitrogen concentration present in Norway spruce needle at Gerolstein area no statement about the spatial variation of photosynthesis can be made. To increase variation in foliar nitrogen, the study has to be extended towards other ecosystems, such as deciduous forest, vine yards and orchards or grassland.

Future perspectives

Based on the results attained in present investigation, diverse perspectives for improved remote sensing of forests emerge:

The methods developed to determine structural forest attributes have evolved considerably in the past few decades. Vegetation indices which are by far the most widely used method are computationally efficient, but difficult to interpret. Both field and modeling studies show that vegetation indices are difficult to interpret with respect to a single structural forest attribute. Vegetation indices will continue to play an important role in remote sensing of forests and their improvement over time is warranted (Asner et al., 2003).

The use of canopy reflectance models to retrieve forest attributes from remote sensing data is still at its beginning. Most studies so far focused on evaluating model performance. Many of the newest 3-D models can accurately simulate the spectral and angular reflectance properties of forests. Future forward modeling studies will improve the understanding of how structural and chemical attributes govern the reflectance of forest canopies (Asner et al., 2003). On the other hand, little research has been done to invert models with remotely sensed data and validate the retrieved forest attributes with ground truth data.

To improve mapping of forest attributes through inverse modeling, future efforts should focus on developing new inversion techniques and making use of additional data dimensions. Improved inversion strategies could, for instance, combine an optimal spectral sampling with algorithms to find powerful predictive models. Lately, genetic algorithms have been identified as a powerful tool for finding optimal set of spectral variables to be included into a model. The utilisation of multi-view angle data is considered a prime option for advanced quantitative analysis of forested areas. Currently, the CHRIS sensor on the PROBA platform provides hyperspectral data with 17-34 m spatial resolution collected in five different view angles. Using such data could probably improve mapping of forest structural attributes.

In the future, the users of remote sensing products will ask for a growing selection of higher-level and value-added products that are consistent in quality, reliably available and easy to

use. This requires that validation and quality considerations of data products will have to receive much more attention than in the past (Peddle et al., 2003).

References

- AHERN, F. J., GOODENOUGH, D. G., JAIN, C. 1977: Use of clear lakes as standard reflectors for atmospheric measurements. *Proc. 11th Int. Symp. on Remote Sensing of Environment* Ann Arbor. 731-755.
- ARBEITSKREIS STANDORTKARTIERUNG 1985: Forstliche Wuchsgebiete und Wuchsbezirke in der BRD. Münster.
- ASNER, G. P. 1998: Biophysical and biochemical sources of variability in canopy reflectance. *Remote Sensing of Environment*, 64: 234-253.
- ASNER, G. P., HICKE, J. A., LOBELL, D. B. 2003: Per-pixel analysis of forest structure: Vegetation indices, spectral mixture analysis and canopy reflectance modeling. In: Wulder, M. A., Franklin, E. (Eds.): *Remote sensing of forest environments - Concepts and case studies*. Boston, Dordrecht, London. Kluwer Academic Publishers: 209-254.
- ATZBERGER, C. & SCHLERF, M. 2002: Automatisierte Bestimmung der Bestockungsdichte in Nadelwäldern aus räumlich hochauflösenden Ortholuftbildern. *Photogrammetrie-Fernerkundung-Geoinformation*, 3/2002: 171-180.
- ATZBERGER, C. & WERNER, W. 1998: Needle reflectance of healthy and diseased spruce stands. In: Schaepman, M. et al. (Eds.): *1st EARSeL workshop on imaging spectroscopy*. Zurich: 271-283.
- ATZBERGER, C. 1998: Estimates of winter wheat production through remote sensing and crop growth modeling. Berlin. Verlag für Wissenschaft und Forschung.
- ATZBERGER, C. 2000: Development of an invertible forest reflectance model: The INFORM-Model. In: Buchroithner, M. (Ed.): *A decade of trans-european remote sensing cooperation. Proceedings of the 20th EARSeL Symposium Dresden, Germany, 14-16 June 2000*: 39-44.
- ATZBERGER, C. 2003: Möglichkeiten und Grenzen der fernerkundlichen Bestimmung biophysikalischer Vegetationsparameter mittels physikalisch basierter Reflexionsmodelle. *Photogrammetrie-Fernerkundung-Geoinformation*, 1/2003: 51-61.
- BADHWAR, G. D., MACDONALD, R. B., HALL, F. G. 1986: Spectral characterization of biophysical characteristics in a boreal forest: Relationship between Thematic Mapper band reflectance and leaf area index for aspen. *IEEE Transactions on Geoscience and Remote Sensing*, GE-24, 3: 322-326.
- BALDOCCHI, D., VALENTINI, R., RUNNING, S., OECHEL, W., DAHLMAN, R. 1996: Strategies for measuring and modeling carbon dioxide and water vapour fluxes over terrestrial ecosystems. *Global Change Biol.*, 3: 159-168.
- BARET, F. & GUYOT, G. 1991: Potential and limits of vegetation indices for LAI and APAR assessment. *Remote Sensing of Environment*, 35: 161-173.

- BARET, F. & JACQUEMOUD, S. 1994: Modeling canopy spectral properties to retrieve biophysical and biochemical characteristics. In: Hill, J., Megier, J. (Eds.): *Imaging spectrometry - a tool for environmental observations*. Dordrecht, Kluwer Academic Publishers: 145-167.
- BARET, F. 1991: Vegetation canopy reflectance - factors of variation and application for agriculture. In: Belward & Valenzuela (Eds.): *Remote Sensing and Geographical Information Systems for Resource Management in Developing Countries*. Dordrecht, Kluwer Academic Publishers: 145-167.
- BARET, F., GUYOT, G., MAJOR, D. J. 1989: Crop biomass evaluation using radiometric measurements. *Photogrammetria (PRS)*, 43: 241-256.
- BAUMGARDNER, M. F., SILVA, L. F., BIEHL, L. L. 1985: Reflectance properties of soils. *Advances in Agronomy*, 38: 1-44.
- BICHERON, P. & LEROY, M. 1999: A method of biophysical parameter retrieval at global scale by inversion of a vegetation reflectance model. *Remote Sensing of Environment*, 67: 251-266.
- BISHOP, C. 1995. *Neural Networks for Pattern Recognition*. Oxford: University Press.
- BLACKBURN, G. A. 1998: Quantifying chlorophylls and carotenoids at leaf and canopy scales: An evaluation of some hyperspectral approaches. *Remote Sensing of Environment*, 66: 273-285.
- BLACKBURN, G. A. 2002: Remote sensing of forest pigments using airborne imaging spectrometer and LIDAR imagery. *Remote Sensing of Environment*, 82: 311-321.
- BLOCK, J. 1993: *Bodenzustand und Nährstoffversorgung der Waldökosysteme*. Mainz.
- BLOCK, J., BOPP, O., GATTI, M. 1991: *Waldschäden, Nähr- und Schadstoffgehalte in Nadeln und Waldböden in Rheinland-Pfalz*. Trippstadt.
- BOEGH, E.; SOEGAARD, H.; BROGE, N. 2002: Airborne multispectral data for quantifying leaf area index, nitrogen concentration, and photosynthetic efficiency in agriculture. *Remote Sensing of Environment*, 81: 179-193.
- BONHAM-CARTER, G. F. 1988: Numerical procedures and computer program for fitting an inverted Gaussian model to vegetation reflectance data. *Computer & Geosciences*, 14: 339-356.
- BOYD, D. S., WICKS, T. E., CURRAN, P. J. 2000: Use of middle infrared radiation to estimate the leaf area index of a boreal forest. *Tree Physiology*, 20: 755-760.
- BROGE, N. H. & LEBLANC, E. 2000: Comparing prediction power and stability of broadband and hyperspectral vegetation indices for estimation of green leaf area index and canopy chlorophyll density. *Remote Sensing of Environment*, 76: 156-172.
- BROGE, N. H. & MORTENSEN, J. V. 2002: Deriving green crop area index and canopy chlorophyll density of winter wheat from spectral reflectance data. *Remote Sensing of Environment*, 81: 45-57.
- BROWN, L., CHEN, J. M., LEBLANC, G. 2000: A shortwave infrared modification to the simple ratio for LAI retrieval in boreal forests: An image and model analysis. *Remote Sensing of Environment*, 71: 16-25.
- BRYANT, E., DODGE, A. G., WARREN, S. D. 1980: Landsat for practical forest type mapping: a test case. *Photogramm. Eng. Remote Sens.* 46(12): 1575-1584.

- BUDDENBAUM, H. 2004: Ableitung von Forstparametern aus hyperspektralen Fernerkundungsdaten unter Verwendung geostatistischer Verfahren. M.Sc.-thesis. University of Trier.
- BUDDENBAUM, H., SCHLERF, M., HILL, J. 2005: Classification of coniferous tree species and age classes using hyperspectral data and geostatistical methods. *International Journal of Remote Sensing*, 26(24): 5453–5465.
- BUNDESMINISTERIUM FÜR VERBRAUCHERSCHUTZ, ERNÄHRUNG UND LANDWIRTSCHAFT 2004: Die zweite Bundeswaldinventur. Berlin.
- CANADELL, J. G., MOONEY, H. A., BALDOCCHI, D. D., BERRY, J. A., EHLERINGER, J. R., FIELD, C. B., GOWER, S. T., HOLLINGER, D. Y., HUNT, J. E., JACKSON, R. B., RUNNING, S. W., SHAVER, G. R., STEFFE, W., TRUMBORE, S. E., VALENTINI, R., BOND, B. Y. 2000: Carbon metabolism of the terrestrial biosphere: A multitechnique approach for improved understanding. *Ecosystems*, 3: 115-130.
- CARD, D. H., PETERSON, D. L., MATSON, P. A. 1988: Prediction of leaf chemistry by the use of visible and near infrared reflectance spectroscopy. *Remote Sensing of Environment*, 26: 123-147.
- CHEN, J. M. & CIHLAR, J. 1996: Retrieving leaf area index of boreal conifer forests using Landsat TM images. *Remote Sensing of Environment*, 55: 153-162.
- CHEN, J. M. 1996: Optically-based methods for measuring seasonal variation in leaf area index of boreal conifer forest. *Agriculture and Forest Meteorology*, 80: 135-163.
- CHEN, J. M., LEBLANC, G., MILLER, J. R. 1999: Compact Airborne Spectrographic Imager (CASI) used for mapping biophysical parameters of boreal forests. *Journal of Geophysical Research*, 104: 27945-27959.
- CHEN, J. M., PAVLIC, G., BROWN, L., CIHLAR, J., LEBLANC, S. G., WHITE, H. P., HALL, R. J., PEDDLE, D. R., KING, D. J., TROFYMOW, J. A., SWIFT, E., VAN DER SANDEN, J., PELLIKKA, P. K. E. 2002: Derivation and validation of Canada-wide coarse-resolution leaf area index maps using high-resolution satellite imagery and ground measurements. *Remote Sensing of Environment*, 80: 165-184.
- CHRIST, E.P. & CICONE, R.C. 1984: A physically-based transformation of Thematic Mapper data - the TM Tasseled Cap. *IEEE Transactions on Geoscience and Remote Sensing*, GE22, 3: 256-263.
- CIHLAR, J., LATIFOVIC, R., BEAUBIEN, J., TRISHCHENKO, A., CHEN, J., FEDOSEJEVS, G. 2003: National scale forest information extraction from coarse resolution satellite data, Part 1. In: Wulder, M. A., Franklin, E. (Eds.): *Remote sensing of forest environments - Concepts and case studies*. Boston, Dordrecht, London. Kluwer Academic Publishers: 337-358.
- CLARK, R. N. & ROUSH, T. L. 1984: Reflectance spectroscopy: Quantitative analysis techniques for remote sensing applications. *Journal of Geophysical Research*, 89, B7: 6329-6340.
- CLARK, R. N. 1999: Spectroscopy of rocks and minerals and principles of spectroscopy. In: Rencz, A. N. (Ed.): *Remote sensing for the Earth sciences: Manual of remote sensing*, 3rd ed., Vol. 3 New York, Chichester, Weinheim. John Wiley & Sons, Inc.: 3-58.
- COCHRANE, M. A. 2000: Using vegetation reflectance variability for species level classification of hyperspectral data. *International Journal of Remote Sensing*, 10: 2075-2087.

- COCKS, T., JENSSEN, R., STEWART, A. 1998: The HyMap airborne hyperspectral sensor: The system, calibration and performance. In: Schaepman, M. et al. (Eds.): *1st EARSeL workshop on imaging spectroscopy*. Zurich: 37-42.
- COHEN, W. B., MAIERSPERGER, T. K., GOWER, T., TURNER, D. P. 2003: An improved strategy for regression of biophysical variables and Landsat ETM+ data. *Remote Sensing of Environment*: 561-571.
- COLEMAN, T. L., GUDAPATI, L., DERRINGTON, J. 1990: Monitoring of forest plantations using Landsat Thematic Mapper data. *Remote Sensing of Environment*, 33: 211-221.
- COLMAN, A. M. 2001: A Dictionary of Psychology. Oxford University Press. (= Oxford Reference Online, Oxford University Press, 18 March 2003).
- COMBAL, B., OSHCHEPKOV, S. L., SINYUK, A., ISAKA, H. 2000: Statistical framework of the inverse problem in retrieval of vegetation parameters. *Agronomy*, 20(1): 65-77.
- COOPS, N. C. & WHITE, J. D. 2003: Modeling forest productivity using data acquired through remote sensing. In: Wulder, M. A., Franklin, E. (Eds.): *Remote sensing of forest environments - Concepts and case studies*. Boston, Dordrecht, London. Kluwer Academic Publishers: 411-432.
- CURRAN, P. J. 1989: Remote sensing of foliar chemistry. *Remote Sensing of Environment*, 30: 271-278.
- CURRAN, P. J. 1994: Imaging spectrometry. *Progress in Physical Geography*, 18(2): 247-266.
- CURRAN, P. J. 1994a: Attempts to drive ecosystem simulation models at local to regional scales. In: Foody, G. M. (Ed.): *Environmental remote sensing from regional to global scales*. Chichester. Wiley: 149-166.
- CURRAN, P. J. 2001: Imaging spectrometry for ecological applications. *International Journal of Applied Earth Observation and Geoinformation*, 3(4): 305-312.
- CURRAN, P. J., DUNGAN, J. L., GHOLZ, H. L. 1990: Exploring the relationship between the reflectance red edge and chlorophyll content in slash pine. *Tree Physiology*, 7: 33-48.
- CURRAN, P. J., DUNGAN, J. L., GHOLZ, H. L. 1992: Seasonal LAI in slash pine estimated with Landsat TM. *Remote Sensing of Environment*, 39: 3-13.
- CURRAN, P. J., DUNGAN, J. L., MACLER, B. A. 1991: The effect of a red leaf pigment on the relationship between red edge and chlorophyll concentration. *Remote Sensing of Environment*, 35: 69-76.
- CURRAN, P. J., DUNGAN, J. L., MACLER, B. A., PLUMMER, E., PETERSON, D. L. 1992a: Reflectance spectroscopy of fresh whole leaves for the estimation of chemical concentration. *Remote Sensing of Environment*, 39: 153-166.
- CURRAN, P. J., DUNGAN, J. L., PETERSON, D. L. 2001: Estimating the foliar biochemical concentration of leaves with reflectance spectrometry - Testing the Kokaly and Clark methodologies. *Remote Sensing of Environment*, 76: 349-359.
- CURRAN, P. J.; KUPIEC, J. A.; SMITH, G. M. 1997: Remote sensing of biochemical composition of a slash pine canopy. *IEEE Transactions on Geoscience and Remote Sensing*, 35: 415-420.
- CURRAN, P. J. 1985: Principles of remote sensing. Longman. London, New York.
- DANSON, F. M. & CURRAN, P. J. 1993: Factors affecting the remotely sensed response of coniferous forest plantations. *Remote Sensing of Environment*, 43: 55-65.

- DANSON, F. M. & PLUMMER, E. 1995: Red-edge response to forest leaf area index. *International Journal of Remote Sensing*, 16: 183-188.
- DATT, B. 1998: Remote sensing of chlorophyll a, chlorophyll b, chlorophyll a+b, and total carotenoid content in eucalyptus leaves. *Remote Sensing of Environment*, 66: 111-121.
- DAUGHTRY, C. S., WALTHALL, C. L., KIM, M. 2000: Estimating corn leaf chlorophyll concentration from leaf and canopy reflectance. *Remote Sensing of Environment*, 74: 229-239.
- DAWSON, T. P. & CURRAN, P. J. 1998: A new technique for interpolating the reflectance red edge position. *International Journal of Remote Sensing*, 19(11): 2133-2139.
- DAWSON, T. P., CURRAN, P. J., PLUMMER, E. 1998: LIBERTY - Modeling the effects of leaf biochemical concentration on reflectance spectra. *Remote Sensing of Environment*, 65: 50-60.
- DAWSON, T. P., CURRAN, P. J., PLUMMER, E. 1998a: The biochemical decomposition of slash pine needles from reflectance spectra using neural networks. *International Journal of Remote Sensing*, 7: 1433-1438.
- DEMAREZ, V. & GASTELLU-ETCHEGORRY, J. P. 2000: A modeling approach for studying forest chlorophyll content. *Remote Sensing of Environment*, 71: 226-238.
- DEMETRIADES-SHAH T. H., STEVEN, M. D., CLARK, J. A. 1990: High resolution derivative spectra in remote sensing. *Remote Sensing of Environment*, 33: 55-64.
- DEMUTH, H. & BEALE, M. 2003: Neural Network Toolbox User's Guide, Version 4. The Mathworks.
- DESPAN, D. & JACQUEMOUD, S. 2004: Optical properties of soil and leaf: Necessity and problems of modeling. In: Schönemark, M. von, Geiger, B., Röser, H. P. (Eds.): *Reflection properties of vegetation and soil*. Berlin. Wissenschaft und Technik Verlag: 39-70.
- DIXIT, L. & RAM, S. 1985: Quantitative analysis by derivative electronic spectroscopy. *Applied Spectroscopy Reviews*, 21(4): 311-418.
- DUCKWORTH, J. 1998: Spectroscopic quantitative analysis. In: Workman, J., Springsteen, A. W. (Eds.): *Applied spectroscopy. A compact reference for practitioners*. San Diego, New York, London. Academic Press: 93-164.
- EKLUNDH, L., HARRIE, L., KUUSK, A. 2001: Investigating relationships between Landsat ETM+ sensor data and leaf area index in a boreal conifer forest. *Remote Sensing of Environment*, 78: 239-251.
- ELVIDGE, C. D. 1990: Visible and near infrared reflectance characteristics of dry plant materials *International Journal of Remote Sensing*, 11: 1775-1795.
- FASSNACHT, K. S., GOWER, T., MACKENZIE, M. D. 1997: Estimating the leaf area index of north central Wisconsin forests using the Landsat Thematic Mapper. *Remote Sensing of Environment*, 61: 229-245.
- FASSNACHT, K. S., GOWER, T., NORMAN, J. M. 1994: A comparison of optical and direct methods for estimating foliage surface area index in forests. *Agriculture and Forest Meteorology*, 71: 183-207.

- FERNANDES, R., MILLER, J. R., CHEN, J. M., RUBINSTEIN, I. G. 2004: Evaluating image-based estimates of leaf area index in boreal conifer stands over a range of scales using high-resolution CASI imagery. *Remote Sensing of Environment*, 89: 200-216.
- FERNANDES, R., MILLER, J. R., HU, B. 2002: A multi-scale approach to mapping effective leaf area index in boreal *Picea marina* stands using high spatial resolution CASI imagery. *International Journal of Remote Sensing*, 23(18): 3547-3568.
- FOODY, G.M. 2002: Status of land cover classification accuracy assessment. *Remote Sensing of Environment*, 80: 185-201.
- FOURNIER, R. A., MAILLY, D., WALTER, J.-M. N., SOUDANI, K. 2003: Indirect measurements of forest canopy structure from in situ optical sensors. In: Wulder, M. A., Franklin, E. (Eds.): *Remote sensing of forest environments - Concepts and case studies*. Boston, Dordrecht, London. Kluwer Academic Publishers: 77-114.
- FOURTY, T. & BARET, F. 1997: Vegetation water and dry matter contents estimated from top-of-the-atmosphere reflectance data: A simulation study. *Remote Sensing of Environment*, 61: 34-45.
- FOURTY, T. & BARET, F. 1998: On spectral estimates of fresh leaf biochemistry. *International Journal of Remote Sensing*, 7: 1283-1297.
- FOURTY, T., BARET, F., JACQUEMOUD, S., SCHMUCK, G., VERDEBOUT, J. 1996: Leaf optical properties with explicit description of its biochemical compositions: Direct and inverse problems. *Remote Sensing of Environment*, 56: 104-117.
- FRANKLIN, E. 1994: Discrimination of subalpine forest species and canopy density using digital CASI, SPOT PLA, and Landsat TM data. *Photogrammetric Engineering & Remote Sensing*, 60(10): 1233-1241.
- FRANKLIN, E., LAVIGNE, M. B., DEULING, M. 1997: Estimation of forest leaf area index using remote sensing and GIS data for modeling net primary production. *International Journal of Remote Sensing*, 18(16): 3459-3471.
- FRANKLIN, J., PHINN, R., WOODCOCK, C. E., ROGAN, J. 2003: Rationale and conceptual framework for classification approaches to assess forest resources and properties. In: Wulder, M. A., Franklin, E. (Eds.): *Remote sensing of forest environments - Concepts and case studies*. Boston, Dordrecht, London. Kluwer Academic Publishers: 279-300.
- GAO, B.-C. & GOETZ, A. F. H. 1994: Extraction of dry leaf spectral features from reflectance spectra of green vegetation. *Remote Sensing of Environment*, 47: 369-374.
- GAO, B.-C. & GOETZ, A. F. H. 1995: Retrieval of equivalent water thickness and information related to biochemical components of vegetation canopies from AVIRIS data. *Remote Sensing of Environment*, 52: 155-162.
- GASTELLU-ETCHEGORRY, J. P., DEMAREZ, V., PINEL, V., ZAGOLSKI, F. 1996: Modeling radiative transfer in heterogeneous 3-D vegetation canopies. *Remote Sensing of Environment*, 58: 131-156.
- GASTELLU-ETCHEGORRY, J. P., ZAGOLSKI, F., MOUGIN, E., MARTY, G., GIORDANO, G. 1995: An assessment of canopy chemistry with AVIRIS - a case study in the Landes Forest, South-west France. *International Journal of Remote Sensing*, 3: 487-501.
- GEMMELL, F. & VARJO, J. 1999: Utility of reflectance model inversion versus two spectral indices for estimating biophysical characteristics in a boreal forest test site. *Remote Sensing of Environment*, 68: 95-111.

- GEMMELL, F. 1999: Estimating conifer forest cover with Thematic Mapper data using reflectance model inversion and two spectral indices in a site with variable background characteristics. *Remote Sensing of Environment*, 69: 105-121.
- GEMMELL, F. 2000: Testing the utility of multi-angle spectral data for reducing the effects of background spectral variations in forest reflectance model inversion. *Remote Sensing of Environment*, 72: 46-63.
- GEMMELL, F., VARJO, J., STRANDSTROM, M., KUUSK, A. 2002: Comparison of measured boreal forest characteristics with estimates from TM data and limited ancillary information using reflectance model inversion. *Remote Sensing of Environment*, 81: 365-377.
- GHOLZ, H. L., CURRAN, P. J., KUPIEC, J. A., SMITH, G. M. 1996: Assessing leaf area and canopy biochemistry of florida pine plantations using remote sensing. In: Gholz, H. L., Nakane, K., Shimoda, H. (Eds.): *The use of remote sensing in the modeling of forest productivity*. Dordrecht, The Netherlands. Kluwer Acad. Publ.: 3-22.
- GITELSON, A. A. & MERZLYAK, M. N. 1996: Signature analysis of leaf reflectance spectra: Algorithm development for remote sensing of chlorophyll. *J. Plant Physiol.* 148: 494-500.
- GOEL, N. 1988: Models of vegetation canopy reflectance and their use in estimation of biophysical parameters from reflectance data. *Remote Sensing Reviews*, 4: 1-212.
- GOEL, N. 1989: Inversion of canopy reflectance models for estimation of biophysical parameters from reflectance data. In: Asrar, G. (Ed.): *Theory and applications of optical remote sensing*. New York. John Wiley & Sons: 205-251.
- GOEL, N. S. & DEERING, D. W. 1985: Evaluation of a canopy reflectance model for LAI estimation through its inversion. *IEEE Transactions on Geoscience and Remote Sensing*, GE-23(5): 674-684.
- GOEL, N. S. & THOMPSON, R. L. 1984: Inversion of vegetation canopy reflectance models for estimating agronomic variables. V. Estimation of leaf area index and average leaf angle using measured canopy reflectance. *Remote Sensing of Environment*, 16: 69-85.
- GONG, P., PU, R., BIGING, G., LARRIEU, M. 2003: Estimation of forest leaf area index using vegetation indices derived from Hyperion hyperspectral data. *IEEE Transactions on Geoscience and Remote Sensing*, 41: 1355-1362.
- GONG, P., PU, R., MILLER, J. R. 1992: Correlating leaf area index of Ponderosa pine with hyperspectral CASI data. *Canadian Journal of Remote Sensing*, 18: 275-282.
- GONG, P., PU, R., MILLER, J. R. 1995: Coniferous forest leaf area index estimation along the Oregon transect using Compact Airborne Spectrographic Imager data. *Photogrammetric Engineering & Remote Sensing*, 61: 1107-1117.
- GONG, P., PU, R., YU, B. 1997: Conifer species recognition: an exploratory analysis of in situ hyperspectral data. *Remote Sensing of Environment*, 62: 189-200.
- GONG, P., WANG, D. X., LIANG, S. 1999: Inverting a canopy reflectance model using a neural network. *International Journal of Remote Sensing*, 20(20): 111-122.
- GOVAERTS, Y., JACQUEMOUD, S., VERSTRAETE, M. M, USTIN, L. 1996: Three-dimensional radiation transfer modeling in dicotyledon leaf. *Appl. Opt.*, 35(33): 6585-6598.

- GREEN, A. A., BERMAN, M., SWITZER, P., CRAIG, M. D. 1988: A transformation for ordering multispectral data in terms of image quality with implications for noise removal. *IEEE Transactions on Geoscience and Remote Sensing*, 26(1): 65-74.
- GROSSMAN, Y. L., USTIN, L., JACQUEMOUD, S., SANDERSON, E. W., SCHMUCK, G., VERDEBOUT, J. 1996: Critique of stepwise multiple linear regression for the extraction of leaf biochemistry information from leaf reflectance data. *Remote Sensing of Environment*, 56: 182-193.
- GUYOT, G. 1990: Optical properties of vegetation canopies. In: Steven, M. D., Clark, J. A. (Eds.): *Applications of remote sensing in agriculture*. London. Butterworths: 19-43.
- GUYOT, G., BARET, F., JACQUEMOUD, S. 1992: Imaging spectroscopy for vegetation studies. In: Toselli, F., Bodechtel, J. (Eds.): *Imaging spectroscopy: Fundamentals and prospective applications*: 145-165.
- HABOUDANE, D., MILLER, J. R., TREMBLAY, N., ZARCO-TEJADA, P., DEXTRAZE, L. 2002: Integrated narrow-band vegetation indices for prediction of crop chlorophyll content for application to precision agriculture. *Remote Sensing of Environment*, 81: 416-426.
- HALL, F. G., SHIMABUKURU, Y. E., HUENNRICH, K. F. 1995: Remote sensing of forest biophysical structure in boreal stands of *Picea marina* using mixture decompositions and geometric reflectance models. *Ecological Applications*, 5: 993-1013.
- HARMAN, H. H. 1976: *Modern Factor Analysis*, 3rd Edition. Chicago. University of Chicago Press.
- HÄUSLER, A. & SCHERER-LORENZEN, M. 2001: Sustainable Forest Management in Germany: The ecosystem approach of the biodiversity convention reconsidered. German Federal Agency for Nature Conservation, BfN –Skripten 51.
- HAYKIN, S. 1994. *Neural Networks: A Comprehensive Foundation*. New York: Macmillan Publishing.
- HERWITZ, S., PETERSON, D. L., EASTMAN, J. R. 1990: Thematic Mapper detection of changes in the leaf area of closed canopy pine plantations in Central Massachusetts. *Remote Sensing of Environment*, 30: 129-140.
- HILDEBRANDT, G. 1993: Fernerkundung in der Forstwirtschaft. *Zeitschrift für Photogrammetrie und Fernerkundung*, 4: 135-138.
- HILDEBRANDT, G. 1996: *Fernerkundung und Luftbildmessung*. Heidelberg. Herbert Wichmann Verlag.
- HILL, J. & MEGIER, J. (Eds.) 1994: *Imaging spectrometry - A tool for environmental observations* Dordrecht. Kluwer Academic Publishers.
- HILL, J. & MEHL, W. 2003: Georadiometrische Aufbereitung multi- und hyperspektraler Daten zur Erzeugung langjähriger kalibrierter Zeitreihen. *Photogrammetrie-Fernerkundung-Geoinformation*, 1/2003: 7-14.
- HILL, J. & STURM, B. 1991: Radiometric correction of multi-temporal Thematic Mapper data for use in agricultural land-cover classification and vegetation monitoring. *International Journal of Remote Sensing*, 12: 1471-1491.
- HILL, J. 1993: High precision land cover mapping and inventory with multi-temporal earth observation satellite data - The Ardèche experiment. Luxembourg. Office for official publications of the European Communities.

- HILL, J. 2002: Sensorkalibration und atmosphärische Korrektur von hyperspektralen Fernerkundungsdaten (HyMap). In: Müller, P., Rumpf, S., Monheim, H. (Eds.): *Umwelt und Region - Aus der Werkstatt des Sonderforschungsbereichs 522*. Trier. Selbstverlag: 163-173.
- HILL, J., MEHL, W., RADELOFF, V. 1995: Improved forest mapping by combining corrections of atmospheric and topographic effects in Landsat TM imagery. In: Askne, J. (Ed.): *Sensors and environmental applications of remote sensing. Proc. 14th EARSeL Symposium, Göteborg, Sweden, 6-8 June 1994*. Rotterdam. Balkema: 143-151.
- HORLER, D. N., DOCKRAY, M., BARBER, J. 1983: The red edge of plant leaf reflectance. *International Journal of Remote Sensing*, 4: 273-288.
- HOWARD, J. A. 1991: Remote sensing of forest resources. London, New York, Tokyo, Melbourne, Madras. Chapman & Hall.
- HU, B., INANNEN, K., MILLER, J. R. 2000: Retrieval of leaf area index and canopy closure from CASI data over the BOREAS flux tower sites. *Remote Sensing of Environment*, 74: 255-274.
- HÜTTL, R. F. 1992: Die Blattanalyse als Diagnose- und Monitoringinstrument in Waldökosystemen. *Freiburger Bodenkundliche Abhandlungen*, 30: 31-59.
- IAQUINTA, J., PINTY, B., PRIVETTE, J. L. 1997: Inversion of a physically based bidirectional reflectance model of vegetation. *IEEE Transactions on Geoscience and Remote Sensing*, 35(3): 687-698.
- JACQUEMOUD, F. & BARET, F. 1990: PROSPECT: A model of leaf optical properties spectra. *Remote Sensing of Environment*, 34: 75-91.
- JACQUEMOUD, S. & BARET, F. 1993: Estimating vegetation biophysical parameters by inversion of a reflectance model on high spectral resolution data. In: Varlet-Grancher et al. (Eds.): *Crop structure and light microclimate: Characterisation and application*. Meeting held at the Chateau de Saumane, Vaucluse, France. INRA-Editions: 339-350.
- JACQUEMOUD, S., BACOUR, C., POILVE, H., FRANGI, J.-P. 2000: Comparison of four radiative transfer models to simulate plant canopies reflectance: Direct and inverse mode. *Remote Sensing of Environment*, 74: 471-481.
- JACQUEMOUD, S., USTIN, S. L., VERDEBOUT, J. 1996: Estimating leaf biochemistry using the PROSPECT leaf optical properties model. *Remote Sensing of Environment*, 56: 194-202.
- JACQUEMOUD, S., VERDEBOUT, J., SCHMUCK, G., ANDREOLI, G., HOSGOOD, B. 1995: Investigation of leaf biochemistry by statistics. *Remote Sensing of Environment*, 54: 180-188.
- JAGO, R. A., CUTLER, M. E., CURRAN, P. J. 1999: Estimating canopy chlorophyll concentration from field and airborne spectra. *Remote Sensing of Environment*, 68: 217-224.
- JOHNSON, L. F., HLAVKA, C. A., PETERSON, D. L. 1994: Multivariate analysis of AVIRIS data for canopy biochemical estimation along the Oregon transect. *Remote Sensing of Environment*, 47: 216-230.
- KAUFMAN, Y. J. 1989: The atmospheric effect on remote sensing and its correction. In: Asrar, G. (Ed.): *Theory and applications of optical remote sensing*. New York. John Wiley & Sons: 336-428.

- KENNEDY, R. O., COHEN, W. B., TAKAO, G. 1997: Empirical methods to compensate for a view-angle dependent brightness gradient in AVIRIS imagery. *Remote Sensing of Environment*, 62: 277-291.
- KIMBALL, J. S., WHITE, M. A., RUNNING, S. W. 1997: Biome-BGC simulations of stand hydrologic process for BOREAS. *Journal of Geophysical Research*, 102(D24): 29043-29051.
- KIMES, D. 1983: Dynamics of directional reflectance factor distribution for vegetation canopies. *Appl. Opt.*, 22: 1364-1372.
- KIMES, D. S., HOLBEN, B. N., NICKESON, J. E., MCKEE, W. A. 1996: Extracting forest age in a Pacific Northwest forest from Thematic Mapper and topographic data. *Remote Sensing of Environment*, 56: 133-140.
- KIMES, D., GASTELLU-ETCHEGORRY, J, ESTÈVE, P. 2002: Recovery of forest canopy characteristics through inversion of a complex 3D model. *Remote Sensing of Environment*, 79: 320-328.
- KÖHL, M. & LAUTNER, M. 2001: Erfassung von Waldökosystemen durch Hyperspektraldaten. *Photogrammetrie, Fernerkundung, Geoinformation* 2001(2): 107-117.
- KOKALY, R. F. & CLARK, R. N. 1999: Spectroscopic determination of leaf biochemistry using band-depth analysis of absorption features and stepwise multiple linear regression. *Remote Sensing of Environment*, 67: 267-287.
- KOKALY, R. F. 2001: Investigating a physical basis for spectroscopic estimates of leaf nitrogen concentration *Remote Sensing of Environment*, 75: 153-161.
- KÖTZ, B., SCHAEPMAN, M., MORSDORF, F., BOWYER, P., ITTEN, K., ALLGÖWER, B. 2004: Radiative transfer modeling within a heterogenous canopy for estimation of forest fire fuel properties. *Remote Sensing of Environment*, 92: 332-344.
- KRAUS, K. & SCHNEIDER, W. 1988: Fernerkundung, Band 1: Physikalische Grundlagen und Aufnahmetechniken. Bonn. Ferd. Dümmler Verlag.
- KRUSE, F. A. 1999: Visible-infrared sensors and case studies. In: Rencz, A. N. (Ed.): *Remote sensing for the Earth sciences: Manual of remote sensing, 3rd ed., Vol. 3*. New York, Chichester, Weinheim. John Wiley & Sons.
- KRUSE, F. A., LEFKOFF, A. B., BOARDMAN, J. W. 1993: The Spectral Image Processing System (SIPS) - Interactive visualization and analysis of imaging spectrometer data. *Remote Sensing of Environment*, 44: 145-163.
- KUPIEC, J. A. & CURRAN, P. J. 1995: Decoupling effects of the canopy and foliar biochemicals in AVIRIS spectra. *International Journal of Remote Sensing*, 9: 1731-1739.
- KUPIEC, J. A. 1994: The remote sensing of foliar chemistry. University of Wales, Swansea. Ph.D.-thesis.
- KUUSK, A. 1998: Monitoring of vegetation parameters on large areas by the inversion of a canopy reflectance model. *International Journal of Remote Sensing*, 19(15): 2893-2905.
- LAMB, D. W., STEYN-ROSS, M., SCHAARE, P., HANNA, M. M., SILVESTER, W., STEYN-ROSS, A. 2002: Estimating leaf nitrogen concentration in ryegrass (*Lolium* spp.) pasture using the chlorophyll red-edge: theoretical modeling and experimental observations. *International Journal of Remote Sensing*, 23(18): 3619-3648.

- LECKIE, D. G. 1990: Advances in remote sensing technologies for forest surveys and management. *Canadian Journal of Forest Research*, 20(4): 464-483.
- LEE, J. B., WOODYATT, A. S., BERMAN, M. 1990: Enhancement of high spectral resolution remote-sensing data by a noise-adjusted principal components transform. *IEEE Transactions on Geoscience and Remote Sensing*, 28: 295-304.
- LEE, K.-S., COHEN, W. B., KENNEDY, R. E., MAIERSPERGER, T. K., GOWER, T. 2004: Hyperspectral versus multispectral data for estimating leaf area index in four different biomes. *Remote Sensing of Environment*, 91: 508-520.
- LEFSKY, M. E. & COHEN, W. B. 2003: Selection of remotely sensed data. In: Wulder, M. A., Franklin, E. (Eds.): *Remote sensing of forest environments - Concepts and case studies*. Boston, Dordrecht, London. Kluwer Academic Publishers: 13-46.
- LI, X. & STRAHLER, A. H. 1985: Geometric-optical modeling of a conifer forest. *IEEE Transactions on Geoscience and Remote Sensing*, GE-23(5): 705-721.
- LICHTENTHALER, H. K. 1987: Chlorophylls and carotenoids, the pigments of the photosynthetic biomembranes. *Methods in Enzymology*, 148: 350-382.
- LILIENTHAL, H., HANEKLAUS, S., SCHNUG, E. 2000: Utilisation of hyperspectral data for the evaluation of the spatial variability of the nitrogen status of wheat. *Aspects of Applied Biology*, 60: 189-194
- LILLESAND, T. M. & KIEFER, R. W. 2000: Remote sensing and image interpretation. New York. John Wiley & Sons.
- LUCAS, N. S. & CURRAN, P. J. 1999: Forest ecosystem simulation modeling: The role of remote sensing. *Progress in Physical Geography*, 23(3): 391-423.
- LUCAS, N. S. 1995: Coupling remotely sensed data to a forest ecosystem simulation model. Ph.D.-thesis. University of Swansea, Wales.
- LUCAS, N. S., CURRAN, P. J., PLUMMER, S. E., DANSON, F. M. 2000: Estimating the stem carbon production of a coniferous forest using an ecosystem simulation model driven by the remotely sensed red edge. *International Journal of Remote Sensing*, 21(4): 619-631.
- LUCHT, W. 2004: Viewing the earth from multiple angles: Global change and the science of multiangular reflectance. In: Schönemark, M. von, Geiger, B., Röser, H. P. (Eds.): *Reflection properties of vegetation and soil*. Berlin. Wissenschaft und Technik Verlag: 9-30.
- MARTIN, L. & HOWARTH, P. 1989: Change-detection accuracy assessment using SPOT multispectral imagery of the rural-urban fringe. *Remote Sensing of Environment*, 30: 55-66.
- MARTIN, M. E., NEWMAN, S.D., ABER, J.D., CONGALTON, R.G. 1998: Determining forest species composition using high spectral resolution remote sensing data *Remote Sensing of Environment*, 65: 249-254.
- MCDONALD, A. J., GEMMELL, F. M., LEWIS, P. E. 1998: Investigation of the utility of spectral vegetation indices for determining information on coniferous forests. *Remote Sensing of Environment*, 66: 250-272.
- MEISTER, G., TORNOW, C., NI, W. 2004: Geometrical-optical BRDF models. In: Schönemark, M. von, Geiger, B., Röser, H. P. (Eds.): *Reflection properties of vegetation and soil*. Berlin. Wissenschaft und Technik Verlag: 82-104.

- MELILLO, J. M., ABER, J. D., MURATORE, J. F. 1982: Nitrogen and lignin control of hardwood leaf litter decomposition dynamics. *Ecology*, 63: 621-630.
- MERONI, M., COLOMBO, R., PANIGADA, C. 2004: Inversion of a radiative transfer model with hyperspectral observations for LAI mapping in poplar plantations. *Remote Sensing of Environment*, 92: 195-206.
- MINISTERIUM FÜR UMWELT UND FORSTEN RHEINLAND-PFALZ 1995: Waldzustandsbericht 1995 für Rheinland-Pfalz. Mainz.
- MOONEY, H., VITOUSEK, P., MATSON, P. 1987: Exchange of materials between terrestrial ecosystems and the atmosphere. *Science*, 238: 926-932.
- MUTANGA, O. & SKIDMORE, A. K. 2004: Integrating imaging spectroscopy and neural networks to map grass quality in the Kruger National Park, South Africa. *Remote Sensing of Environment*, 90: 104-115.
- NIEMANN, K. O. & GOODENOUGH, D. G. 2003: Estimation of foliar chemistry of western hemlock using hyperspectral data. In: Wulder, M. A., Franklin, E. (Eds.): *Remote sensing of forest environments - Concepts and case studies*. Boston, Dordrecht, London. Kluwer Academic Publishers: 447-467.
- NIEMANN, K. O. 1995: Remote sensing of forest stand age using airborne spectrometer data. *Photogrammetric Engineering & Remote Sensing*, 61(9): 1119-1127.
- NILSON, T. & PETERSON, U. 1994: Age dependence of forest reflectance: Analysis of main driving factors. *Remote Sensing of Environment*, 48: 319-331.
- NORRIS, K. H., BARNES, R. F., MOORE, J. E., SHENK, J. 1976: Predicting forage quality by infrared reflectance spectroscopy. *Journal of Animal Science*, 43: 889-897.
- O'NEILL, A. L., KUPIEC, J. A., CURRAN, P. J. 2002: Biochemical and reflectance variation throughout a Sitka spruce canopy. *Remote Sensing of Environment*, 80: 134-142.
- OXFORD REFERENCE ONLINE 2004: A Dictionary of Chemistry, Oxford University Press 2000. <http://www.oxfordreference.com/views/ENTRY.html?subview=Main&entry=t81.e914>.
- OXFORD REFERENCE ONLINE 2005: A Dictionary of Biology, Oxford University Press 2004. <http://www.oxfordreference.com/views/ENTRY.html?subview=Main&entry=t6.e2710>.
- OXFORD REFERENCE ONLINE 2005a: A Dictionary of Plant Sciences. Ed. M. Allaby. Oxford University Press 1998. <http://www.oxfordreference.com/views/ENTRY.html?subview=Main&entry=t7.e1401>.
- PEARSON, R. L. & MILLER, L. D. 1972: Remote mapping of standing crop biomass for estimation of the productivity of the short-grass prairie, Pawnee National Grasslands, Colorado. *Proceedings of the 8th International Symposium on Remote Sensing of Environment, ERIM International*: 1357-1381.
- PEDDLE, D. R., TEILLET, P. M., WULDER, M. A. 2003: Radiometric image processing. In: Wulder, M. A., Franklin, E. (Eds.): *Remote sensing of forest environments - Concepts and case studies*. Boston, Dordrecht, London. Kluwer Academic Publishers: 181-208.
- PENUELAS, J., GAMON, J. A., FREDEEN, A. L., MERINO, J., FIELD, C. B. 1994: Reflectance indices associated with physiological changes in nitrogen- and water-limited sunflower leaves. *Remote Sensing of Environment*, 48: 135-146.

- PETERSON, D. L. & HUBBARD, G. S. 1992: Scientific issues and potential remote-sensing requirements for plant biochemical content. *Journal of Imaging Science and Technology*, 36: 446-456.
- PETERSON, D. L. & RUNNING, S. W. 1989: Application in forest science and management In: Asrar, G. (Ed.): *Theory and applications of optical remote sensing*. New York. John Wiley & Sons: 429-473.
- PETERSON, D. L., ABER, J. D., MATSON, P. A., CARD, D. H., SWANBERG, N., WESSMAN, C., SPANNER, M. 1988: Remote sensing of forest canopy and leaf biochemical contents. *Remote Sensing of Environment*, 24: 85-108.
- PETERSON, D. L., SPANNER, M. A., RUNNING, S. W. 1987: Relationship of Thematic Mapper simulator data to leaf area index of temperate coniferous forests. *Remote Sensing of Environment*, 22: 323-341.
- PINAR, A. & CURRAN, P. J. 1996: Grass chlorophyll and the reflectance red edge. *International Journal of Remote Sensing*, 17(2): 351-357.
- RAUTIAINEN, M., STENBERG, P., NILSON, T., KUUSK, A. 2004: The effect of crown shape on the reflectance of coniferous stands. *Remote Sensing of Environment*, 89: 41-52.
- REICHERT, H. & STETS, J. 1980: Der südwestliche Hunsrück - Hochwald und Idarwald. Köln.
- RICHARDS, J. A. 1993: Remote sensing digital image analysis. Berlin, Heidelberg, New York. Springer-Verlag.
- RICHARDSON, A. J. & WIEGAND, C. L. 1977: Distinguishing vegetation from soil background information. *Photogrammetric Engineering & Remote Sensing*, 43: 1541-1552.
- ROBERTS, G. 2001: A review of the application of BRDF models to infer land cover parameters at regional and global scales. *Progress in Physical Geography*, 25(4): 483-511.
- ROCK, B. N., HOSHIZAKI, T., MILLER, J. R. 1988: Comparison of in situ and airborne spectral measurements of the blue shift associated with forest decline. *Remote Sensing of Environment*, 24: 109-127.
- ROSEMA, A., VERHOEF, W., NOORBERGEN, H., BORGESIU, J. J. 1992: A new forest light interaction model in support of forest monitoring. *Remote Sensing of Environment*, 42: 23-41.
- ROUSE, J.W., HAAS, R.H., SCHELL, J.A. 1974: Monitoring the vernal advancement of retrogradation of natural vegetation. Greenbelt, MD, USA.
- RUMELHART, D.E., HINTON, G.E., WILLIAMS, R.J. 1986. Learning internal representations by error propagation. In: Rumelhart, D.E. & McClelland, J.L. (Eds.): *Parallel Distributed Processing, Vol 1*. Cambridge, MA: MIT Press.
- RUNNING, W. & COUGHLAN, J. C. 1988: A general model for forest ecosystem processes for regional applications. I. Hydrologic balance, canopy gas exchange and primary production processes. *Ecological Modeling*, 42: 125-154.
- RUNNING, W. & GOWER, T. 1991: Forest-BGC, a general model for forest ecosystem processes for regional applications. II. Dynamic carbon allocation and nitrogen budgets. *Tree Physiology*, 9: 147-160.
- RUNNING, W., PETERSON, D. L., SPANNER, M. A. 1986: Remote sensing of coniferous forest leaf area. *Ecology*, 67(1): 273-276.

- SALISBURY, J., MILTON, N. M., WALSH, P. A. 1987: Significance of non-isotropic scattering from vegetation for geobotanical remote sensing. *International Journal of Remote Sensing*, 8: 997-1009.
- SANDMEIER, S. 2004: Spectral BRDF. In: Schönermark, M. von, Geiger, B., Röser, H. P. (Eds.): *Reflection properties of vegetation and soil*. Berlin. Wissenschaft und Technik Verlag: 131-146.
- SANDMEIER, S., MÜLLER, C., HOSGOOD, B., ANDREOLI, G. 1998: Physical mechanisms in hyperspectral BRDF data of grass and watercress. *Remote Sensing of Environment*, 66: 222-233.
- SCHIMEL, D. S. 1995: Terrestrial biogeochemical cycles: Global estimates with remote sensing. *Remote Sensing of Environment*, 51: 49-56.
- SCHIMEL, D. S., HOUSE, J. I., HIBBARD, K. A. 2001: Recent patterns and mechanisms of carbon exchange by terrestrial ecosystems. *Nature*, 414: 169-172.
- SCHIMEL, D., MELILLO, J., TIAN, H., MCGUIRE, A. D., KICKLIGHTER, D., KITTEL, T., ROSENBLUM, N., RUNNING, S., THORNTON, P., OJIMA, D., PARTON, W., KELLY, R., SYKES, M., NEILSON, R., RIZZO, B. 2000: Contribution of increasing CO₂ and climate to carbon storage by ecosystems in the United States. *Science*, 287: 2004-2006.
- SCHLÄPFER D., SCHAEPMAN M. E., ITTEN K. I. 1998: PARGE: Parametric Geocoding Based on GCP- Calibrated Auxiliary Data. *SPIE Int. Symp. on Opt. Sc., Eng. and Instr.* San Diego, CA: 334-344.
- SCHLERF, M. & ATZBERGER, C. 2002: Use of a forest reflectance model for empirical estimation of Norway spruce characteristics from hyperspectral remote sensing imagery. In: Sobrino, J. (Ed.): *Recent advances in quantitative remote sensing, Proc. of the 1st International Symposium*, Valencia: 121-128.
- SCHLERF, M. & ATZBERGER, C. 2006: Inversion of a forest reflectance model to estimate structural vegetation attributes using hyperspectral remote sensing data. *Remote Sensing of Environment*, 100: 281-294.
- SCHLERF, M., ATZBERGER, C., HILL, J. 2005: Remote sensing of forest biophysical variables using HyMap imaging spectrometer data. *Remote Sensing of Environment*, 95: 177-194.
- SCHLERF, M., ATZBERGER, C., UDELHOVEN, T., JARMER, S., MADER, WERNER, W., HILL, J. 2003a: Spectrometric estimation of leaf pigments in Norway spruce needles using band-depth analysis, partial least-square regression and inversion of a conifer leaf model. *3rd EARSeL Workshop on Imaging Spectroscopy, Herrsching, May 13-16, 2003*: 559-568.
- SCHLERF, M., HILL, J., BÄRISCH, S., ATZBERGER, C. 2003: Einfluss der spektralen und räumlichen Auflösung von Fernerkundungsdaten bei der Nadelwaldklassifikation. *Photogrammetrie-Fernerkundung-Geoinformation*, 1/2003: 27-34.
- SCHOTT, J. R. 1997: Remote sensing - the image chain approach. New York, Oxford. Oxford University Press.
- SCHULTZ, J. 2000: Handbuch der Ökozonen. Stuttgart. Ulmer.
- SCHWIND, W. & SCHÜLER, G. 2001: Substratreihen in der Zentralfifel. Mitteilungen der Landesforstverwaltung Rheinland-Pfalz. Ministerium für Umwelt und Forsten, Mainz.
- SEDLMAYER 2004: <http://www.sedlmayer.de/holzneu/fichte.htm>.

- SERRANO, L., PENUELAS, J., USTIN, S. L. 2002: Remote sensing of nitrogen and lignin in Mediterranean vegetation from AVIRIS data: Decomposing biochemical from structural signals. *Remote Sensing of Environment*, 81: 355-364.
- SMITH, G. M. & CURRAN, P. J. 1996: The signal-to-noise ratio (SNR) required for the estimation of foliar biochemical concentrations. *International Journal of Remote Sensing*, 5: 1031-1058.
- SMITH, M. O., ADAMS, J. B., SABOL, D. E. 1994: Mapping sparse vegetation canopies. In: Hill, J., Megier, J. (Eds.): *Imaging spectrometry - a tool for environmental observations*. Dordrecht, Kluwer Academic Publishers: 221-236.
- SOUDANI, K., TRAUTMANN, J., WALTER, J. M. 2002: Leaf area index and canopy stratification in Scots pine stands. *International Journal of Remote Sensing*, 23(18): 3605-3618.
- SPANNER, M. A., PIERCE, L. A., PETERSON, D. A. 1990a: Remote sensing of temperate coniferous forest leaf area index - The influence of canopy closure, understory vegetation and background reflectance. *International Journal of Remote Sensing*, 11(1): 95-111.
- SPANNER, M. A., PIERCE, L. L., RUNNING, S. W., PETERSON, D. L. 1990: The seasonality of AVHRR data of temperate coniferous forests: Relationship with leaf area index. *Remote Sensing of Environment*, 33: 97-112.
- STATSOFT, INC., 2004: <http://www.statsoftinc.com/textbook/stathome.html>.
- STENBERG, P. 1996: Correcting LAI-2000 estimates for the clumping of needles in shoots of conifers. *Agriculture and Forest Meteorology*, 79: 1-8.
- STRAHLER, A. H., WOODCOCK, C. E., SMITH, J. A. 1986: On the nature of models in remote sensing. *Remote Sensing of Environment*, 20: 121-139.
- SUITS, G. H. 1972: The calculation of directional reflectance of a vegetation canopy. *Remote Sensing of Environment*, 2: 117-125.
- TANRE, D., DEROO, P., DUHAUT, P. 1985: Effets atmosphériques en télédétection, logiciel de simulation du signal satellitaire dans le spectre solaire. Les Arcs, France.
- TANRÉ, D., DUHAUT, P., HERMAN, M. 1990: Description of a computer code to simulate the signal in the solar spectrum: the 5S code. *International Journal of Remote Sensing*, 11(4): 659-668.
- TENHUNEN, J. D., VALENTINI, R., KOSTNER, B., ZIMMERMANN, R., GRANIER, A. 1998: Variation in forest gas exchange at landscape to continental scales. *Ann. For. Sci.*, 55: 1-11.
- THENKABAIL, P. S., SMITH, R. B., DE PAUW, E. 2000: Hyperspectral vegetation indices and their relationship with agricultural crop characteristics. *Remote Sensing of Environment*, 71: 158-182.
- TREITZ, P. M. & HOWARTH, P. J. 1999: Hyperspectral remote sensing for estimating biophysical parameters of forest ecosystems. *Progress in Physical Geography*, 23(3): 359-390.
- UDELHOVEN, T., ATZBERGER, C., HILL, J. 2000: Retrieving structural and biochemical forest characteristics using artificial neural networks and physically based reflectance models. In: Buchroithner, M. (Ed.): *A decade of trans-european remote sensing cooperation. Proceedings of the 20th EARSeL Symposium Dresden, Germany, 14-16 June 2000*: 205-211.

- USTIN, S. L., SMITH, M. O., JACQUEMOUD, S. 1999: Geobotany: Vegetation mapping for Earth Sciences. In: Rencz, A. N. (Ed.): *Remote sensing for the Earth sciences: Manual of remote sensing, 3rd ed., Vol. 3*. New York, Chichester, Weinheim. John Wiley & Sons: 189-248.
- USTIN, S. L., SMITH, M. O., JACQUEMOUD, S. 1999: Geobotany: Vegetation mapping for Earth sciences. In: Rencz, A. N. (Ed.): *Remote sensing for the Earth sciences: Manual of remote sensing, 3rd ed., Vol. 3*. New York, Chichester, Weinheim. John Wiley & Sons: 189-238.
- USTIN, S. L., WESSMAN, C. A., CURTISS, B. 1991: Opportunities for using the EOS imaging spectrometers and synthetic aperture radar in ecological models. *Ecology*, 72(6): 1934-1945.
- VALENTINI, R., MATTEUCCI, G., DOLMAN, A. J., SCHULZE, E.-D., REBMANN, C., MOORS, E. J., GRANIER, A., GROSS, P., JENSEN, N. O., PILEGAARD, K., LINDROTH, A., GRELE, A., BERNHOFER, C., GRÜNWARD, T., AUBINET, M., CEULEMANS, R., KOWALSKI, A. S., VESALA, T., RANNIK, Ü., BERBIGIER, P., LOUSTAU, D., GUDMUNDSSON, J., THORGEIRSSON, H., IBROM, A., MORGENSTERN, K., CLEMENT, R., MONCRIEFF, J., MONTAGNANI, L., MINERBI, S., JARVIS, P. G. 2000: Respiration as the main determinant of carbon balance in European forests. *Nature*, 404: 861-865.
- VAN DER MEER, F. D. & DE JONG, S. M. 2001: Imaging spectrometry – Basic principles and prospective applications. Dordrecht, Boston, London. Kluwer Academic Publishers.
- VAN DER MEER, F. D. 1994: Extraction of mineral absorption features from high-spectral resolution data using non-parametric geostatistical techniques. *International Journal of Remote Sensing*, 15: 2193-2214.
- VANE, G. & GOETZ, A. F. 1988: Terrestrial imaging spectroscopy. *Remote Sensing of Environment*, 24: 1-28.
- VANE, G. & GOETZ, A. F. 1993: Terrestrial imaging spectrometry: Current status, future trends. *Remote Sensing of Environment*, 44: 117-126.
- VERDEBOUT, J., JACQUEMOUD, S., SCHMUCK, G. 1994: Optical properties of leaves: Modeling and experimental studies. In: Hill, J., Megier, J. (Eds.): *Imaging spectrometry - a tool for environmental observations*. Dordrecht. Kluwer Academic Publishers: 169-191.
- VERHOEF, W. 1984: Light scattering by leaf layers with application to canopy reflectance modeling: The SAIL model. *Remote Sensing of Environment*, 16: 125-141.
- VERSTRAETE, M. M. & PINTY, B. 1996: Designing optimal spectral indices for remote sensing applications. *IEEE Transactions on Geoscience and Remote Sensing*, 34: 1254-1265.
- VERSTRAETE, M. M., PINTY, B., MYENI, R. B. 1996: Potential and limitations of information extraction on the terrestrial biosphere from satellite remote sensing. *Remote Sensing of Environment*, 58: 201-214.
- VITOUSEK, P. M. 1982: Nutrient cycling and nutrient use efficiency. *Nature*, 119: 553-572.
- VOHLAND, M. 1997: Einsatz von Satellitenbilddaten (Landsat TM) zur Ableitung forstlicher Bestandsparameter und Waldschadensindikatoren. M.Sc.-thesis. University of Trier.
- VOSE, J. M., DOUGHERTY, P. M., LONG, J. N. 1994: Factors influencing the amount and distribution of leaf area of pine stands. *Ecological Bulletins*, 43: 102-114.
- WALSH, S. J. 1980: Coniferous tree species mapping using Landsat data. *Remote Sensing of Environment*, 9: 11-26.

- WARING, R. H. & RUNNING, S. W. 1998: Forest ecosystems - Analysis at multiple scales. San Diego, London, Boston. Academic Press.
- WARING, R. H. & RUNNING, S. W. 1999: Remote sensing requirements to drive ecosystem models at the landscape and regional scale. In: Kabat, P. & Tenhunen, J. D. (Eds.): *Integrating Hydrology, Ecosystem Dynamics and Biogeochemistry in Complex Landscapes*. John Wiley & Sons: 23-37.
- WELLES, J. M. & NORMAN, J. M. 1991: Instrument for indirect measurement of canopy architecture. *Agronomy Journal*, 83: 818-825.
- WESSMAN, C. A. 1994: Remote sensing and the estimation of ecosystem parameters and functions. In: Hill, J., Megier, J. (Eds.): *Imaging spectrometry - a tool for environmental observations*. Dordrecht. Kluwer Academic Publishers: 39-55.
- WESSMAN, C. A. 1994a: Estimating canopy biochemistry through imaging spectrometry. In: Hill, J., Megier, J. (Eds.): *Imaging spectrometry - a tool for environmental observations*. Dordrecht. Kluwer Academic Publishers: 57-69.
- WESSMAN, C. A., ABER, J. D., PETERSON, D. L. 1989: An evaluation of imaging spectrometry for estimating forest canopy chemistry. *International Journal of Remote Sensing*, 10: 1293-1316.
- WESSMAN, C. A., ABER, J. D., PETERSON, D. L., MELILLO, J. M. 1988: Remote sensing of canopy chemistry and nitrogen cycling in temperate forest ecosystems. *Nature*, 335: 154-156.
- WEST, P. W. 2004: Tree and forest measurement. Berlin, Heidelberg, New York. Springer.
- WEYER, L. G. 1985: Near-infrared spectroscopy of organic substances. *Applied Spectroscopy Reviews*, 21(1): 1-43.
- WHITE, J. D., RUNNING, S. W., NEMANI, R. 1997: Measurement and remote sensing of LAI in Rocky Mountains montane ecosystems. *Canadian Journal of Forest Research*, 27: 1714-1727.
- WICKS, T. E. & CURRAN, P. J. 2003: Flipping forests: estimating future carbon sequestration of the boreal forest using remotely sensed data. *International Journal of Remote Sensing*, 24: 835-842.
- WILLIAMS, D. L. 1991: A comparison of spectral reflectance properties at the needle, branch, and canopy level for selected conifer species. *Remote Sensing of Environment*, 35: 79-93.
- WILSON, P. R. 1990: A new instrument concept for nitrogen / protein analysis - a challenge to the Kjeldahl method. *Aspects of Applied Biology*, 25: 443-446.
- WOODCOCK, C. E., COLLINS, J. B., GOPAL, S., S., JAKABHAZY, V. D., LI, X. 1994: Mapping forest vegetation using Landsat TM imagery and a canopy reflectance model. *Remote Sensing of Environment*, 50: 240-254.
- WULDER, M. 1998: Optical remote-sensing techniques for the assessment of forest inventory and biophysical parameters. *Progress in Physical Geography*, 22(4): 449-476.
- WULDER, M. A. & FRANKLIN, E. 2003: Remote sensing of forest environments - the transition from theory to information. In: Wulder, M. A., Franklin, E. (Eds.): *Remote sensing of forest environments - Concepts and case studies*. Boston, Dordrecht, London. Kluwer Academic Publishers: 3-12.

- ZARCO-TEJADA, P. J., MILLER, J. R., HARRON, J., HU, B., NOLAND, T. L., GOEL, N., MOHAMMED, G. H., SAMPSON, P. 2004a: Needle chlorophyll content estimation *Remote Sensing of Environment*, 89: 189-199.
- ZARCO-TEJADA, P. J., MILLER, J. R., MORALES, A., BERJÓN, A., AGÜERA, J. 2004: Hyperspectral indices and model simulation for chlorophyll estimation in open-canopy tree crops. *Remote Sensing of Environment*, 90: 463-476.
- ZARCO-TEJADA, P. J., MILLER, J. R., NOLAND, T. L. ., MOHAMMED, G. H., SAMPSON, P. H. 2001: Scaling-up and model inversion methods with narrowband optical indices for chlorophyll content estimation in closed forest canopies with hyperspectral data. *IEEE Transactions on Geoscience and Remote Sensing*, 39(7): 1491-1506.

Summary

Forest ecosystems cover large parts of the Earth's surface and play an important role in the global carbon budget. An understanding of their function requires determining their properties in space and time. The ability to remotely sense forest canopy properties would offer great potential for applications at regional to global scales such as environmental change assessment, forest inventory and management, and monitoring of forest fire and disease. A relatively new concept, hyperspectral remote sensing, may provide more information about the properties of forest canopies than conventional broadband sensor types, such as Landsat or SPOT.

Previous research studies in remote sensing attempted to estimate forest attributes with varying success. A lot of research has been done on the estimation of forest structural attributes, in particular leaf area index (LAI) from remote sensing data within about the last 15 years. Most of the studies on forests used broadband multispectral data, but very recently a few authors used hyperspectral remote sensing data to assess forest LAI. Few studies have reported on the application of multi- and hyperspectral data in mapping forest species and forest age classes. Laboratory studies on dry and ground leaves showed strong relations between leaf reflectance and foliar chemicals, but results on fresh whole leaves were generally poorer. From intensive research activities during the last decade it was concluded that a reliable estimation of canopy chemical concentrations from remote sensors needs an improvement of data quality and analysing techniques.

The aim of this research was to investigate the use of hyperspectral remote sensing data to determine important forest attributes. The work was conducted in forest plots (*Picea abies* L. Karst.) in Eifel and Hunsrück mountains, Germany. It focused on three broad types of forest attributes: cover type, structural attributes and chemical attributes. As such information is not explicitly recorded by a sensor it has to be extracted from remote sensing data for which a number of methodological approaches are generally available. The main focus of this work was to use and modify existing methods and to develop new approaches to successfully determine the forest attributes of interest. Major attention was paid to systematically compare different methods and data types.

The study on forest cover type compared the classification performance of four different remote sensing datasets of different spectral and spatial resolution to map forest species and age classes. To generate synthetic, multispectral broadband data, the HyMap image was spectrally resampled to Landsat TM wavebands and spatially degraded to 30 meter pixels. The results of the image classification showed that the overall accuracy and Kappa coefficient using the HyMap datasets were substantially larger than using the TM datasets. These results confirm that hyperspectral data contain more information relevant to the mapping of forest type than broadband multispectral data. Interestingly, degradation of the high spatial resolution to coarser image pixels considerably increased the classification accuracies.

The study on structural attributes compared empirical and physically-based approaches. In the empirical section linear predictive models between vegetation indices (VIs) derived from HyMap data and field measurements of structural forest stand attributes (n=39) were systematically evaluated. Ratio-based and soil-line related broadband VIs were calculated after HyMap reflectance had been spectrally resampled to Landsat TM channels.

Hyperspectral VIs involved all possible types of 2-band combinations of ratio VIs (RVI) and perpendicular VIs (PVI) and the red-edge inflection point (REIP) computed from two techniques. A PVI based on wavebands at 1088 nm and 1148 nm was linearly related to leaf area index ($R^2=0.77$, $rmse=0.54 \text{ m}^2\text{m}^{-2}$ (17% of mean)). A similar index was linearly related to the crown volume that had been derived from measured structural attributes through factor analysis. The study demonstrates that for hyperspectral image data, linear regression models can be applied to quantify LAI and VOL with good accuracy. For broadband multispectral data, the accuracy was generally lower. Best hyperspectral VIs in relation with LAI were typically based on wavebands related to prominent water absorption features.

The physically-based approach used the invertible forest reflectance model (INFORM), a combination of well established sub-models FLIM, SAIL and LIBERTY. The model was inverted with HyMap data using a neural network approach. To identify the optimum 2-band spectral subset to be used in the inversion process, all 2-band combinations were systematically evaluated for model inversion. LAI field measurements from 39 forest stands were used to validate the LAI maps produced from HyMap imagery. Using two HyMap wavebands at 837 nm and 1148 nm the obtained accuracy of the LAI map amounts to an $rmse$ of $0.58 \text{ m}^2\text{m}^{-2}$ (18% of mean). The approach could be shown to potentially work also on operational multispectral sensors. With HyMap data resampled to Landsat TM spectral bands and using two bands at 840 nm and 1650 nm, the $rmse$ was 0.66 and relative $rmse$ amounted to 21 %. In comparison to the empirical approach, it could be shown that the reflectance model inversion works equally well. In opposition to empirically derived prediction functions that are generally limited to the local conditions at a certain point in time and to a specified sensor type, the calibrated reflectance model can be applied more easily to different optical remote sensing data acquired over central European forests.

The study on chemical forest attributes evaluated the information content of HyMap data for the estimation of nitrogen, chlorophyll and water concentration. A number of needle samples ($n=78$) of Norway spruce were analysed for their total chlorophyll (C_{AB}), nitrogen (C_N) and water (C_W) concentrations. The research was divided into two areas: needle spectra measured in the laboratory and canopy spectra measured by the HyMap sensor. The objective was to find empirical models by stepwise multiple linear regression (SMR) analysis using certain absorption features to determine foliar chemicals.

Laboratory reflectance measurements were made for layer stacks of whole green needles. To test the transferability of the approach from the leaf to the canopy level, the effects of sensor bandwidth and sensor noise on the estimation of the chemical concentrations was investigated. SMR analysis showed that C_{AB} was well estimated and just slightly affected by a decrease of the spectral resolution or adding of noise, C_N was moderately well estimated and just slightly affected by a decrease of the spectral resolution or adding of noise and C_W was well estimated but strongly affected by noise addition. The wavebands selected to estimate C_{AB} were typically located in the red edge region and along the edge of the chlorophyll absorption feature. For C_N , the wavebands selected in the regression models were often related to the chlorophyll absorption feature, the red edge region and to known protein absorption features. Regression models to estimate C_W often employed wavebands related to C_{AB} or wavebands located at the edge of water absorption features.

Scaling up from leaf to canopy level was achieved through directly establishing statistical relationships between ground-measured chemical data and canopy-measured reflectances. Five different types of derivatives of reflectance were compared in estimating foliar chemicals: reflectance, first-difference of reflectance, continuum-removed spectra, band-depth normalised spectra (BDN) and water removed spectra. The best predictive model to estimate C_{AB} was achieved by BDN with a cross-validated R^2 of 0.90 and a relative $rmse$ of 2.8 percent ($n=13$). C_N was moderately well estimated (relative $rmse$ below 5 percent). Selected wavebands, although most often not attributable to known absorption features, were often located in spectral regions that are known to be important for chlorophyll detection (red edge, green peak). Predictive models were applied on the HyMap image to compute maps of chlorophyll concentration and nitrogen concentration. Results of map overlay operations revealed coherence between C_{AB} and zones of stand development stage and between C_{AB} and zones of soil type. Larger values of C_{AB} occurred over soils with large base saturation (formed

of basalt and colluvium) whereas poorly base saturated soils over sandstone showed lower C_{AB} values.

Finally, it can be stated that the hyperspectral remote sensing data generally contains more information relevant to the estimation of the forest attributes compared to multispectral data. Structural forest attributes can be determined with good accuracy from a hyperspectral sensor type like HyMap. Among the chemical attributes, chlorophyll concentration can be determined with good accuracy and nitrogen concentration with moderate accuracy. For future research, additional dimensions have to be taken into account, for instance through exploitation of multi-view angle data.

Zusammenfassung

Die fernerkundliche Erfassung struktureller und chemischer Forstattribute ist in der aktuellen Ökosystemforschung, der Entwicklung zukünftiger Inventarisierungsverfahren und für das Umweltmonitoring von hoher Relevanz. Bisherige Untersuchungen zur Quantifizierung von Forstattributen aus Fernerkundungsdaten, die zumeist auf der Auswertung multispektraler Satellitenbilder basierten, verliefen mit unterschiedlichem Erfolg.

Das Ziel dieser Forschungsarbeit liegt in der Bewertung der Möglichkeiten, strukturelle und chemische Forstattribute mit hyperspektralen Fernerkundungsdaten bestimmen zu können. Untersucht werden Fichtenforsten in Eifel und Hunsrück. Die Gemeine Fichte (*Picea abies* L. Karst.) ist aufgrund ihrer starken Verbreitung in den Untersuchungsgebieten und ihrer geringen jahreszeitlichen Dynamik gut für eine fernerkundliche Charakterisierung geeignet. Die entsprechenden Forstgrößen werden jedoch nicht explizit vom Sensor erfasst, sondern müssen zunächst aus den fernerkundlichen Rohdaten über eine Reihe von Prozessierungs- und Analyseschritte abgeleitet werden. Ein maßgeblicher Aspekt der Untersuchungen stellt die Nutzung und Modifizierung bestehender sowie die Entwicklung neuer Methodenansätze zur erfolgreichen Bestimmung der Zielgrößen dar. Besonderes Gewicht liegt auf dem Vergleich unterschiedlicher Methoden und Datentypen. Die dazu benötigten Referenzdaten wurden im Rahmen von Gelände- und Laborarbeiten erhoben oder standen bereits in Form eines Forstlichen Geographischen Informationssystems zur Verfügung. Bildspektrometerdaten (HyMap-Sensor) wurden 1999 und 2003 akquiriert und radiometrisch und geometrisch korrigiert. Es werden drei Attributklassen untersucht: i) Forsttyp, ii) strukturelle Forstattribute und iii) chemische Forstattribute.

Zur fernerkundlichen Kartierung von Forsttypen, das heißt von Forstbeständen einer bestimmten Baumart und Altersklasse, werden aus den HyMap-Daten synthetische Bilder unterschiedlicher spektraler und geometrischer Auflösung erzeugt und hinsichtlich ihrer Klassifikationsgenauigkeiten miteinander verglichen. Die Datensätze wurden mit dem so genannten „Spectral Angle Mapper“ klassifiziert. Die Ergebnisse zeigen, dass Hyperspektraldaten mit einer deutlich höheren Genauigkeit klassifiziert werden können als Multispektraldaten. Eine Reduzierung der geometrischen Auflösung führt auf den relativ großflächigen, homogenen Fichtenbeständen zu einer Verbesserung der Gesamtklassifikationsgenauigkeit, was mit einer geringeren Bildvarianz erklärt werden kann. Insgesamt kann mit dem hyperspektralen Datensatz geringer Pixelgröße eine gute bis sehr gute Differenzierung der Alterklassen Dichtung, Stangenholz, Baumholz und Altholz erzielt werden.

Für die Bestimmung der strukturellen Forstattribute wurden empirisch-statistische und physikalisch-basierte Verfahren implementiert. Im empirischen Teil der Studie wird der Zusammenhang zwischen Vegetationsindizes, die aus HyMap-Daten berechneten wurden, und im Gelände gemessenen Bestandsvariablen analysiert. Die Geländeerhebungen umfassen

die standardisierte Bestimmung wichtiger Strukturgrößen in 42 Fichtenbeständen, darunter Blattflächenindex, Bestockungsdichte, Kronenschlussgrad, Brusthöhendurchmesser und Bestandeshöhe. Der effektive Blattflächenindex (LAI) wurde über ein optisches Verfahren (LI-COR LAI-2000) bestimmt. Es werden unterschiedliche breit- und schmalbandige sowie „ratio“- und „soil line“-basierte Vegetationsindizes und darüber hinaus Verfahren zur Bestimmung des Inflexionspunktes systematisch untersucht. Die ausgewählten breitbandigen Vegetationsindizes (SR, NDVI, PVI, SAVI, TSAVI, u. a.) wurden zwar schon in Einzelstudien angewendet, bisher aber noch nicht einem systematischen Vergleich auf Wäldern unterzogen. Die schmalbandigen VIs umfassen sämtliche 2-Band Kombinationen hyperspektraler „Ratio“-VIs (RVI) und „Perpendicular“-VIs (PVI). Als Gütemaß zur Bewertung der unterschiedlichen Indizes dienen kreuzvalidiertes Bestimmungsmaß (R^2) und kreuzvalidierter rms Fehler („root mean squared error“). Bester Index ist ein hyperspektraler PVI basierend auf Spektralbändern bei 1088 nm und 1148 nm, der linear zum LAI in Beziehung gesetzt wird ($R^2 = 0,77$, $rmse = 0,54 \text{ m}^2 \text{ m}^{-2}$ (17 % des Mittelwertes)). Ein ähnlicher Index zeigt einen engen Zusammenhang zum Kronenvolumen, das zuvor aus den im Gelände erhobenen Attributen mittels Faktorenanalyse bestimmt worden ist. Breitband VIs erzielen generell geringere Genauigkeiten. Zur Stammbiomasse konnten keine Beziehungen gefunden werden. Die Positionen der in den Indizes verwendeten Spektralbänder befinden sich in der Nähe prominenter Wasserabsorptionsbanden – ein Beweis dafür, dass der Differenzierung nach LAI maßgeblich der Bestandswassergehalt zu Grunde liegt. Die Bedeutung der Spektralbänder im mittleren Infrarot für die Charakterisierung von Wäldern ist auch durch andere Untersuchungen bestätigt worden. Ferner spiegelt die festgestellte Veränderung des LAI mit dem Bestandsalter deutlich die waldbaulichen Maßnahmen wider. Die Studie demonstriert, dass Hyperspektraldaten gut zur Quantifizierung wichtiger Forstattribute wie LAI und Kronenvolumen, aber nicht biomassebezogener Größen geeignet sind.

Der physikalisch-basierte Ansatz verwendet das Invertierbare Forstreflexionsmodell (INFORM), eine Kombination aus etablierten Untermodellen FLIM, SAIL und LIBERTY. Nachdem das Modell mit Attributdaten aus Geländeerhebungen parametrisiert worden ist, wird es auf HyMap-Daten mittels Künstlicher Neuronaler Netze (KNN) invertiert. Zur Identifizierung geeigneter Spektralkanäle werden bei der Invertierung alle 2-Band Kombinationen systematisch untersucht. Die aus der Modellinversion resultierenden Parameterkarten werden mit den Geländedaten validiert. Mit zwei Spektralbändern bei 837 nm und 1148 nm kann für LAI eine Fehlergenauigkeit von $0,58 \text{ m}^2 \text{ m}^{-2}$ (18% vom Mittelwert) erzielt werden. Auf spektral reduzierten Daten (Landsat TM) ergibt sich unter Verwendung der Spektralbänder bei 840 nm und 1650 nm ein Fehler von $0,66 \text{ m}^2 \text{ m}^{-2}$. Die Genauigkeit, die mit dem physikalisch-basierten Ansatz erzielt wird, ist mit den Fehlerwerten empirischer Verfahren vergleichbar. Kalibrierte Reflexionsmodelle haben jedoch den Vorteil, dass sie generell auf unterschiedliche Sensortypen und unter wechselnden Rahmenbedingungen anwendbar sind.

Die Untersuchung chemischer Forstattribute hat zum Ziel, den Informationsgehalt von Bildspektrometerdaten hinsichtlich der Bestimmung von Stoffkonzentrationen in Fichtennadeln zu bewerten. Empirisch-statistische Modelle werden mittels Schrittweiser Multipler Regression zunächst auf Laborspektren entwickelt und anschließend auf Bestandsebene übertragen. Das Potential unterschiedlicher Reflexionsderivate (Reflexionsspektren, Ableitungsspektren, kontinuum-bereinigte Spektren, bandtiefen-normalisierte Spektren und wasserbereinigte Spektren) zur spektrometrischen Bestimmung wird systematisch untersucht. Die im Gelände in 13 Fichtenbeständen standardisiert entnommenen Nadelproben ($n=78$) sind in frischem Zustand im Labor mit einem

Spekroradiometer (Field-Spec-II) gemessen und anschließend auf ihre Stoffkonzentrationen von Chlorophyll, Stickstoff, Wasser hin analysiert worden. Um die Übertragbarkeit auf Bilddaten abschätzen zu können, wird der Einfluss von spektraler Bandbreite und Sensorrauschen auf die Genauigkeit der statistischen Modelle untersucht. Die erzielten Ergebnisse zeigen, dass die Genauigkeit bei der Bestimmung der Blattinhaltsstoffe aus Laborspektren nur in geringem Maße durch eine verminderte spektrale Auflösung oder durch Sensorrauschen reduziert wird. Zum Hochskalieren von Blatt- auf Bestandsebene werden direkte Beziehung zwischen Blattanalysen und Bestandsspektren erstellt. Die Chlorophyllkonzentration wird von allen Verfahren, jedoch mit unterschiedlicher, aber guter Genauigkeit bestimmt (kreuzvalidierter relativer rmse 2.8-6.9 % des Mittelwerts; kreuzvalidiertes $R^2 = 0.90-0.46$). Die Bestimmung der Stickstoffkonzentration kann nur von drei Verfahren (wasserbereinigte Spektren, kontinuum-bereinigte Spektren und Ableitungsspektren) mit mäßiger Genauigkeit (rmse = 4.6-4.9 % des Mittelwerts; $R^2 = 0.52-0.57$) geleistet werden. Für den Blattwassergehalt können hingegen keine signifikanten Beziehungen gefunden werden. Selektierte Wellenlängen zur Schätzung von Chlorophyll befinden sich typischerweise im „red edge“ und im Randbereich der Chlorophyllabsorptionsbanden. Regressionsmodelle zur Schätzung von Stickstoff haben meist einen deutlichen Bezug zu den Absorptionsbanden von Chlorophyll oder Protein oder zum „red edge“. Die Verwendung der genannten Absorptionsbanden wird auch durch vergleichbare Untersuchungen anderer Vegetationstypen bestätigt. Die räumliche Verteilung der Blattchlorophyllkonzentration im Untersuchungsgebiet spiegelt die Nährstoffversorgung der Böden wider. So werden über basenreichen Basaltverwitterungslehmen im Mittel deutlich höhere Chlorophyllkonzentrationen beobachtet als auf den basenarmen Sanden des Mittleren Buntsandsteins.

Im Rahmen der vorliegenden Arbeit wurden Bildspektrometerdaten verwendet, um quantitative Bestandsattribute in Fichtenforsten fernerkundlich abzuleiten. Die abgeleiteten Parameterkarten können als wichtiger Beitrag zur Entwicklung fortgeschrittener Inventarisierungsstrategien und zur Parametrisierung von Stoff- und Energieflussmodellen angesehen werden. Zukünftige Strategien sollten weitere Dimensionen, wie z. B. multidirektionelle Beobachtungen, in den Auswerteprozess miteinbeziehen, um eine verbesserte Bestimmung wichtiger Oberflächenparameter zu erzielen. Zudem ist eine weitere Verbesserung bestehender Bestandsreflexionsmodelle anzustreben.

Appendix A: Field data

A1: Plots at Idarwald test site

Plot-ID	Stand number	E	N	Stand age [yrs]	PBH [m]	SD [/ha]	CO	LAI	H [m]	CD [m]	Comment
38	171a	2586713	5524702	46	0.92	622	0.45	3.81	18.0	-	ok
59	155a	2587195	5524101	20	0.48	1489	0.65	5.47	9.3	-	ok
65	165	2586664	5523910	68	1.15	511	0.40	3.31	29.3	4.9	ok
81	148b	2587394	5523645	18	0.49	1333	0.60	4.94	6.2	-	ok
82	157a	2586433	5523369	135	1.57	278	0.50	2.48	30.6	7.2	ok
83	156a	2587024	5523430	10	0.27	2444	0.70	4.23	5.0	-	ok
85	149a	2587282	5523455	49	0.81	800	0.50	2.63	23.0	-	recent thinning
100	158a	2586294	5523166	57	0.91	467	0.35	2.88	23.8	-	ok
110	150b1	2586687	5522995	119	1.24	478	0.35	2.97	30.1	4.1	ok
111	144a	2587696	5523082	95	1.55	244	0.30	1.66	26.9	6.5	ok
115	158a	2586477	5522942	148	1.62	511	0.60	2.90	39.1	7.0	ok
118	125a1	2585601	5522574	48	1.36	267	0.40	2.66	33.7	6.8	ok
125	145	2587196	5522843	104	1.27	367	0.45	3.31	26.9	6.3	ok
129	150a2	2586913	5522671	119	1.38	378	0.40	2.24	27.3	6.1	ok
137	142a	2587548	5522577	34	0.81	955	0.55	4.08	13.0	-	ok
138	126a	2585435	5522317	62	0.90	611	0.35	2.98	27.1	3.8	ok
144	111a	2586099	5522455	108	1.33	367	0.35	2.12	30.8	-	ok
151	112a	2585852	5522190	111	1.09	578	0.60	2.42	26.6	5.6	ok
157	146a	2587324	5522264	70	1.15	600	0.55	5.07	26.3	4.5	ok
169	104	2586216	5521758	81	1.17	367	0.45	2.60	35.4	4.6	ok
187	125a2	2585752	5522695	64	1.06	422	0.30	2.52	26.0	4.5	ok
191	95a	2586627	5522094	80	1.63	411	0.55	2.70	30.3	6.3	ok
195	149a3	2587387	5523456	93	1.29	356	0.35	2.36	26.3	4.8	ok
208	162a	2587563	5525251	69	1.09	456	0.40	2.53	31.9	5.0	ok
218	113b	2585104	5521825	53	1.07	433	0.50	3.27	21.4	-	ok
219	128b	2584541	5521843	68	1.12	589	0.55	1.86	26.7	6.1	ok

A1: Plots at Idarwald test site (continued)

Plot-ID	Stand number	E	N	Stand age [yrs]	PBH [m]	SD [/ha]	CO	LAI	H [m]	CD [m]	Comment
220	118a2	2583737	5520076	87	0.91	722	0.35	2.71	25.0	3.9	ok
223	101c	2584336	5519335	106	1.21	433	0.35	2.28	27.5	3.9	outside HyMap stripe
252	106a	2585225	5520983	68	1.07	522	0.55	3.20	25.9	5.5	ok
254	115a	2584710	5520838	70	1.09	567	0.55	2.28	26.0	5.7	ok
263	116b	2584361	5520543	10	0.40	2044	0.70	5.22	6.5	-	ok
271	107c	2585159	5520472	90	1.27	389	0.40	2.66	28.2	5.5	ok
283	69b	2583502	5519911	47	0.98	533	0.55	3.66	23.0	-	ok
292	58a	2583839	5519562	64	1.19	411	0.40	3.35	25.1	5.1	ok
298	55a2	2583833	5519305	99	1.19	444	0.50	4.01	30.4	5.1	ok
301	55a3	2583717	5519228	120	1.28	344	0.40	3.06	35.1	6.1	ok
308	71a	2582893	5519122	20	0.57	1378	0.70	5.16	14.0	-	ok
335	73a	2581995	5518293	44	0.82	955	0.65	4.67	22.2	-	ok
345	73c	2581881	5517925	126	1.49	278	0.40	2.23	36.6	6.3	ok
361	63a2	2581768	5517253	68	1.10	611	0.50	4.11	25.0	4.5	ok
389	108b	2584646	5520290	91	1.21	411	0.40	2.76	28.0	6.2	ok
391	110as	2584138	5519371	100	1.30	378	0.45	3.52	28.6	5.8	ok

A2: Plots at Gerolstein test site

Plot-ID	E	N	Owner	Stand number	Stand age [yrs]	Type of substrate	Base saturation	C _{AB} [mg/g dry matter]	C _w [% dry matter]	C _N [% dry matter]
GS2	2548432	5568600	Rockeskyll	4d	51	BVL	high	3.32	132.8	1.16
GS3	2549121	5568205	Rockeskyll	4b	44	DLB	high	3.46	133.2	1.25
GS4	2548350	5568119	Rockeskyll	4e	55	Kol+	high	3.40	127.3	1.13
GS8	2550398	5566541	Pelm	20b	48	BVL	high	3.62	137.1	1.31
GS9	2548329	5566132	Pelm	23a	132	KVL	very high	2.99	139.5	1.18
GS10b	2548684	5565191	Pelm	19a	135	KVL	very high	3.23	139.5	1.29
GS16	2549466	5562358	State	307a	99	Vldu	low-medium	3.20	148.2	1.23
GS17	2550294	5563632	Pelm	9b	52	wDLT	medium	2.79	140.7	1.08
GS18	2550071	5563813	Pelm	11a	70	wDLT	medium	3.56	144.1	1.26
GS19	2548682	5564080	Pelm	17d	46	Ssm	very low	2.71	122.5	1.08
GS21	2549041	5564175	Pelm	16b	105	Ssm	very low	2.82	125.9	1.08
GS24	2549699	5563585	Pelm	9c	48	DLsm	low	3.20	149.0	1.25
GS25	2547944	5564210	Private	Fam. Moss	50	DLsm	low	3.42	134.7	1.22

Appendix B: Chemical analysis data

B1: Needle samples

Sample	C _A [mg/g dry matter]	C _B [mg/g dry matter]	C _{AB} [mg/g dry matter]	C _W [% dry matter]	C _N [% dry matter]
GS2-1.1	3.09	1.73	4.82	145.6	1.20
GS2-1.3	3.74	2.15	5.89	120.7	1.22
GS2-2.1	2.31	1.46	3.77	145.8	1.15
GS2-2.3	3.19	2.03	5.22	109.6	1.15
GS2-3.1	2.72	1.68	4.40	156.5	1.18
GS2-3.3	3.25	1.96	5.21	118.4	1.06
GS3-1.1	2.23	0.58	2.81	147.5	1.26
GS3-1.3	2.63	0.82	3.46	120.4	1.21
GS3-2.1	2.51	0.61	3.12	161.6	1.29
GS3-2.3	0.96	1.52	2.49	122.5	1.22
GS3-3.1	2.43	0.63	3.06	138.4	1.31
GS3-3.3	2.38	0.68	3.06	108.7	1.19
GS4-1.1	2.25	0.57	2.82	143.1	1.22
GS4-1.3	3.41	1.30	4.71	108.5	1.11
GS4-2.1	2.33	1.32	3.65	143.2	1.01
GS4-2.3	3.25	1.87	5.12	112.7	1.06
GS4-3.1	2.45	1.07	3.51	138.6	1.25
GS4-3.3	3.20	1.65	4.85	117.8	1.13
GS8-1.1	2.16	0.52	2.68	159.1	1.34
GS8-1.3	3.32	0.97	4.29	131.5	1.27
GS8-2.1	2.59	0.69	3.27	155.0	1.40
GS8-2.3	2.43	0.72	3.15	114.6	1.23

B1: Needle samples (continued)

Sample	C _A [mg/g dry matter]	C _B [mg/g dry matter]	C _{AB} [mg/g dry matter]	C _W [% dry matter]	C _N [% dry matter]
GS8-3.1	2.37	0.59	2.97	147.4	1.46
GS8-3.3	2.68	0.79	3.47	114.9	1.16
GS9-1.1	1.96	0.47	2.43	158.4	1.27
GS9-1.3	2.38	0.62	2.99	127.8	1.24
GS9-2.1	1.57	0.39	1.97	151.8	1.00
GS9-2.3	2.11	0.61	2.72	127.5	1.05
GS9-3.1	1.90	0.48	2.39	153.0	1.19
GS9-3.3	2.80	0.86	3.66	118.3	1.30
GS10b-1.1	1.94	0.51	2.44	146.2	1.31
GS10b-1.3	2.94	0.96	3.90	113.3	1.34
GS10b-2.1	1.85	0.46	2.31	156.9	1.33
GS10b-2.3	2.54	0.76	3.30	129.6	NaN
GS10b-3.1	1.73	0.42	2.16	166.3	1.26
GS10b-3.3	2.57	0.74	3.31	124.6	1.22
GS16-1.1	1.92	0.60	2.52	161.3	1.23
GS16-1.3	2.26	0.82	3.08	128.2	1.09
GS16-2.1	1.92	0.51	2.43	153.7	1.19
GS16-2.3	2.90	1.27	4.17	138.8	1.16
GS16-3.1	2.19	0.58	2.76	166.7	1.31
GS16-3.3	2.83	0.91	3.74	140.4	1.37
GS17-1.1	1.64	0.39	2.03	148.8	1.16
GS17-1.3	2.24	0.64	2.88	123.5	1.10
GS17-2.1	1.31	0.40	1.71	136.1	0.91
GS17-2.3	1.58	0.55	2.13	133.5	0.88
GS17-3.1	2.70	0.71	3.41	164.2	1.30
GS17-3.3	2.61	0.90	3.51	138.2	1.11

B1: Needle samples (continued)

Sample	C _A [mg/g dry matter]	C _B [mg/g dry matter]	C _{AB} [mg/g dry matter]	C _w [% dry matter]	C _N [% dry matter]
GS18-1.1	2.10	0.54	2.64	155.0	1.18
GS18-1.3	2.64	0.81	3.45	128.7	1.13
GS18-2.1	2.28	0.62	2.91	169.2	1.40
GS18-2.3	3.11	0.95	4.06	127.5	1.28
GS18-3.1	2.50	0.70	3.20	146.2	1.32
GS18-3.3	2.83	0.85	3.68	138.0	1.24
GS19-1.1	1.62	0.40	2.02	126.2	0.98
GS19-1.3	2.06	0.61	2.66	113.7	1.07
GS19-2.1	1.99	0.51	2.50	141.2	1.16
GS19-2.3	2.13	0.61	2.74	112.7	1.06
GS19-3.1	1.75	0.45	2.19	130.6	1.12
GS19-3.3	2.22	0.66	2.88	110.4	1.06
GS21-1.1	2.16	0.54	2.70	137.4	1.17
GS21-1.3	2.70	0.80	3.50	112.5	1.09
GS21-2.1	1.76	0.45	2.21	142.4	1.09
GS21-2.3	2.11	0.64	2.74	107.9	1.06
GS21-3.1	1.66	0.48	2.14	138.7	1.07
GS21-3.3	1.76	0.53	2.29	116.6	0.99
GS24-1.1	1.90	0.45	2.36	163.2	1.29
GS24-1.3	2.39	0.74	3.13	129.0	1.19
GS24-2.1	2.35	0.62	2.97	150.4	1.32
GS24-2.3	2.46	0.69	3.15	141.8	1.22
GS24-3.1	2.20	0.57	2.76	170.8	1.28
GS24-3.3	2.51	0.74	3.24	138.6	1.18

Appendix C: Matlab code

C1: INFORM model

```
% _____  
function [r_forest,r_soil,r_understorey,r_c_inf,co,C,G,r_needle,t_needle,t_s,t_o]= ...  
    inform_liberty(PARA_LIBERTY,PARA_INFORM,teta_o,teta_s,phi,skyl,r_soil,r_wood,data,liberty_data_hymap);  
  
% INFORM_LIBERTY - The INvertible FOrEst Reflectance Model coupled with LIBERTY  
  
% INFORM (Atzberger, 2000; Schlerf&Atzberger, 2005) simulates the bi-directional reflectance  
% of forest stands between 400 and 2500 nm. INFORM is essentially an innovative combination of  
% FLIM (Rosema et al., 1992), SAIL (Verhoef, 1984), and PROSPECT (Jacquemoud & Baret, 1990) or  
% LIBERTY (Dawson et al., 1998).  
  
% Atzberger, C. 2000: Development of an invertible forest reflectance model: The INFORM-Model.  
% In: Buchroithner (Ed.): A decade of trans-european remote sensing cooperation. Proceedings  
% of the 20th EARSeL Symposium Dresden, Germany, 14.-16. June 2000: 39-44.  
  
% Schlerf, M. & Atzberger, C. (2005): Inversion of a forest reflectance model to estimate biophysical  
% canopy variables from hyperspectral remote sensing data. Submitted to Remote Sensing of Environment.  
  
% Rosema, A., Verhoef, W., Noorbergen, H. 1992: A new forest light interaction model in support of forest  
% monitoring. Remote Sensing of Environment, 42: 23-41.  
  
% Jacquemoud, F. & Baret, F. 1990: PROSPECT: A model of leaf optical properties spectra. Remote Sensing of  
% Environment, 34: 75-91.  
  
% Dawson, T. P., Curran, P. J., Plummer, S. E. 1998: LIBERTY - Modeling the effects of leaf biochemical  
% concentration on reflectance spectra. Remote Sensing of Environment, 65: 50-60.  
  
% Verhoef, W. 1984: Light scattering by leaf layers with application to canopy reflectance modeling: The  
% SAIL model. Remote Sensing of Environment, 16: 125-141.
```

C1: INFORM model (continued)

```

% Basic version of INFORM: Clement Atzberger, 1999
% Implementation of LIBERTY: Sebastian Mader, 2002
% INFORM modifications and validation: Martin Schlerf, 2004
%
%-----% SUBROUTINES
%
% M-File          Function
% sail_background.m  SAIL-PROSPECT-SOIL to compute background reflectance
% sail_inf.m        SAIL-PROSPECT-SOIL to compute infinite crown reflectance
% sail_t_s.m       SAIL-PROSPECT-SOIL to compute crown transmittance for sun direction
% sail_t_o.m       SAIL-PROSPECT-SOIL to compute crown transmittance for observation direction
% liberty.m        Needle reflectance model LIBERTY
% prospect.m       Leaf reflectance model PROSPECT (to compute understorey leaf reflectance)
% S13AAF.M        Integral
% TAV.M           Refraction index
%
%-----
% INPUT VARIABLES
%
% PARA_LIBERTY: Needle Input Parameters
%
% Variable          Designation          Unit          Default value
% Cell diameter     d          µm           40
% Intercellular air space  i          arbitrary    0.045
% Leaf thickness    t          arbitrary    1.6
% Baseline absorption  b          arbitrary    0.0006
% Albino absorption  a          arbitrary    2
% Chlorophyll content  cab        mg m-2      200
% Water content      cw         g m-2       100
% Lignin and cellulose content  cl        g m-2       40
% Nitrogen content    cp         g m-2       1

```

C1: INFORM model (continued)

```
% PARA_INFORM: Canopy Input Parameters
```

% Variable	Designation	Unit	Default value
% Single tree leaf area index	lai	m ² m ⁻²	7
% Leaf area index of understorey	laiu	m ² m ⁻²	0.1
% PROSPECT parameter	vaiprosu	arbitrary	2
% Stem density	sd	ha ⁻¹	650
% Tree height	h	m	20
% Crown diameter	cd	m	4.5
% Average leaf angle of tree canopy	ala	deg	55
% Scale factor for soil reflectance	scale	fraction	1

```
% External Input Parameters
```

% Variable	Designation	Unit	Default value
% Sun zenith angle	teta_s	deg	30
% Observation zenith angle	teta_o	deg	0
% Azimuth angle	phi	deg	0
% Fraction of diffuse radiation	skyl	fraction	0.1

```
% Other Input Data
```

% Variable	Designation
% r_soil	Soil spectrum
% data	PROSPECT coefficients resampled to HyMap wavebands
% liberty_data_hymap	LIBERTY coefficients resampled to HyMap wavebands

```
%
```

```
% OUTPUT VARIABLES
```

% Variable	Designation
% Forest reflectance	r_forest
% Soil reflectance	r_soil
% Understorey reflectance	r_understorey
% Infinite canopy reflectance	r_c_inf
% Canopy cover	co
% Crown factor	C
% Ground factor	G

C1: INFORM model (continued)

```

% Needle reflectance           r_needle
% Needle transmittance        t_needle
% Crown transmittance for teta_s  t_s
% Crown transmittance for teta_o  t_o
%
% -----

lai=PARAM_INFORM(1);
laiu=PARAM_INFORM(2);
vaiprosu=PARAM_INFORM(4);
sd=PARAM_INFORM(6);
h=PARAM_INFORM(7);
cd=PARAM_INFORM(8);
ala=PARAM_INFORM(9);
scale=PARAM_INFORM(10);

% -----

% Computation of spectral components (SAIL, PROSPECT, LIBERTY models)

% Scaling of soil spectrum (to account for effects due to shadow and soil moisture)
r_soil=scale*r_soil;

% Computation of understorey reflectance for dicotyledoneae (ala=45, hot=0, cab=30, cw=0.05, N=2.5)
r_understorey=sail_background(laiu,45,0,30,0.05,vaiprosu,teta_o,teta_s,phi,skyl,r_soil,data);

% Computation of needle reflectance and transmittance for HyMap wavebands by LIBERTY
% [r_needle,t_needle]=liberty(PARAM_LIBERTY', liberty_data_hymap);
[rt]=prospect(1.2,40,0.015,data); r_needle=rt(:,1); t_needle=rt(:,2);

% Computation of infinitive crown reflectance for a very dense forest canopy with LAI=15 (hot=0, N=1.5)
r_c_inf=sail_inf(15,ala,0,teta_o,teta_s,phi,skyl,r_understorey,r_needle,t_needle);
% -----

% Ground coverage (FLIM model)

% Computation of the average horizontal area of a single tree crown in hectare (k) corrected by the factor 'adapt'.

```

C1: INFORM model (continued)

```

% 'adapt' was adjusted in such a way, that modelled values of 'co' agreed with measured values of 'co' for a given
% stand structure (as defined by 'cd' and 'sd'). To compare measured with modelled stands for certain values of canopy
% lai (lai_c), an empirical relation between 'lai_c' and 'co' was derived from field data at Idarwald site
% (co=0.078*lai_c+0.23, n=40).

% adapt=1; % no correction
adapt=0.6;

k=adapt*(pi*(cd/2).^2)/10000;

% angles (degree) to angles (radian)
teta_o=teta_o*pi/180;
teta_s=teta_s*pi/180;
phi=phi*pi/180;

% Observed ground coverage by crowns (co) under observation zenith angle teta_o
co=1-exp(-k*sd/cos(teta_o));

% Ground coverage by shadow (cs) under a solar zenith angle teta_s
cs=1-exp(-k*sd/cos(teta_s));

% Geometrical factor (g) depending on the illumination and viewing geometry
g=((tan(teta_o)).^2+(tan(teta_s)).^2-2*tan(teta_o)*tan(teta_s)*cos(phi)).^(0.5);

% Correlation coefficient (p)
p=exp(-g*h/cd);

% _____

% Ground surface fractions (FLIM model)

% Tree crowns with shadowed background (Fcd)
Fcd=co*cs+p*(co*(1-co)*cs*(1-cs)).^(0.5);

% Tree crowns with sunlit background (Fcs)
Fcs=co*(1-cs)-p*(co*(1-co)*cs*(1-cs)).^(0.5)

```

C1: INFORM model (continued)

```
% Shadowed open space (Fod)
Fod=(1-co)*cs-p*(co*(1-co)*cs*(1-cs)).^(0.5);

% Sunlit open space (Fos)
Fos=(1-co)*(1-cs)+p*(co*(1-co)*cs*(1-cs)).^(0.5);

% _____

% Crown transmittance (SAIL model)

% Angles (radian) to angles (degree)
teta_s=teta_s*180/pi;
teta_o=teta_o*180/pi;
% Crown transmittance in sun direction (t_s)
t_s=sail_t_s(lai,ala,0,teta_s,skyl,r_understorey,teta_o,phi,r_needle,t_needle);

% Crown transmittance in observation direction (t_o)
t_o=sail_t_o(lai,ala,0,teta_o,skyl,r_understorey,teta_s,phi,r_needle,t_needle);

% _____

% Forest reflectance (FLIM model)

% Ground factor (G); that is ground contribution to scene reflectance
G=Fcd.*t_s.*t_o+Fcs.*t_o+Fod.*t_s+Fos;

% Crown factor (C); that is crown contribution to scene reflectance
C=(1-t_s.*t_o)*cs*co; % Original formula

% Forest reflectance
r_forest=r_c_inf.*C+r_understorey.*G;
% _____
```

C2: Inversion routine

```
% _____  
  
% NN_INFORM  
% Matlab Neural Network Toolbox 4, page 5-66 - 5-70  
% 24.08.04  
% Martin Schlerf  
  
% Load calibration data  
% PARA_INFORM: Simulated INFORM parameters  
% R_FOREST: Simulated forest canopy reflectances  
% lambda: HyMap wavebands  
load data_cal  
  
% Load validation parameters (LAI_val, CO_val, SD_val) and  
% HyMap spectra (r)  
load data_val  
  
% Position of varying parameters  
Par=[1 6 8];  
  
% Define target  
t=PARA_INFORM(:,Par)';  
  
% Pre-standardise target  
[tn,meant,stdt]=prestd(t);  
  
%Divide target into training and test subsets  
Q=length(tn);  
iitr=[1:4:Q 3:4:Q];  
iite=[2:4:Q 4:4:Q];  
ttr=tn(:,iitr);  
test.T=tn(:,iite);
```


C2: Inversion routine (continued)

```
% Define wavebands
wl=[837.2 1148.4];

for K=1:length(wl)
    pos(K)=find(lambda==wl(K));
end

% Define input vector
p=R_FOREST(pos,:);

% Pre-standardise input
[pn,meanp,stdp]=prestd(p);

%Divide input into training and test subsets
test.P=pn(:,iite);
ptr=pn(:,iitr);
%


---


% Network architecture: 2-layer network, tan-sigmoidal transfer
% function in the hidden layer, linear transfer function in the
% output layer, 1 neurons in the hidden layer, 3 output neurons
% (3 parameters to be estimated), resilient backpropagation algorithm
% (RPROP) for training.
net=newff(minmax(ptr),[1 3],{'tansig' 'purelin'},'trainrp');

% Definition of additional training specifications
net.trainParam.show=5;
net.trainParam.epochs=5000;

% Train network
[net,tr]=train(net,ptr,ttr,[],[],test,[]);

% Pre-standardise HyMap reflectances
[rn]=trastd(r(pos,:),meanp,stdp);
```

C2: Inversion routine (continued)

```
% Estimation of parameters
an=sim(net,rn);

% Unnormalise estimated parameters
[a]=poststd(an,meant,stdt);
% _____

% Compute CO (crown cover) from SD (stem density) and CD (crown diameter)
adapt=0.6;
teta_o=0; teta_o=teta_o*pi/180;
teta_s=30; teta_s=teta_s*pi/180;
phi=0;
CD_est=a(3,:);
k=adapt*(pi*(CD_est/2).^2)/10000;
SD_est=a(2,:);
CO_est=1-exp(-k*SD_est/cos(teta_o));
LAI_est=a(1,:).*CO;
% _____

% Compute validation statistics
r2_LAI=corrcoef(LAI_est,LAI_val).^2;r2_LAI=r2_LAI(1,2);
rmse_LAI=(mean((LAI_est-LAI_val).^2))^0.5;
r2_CO=corrcoef(CO_est,CO_val).^2;r2_CO=r2_CO(1,2);
rmse_CO=(mean((CO_est-CO_val).^2))^0.5;
r2_SD=corrcoef(SD_est,SD_val).^2;r2_SD=r2_SD(1,2);
rmse_SD=(mean((SD_est-SD_val).^2))^0.5;
% _____
```

Acknowledgements

I would like to acknowledge the following people for their highly appreciated support during the course of this research work:

My supervisor, Prof. Dr. Joachim Hill, for his confidence and advice during the past years. The work drew substantial benefit from his expertise; in particular, his experience in radiometric data processing was indispensable for the correction of the hyperspectral imagery

My second supervisor, Prof. Dr. Willy Werner, for his interest in the topic of the work, for thorough discussions on ecological concerns and for providing the chemical analysis of leaf samples

Assistant Prof. Dr. Clement Atzberger (now at ITC, Enschede) for sharing his knowledge of concepts and implementations, and for his enthusiasm, advice and encouragement during the past five years

My colleagues at RSD for their manifold support and for the pleasant and motivating atmosphere, particularly

Jun. Prof. Dr. Michael Vohland for his precursory studies at the Idarwald site, Dr. Thomas Udelhoven for his help with all kinds of statistical concerns and Dr. Thomas Jarmer for his assistance in spectrometric measurements

All student staff who contributed to different aspects of the work. In particular Henning Buddenbaum who significantly supported the research, especially by providing programming codes with polished graphical interfaces; Sebastian Mader for his support in data processing and programming; Samuel Bärtsch for his help with fieldwork at the Idarwald and Gerolstein test sites, for solving any kind of technical problem and for never losing orientation even in the deepest forest

Stephan Seeling for the opportunities he made available to me in the WARELA project

Hermine Marx for her outstanding talent to organize stuff and to make things work

Clement Atzberger Michael Vohland and Achim Röder for correcting the manuscript

Achim Röder and Patrick Hostert for making life in Trier enjoyable

Andreas Müller, Andrea Hausold and Stefanie Holzwarth (DLR, Oberpfaffenhofen) for organising flight campaigns

Dr. habil. Gebhard Schüler (FAWF, Trippstadt), Dr. Werner Schwind and some brave woodmen for their support during fieldwork at Gerolstein test site

The research of this work was partly carried out within the framework of the Sonderforschungsbereich 522 "Umwelt und Region" and the research project "Ableitung biochemischer Forstparameter mit Bildspektrometerdaten", both funded by the Deutsche Forschungsgemeinschaft (DFG). Additionally, the following organisations contributed to this research work: Deutsche Luft- und Raumfahrtgesellschaft (DLR); Forschungsanstalt für Waldökologie und Forstwirtschaft Rheinland-Pfalz (FAWF); University of Trier: Geobotany Department, Department of Biogeography and Remote Sensing Department (RSD).

Finally, I would like to thank my partner Eve who gave me moral support during the whole time of the work.

Lebenslauf

Name: Martin Schlerf
Wohnort: Deutschherrenstrasse 48a, D-54290 Trier
Geburtsdatum: 23.06.1972
Geburtsort: Friedberg (Hess.)
Staatsangehörigkeit: Deutschland

Schulbildung

08/1982 – 07/1991 Ernst-Ludwig-Gymnasium, Bad Nauheim
08/1978 – 07/1982 Grundschule Wettertal, Bad Nauheim

Studium

04/2002 – 09/2003 Promotionsstudium, Universität Trier
10/1999 – 09/2000 International Institute for Geo-Information Science and Earth
Observation, Enschede
Abschluss: Professional Master
10/1993 – 09/1999 Geographie, Justus-Liebig-Universität Gießen
Abschluss: Diplom-Geograph
Thema der Abschlussarbeit: GIS-gestützte Untersuchung von
Permafrost und Hanginstabilitäten im Gornergratgebiet, Wallis

Berufstätigkeit

09/2003 – 2006 Wissenschaftlicher Mitarbeiter im EU-Projekt WARELA,
Universität Trier
04/2003 – 2006 Wissenschaftlicher Mitarbeiter im Fach Fernerkundung,
Universität Trier
10/2000 – 03/2003 Wissenschaftlicher Mitarbeiter im Sonderforschungsbereich 522
„Umwelt und Region“, Universität Trier